THÈSE

Pour l'obtention du grade de
DOCTEUR DE L'UNIVERSITÉ DE POITIERS
UFR des sciences fondamentales et appliquées
Institut de chimie des milieux et matériaux de Poitiers - IC2MP
(Diplôme National - Arrêté du 25 mai 2016)

École doctorale : Chimie, Écologie, Géosciences et AgroSciences Théodore Monod (Poitiers)
Secteur de recherche : Chimie organique, minérale, industrielle

Présentée par :
Hussein Issa

Toolbox of post-synthetic mordenite modification strategies : Impact on textural, acidic, and catalytic properties

Directeur(s) de Thèse :
Ludovic Pinard, Alexander Sachse

Soutenue le 13 juin 2019 devant le jury

Jury :

Président	**Vasile Hulea**	Professeur, École Nationale Supérieure de Chimie, Montpellier
Rapporteur	**Jean-Pierre Gilson**	Professeur, École nationale supérieure d'ingénieurs, Caen
Rapporteur	**Pascale Massiani**	Directrice de recherche CNRS, IMPC, Paris
Membre	**Ludovic Pinard**	Maître de conférences, IC2MP, Université de Poitiers
Membre	**Alexander Sachse**	Chargé de recherche CNRS, IC2MP, Université de Poitiers
Membre	**Tayssir Hamieh**	Professeur, Université libanaise, Beyrouth
Membre	**Joumana Toufaily**	Professeur, Université libanaise, Beyrouth
Membre	**Nicolas Bats**	Docteur, Johnson Matthey, Billingham, Royaume-Uni

Pour citer cette thèse :
Hussein Issa. *Toolbox of post-synthetic mordenite modification strategies : Impact on textural, acidic, and catalytic properties* [En ligne]. Thèse Chimie organique, minérale, industrielle. Poitiers : Université de Poitiers, 2019. Disponible sur Internet <http://theses.univ-poitiers.fr>

THESE

Pour l'obtention du Grade de
DOCTEUR DE L'UNIVERSITE DE POITIERS

(Faculté des Sciences Fondamentales et Appliquées)
(Diplôme National - Arrêté du 25 mai 2016)

Ecole Doctorale : Chimie Ecologie Géosciences Agrosciences « *Théodore Monod* »
Secteur de Recherche : Chimie organique, minérale, industrielle
Présentée par:

ISSA Hussein

****

Toolbox of post-synthetic mordenite modification strategies: Impact on textural, acidic, and catalytic properties

****

Directeur de Thèse : **PINARD Ludovic**, Maître de Conférences -HDR, Université de Poitiers
Co-directeur de Thèse : **SACHSE Alexander**, Chargé de Recherche CNRS, IC2MP, Poitiers

****

Soutenance prévue le 13 Juin 2019 devant la Commission d'Examen

****

JURY

Rapporteurs :	GILSON Jean-Pierre (Professeur, Ecole Nationale Supérieure d'Ingénieurs de Caen)
	MASSIANI Pascale (Directrice de Recherche CNRS, IMPC, Paris)
Examinateurs :	HULEA Vasile (Professeur, Ecole Nationale Supérieure de Chimie de Montpellier)
	BATS Nicolas (Docteur, Johnson Matthey)
	HAMIEH Tayssir (Professeur, Université Libanaise)
	TOUFAILY Joumana (Professeure, Université Libanaise)
	PINARD Ludovic (Maître de Conférences-HDR, Université de Poitiers)
	SACHSE Alexander (Chargé de Recherche CNRS, IC2MP, Poitiers)

Abstract

Zeolites are extremely useful heterogeneous catalysts and find widespread industrial applications. Yet, their extended microporous system leads to rather low efficiency factors and favors the development of secondary reactions that can substantially reduce catalytic selectivity and stability. Hierarchization of zeolites has been proposed as strategy for efficiently reducing the diffusion path length, hence allowing to increase the efficiency factor in catalysis. Among the plethora of disclosed hierarchization strategies, the real impact of the structural and chemical modifications on the catalytic key parameters is oftentimes neglected.

The aim of this PhD thesis is thus to shed light on the effective quality of zeolite hierarchization through the rational study of structure/catalytic property dependency. Mordenite is a zeolite of particular importance due to its strong acidity and monodimensional channel system, which explains why mordenite is industrially extensively employed in a variety of processes including alkylations, isomerizations, dehydrations and aminations.

A toolbox of post-synthetic hierarchization strategies on aluminium rich and poor mordenites has been developed based on basic treatments assisted by CTAB and pyridine at various temperatures (in conventional and microwave heating) and acid HF etching in aqueous and organic medium. A systematic study of over 30 post-synthetically modified mordenites was conducted, which allowed us to assess the impact of each of the hierarchization strategy on textural, morphological, chemical and catalytic properties. Major correlations between structural features and catalytic activity, selectivity and stability in *n*-hexane cracking and toluene disproportionation were deduced. A roadmap on the quality of each hierarchization strategy was thus developed.

Key words: zeolite, mordenite, hierarchization, pyridine, *n*-hexane cracking, toluene disproportionation.

Résume

Les zéolithes sont des catalyseurs hétérogènes extrêmement utiles et trouvent des applications industrielles répandues. Cependant, leur système microporeux étendu conduit à des facteurs d'efficacité plutôt faibles et favorise le développement de réactions secondaires pouvant réduire considérablement la sélectivité et la stabilité catalytique. L'hiérarchisation des zéolithes a été proposée comme stratégie permettant de réduire le chemin diffusionnel, permettant ainsi d'augmenter le facteur d'efficacité en catalyse. Parmi ces différentes stratégies, l'impact réel des modifications structurelles et chimiques sur les paramètres clés catalytiques est souvent négligé.

Le but de cette thèse est donc de comprendre la qualité des differents strategies d'hiérarchisation des zéolites à travers l'étude rationnelle des propriétés de texture et catalytique. Notre étude porte sur la mordénite, cette zéolite relève d'une importance particulière en raison de sa forte acidité et de son système de canaux monodimensionnel, ce qui explique pourquoi la mordénite est largement utilisée industriellement dans divers procédés, notamment l'alkylation d'aromatiques, les isomérisations d'alcanes, et la déshydratation d'alcools.

Des stratégies de post-traitement sur des mordénites riches et pauvres en aluminium ont été développées sur la base de traitements basique assistés par le CTAB et la pyridine à différentes températures (en chauffage conventionnel et par micro-ondes), et par attaque chimique HF en milieu aqueux et organique. Une étude systématique de plus de 30 échantillons a été menée, ce qui nous a permis d'évaluer l'impact de chaque stratégie sur les propriétés texturales, morphologiques, chimiques et catalytiques. Des corrélations majeures entre les caractéristiques structurelles et l'activité, la sélectivité et la stabilité catalytique pour le craquage du *n*-hexane et dismutation du toluène ont été déduites. Une comparison sur la qualité de chaque stratégie a ainsi été élaborée.

Mots-clés : zéolithe, mordénite, hiérarchisation, pyridine, craquage du *n*-hexane, dismutation du toluene.

Acknowledgements

I would like to begin by expressing my gratitude to Dr. Ludovic Pinard for believing in my capabilities, for all the encouragement, for the consideration that he always expressed for me and for my work and for his kindness and attention.

I want to thank deeply Dr. Alexander Sachse for his support and sincere follow-up. He taught me a lot of skills and my study earned more value after his introduction. Without his interest and patience, this Ph. D. would not have been possible.

To Professor Joumana Toufaliy, I present my sincere thanks for her scientific and bureaucratic guidance, and for the availability throughout all these years Moreover, I present my thanks to Professor Tayssir Hamieh for all his contributions.

I wish to thank my lab co-workers of the IC2MP research lab for all the help you have given me during this thesis. A special thanks to all the friends that I have made, in particular to those with which I have shared my office, on the IC2MP during this thesis for their help, good spirit and for all the good memories from the times spent together.

To all the technicians who were part of this success, special thanks for your patience anyway.

To all my family and friends, thank you for being part of my life.

Most important, I am more than grateful to my dad Khalil and mom Nadia, to my sister Lama and her husband Youssef, to my brothers Ali, Wissam, and Hasan for the unconditional support and affection.

I would like to express my gratitude to the "Islamic Association for Guidance and Higher Education" for the financial support during my Ph. D.

Poitiers, 13 June 2019

Hussein Issa

Table of contents

List of Tables

Chapter I

Chapter II

Chapter III

Chapter IV

Chapter V

List of Figures

Chapter I

Chapter II

Chapter III

Chapter IV

Chapter V

List of Schemes

Chapter I

Chapter III

Chapter IV

List of abbreviations

$A^=$	Alkene products
AHFS	Ammonium hexaflurosilicate
B	Bimolecular
BAS	Brønsted Acid Sites
*BEA	Beta
BET	Brunauer, Emmett and Teller
BJH	Barret, Joyner and Halenda
CBU	Composite Building Unit
CCS	Coherent Crystal Size
CHA	Chabazite
CTAB	Cetyltrimethylammonium bromine
EFAL	Extra-Framework Aluminum
EFSI	Extra-Framework silica
FAL	Framework ALuminium
FAU	Faujasite
FER	Ferrierite
FID	Flame Ionization Detector
FSD	Fourier Self-Deconvolution
FT-IR	Fourier-Transform Infrared
FWHM	Full Width at Half Maximum
GC	Gas Chromatography
H.C.	HydroCarbons
HSE	Health, Safety, Environmental
I	Isomers
ICP-AES	Induced Coupled Plasma - Atomic Emission Spectroscopy
IUPAC	International Union of Pure and Applied Chemistry
IZA	International Zeolite Association
LTA	Linde Type-A
M	Monomolecular
MAS-NMR	Magic Angles Spinning Nuclear Magnetic Spectroscopy
MCM-48	Mobil Composition of Matter no. 48
MCM-41	Mobil Composition of Matter no. 41
MFI	Mobil Five
MOR	Mordenite

MR	Membered Ring
MTG	Methanol to Gasoline
MTO	Methanol to Olefin
MTT	Zeolite Type ZSM-Twenty-Three
MTW	Zeolite Type ZSM-Twelve
MWW	Zeolite Type M-twenty-two
OMM	Ordered Mesoporous Materials
Py	Pyridine
PBU	Primary Building Unit
RED	Rotation Electron Diffraction
RH	Alkane Reactant
R^+, R_i^+	Carbenium ions
SBA-15	Santa Barbara Amorphous no.15
SBA-16	Santa Barbara Amorphous no.16
SAPO-34	SilicoAluminophosphate-34
SBU	Secondary Building Units
SCC	Steam Catalytic Cracking
SDA	Structure Directing Agent
SOD	Sodalite
TEM	Transmission Electron Microscopy
TDP	Toluene Disproportionation
TGA	Thermo-Gravimetric Analysis
TMB	Trimethyl Benzene
TOF	Turnover frequency
TOS	Time-on-Stream
TPAOH	Tetrapropyl ammonium hydroxide
TPD	Temperature-Programmed Desorption
TMAO	Tetramethyl ammonium hydroxide
USY	Ultra Stable Faujasite
XRD	X-Ray Diffraction
ZSM-5	Zeolite Socony Mobil –Five
ZSM-12	Zeolite Socony Mobil -Twelve

General Introduction

Zeolites are crystalline aluminosilicate minerals of the family of microporous solids. There exist approximately 40 natural zeolites that can be found in sedimentary and volcanic rocks, such as clinoptilolite, chabazite and mordenite. Additionally, over 240 artificial zeolites have been synthesized by chemists. Zeolites are widely used in agriculture, water treatment, medical fields as dietary supplements for e.g. diarrhea treatment. Moreover, zeolites find massive use in the refining and petrochemical industry, as adsorbents, ion exchangers and catalysts for catalyzing many industrial processes. Their extensive use is ascribable to the versatile properties these materials feature, such as high surface area, hydrothermal and mechanical stability, compositional framework flexibility, non-toxicity, cation exchange capacity, and Brønsted acidity.

The use of zeolites in industrial catalytic reactions is due to their microporous structure, consisting of cages and channels, which sizes are comparable to ordinary organic compounds and in which most of the catalytic active sites are located and where the reactions occur. The unique size restrictions of micropores allow for shape selectivity. Yet, the drawback of this is the reduction of the access rate of molecules into the crystals and the undesired adsorption of the reactants or the products during the catalytic process. This can lead to undesired secondary reactions on the active acid sites, which might cause the deactivation of the catalyst. Furthermore, accessibility issues occur for bulky molecules that cannot enter the micropores, which hence leads to low catalytic efficiency.

The quest to overcome these drawbacks eventually motivated the development of mesoporous materials. The discovery of ordered mesoporous materials with regular pores larger in size than that of micropores (2-15 nm), however, failed to replace the use of zeolites in industrial applications, as these do not possess the unique zeolite properties, such as strong acidity, shape selectivity, confinement effects, and hydrothermal stability. Numerous studies tried to overcome the inconvenience of these mesoporous materials and to generate active sites comparable to those of zeolites. Yet with very little success. Hence zeolite modification strategies are the most promising strategies for controlling diffusion limitation and increase accessibility to active sites, these are: (i) synthesizing zeolites with larger micropores and (ii) reducing diffusion path length through the design of nano-zeolites or hierarchical zeolites.

The synthesis of hierarchical zeolites relies on the development of a secondary mesoporous system to the primary microporous one within the zeolite crystals. Such strategies have proven extremely efficient for reducing diffusion path lengths and increasing accessibility to active sites, hence improving catalytic activity, selectivity and stability.

Two approaches have been developed that permit for the development of hierarchical zeolites: (i) constructive strategies (bottom-up approaches) and (ii) destructive strategies (top down approaches). The constructive approaches rely on the development of the secondary porous system during zeolite synthesis assisted by structural directing agents. In contrast, the destructive strategies rely on post-synthetic treatments of already synthesized zeolites through the selective extraction of atoms from the zeolitic framework. These destructive processes are highly promising due to their simplicity, cost efficiency and negligible HSE concerns (Health, Safety, Environmental issues). In the first chapter of this thesis, a through overview on the different destructive strategies allowing for the development of hierarchical zeolites will be given.

Among the over 240 known zeolite structures, mordenite is one of great importance in petrochemistry and finds applications in toluene disproportionation, alkylation, hydroisomerization, carbonylation, etc. Mordenite features a fascinating pore structure with various levels of microporosity. Yet, it is the particular structural features of this zeolite that renders it extremely prone to diffusion limitations and to catalyst deactivation. Indeed, none of the industrially important zeolites, such as *BEA and FAU present diffusion limitations when used as catalyst in *n*-hexane cracking, except mordenite. It was thus the aim of the present PhD thesis to allow to compare post-synthetic modification strategies of mordenite with the goal to assess their impact on textural, morphological and acidic properties and hence their effect on the catalytic key parameters, which are activity, selectivity and stability. As such, two new post synthetic mordenite modification strategies have been disclosed.

In chapter III, the addition of pyridine during the desilication treatment revealed to impact mordenites properties through a dual action on textural and chemical properties; substantially different in comparison to the classical alkaline treatment or CTAB assisted desilication.

In chapter IV, chemical etching with hydrofluoric acid in pyridine medium has been developed as efficient strategy for the crystal engineering of mordenite zeolites. Contrary to the HF etching in aqueous medium, the etching in pyridine allows to preserve the global composition and acidity of parent mordenites.

Finally, the last chapter of the present thesis presents an overview intended to rationalize the quality of different zeolite hierarchization strategies through the study of structure/catalytic property dependency. To this aim a systematic study of over 50 post-synthetically modified mordenites was conducted, which allowed to assess the impact of each of the hierarchization

strategy on textural, morphological, chemical and catalytic properties. Major correlations between structural features and catalytic activity, selectivity and stability in both the monomolecular *n*-hexane cracking and the bimolecular toluene disproportionation could be deduced.

Chapter I: Literature Review

1. General introduction to zeolites

The term zeolite was coined in 1756 by Swedish mineralogist Axel F. Cronstedt, who observed that upon rapidly heating a natural zeolite mineral, a large amount of water steam was produced that had been adsorbed by the material. Based on this, he named the material *zeolite*, from two Greek words, “zeo” meaning to boil and “lithos” meaning stone.[1] Up to date, 40 zeolites of different structures have been found in nature while more than 240 have been synthesized. The first synthetic zeolites (named X, Y and A) have found widespread applications as adsorbents, catalysts and ion exchangers. Today, much research is focused on the development of new zeolite structures and a huge number of theoretical structures have been proposed based on theortical considerations.[2]

Zeolites are defined as crystallized microporous aluminosilicates, with pore diameters of less than 20 Å. Their particular structure is related to the regular polymeric combination of Primary Building Units (PBU), with tetrahedral geometry. Each oxygen atom, that forms the vertices of the tetrahedra is connected to two trivalent or tetravalent T elements (T = Si or Al) located in the center of each tetrahedron (O-T-O-T-O sequence, illustrated in Scheme I.1). The O / T ratio is thus strictly equal to 2.

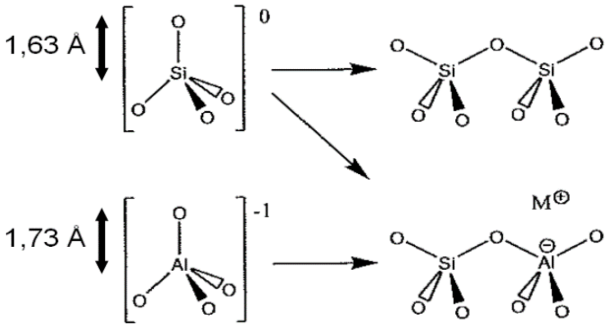

Scheme I.1. Tetrahedral assemblies of SiO_4 and AlO_4^-.

These assemblies of PBU form the meshes or the Secondary Building Units (SBU) of the zeolitic framework. In 2007, 23 SBUs were listed, which can recombine with each other to form one of the 47 Composite Building Units (CBUs). Finally, the periodic assembly of these CBUs in combination with SBUs and/or CBUs build up the zeolite structure, characterized by a single porous network consisting of channels and cavities with defined morphologies and sizes between 0.3 and 1.5 nm. It is to note that micoporous networks with pore sizes of up to 2 nm can be achieved for germanosilicates or metallphosphates (*i.e.* zeotypes).[3,4] Scheme I.2 illustrates various combinations of CBUs, which lead to various zeolite structures.

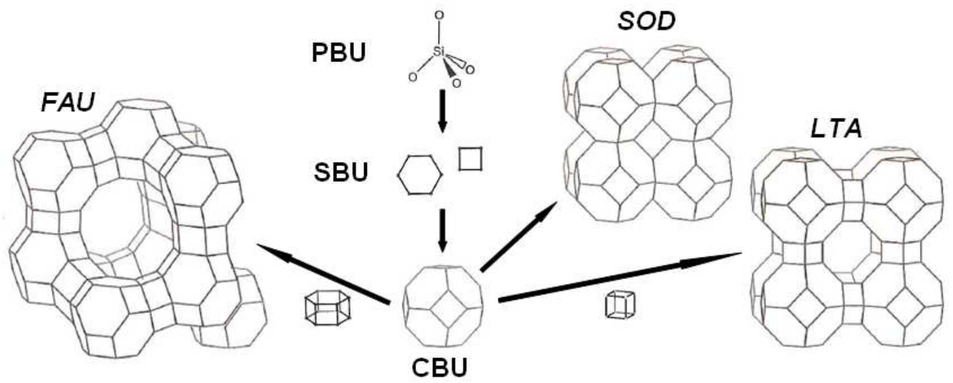

Scheme I.2. Formation of FAU, LTA and SOD zeolite structures from the same “sod” CBU, through combination of PBU and SBUs.

To differentiate zeolite structures, the International Zeolite Association (IZA) defined a three capital letters code for each structure. For example, MOR corresponds to the mordenite structure.

The chemical formula of these aluminosilicates can be written as:[5]

$$|M_{y/q}(H_2O)_z| \ [Si_xAl_yO_{2(x+y)}] \text{ with } q = 1 \text{ or } 2 \text{ and } x/y \geq 1$$

Where M represents an exchangeable cation such as an alkali metal, alkaline earth metal, transition metal, ammonium or a proton and represents as the zeolite active site. The cation compensates the negative charge induced by the presence of trivalent AlO_4^- tetrahedra within the zeolite framework. q is the electronic charge of M and z the quantity of physisorbed water.

The term zeolite designates exclusively aluminosilicates. Zeotypes, crystallize in zeolite structures but part or all of the silicon and/or aluminum is substituted by trivalent elements (Al, Fe, B, Ga, etc.), tetravalent elements (Ge, Ti, Zr, etc.) or pentavalent elements (P, As).[5-7]

The large majority of the active sites of zeolites are located in the micropores. Hence, adsorption and catalytic reactions require the diffusion of organic molecules into the micropores of zeolites. That is why only micropores having opening pores containing at least 8 T atoms (Al and Si) are sufficiently wide to allow for diffusion. Zeolites are classified into four main categories according to their porosity:[5,8]

- Small pore zeolites: the opening of the pores is delimited by 8 T atoms (8 Membered rings) with a free diameter of 0.30 to 0.45 nm (e.g. LTA, CHA).
- Medium pore zeolites: the opening of the pores is delimited by 10 T atoms (10-MR) with a free diameter of 0.45 to 0.60 nm (e.g. MFI).

- Large pore zeolites: the opening of the pores is delimited by 12 T atoms (12-MR) with a free diameter of 0.6 to 0.8 nm (e.g. FAU, *BEA).
- Extra-large pore zeolites: the opening of the pores is delimited by 14 atoms (O or T) with a free diameter of 0.7 to 1.0 nm (e.g. UTD-1)

Some zeolites have combined systems with various pore sizes. e.g. MOR (8 and 12-MRs), MWW (10 and 12-MRs).

The comparison of zeolite pores with the kinetic diameter of organic molecules (e.g. *n*-butane 0.43 nm, isobutane 0.50 nm, benzene 0.58 nm, etc.)[9] suggests that zeolites can be used as molecular sieves.

2. Mordenite

Mordenite is one of the big five zeolites next to ZSM-5, *BEA, FER, and FAU. It is massively used in industry and especially in isomerization and alkylation reactions. The mordenite zeolite features the structural code MOR according to the IZA classification. Mordenite is a natural zeolite and presents Si/Al ratios of about 5.[10] Leonard was the first who synthesized mordenite in 1927, from feldspar (colorless crystals that consist of calcium, potassium and sodium aluminosilicates and alkaline carbonates) at 200 °C, 15 atm and 7 days. However, the characterization of the product has been questioned. The first qualified synthesis of mordenite was achieved by Barrer.[11] In this study, mordenite crystallised in good yield from an aqueous suspension of sodium aluminosilicate gel of composition ranging from Na_2O, Al_2O_3, $8.1SiO_2$, nH_2O to Na_2O, Al_2O_3, $12.3SiO_2$, nH20. The temperature range was 285-295 °C and the pH range was between 8 and 10 in the cold mother-liquor after crystallisation.[11]

Due to its unique textural properties and strong acidity, mordenite has been widely employed as heterogeneous catalyst in the petrochemical industry. Its superior acidic and shape selective properties are used in numerous processes, such as toluene disproportionation, alkylation, hydroisomerization, carbonylation, etc. (Table I.1).

2.1 Structure of mordenite

Mordenite belongs to the category of large pore zeolites. Its framework is formed by the intergrowth of 5-linked atoms laterally to form a three-dimensional network (Figure I.1). This stack generates two one-dimensional porous systems in the [001] direction. The first is in the form of channels with 12-MR (7.0 x 6.5 Å), which communicate with each other through apertures of 8-MRs (3.4 x 4.8 Å), these are also named side pockets. The second is a network of one-dimensional channels of 8-MRs (2.6 x 5.7 Å), which are adjacent to the 12-MRs. Mordenite crystallizes in the orthorhombic system (Cmcm, a = 18.1 Å, b = 20.5 Å, and c = 7.5 Å, network density: 17.2 T / 1000 Å^3) for a Si/Al ratio of 4 ([$Al_8Si_{40}O_{96}$]-MOR).[12,13]

In practice, mordenite is considered to be a one-dimensional zeolite, because the 8-MRs are too narrow for most organic molecules, which can hence only diffuse in 12-MRs channels. This fundamental characteristic has very important implications on the properties of this zeolite. First, single-dimensional mass transfer is intrinsically slower than three-dimensional diffusion. The diffusion is even slower when the size of the molecules is close to that of the pores, thus forcing them to move like an ordered chain of particles, which cannot cross each other (single-file diffusion).[13] This implies that, under the typical operating conditions of a reaction, only a small fraction of the pore volume is accessible to the molecules; in this case that one which is close to the pore openings (low effectiveness factor). Furthermore, a one-dimensional porous system is very sensitive to the effects of pore blockage. Indeed, a channel becomes totally inaccessible if it is blocked near the opening of the pore.[12]

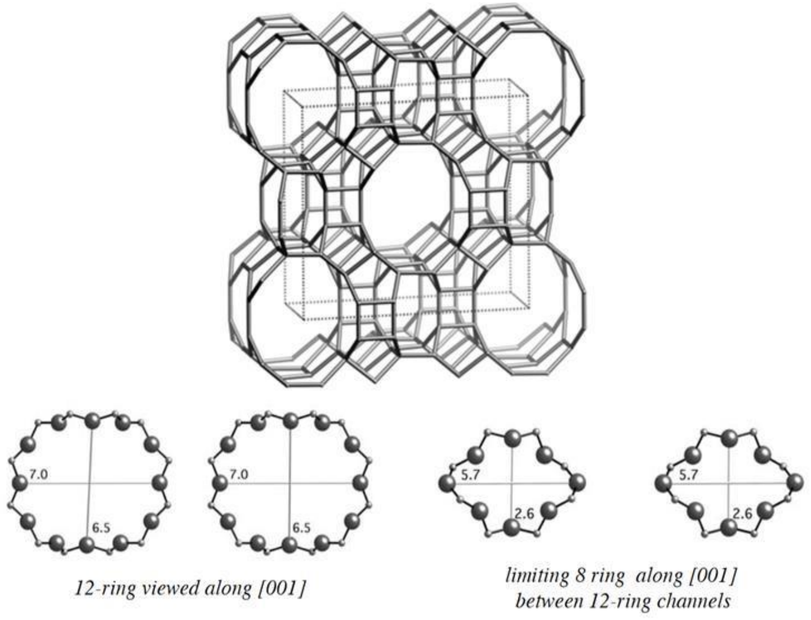

Figure I.1. Structure of mordenite.[13]

2.2 Acidity of mordenite

Most of hydrocarbon reactions as well as many transformations of functionalized compounds are catalyzed by Brønsted sites rather than Lewis sites. Protonic acidity originates from protons that compensate the negative charge of the AlO_4^- tetrahedra and has the form of bridged hydroxyls (Al(OH)Si). Other types of hydroxyl groups are present after post synthetic treatment of zeolites, e.g. through dealumination: silanol groups, hydroxylated extra-framework aluminum species (EFAL), etc. In some cases, these hydroxyl groups have a sufficient acidic force to catalyze certain reactions.[5]

In acid catalysis, the activity of a zeolite depends on the number of proton sites and their activity. The activity of proton sites depends on their location (accessibility), their strength (the stronger the site, the more active it is) and their concentration.[5] Lewis sites may have an indirect effect on acidity through increasing the acid strength of neighboring proton sites. Yet, they do not intervene directly in catalytic reactions.[5]

Dehydroxylation and dealumination generate EFAL species (octahedral or tetrahedral aluminium atoms),[5,14] together with tri-coordinated Al located in the structural defects are responsible for the Lewis acidity in the zeolites. There are numerous types of Lewis acid sites in zeolites, such as: Al^{3+}, AlO^+, $Al(OH)^{2+}$, $Al(OH)_2^+$, AlOOH, Al_2O_3 (neutral Al), $\equiv Si^+$ (silicate species).[15,16]

The protonated oxygen of the bridged hydroxyls forms three different bonds. The high electronegativity of the oxygen atom allows a displacement of the electron from the hydrogen towards the first. Consequently, the positive charge transfer to the hydrogen gives the O-H bond a weak ionic character that can be easily broken. This explains why Brønsted acid sites (BAS) are at the origin of the proton mobility over the zeolite structure as shown in Scheme I.3.[5,17,18]

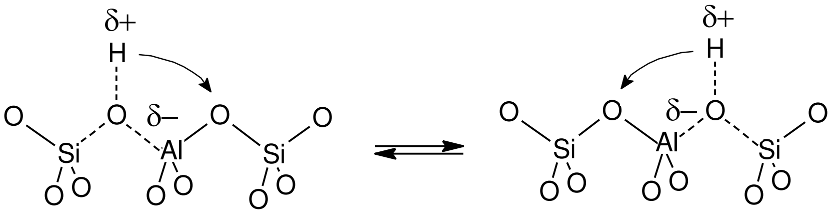

Scheme I.3. Proton mobility in a zeolite.

The maximum number of protonic sites is theoretically equal to the number of framework aluminium (FAL) atoms, but the actual number is smaller due to incomplete cation exchange, dihydroxylation, and dealumination during activation at high temperature.

Numerous parameters affect the acid strength, which are illustrated in Scheme I.4

The acidic strength of the protonic sites depends on the amount of alkaline cations present in the zeolite. The acid strength further depends on the angle of the TOT connection. The larger the angle, the higher the acidic strength: thus the H-MOR proton sites (angle of 143° to 180°) are stronger than those of H-MFI (133° to 177°) and H-FAU (138° to 147°).[5]

Confinement effects have furthermore been put forward to explain acid strength in zeolites. Iglesia *et al.*[19] have shown that the Brønsted acidity increases with increasing confinement. As that, the protonic sites in the 8-MRs are stronger than those located in the 12-MRs.

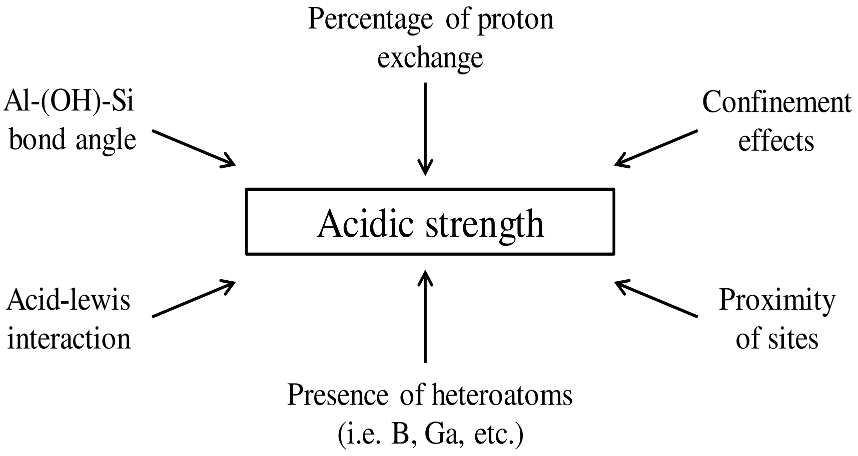

Scheme I.4. Parameters determining the acidic strength of the protonic sites.

The interaction energy of ammonia with the acidic sites is typically used to compare the strength of protonic sites.[20] The majority of the protonic acid sites of mordenite (Si/Al = 13) have an average enthalpy of NH_3 adsorption of 160 kJ mol^{-1},[20] while it is 150 kJ mol^{-1} for H-ZSM-5, H-ZSM-12, and H-Y.[21] In addition, the adsorption enthalpies for pyridine are between approximately 200 and 210 kJ mol^{-1} for H-ZSM-5, H-ZSM-12, and H-MOR but only180 kJ mol^{-1} for H-Y.[21]

The mordenite zeolite contains four crystallographically different T atoms (T1-T4) that are linked to ten crystallographically distinct oxygen atoms (O1-O10). Therefore, in principle, there could be ten different acidic hydroxyls (BAS) associated with these ten oxygen atoms, e.g., O1-H, O2-H, O3-H, etc. Obviously, the accessibility and catalytic properties of the BAS in various locations should be very different due to the different local environments of O1-O10 atoms (Figure I.2).

Thus, to understand the catalytic properties of the distinct BAS in mordenites, the number and the exact positions of these distinct BAS should be known. Several attempts have been sought in experimental and theoretical studies for a long time to achieve this issue. The early crystallographic studies of the single crystals of the natural H-form mordenite (ptilolite) have shown that there is no preferential attachment of protons to any particular framework oxygen atoms,[23] thus indicating the possibility of a variety of distinct BAS. This result is in agreementwith theoretical studies of the exact location of BAS mordenite zeolites that (i) reveal that there is no significant difference between different locations in term of energy[24,25] and (ii) designate different locations for the most energetically favorable sites when carried out by different research groups that utilize different methods, e.g. sites O2-H and O6-H,[24] site O3-H,[25] and site O7-H.[26] In contrast, many authors that studied the distribution of BAS in mordenites by Infrared spectroscopy considered acidic sites in mordenites as two populations only; one being located in the small 8-MR channels or/and side pockets and another one in the large 12-MR channels.[27,28] This consideration was based on the deconvolution of the observed asymmetric IR band at ~3610 cm^{-1} into two components with low and high frequency. The low frequency component was perturbed by adsorption of small molecules (*i.e.* NH_3)[29] but was not influenced by adsorption of bulkier molecules (benzene or cyclohexane), suggesting that relevant OH groups are located in the 8-MRs of the mordenite framework.[28]

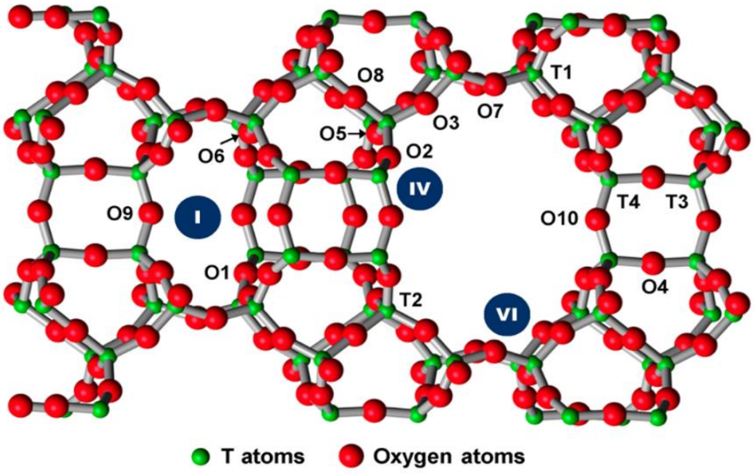

Figure I.2. Structure of the MOR zeolite shown alongside large 12-MRs and small 8-MRs channels with three positions of Na^+ cations (I, IV and VI).[22]

The low frequency vibration band is thus generated due a strong interaction of the OH groups in the side pockets with the neighboring oxygen atoms under the action of hydrogen bonding, in agreement with the pioneering work of Jacobs and Mortier who noticed that OH groups vibrating in 8-MRs undergo a shift to lower wavenumber when compared to the frequency of OH groups vibrating in 12-MRs.[30] However, three different cationic sites were determined for sodium cations in defect-free Na-mordenite samples (positions I, IV, and VI in

Figure I.2)[31] which implies three different locations of negative charge to compensate and thus three different Brønsted acidic OH types in the framework of H-mordenite after exchange of sodium cations by protons. Further differentiation between BAS in mordenites has been proposed in different experimental and theoretical studies,[24,25,32-35] but the proposed numbers of distinct BAS varied (from 3 to 5) and the assignments of these BAS to particular oxygen atoms were contradicting. For example, the preferred location of BAS in the small channels was identified on O1,[25,35] O6,[24,34,36] and O9[32,33,35] atoms, however all research groups considered the presence of only one distinct type of BAS in the small channels. The agreement was also quite poor on the exact locations of BAS in the large channels, since, in fact, all possible locations available in these channels (see Figure I.2) were suggested by different authors: O2,[24] O3,[25] O2 and O7,[32,33] O5 and O10,[34] O2, O5 and O10.[35] To remove these contradictions, Lukyanov and coworkers reported the first application of the Fourier self-deconvolution (FSD) method for the analysis of infrared (IR) spectra of functional groups in porous materials.[37] By this method, they concluded that the asymmetric band at 3610 cm^{-1} in the IR spectra of acidic mordeinte zeolites is, in fact, a superposition of six individual bands, which they tentatively assigned to acidic hydroxyls located in the large and small channels of the mordenite structure[37] (Figure I.3).

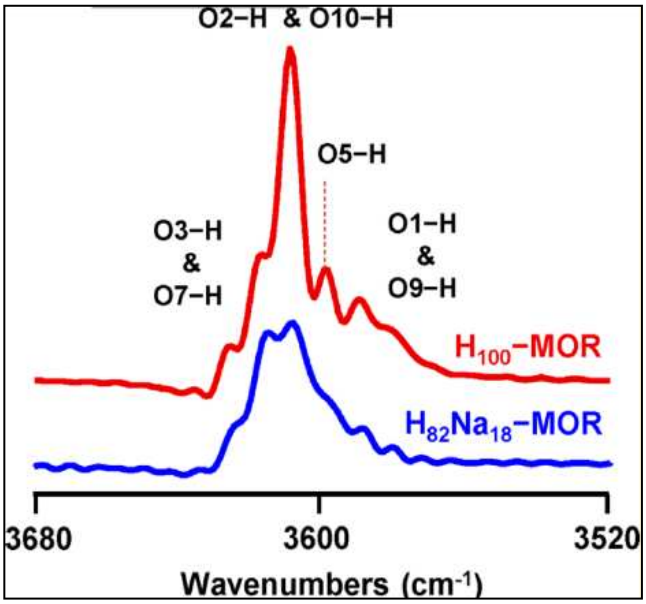

Figure I.3. FSD traces of the IR spectra of H-MOR and $H_{82}Na_{18}$-MOR zeolites.[22]

This attempt was successful to rationalize the apparent discrepancies between different locations of BAS in mordenites proposed in the literature, but it did not identify the exact locations of BAS. Aditionally, the contradiction between the finding of six distinct locations of

BAS in mordenites[37] and the theoretical prediction[33] of the existence of maximum four possible locations was not explained. Another study of the same group was undertaken with the to verify their initial data on the existence of six distinct BAS in the mordenite structure[37] and to generate insights into exact locations of these Brønsted acid sites.[22] They investigated the Fourier-transform infrared (FT-IR) of BAS present in the purely acidic and partially Na-exchanged mordenites. As a result, they confirmed their previous suggestion about the existence of the six distinct BAS into mordenite zeolite. This conclusion contracted the earlier prediction of just four distinct BAS in mordenites. The assignment of the six single IR bands, revealed clearly in the FSD trace of the IR spectra of the protonic and partially Na-exchanged mordenites, completed depending on the experimental data of adsorption of ammonia and *n*-hexane and the structural information available in the literature. Two single bands at 3581 and 3590 cm^{-1} were related to acidic hydroxyls O1-H and O9-H that vibrate in the 8-MR channels and thus linked to the Na-exchange position I, as can be shown in Figure I.2. The 3599 cm^{-1} single band was related to O5-H hydroxyls that can vibrate in the intersection between the small and large channels and the 3609 cm^{-1} single band was corresponded to O2-H or/and O10-H hydroxyls vibrating in 12-MR channels. These three hydroxyls (O2-H, O5-H, and O10-H) were associated with the Na-exchange position IV (Figure I.2). The last two single IR bands at 3617 and 3625 cm^{-1} associated with O3-H and O10-H hydroxyls located in the 12-MR channels and responsible for the Na-exchange position VI. Moreover, the authors quantitatively estimated the amount of each distinct BAS in the purely protonic and partially sodium exchanged mordenites using the six-band deconvolution method, which shows that in the purely acidic mordenite about 25% of BAS are located in the 8-MR channels, 13% of BAS are at the intersections between the side pockets and the 12-MR channels and ~ 62% of BAS are located in the 12-MR channels (~39% for O2-H or/and O10-H hydroxyls and the remaining 23% for O3-H and O7-H hydroxyls).

3. Modification of zeolites

The presence of micropores in zeolites gives rise to their use as shape selective catalysts. Yet, the presence of micropores leads to important diffusion limitations of reactant molecules to and from the active sites, especially in reactions involving bulky molecules, which severely restricts the range of catalytic applications.[38] In addition, the purely micropores system decreases catalyst lifetime through deactivation by e.g. carbonaceous species adsorbing on or blocking active sites.[39,40] Moreover, a reduction of the selectivity of the catalytic process can occur as a result of secondary reactions that are favored by several acidic steps, such as rearrangements and further cracking.

3.1 Structure related restrictions on mass transfer

In reaction engineering, the degree of catalyst utilisation can be measured using the effectiveness factor (η) (Figure I.4). The effectiveness factor relates the observed reaction rate with the intrinsic reaction rate. Its value is equal to one when all the catalyst active sites participate to the catalytic event and is observed when the reaction rate equals the intrinsic reaction rate. In this case, the reaction operates in the chemical regime, *i.e.* free of any diffusion limitations.

Concentration profile

$$C = C_s \frac{\cosh(\frac{\phi X}{L})}{\cosh(\phi)}$$

Thiele modulus

$$\Phi = \frac{r_{intrinsic}}{r_{diffusion}} = L\sqrt{\frac{k_v}{D_{eff}}}$$

Effectiveness factor

$$\eta = \frac{r_{observed}}{r_{intrinsic}} = \frac{\tanh \phi}{\phi}$$

Where C is the observed concentration, Cs is the substrate concentration, X is the distance from the interface, L is the characteristic length of the catalyst crystals, ϕ is the Thiele modulus, $r_{intrinsic}$ is the intrinsic reaction rate, $r_{observed}$ is the observed reaction rate, $r_{diffusion}$ is the diffusion reaction rate, D_{eff} is the effective diffusion coefficient (Diffusivity), k_v is the rate constant of reaction and η is the effectiveness factor.

Baur and Krishna[41] addressed the applicability of classical definitions of Thiele modulus and effectiveness factor for zeolites using the above three relevant equations, derived assuming steady-state diffusion and reaction, slab model, first-order irreversible reaction and isothermal conditions. The effectiveness factor is inversely proportional to the Thiele modulus.

The transport limitations strongly impact the three key parameters of heterogeneous catalysis: activity, selectivity and stability (lifetime). The Thiele modulus can be minimized through: (i) enhancing the effective diffusivity D_{eff} and/or (ii) shortening the diffusion path length L in the zeolite pores. The intrinsic rate coefficient k_v is fixed for a given reaction and zeolite. Since the 1990s, ordered mesoporous materials (OMMs) with regular pores (2-15 nm) have intensively been developed.[25,42,43] MCM-41 is prototypical in this series. It features a monodimensional ordered array of non-intersecting hexagonal channels (2-10 nm). In such mesopores bulk or Knudsen diffusion is typically observed, which features higher diffusivity in comparison to the microporous zeolites, with intracrystalline diffusion. However, the use of OMMs as catalysts presents several drawbacks, which do not allow to replace the use of zeolites in industrial applications. With the aim to overcome this inconvenience, numerous studies have aimed to chemically modify the amorphous walls in OMMs to generate active sites similar to those of zeolites by e.g. crystallisation[44] or grafting.[45] These are however often complex and time consuming. Hence, alternative approaches have been developed to enhance the accessibility of the active acid sites in zeolites. Two main strategies have been put forward: (i) increasing the size of the micropores or (ii) shortening the diffusion path length. For several decades, the scientific community succeeded to produce new “wide-pore” and “large-cavity” zeolites (up to 2 nm), featuring 16 MRs or more. Most of these are low-framework density structures such as UTD-1[46] which yet feature the same drawbacks as OMMs, *i.e.* monodirectional pore systems, low acid content and low thermal stability. Later, wide-pore zeolites with multidirectional channel systems have been prepared further realising the “promise of emptiness”.[47]

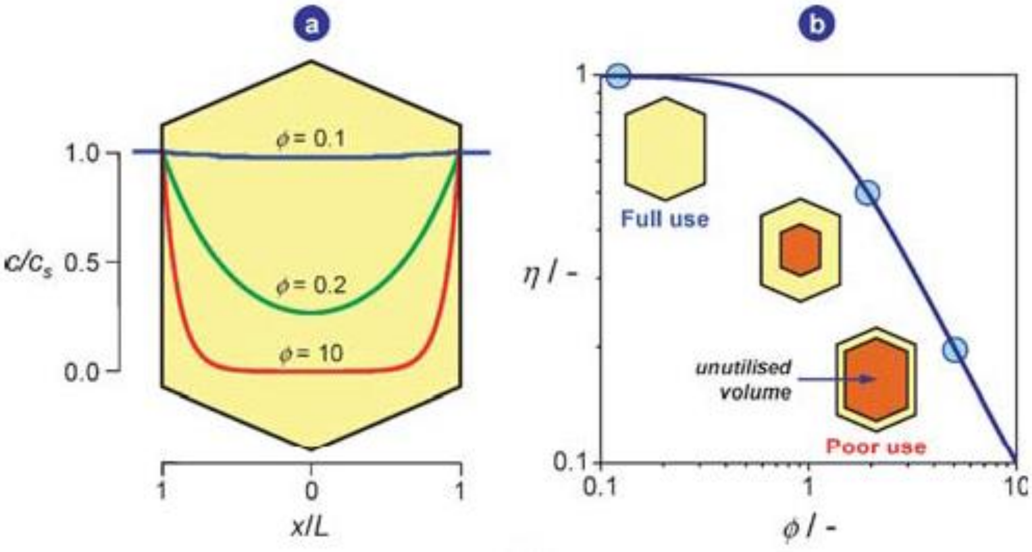

Figure I.4. Concentration profiles across a zeolite crystal (slab geometry) at various values of the Thiele modulus, ϕ (a). The dependence of the effectiveness factor on the Thiele modulus is presented in (b).

One strategy to reduce the diffusion path length in zeolite is the shortening of crystal size *i.e.* fabrication of so-called nanozeolites. A further strategy consists in introducing secondary, interconnected mesoporous system, to give hierarchical zeolites.[48] These improved zeolites furthermore enhance the accessibility of bulky molecules into and out of the pores. The shortening of the diffusion path length permits to reduce the residence time, thus limiting the occurrence of successive reactions, which may lead to the formation of molecules responsible for the deactivation and hence allow increasing catalyst life time.[49,50] Intensive efforts have been dedicated to the synthesis and fabrication of hierarchical zeolites with combined micro- and mesoporous networks,[51,52] and can be divided into (i) bottom-up and (ii) top-down approaches.[53]

3.2 Bottom-up strategies for the development of hierarchical zeolites

Over the last 20 years, important progress has been achieved in developing constructive methods to prepare hierarchical zeolites. These include zeolitization of mesoporous material,[54] double or multiple templating synthesis,[55,56] assembly of nanozeolites or recrystallization,[57,58] as summarized in Figure I.5.

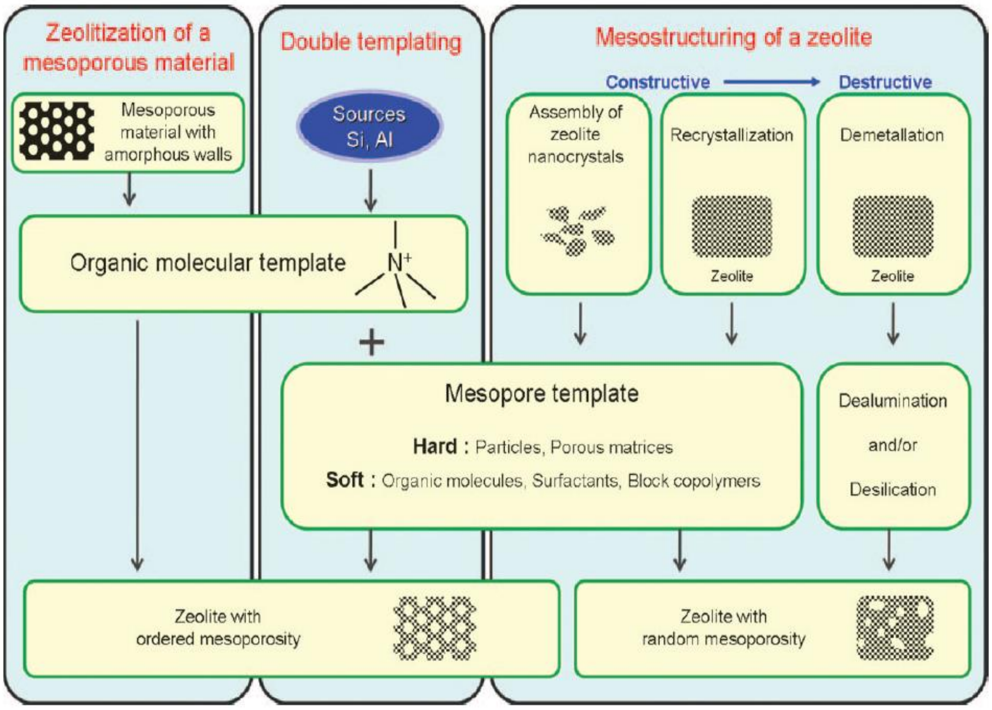

Figure I.5. Brief overview on the various synthesis routes towards hierarchical zeolite materials.[53]

Almost all of these synthetic approaches require the usage of high amounts of organic agents. Their high cost is a major drawback and difficult to apply on large industrial scale synthesis.

3.3 Top-down strategies for the development of hierarchical zeolites

The generation of mesopores in zeolite crystals can be achieved through selective extraction of atoms from the zeolitic framework. As zeolites are considered aluminosilicates, the two most important processes are dealumination and desilication. Much promise is held by these processes, due to their simplicity, cost efficiency and negligible HSE concerns (Health, Safety, Environmental issues).

3.3.1 Dealumination of zeolites through acid treatment and steaming

Dealumination can be achieved by hydrolysis of the Al-O-Si bonds of the zeolite framework through calcinations,[59,60] steaming,[53] acid leaching,[61,62] or other chemical treatments.[53] During the removal of aluminium atoms, hydroxyl nests or internal defects form, which are at the origin of a partial collapse of the framework, thus generating mesopores (Figure I.6). This demetallation type can be used to control the density and the strength of acid sites by increasing the Si/Al ratio of low-silica zeolites.[53]

During thermal treatment, part of the aluminium atoms are removed from the framework to form EFAL species. The bulk Si/Al ratio of the zeolite remains constant and the aluminium species deposit in the pore channels and/or on the external surface, which leads to partial clogging of the micropores. A mild acidic treatment can be applied in order to remove EFAL species to recover micro- and mesoporosity without further extraction of FAL, which hence leads to an increase of the Si/Al ratio.

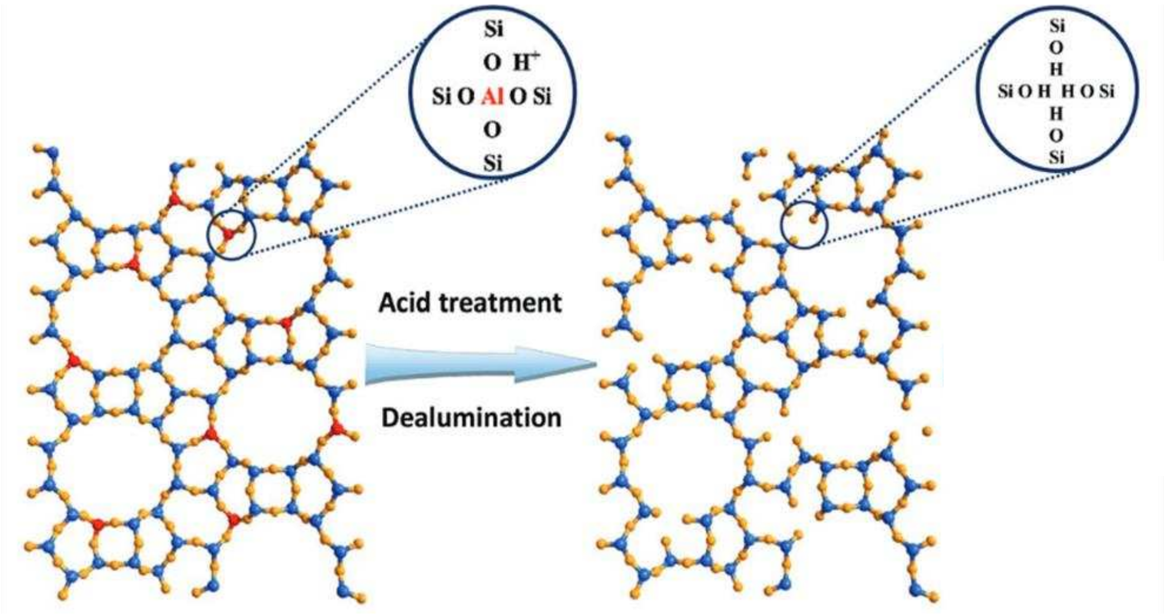

Figure I.6. Formation of mesopores by dealumination treatment in acid medium.[63]

Dealumination can also be carried out via hydrothermal treatment called steaming. It is usually performed at temperatures above 500 °C. The use of steam greatly enhances the mobility of aluminium and silicon species within zeolite crystals.[64] Aluminium is removed from the framwork and causes amorphization of the framework and defects in the zeolite structure. The amorphous material containing mobile alumina and silica species heal part of the framework vacancies. A mild acidic leaching is usually performed to complete the extraction of EFAL species in the form of soluble oxo-anions from pores.[65,66] Concentrated aqueous acids are further efficient for extracting aluminium directly from the zeolite framework (mineral or organic acids). Treatment with certain chemical agents, such as ammonium hexafluorosilicate [$(NH_4)_2F_6Si$] and silicon tetrachloride ($SiCl_4$), can further lead to dealumination. The dealumination by chemical treatments requires a meticulous control of the operating conditions (concentration, pH, temperature) to generate mesopores without the collapse of the zeolite structure.[67,68]

Despite its simplicity, dealumination can lead to some important drawbacks. Partial amorphisation of zeolitic framework leads to a reduction in crystallinity, decreases the amount of acid sites and leads to pore blocking through amorphous debris.[69] Moreover, it is difficult to control the size distribution of mesopores through dealumination.[70,71] Additionally, the treatment is restricted to aluminium-rich zeolites (Si/Al generally less than 10).[5]

3.3.1.1 Dealumination by ammonium hexafluorosilicate (AHFS)

In spite of extensive dealumination of zeolites by various methods, only a limited number of studies have focused on the dealumination of zeolites with AHFS.[72] For large pore zeolites, such as FAU zeolites, an aluminium gradient in the framework after AHFS treatment has been evidenced, which indicates that the process is diffusion controlled.[73] This treatment can hence be used for medium or small pore-size zeolite for selective dealumination of the outer surface of the crystallites, hence eliminating the nonselective acid sites.

Garralon *et al.* concluded that the concentration gradient of aluminium is not only due to a selective removal of aluminium but also to a deposit of silica.[74] In addition, Guisnet *et al.* found a slight decrease in the crystallinity and in the unit cell volume of mordenite zeolite after AHFS treatment. This decrease was expected from the substitution of aluminium atoms in the framework by silicon atoms.[75]

Kao *et al.* investigated the effect of AHFS treatment in the presence and absence of NH_4OAc on the nature of EFAL species in mordenite zeolite.[72] They concluded that, the dealumination in the presence of NH_4OAc extracted Al^{3+} that reacted with F^- to form $(NH_4)_3AlF_6$ species, accompanied by structural defects (silanol groups). Without NH_4OAc, the solution was too acidic and led to the hydrolyzed SiF_6^{2-}, which reacted with both terminal silanols (Si-OH) and Al-OH moieties of intermediate products to form Si-F groups and aluminiumhydroxyflouride ions (AlF_6^{3-}). In the same study, the degree of dealumination was also investigated. In both treatments, the dealumination with a total amount of AHFS corresponding to 100% of total aluminium content of H-MOR resulted in only approximately 13% dealumination.[72] While, on the dealumination of ZSM-5 and Y zeolites, AHFS removed 24% and 50% of FAL atoms, when a total amount of AHFS corresponding to 100% of FAL atoms was used.[74] Therfore, mordenite zeolite is more resistant to AHFS dealumination than zeolite Y and ZSM-5.

3.3.2 Desilication of zeolites through alkaline treatments

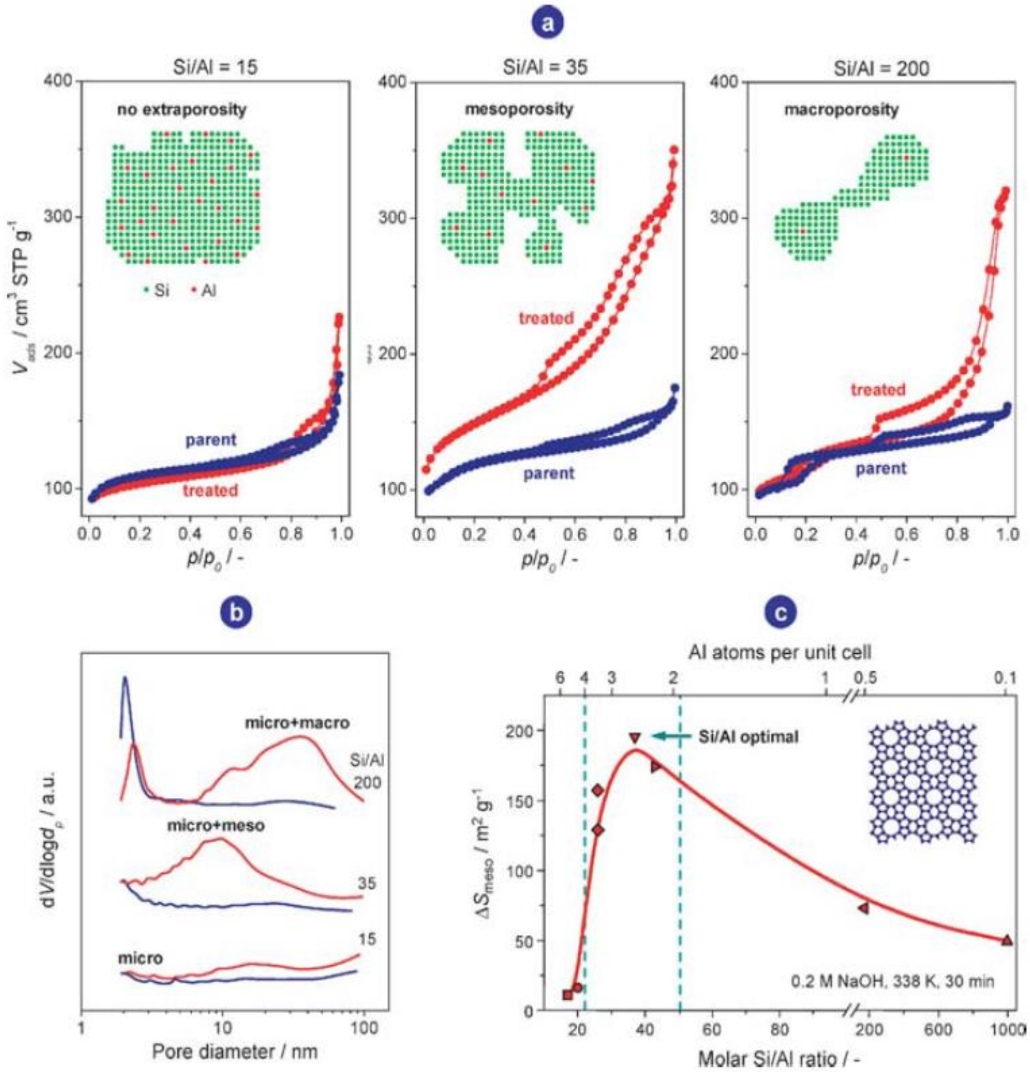

Figure I.7. a) Nitrogen adsorption/desorption isotherms at 77 K for ZSM-5 with Si/Al ratio equal 15, 35, and 200. b) Barret, Joyner and Halenda (BJH) pore size distribution. c) Developed Brunauer, Emmett and Teller (BET) surface area as a function of the molar Si/Al ratio.[51]

Alkaline treatment is a further strategy that allows to create mesoporosity in zeolites through the selective removal of silicon from the framework.[76-78] This method was reported in a patent, in which the selective extraction of silicon from non-dealuminated mordenite through exposure to alkaline solutions was reported.[76] Desilication is more attractive than dealumination, because it yields lower Si/Al ratio with little changes in acid sites.[51,79] An increase of the mesoporous volume and hence in external surface area of desilicated zeolites results by the treatment.[80,81]

As shown in Figure I.7, the introduction of mesopores through desilication strongly depends on the Si/Al ratio. An optimal ratio, to achieve well-controlled mesopores, has been found to be between 25 and 50.[51,79] At lower ratios, as further suggested by Cizmek *et al.*,[82] aluminium significantly slows down the dissolution kinetics, by suppressing the extraction of neighboring silicon species. In this case smaller meso- and macropores are formed, due to unselective extraction of excessive silicon atoms.

A linear relation between zeolite crystal size and desilication rate exists. The extraction of silicon species decreases for small crystals. The presence of crystalline defects increases the desilication rate.[78]

The additional porosity is created by preferential extraction of Si species from the framework through hydrolysis by hydroxyl anions (OH^-). Desilication can be produced by inorganic bases, such as NaOH, Na_2CO_3, $NaAlO_2$, KOH, LiOH, etc.[48,53] First, the hydroxyl group attacks the silicon atom and leads to hydrolysis. Water molecules then extract silicon from the framework as $Si(OH)_4$.[83] The vacancy left by the silicon extraction is at the origin of the mesopore developed (Scheme I.5).

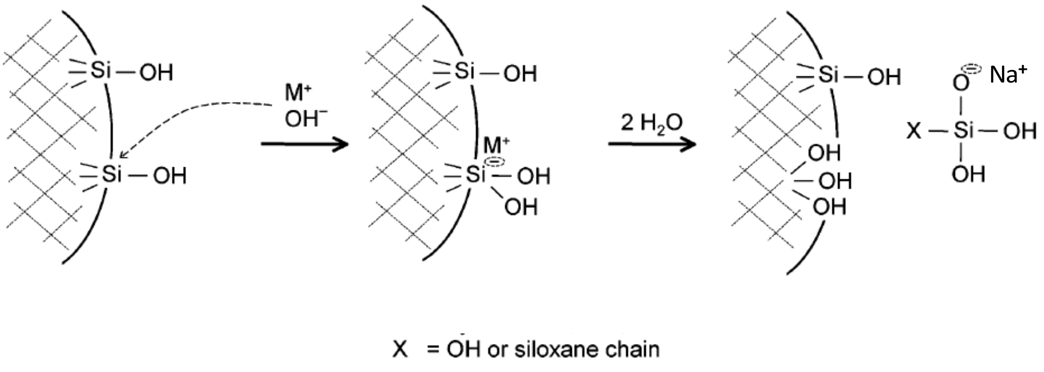

Scheme I.5. Silicon hydrolysis from the zeolite framework in the presence of alkali hydroxides.[48]

Besides the desilication by inorganic bases, zeolites were subjected to organic bases such as organic quaternary ammonium hydroxides (e.g. tetrapropyl ammonium hydroxide (TPAOH), tetramethyl ammonium hydroxide (TMAO), etc.). But, these organic bases are less reactive and less selective on the extraction of silicon than the inorganic counterparts.[53] Their use requires higher temperatures and/or longer reaction times for effective mesopore development.

Groen *et al.*[84] studied the effect of the EFAL species that resulted from previous dealumination, during basic treatment of ZSM-5. They found that the EFAL species prevent the removal of framework silicon. Hence, the independent tailoring of porous and acidic properties can only be successfully accomplished by a successive combination of treatments in which the desilication treatment is performed first followed by dealumination.

AHFS treatment leads to a silica-rich surface,[73,75,85] and intracrystalline mesopores in the zeolite crystals.[86-88] Perez-Ramirez and coworkers found that mesoporous zeolites could be prepared through the combination of AHFS and alkaline treatment.[89] Shen *et al.* further found that AHFS treatment was the crucial factor for the sequential base treatment to form high mesoporous volume in zeolites. Defects generated through AHFS treatment played a crucial role in providing paths for base treatment and increased its efficiency (Figure I.8). The authors named the entire modification procedure: “mesopores formation induced by defects”.[90]

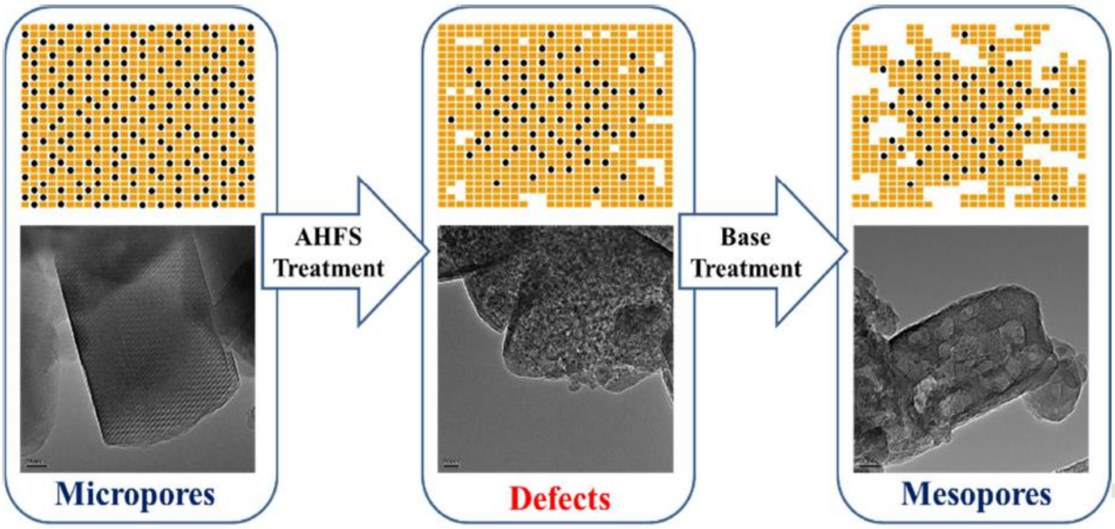

Figure I.8. Mesopores formation in Y zeolite through desilication induced by defects that result from AHFS treatment.[90]

3.3.3 Alkaline treatment in the presence of surfactants

As mentioned before, the optimal Si/Al ratio for desilication, has been found to be between 25 and 50. This range has been expanded to lower and higher ratios by using subsequent acid leaching step[91] and adding surfactants to the alkalin solution.[92] To date, the postsynthetic treatment of zeolites with basic solution in presence of surfactants has allowed to develop two strategies: (i) surfactant-templating[93] (zeolite mesostructuring)[94] and (ii) dissolution-reassembly, which is also referred as pseudomorphic transformation[95,96] or zeolite recrystallization.[97,98]

The first approach avoids the partial dissolution of the zeolite while the second one allows it prior to the addition of the surfactant. In addition, the surfactant-templating route only involves the treatment of the zeolite in mild alkaline conditions (pH = 9-12) within the surfactant, while the dissolution and recrystallization method depends on a two-step process in which the zeolite is first subjected to severe alkaline conditions (0.75-3 M NaOH, for 0.5 - 1 h) followed by the addition of the surfactant and pH adjustment at 8.5.[98-100]

The properties of the obtained materials strongly rely on the treatment conditions and importantly on the basicity of the solution.[101] More specifically, in the case of the dissolution-reassembly process, the intensity of alkaline treatment in the first step controls the degree of the dissolution of the zeolite. When the pH is lowered by the addition of the surfactant, the reassembly of the dissolved silicates around micelles is induced, which leads to the formation of a mesoporous amorphous phase. Moreover, if the severity of the dissolution step is moderate, the production of composite materials containing partially dissolved zeolites and a precipitated mesoporous phase are obtained.

The relative amounts of crystalline/amorphous phase depend on the degree of zeolite dissolution (Figure I.9 RZEO-1 and RZEO-2). Furthermore, if very severe basic conditions are used, the zeolite is completely dissolved and a purely mesoporous material is recovered which features no microporosity (Figure I.9 RZEO-3) [98] The mechanism for mordenite has been claimed to depend first on the dissolution step, by adding the zeolite to the alkali solution and then, after the pH is decreased and the surfactant added, on the assembly of the dissolved species around the micelles of the surfactant leading to the production of the amorphous mesoporous phase with some zeolite fragments, as RZEO-3 in the Figure I.9.

Contrary to the dissolution and reassembly procedure, surfactant-templating process depends on the mesostucturing of the zeolite crystals not on dissolution/desilication of the zeolite. This is obtained by adding the zeolite to the organic or inorganic basic solution in presence of surfactants (pH = 9-12) over a wide range of temperatures (25-150 °C).[102,103] In addition, the zeolite structure and the Si/Al ratio play an important role to prevent the zeolite dissolution and control the amount of introduced mesopores.[104] Consequently, this process yields hierarchical zeolites featuring intracrystalline mesopores (Figure I.9 MZEO).

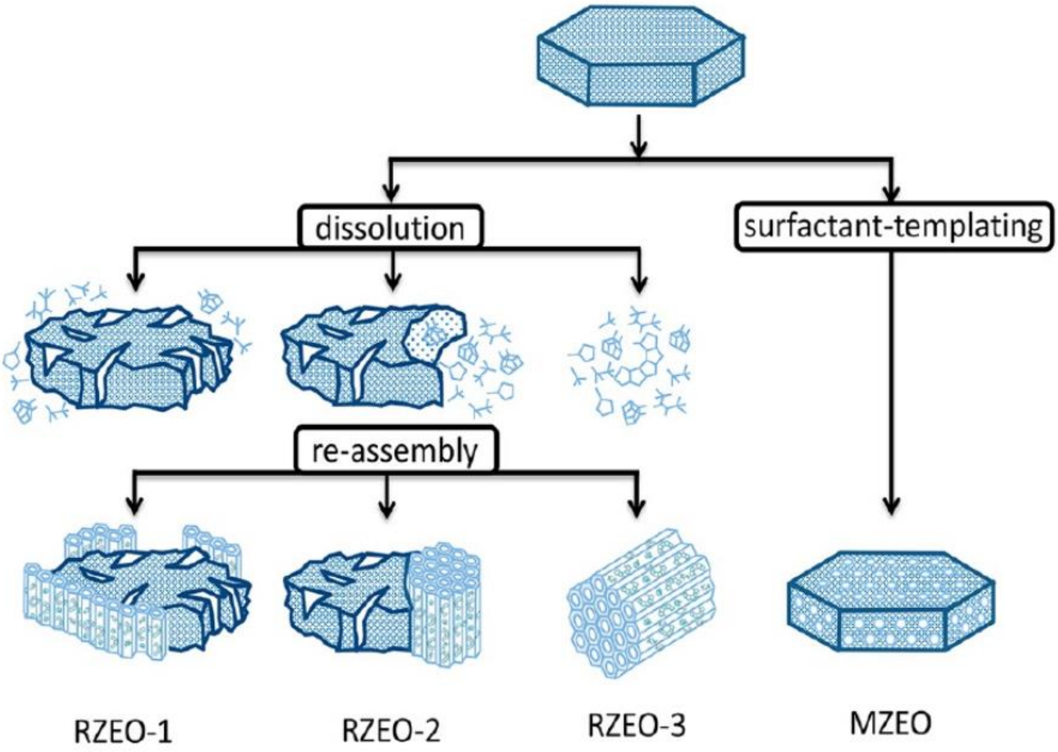

Figure I.9. Difference between dissolution-reassembly and surfactant-templating procedures and the obtained materials.[104]

The combination of rotation electron diffraction (RED), advanced gas adsorption, and electron tomography provides obvious evidence of the single phase nature of the intracrystalline mesoporous zeolite without any amorphous mesoporous material.[83,105,106] According to surfactant-templating, the cleavage of Si-O-Si bond by the action of base produces the negatively charged Si-O$^-$ which induces the diffusion of cationic surfactants into the zeolite crystals by an electrostatic attraction. These surfactant molecules self-assemble into micelles under the right conditions causing the creation of intracrystalline mesoporosity. The authors suggested that no desilication takes place, because there was no clear change in Si/Al ratio.[83] This is in agreement with another study conducted by Sachse *et al.* in 2017.[104] They concluded that zeolite crystals expand in order to accommodate the homogeneously formed mesoporosity with preservation of most of the acidity of the parent zeolite. Furthermore, surface-templating was compared to dissolution/reassembly of zeolites. The authors concluded that the crystallinity and retained microporosity, as well as the acidic properties of the samples prepared by dissolution and reassembly, are lower in comparison to those of the surfactant-templated zeolites, which present uniform intracrystalline mesopores. Moreover, these uniform intracrystalline mesopores are free from any amorphous material despite the decrease in the intensity of the X-ray diffraction (XRD) peaks, which results from the formation of voids in the framework of the zeolite that causes a less effective diffraction.[107]

Ivanova *et al.*[108] clarified the mechanism of surfactant-templated mordenite on the basis of thorough investigation of the intermediate products recovered during three different steps of the recrystallization process: (1) mixing of the mordenite zeolite with alkali solution in presence of cetyltrimethylammonium bromine (CTAB) surfactant; (2) elevating the temperature of the mixture to 423 K and (3) exposing the mixture to hydrothermal treatment at the same temperature for selected periods of time.

Figure I.10 features the proposal mechanism of each step. In the first step, fast ion exchange of protons with sodium cations and the cleavage of Si-O-Si bonds with base is observed, which leads to desilication of mordenite accompanied by the creation of small intracrystalline mesopores (3-20 nm) and large intercrystalline ones (> 30 nm). In the second step, CTAB enters the inter- and intracrystalline voids followed by the ion exchange of sodium with CTA^+ cations, which induces the formation of micelles and nucleation of mesoporous phase within the zeolite mesopores and on the external surface of the crystals. In the last step, the siliceous species extracted during desilication condense around the micelles and lead to the formation of mesoporous fragments with uniform inter- and intracrystalline mesopores (3-4 nm). The resulting mordenite represents disordered ingrown and overgrown mesoporous phase, which cause random orientation of mesopores and therefore good accessibility of retained micropores.[108]

Galarneau *et al.* studied the texture of mesporous FAU-Y zeolite created by surfactant-templating in different basic media at 115 °C for 20 h.[109] They demonstrated that mesoporous FAU-Y zeolites are complex family of materials depending on the NaOH/Si ratio utilized in the reacting mixture. The production of homogenous mesopores (4 nm) begins at NaOH/Si = 0.0625. Then, the mesopore volume increases as the NaOH/Si ratio increases with the decrease in the micropore volume, where the transformation occurs at constant total surface area. The intact FAY-Y crystalline nanodomains presenst in all modified materials, whose size decreases by increasing the NaOH/Si ratio. The decrease in the micropore volume and crystalline zeolite fraction lead to the decrease in the strong acidity. Furthermore, the mesoporous FAU-Y materials family reveals at least three types of hirerarchical structures: FAUmes with crystalline walls containing well-dispersed zeolite nanodomains (100-200 nm) and an interconnected mesopore network ($0.0625 < NaOH/Si < 0.10$), FAUmes with amorphous walls as Al-MCM-41, which coexist with well dispersed zeolite nanodomains range between 5 and 100 nm ($0.125 < NaOH/Si < 0.175$) and Al-MCM-41 materials ($NaOH/Si = 0.25$) with an interconnected macroporous network.[109]

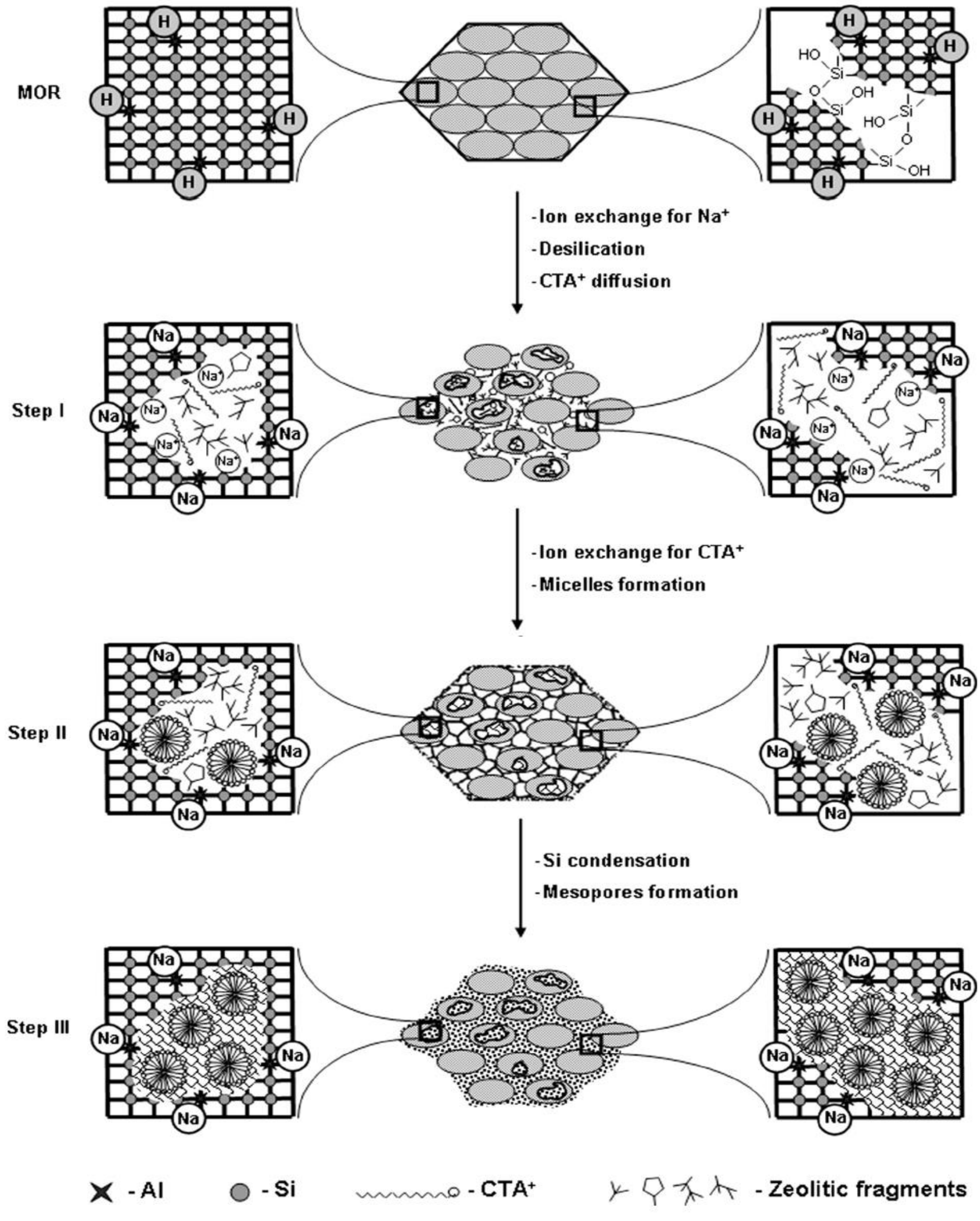

Figure I.10. Mechanism proposed for the recrystallization of mordenite zeolite.[108]

3.3.4 Desilication reassembly under atmospheric conditions

The alkaline treatment using surfactants for generating mesoporosity in zeolite has received much attention recently. Re-assembly treatments are commonly conducted under hydrothermal conditions at 80-150 °C for 24 h, which are close to those proposed for the synthesis of the mesoporous materials, such as MCM-41 as reported in the literature.[98,110]

In 1015, Wei *et al.* made an exploratory study on MCM-49 which was treated in a solution containing 0.27 M CTAB and 0.6 M NaOH at 70 °C for 1 h.[111] They found that NaOH destroyed the framework of the MCM-49 by attacking the regions free from HMI (which was used as structure directing agent (SDA) during the synthesis of the zeolite) and that the dissolved species could be converted into OMM by the action of CTAB.[111] In a further experiment, it was found that, by treating the zeolite with pure CTAB solution (0.27 M) at 70 °C for 1h,[112] the CTAB treatment cleaned off some amorphous particles from the zeolite and that EFAL were inserted into the framework by selective substitution of the Si atoms on the T3 site and filling the defects of T2 or T3 sites directly. Consequently, the acidity was higher.[112]

Similarly, Xu *et al.* prepared hierarchical ZSM-11 by alkaline treatment with CTAB at 75 °C during 15 min.[113] Uniform intracrystalline mesopores were created accompanied by preservation of microporosity. They proposed composite effects of NaOH and CTAB on the formation of mesopores as shown in Figure I.11.

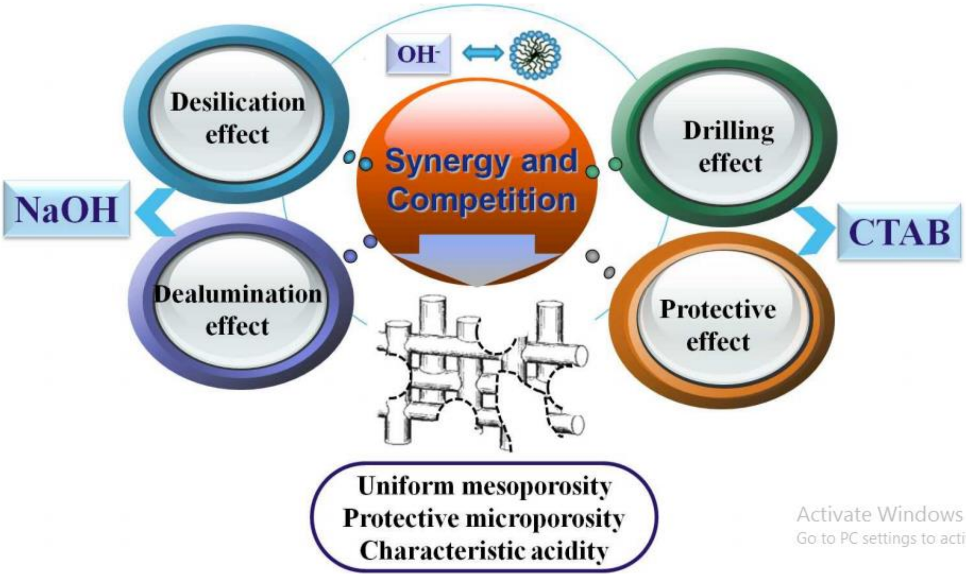

Figure I.11. Composite effects of NaOH and CTAB on production of mesopores over ZSM-11 during alkaline treatment in presence of CTAB.[113]

As mentioned before, NaOH stimulates desilication and releases EFAL species, while the CTAB plays two important roles. The First role known as drilling effect where the CTAB micelles could induce uniform mesopores with a diameter comparable to the micelle diameter.[114] The second role is expressed by protective effect by adsorption of CTAB on the external surface of the zeolite to protect the zeolite through multilayer adsorption especially when the CTAB concentration was high,[115] this adsorption also inhibited largely the surface realumination[116] to be EFAL that comes from simultaneous removal of aluminium species from framework into extraframework. The synergetic and competitive effects between NaOH and CTAB during the reaction were proposed through combining ^{27}Al and ^{29}Si magic angles spinning nuclear magnetic spectroscopy (MAS NMR), N_2 adsorption isotherms, and transmission electron microscopy (TEM) images. At constant CTAB concentration, if the concentration of NaOH is too high, the protective effect is diminished. For too low NaOH concentration, the drilling effect is suppressed.[113]

Table I.2 resumes the different mild and severe conditions of desilication process in presence of CTAB followed by the comparison of the modified materials with the parent ones in terms of textural properties and acidity. Moreover, Table I.2 reports the various types of model reactions used to characterise textural and chemical properties.

3.3.5 Desilication assisted by microwave heating

The microwave heating has been used in zeolite synthesis for more than 25 years.[117] The reported advantages of microwave heating compared to conventional heating are (i) much shorter crystallization times and (ii) better control of morphology and particle size distribution.[118,119] This is specially associated to the rapid and uniform heating time induced by the microwave radiation and its selective interaction with certain reagents and solvents. [118-120] The application of microwaves in post synthesis treatments was firstly used by Pavel and Schmidt.[121] They created a hierarchical titanosilicate ETS-10 with supermicropores (0.85 nm) from its native micropores (0.7 nm) and intracrystalline mesopores (10 nm) by microwave-assissted detitanation in H_2O_2 solutions at 353 K for 15 min. The same treatment with classical heating induced no mesoporosity.[122]

In 2009, Abello and Perez-Ramirez studied for the first time the effect of microwave heating on the alkaline treatment of zeolites for the generation of mesoporosity.[117] They found that microwave irradiation accelerates the generation of defined intracrystalline mesopores by selective silicon extraction in commercial ZSM-5 zeolites compared to the standard treatment. This positive effect is due to the more efficient transfer of thermal heating to the zeolite solution, therefore enhancing the rate of silicon extraction towards mesopore formation. Yet, for both treatments, conventional and microwave, the type of mesopores generated under optimal conditions was equivalent.[117]

Hasan *et al.*[123] obtained mesoporous ZSM-5 zeolite by three different alkaline solutions with microwave and conventional heating under hydrothermal conditions. Both procedures were effective in the formation of mesoporous ZSM-5. However, the microwave method was more efficient than the conventional as it led to well-defined and relatively small mesopores with a narrow size distribution at a shorter treatment time. That is why, the microwave desilicated sample was more effective in producing less bulky products than that obtained with conventional heating in butylation of phenol. Conversely, the formation of bulky products depended on the largest pore size.

Sanhoob *et al.* desilicated MTW under microwave irradiation. Larger mesopores were obtained accompanied by blockage of micropores with silica-rich extra framework deposits. Consequently, the methylation of 2-methylnaphthalene over desilicated zeolites decreased with the increase of the mesopores due to the absence of micropores.[124] In a separating study, the same group evaluated the same desilicated zeolites on the *n*-heptane cracking. They found that the mesoporosity of the zeolite improved the conversion, stability, propylene and aromatic selectivity.[125]

Muraza *et al.* created larger total pore-volume of MTT zeolite after desilication by microwave heating. They concluded that moderate-acid leaching after desilication is very useful to ensure enough porosity of the 1D-pore zeolite. Moreover, they enhanced the selectivity of MTT zeolite to produce high propylene/ethylene ratio in *n*-hexane cracking with better resistance against deactivation.[126]

Martins *et al.* studied the effect of microwave radiation on the alkaline treatment of mordenite zeolite for mesoporosity creation and the results were compared with those obtained in conventional desilication conditions.[127] They found that microwave irradiation is less time consuming and promotes desilication without a significant loss in crystallinity. Morover, this desilication mode enlarges the zeolite micropores, through a transformation of ultramicropores into supermicropores, which permits conservation of the catalytic properties, inherent of the zeolite.[127]

Table I.3 summerizes major publications concerned with microwave assisted heating in zeolite desilication.

3.3.6 Zeolite etching

While steaming and acid leaching lead to extraction of aluminium from the framework, alkaline leaching extracts silicon selectively. As mentioned before, the latter approach attracted considerable attention during the last decade, due to its broad applicability to a variety of high silica zeolite.[128] However, both dealumination and desilication, as the name indicates, lead to a change in the Si/Al ratio of the parent zeolite. Both approaches change the composition and distribution of silicon and aluminum in the zeolite and thus its acidic properties.[129] Therefore, the development of a general approach to design hierarchical zeolites that preserve the initial chemical composition is highly desirable. A solution is zeolite etching, which has revealed as a neither Si nor Al selective demetallation strategy.

3.3.6.1 Etching by hydrofluoric acid (HF)

It is well known that HF reacts with both silicon and aluminium.[128] In 1986 Ghosh and Kydd concluded that etching in concentrated HF solutions (1.5 M) decreased the selectivity of aluminium removal and did not lead to an important change in the Si/Al ratio of mordenite zeolite.[130] They reported that a treatment with diluted HF solutions (≤ 0.25 M) increased the Si/Al ratio of mordenite without affecting its crystallinity. (Figure I.12) Elemental analysis of both treatments showed that small amounts of fluorine were incorporated to the zeolite structure, thus enhancing both the weak Brønsted and strong Lewis acidity.

Lee and Ha studied the difference in the characterization of mordenites treated by HCl/steam and HF.[131] They found selective extraction of FAL in HCl/steam-treated mordenites and simultaneous removal of framework silicon and aluminium in HF-treated mordenite. The lattice parameters were smaller on HCl/steam-treated mordenites. This sample further featured a higher proportion of strong acid sites compared to the HF treated-mordenites. In addition, a terminal silanol group formed at 3740 cm^{-1} in IR was less intense in HF-treated mordenites due to the removal of silanol groups by replacing F with the hydroxyl group in Si-OH.[130,131]

Wloch subjected ZSM-5 to etching with an acetone-aqueous HF solution. Acetone was applied to improve the evolution of gaseous silicon tetraflouride to leave the reaction medium quickly before the decomposition of SiF_4 could take place. Indeed water and alcohols facilitate the decomposition leading to the formation of silicic acids, which can deposit on the surface of the zeolite crystals.[132] Further evidence was found that the etching of the calcined zeolites dissolved the samples completely, while the etching of non-calcined zeolites containing the SDA led to etching just on the crystal surface. The shape and size of the crystals did not change noticeably and the surface became smooth and free of deposits or cracks. This explains why the sorption of *n*-hexane by etched zeolites was faster compared to non-etched ones.[132]

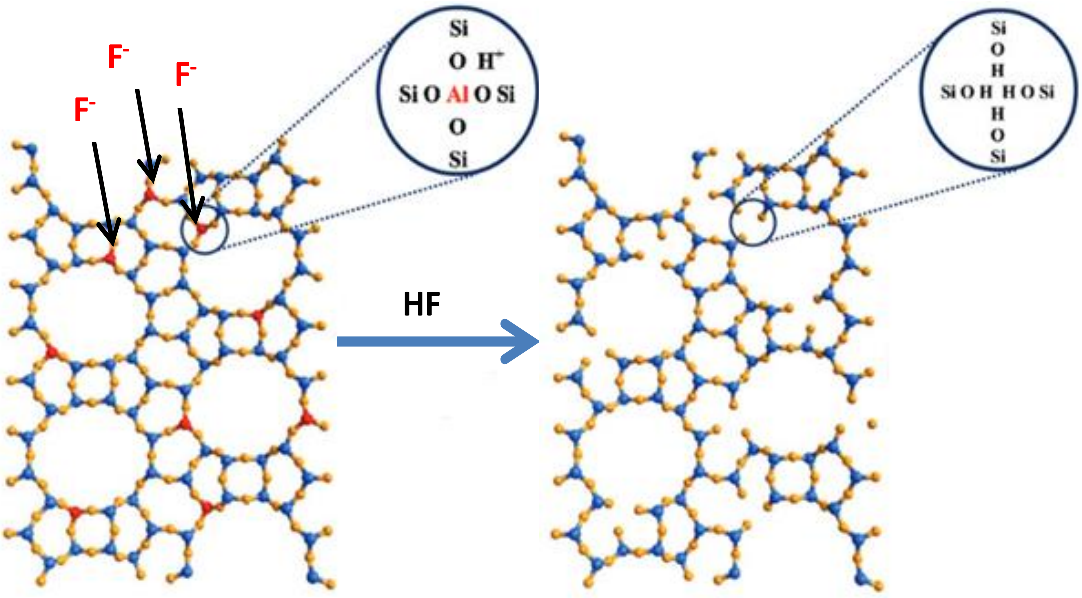

Figure I.12. Chemical etching of zeolite framework.

In another study, ZSM-5 zeolite was etched with different concentrations of HF ranging from 0.5 to 2 M.[133] The mesopore volumes increased with the HF concentration, while the crystallinity was preserved. The SiO_2/Al_2O_3 ratios increased, the Brønsted acid sites decreased and the Lewis acid sites increased with increasing HF concentration. When tested in catalysis, the stabilities of the etched samples improved significantly in the methanol to gasoline reaction (MTG). These results proved that the acidity and the pore structure are two crucial factors in determining the catalytic properties.[133]

Gao *et al.* used diluted hydrofluoric acid solution to de-agglomerate IZM-2 nanocrystals zeolite (600-800 nm) and then generated intercrystalline mesopores among intergrown zeolite nanocrystals (20-50 nm).[134] The treated samples presented high crystallinity, same framework composition and higher external surface area compared to the agglomerated ones. Since the intergrowth boundaries are rich in defects, the acid attack was more effective at these areas and consequently the framework remained intact.[128,134]

In 2018, Anas *et al.* treated ZSM-22 zeolite samples with solutions of various HF concentrations.[135] Zeolites that were treated with a solution of HF concentrations (0.7 and 1.0 wt.%) showed selective removal of aluminium. On the other hand, those treated with a higher concentration (1.5 wt.%) caused more important leaching of silicon.[128] All the samples preserved their zeolitic structure with loss of crystallinity and reduction of agglomeration after the treatment. However, ZSM-22 samples treated with low HF concentrations showed better initial conversions in steam catalytic cracking (SCC), which can be contributed to the preservation of the acidity.[135]

3.3.6.2 Etching by HF in the presence of NH_4F

The treatment with diluted HF solutions leads to an increase in the Si/Al ratio of the treated zeolite and consequently to a reduction of the Brønsted acid sites.[130] However, the utilization of more concentrated HF solution leads to an indiscriminate removal of Si and Al from the zeolite framework without changing significantly the Si/Al ratio. This suggests that, equilibirium shifts of the HF dissolution equilibria allow for unselective extraction of Si and Al from the zeolite framework.[136,137] It is important to understand why a small increase of HF concentration leads to a change in the etching selectivity.[130,138]

It is well known that the different species present in aqueous HF solutions are H^+, F^-, HF_2^- and undissociated HF molecules.[136,139] Also, it is known that there is a linear relationship between the rate of SiO_2 etching and the concentration of HF and HF_2^-.[140] These two species have much higher activities than H^+ in the HF species.[136] This explains why the increase of the HF concentration is not only accompanied by the increase of acidity but also the concentration of the species selective for silicon removal.[128,130]

Valtchev *et al.*[128] developed a new etching method indiscriminately zeolite crystals and apply it in the preparation of hierarchical zeolite with intact framework composition. They utilized a combination of ammonium fluoride dissolved in aqueous hydrofluoric acid, which allows to shift the HF dissociation equilibria. In contrast to other halogen halides, diluted HF has a weak acid behavior.[136] The HF ionization in water can be represented by two equilibria:

$$HF \rightleftarrows H^+ + F^- \qquad (1)$$

$$HF + F^- \rightleftarrows HF_2^- \qquad (2)$$

At 298 K, the equilibrium constant of eq.1 is 6.85×10^{-4} mol L^{-1}, while it is 3.963 mol L^{-1} for eq.2.[141] The addition of the strong electrolyte, NH_4F to the aqueous HF solution shifts the equilibrium 1 to the left and equilibrium 2 to the right, which favors the generation of non-dissociated HF species and bifluoride species HF_2^-, respectively. These two species are active for silicon extraction and the rate of silicon removal with HF_2^- is faster than that with HF by at least four to five times.[140,142] The concentration of HF_2^- in purely aqueous HF solution is very low but it increases noticeably when the concentration of F^- is increased. This shift of equilibrium illustrates why more concentrated HF solutions have less selectivity of aluminum removal. Hence, the presence of NH_4F in more concentrated HF solutions favours the formation of HF_2^-species. Consequently, the extraction of silicon species is increased and unbiased extraction of Al and Si is observed. (Figure I.13) The etched ZSM-5 zeolites achieved through NH_4F-buffered HF solution have similar microporosity, surface area, aluminum content, and acidity (number and distribution of acid sites) as the parent one. In contrast, the treated zeolites display substantially higher catalytic activity than the parent zeolite. This is due to a retained acidity accompanied with improved accessibility of the zeolite micropores. During NH_4F-HF treatment most zeolite crystals are exposed to fragmentation and the small parts of the crystals are cut by preferential dissolution of defect zones. In addition, to the creation of large pores penetrating deeply in the crystals, which lead to an easier access to the micropores, similar to a reduction in the crystal size.[143]

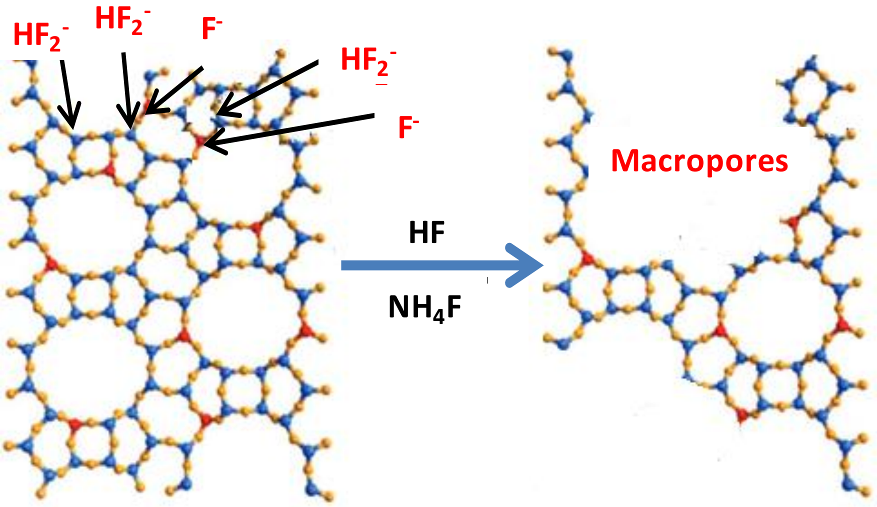

Figure I.13. Chemical etching of zeolite with HF in presence of NH_4F.

Pinard *et al.*[144] compared the effect of different types of porosities introduced by desilication and fluoride etching on the performance of ZSM-5 catalysts in the transformation of methylcyclohexane. The alkaline treatment created additional mesopores interconnected with the native micropores and generated additional Lewis acid sites and silanol groups due to a substantial dissolution of the zeolite framework. On the contrary, the fluoride treatment led to a zeolite combining micropores and macropores without changing the physico-chemical properties. Despite different porosities, the hierarchical zeolites featured the same initial activity and selectivity in the catalytic behavior. Conversely, the presence of mesopores, created by alkaline treatment, enhanced greatly the stability of the desilicated catalyst by favoring desorption of the products. This increase in catalyst stability was related with the shortening of the diffusion path length.[144]

In 2017 and 2018, Meng *et al.*[145] and Ji *et al.*[146] repeated the same innovative procedure of chemical etching on ZSM-5. They applied the treated catalysts in two different catalytic tests: the MTG reaction,[145] and the cracking of *n*-hexane.[146] This study revealed 2017 found that, after the treatment, the external surface area and mesopore volumes increased with preservation of acidity and micrporosity, while the relative crystallinity slightly decreased. Moreover, the catalyst lifetime was prolonged accompanied with a slight increase in the selectivity of the liquid hydrocarbon. This was ascribed to the improved transport through the crystals coupled with the retained acidity of treated zeolite.[145] In the second study,[146] the defects were dissolved resulting in larger mesoporous and macroporous volumes, higher BET surface area, and crystallinity with commensurable acid property and microporous structure compared to the parent ZSM-5. Consequently, the etched zeolites enhanced the catalytic performance of *n*-hexane cracking with less carbon deposition due to superior channel structure. In separating step, one of the treated zeolites was chosen and modified with phosphorous in order to reduce the amount of carbon deposition. After phosphorous modification, the amount of acid decreased with the increase of phosphorous content and led to maintaining catalytic activity and stability at high levels with less amount of carbon deposition, which was four times less than that of the parent ZSM-5 at the optimized conditions.[146]

Due to the success of their protocol, Valtchev and coworkers[147] repeated the etching process with ferrierite. First, the ferrierite was synthesized and then subjected to chemical etching with NH4F-HF aqueous solutions with different HF concentrations and etching duration. The chemical etching created a secondary system of large meso- and macropores with similar chemical composition and acid properties to the parent one. The shape of the developed pores is rectangular and perpendicular to the {100} crystal face, thus providing more accessibility to the 8 and 10-MRs pore systems.[147]

Valtchev *et al.* further tried to adapt this procedure to SAPO-34.[148] They found that the etching slightly affected the morphology, composition and acidity of the SAPO-34. The fluoride treated crystals lost 20 to 30% of their microporous volume accompanied by less intensive X-ray diffraction peaks. In addition, the induced coupled plasma (ICP) analysis and ^{29}Si MAS NMR indicated substantial decrease in the silicon content due to the preferential dissolution of highly defected interface between crystalline domains, enriched with silicon. The catalytic performance of hierarchical SAPO-34 crystals increased, although the number of Brønsted acid sites decreased ultimately. This is attributed to the formation of mesopores parallel to the crystal faces, intersecting with each other to separate crystalline domains, which thus improved the access to the microporosity.[148]

Yu *et al.*[149] applied the fluoride post-treated route for the preparation of hierarchical SAPO-34 zeolite synthesized with different organic templates *i.e.* morpholine, triethylamine and tetraethylammonium hydroxide. They concluded that the dissolution process strongly depended on the type of organic template used. Different etched SAPO-34 zeolites with different distribution of active sites were achieved. All the catalysts exhibited higher selectivity to C_3H_6 in methanol to olefin (MTO) reaction than the parent ones, while an undesired drop of the catalyst life time was observed for catalysts templated by tetraethylammonium hydroxide and morpholine. This drop was related to the reduced crystallinity and quantity of strong acidic sites.[149]

Up to date, the use of the NH_4F/HF etching on mordenite zeolite has been scarcely described. Only two studies from the same group in 2017 have been reported.[150,151] In the first study, they synthesized micron-sized mordenite crystals followed by HF-NH_4F treatment with different reaction durations and HF concentrations. The chemical etching yielded hierarchical mordenites with a secondary porous system of larger mesopores that enhanced the access to the microporous systems. The hierarchical zeolites had similar acidic properties and chemical compositions to the parent mordenite. As a result, the catalytic activity of treated mordenites in the reaction of *m*-xylene transformation was much higher compared to the parent one.[150] In the second study,[151] the group used the optimal mordenite etching conditions at 0.1 M HF and NH_4F treatment for 20 min. The additional step relied on the introducing of zirconia into the framework by incipient wetness impregnation in order to vary type and strength of acidity. The investigation of the acid properties of the Zr-modified catalysts by the temperature-programmed desorption (TPD) of adsorbed ammonia and FT-IR spectra of adsorbed pyridine agreed with NMR data characteristic for the formation of strong Lewis acid sites, where coordinatively unsaturated Zr ions can act as Lewis acid sites. Hence, the obtained mordenites showed high catalytic performance in glycerol esterification using acetic acid and improved selectivity to valuable triacetylglycerol, which formation was favored in the larger pores of hierarchical mordenite accompanied with optimal Brønsted/Lewis acid sites ratio.[151]

Table I.4 summerizes the main conditions of zeolite etching process. A comparison of the etched materials with parent zeolites in terms of textural properties, acidity and catalytic activity was included.

4. Model reaction to characterize zeolites

Based on physical and physicochemical techniques, many methods have been developed to identify the nature of active sites in order to estimate quantitatively their concentration as a function of their strength.[152] Some of the most currently used techniques for characterising the acid or basic sites are: i) TPD of acid or basic probe molecules, the strength of sites being characterised by the desorption temperature;[153] ii) microcalorimetry in which the differential heat of chemisorption of acidic or basic probes can be used to measure the strength of the acid or basic sites;[153] iii) IR spectroscopy, which permits to identify the OH groups related to Brønsted acid sites and to estimate the density of Brønsted and Lewis acidity[154] by using probe molecules such as pyridine; iv) ^{1}H NMR spectroscopy which can detect the acidic OH groups and directly evaluate their strength from their chemical shift, etc.[154] Unfortunately, these methods present major drawbacks,[155] such as:

- The operating conditions chosen for the catalyst pretreatment prior to the catalytic and characterisation experiments are never completely identical, there is often a large difference between the properties of the active and characterised sites.
- The chemisorption of acid or base probe molecules on the active sites is never totally selective. This means that a part of the probe molecules used in the physicochemical characterisation can be chemisorbed on inactive sites.
- The physicochemical methods are well adapted for characterising acidic or basic sites, while they cannot provide the essential characteristics of the acid-base sites active in bifunctional pathways, *i.e.* the proximity and the relative strength of their acid and base contents and hence synergetic effects.

These drawbacks can be exceeded by using test reactions for the characterisation of the acid, base or acid-base active sites.[155] Furthermore, an additional advantage of this method is to monitor the behaviour of the catalyst in presence of the reactant and to evaluate the product molecules (desired or not). The carbonaceous compounds (generally called coke) are among the non-desired products. They are practically always formed having a destructive effect on the activity and often on the selectivity of the catalyst.[156] The utilize of model reactions allows not only to determine the characteristics of the active sites prior any deactivation, either by operating at very low time-on stream (TOS) or by extrapolating the data at zero TOS, but also to relate the destructive effect of "coke" to its impact on the active sites. Additionally, the reactant molecule(s) can be transformed on a catalyst through different routes, each of them including active sites different by their characteristics: nature, strength, concentration, etc. It is thus sometimes rational to make an overall description of the characteristics of all the active sites of a given catalyst from the product distribution obtained in a model reaction.

4.1 Appropriate implementation of model reactions

Model reactions can be used to test the suitability of solid acid-base catalysts for an industrial application and/or to detect the characteristics of their active sites. The sites which can be characterized are only the active ones, for instance the protonic sites in acid catalysis. The reactions selected for characterizing the strength or the concentration of these acid sites must be sensitive to only one of these characteristics.

However, other conditions must be satisfied for obtaining proper information on the characteristics of the active acid sites of solid catalysts. The catalyst activities must rely on the chemical steps of the catalytic process only, which requires that limitations by internal and external heat and mass transfer are to be neglected. This implies a convenient choice of the model reactions, of the physical characteristics of the catalyst solid and of the operating conditions. Thus, very endothermic and especially exothermic reactions must be eliminated, so as, to cancel an effect of heat transfer limitations on the reaction rate. Moreover, external mass transfer limitations can be easily avoided, namely by choosing the temperature range in which the apparent activation energy is constant.[157] Lastly, a simple test was found by Weisz[158] for deciding whether internal mass transfer may be neglected.

This criterion is unit less and can be written:

$$A\ R^2 / (c\ De) \leq 1$$

Where A is the initial activity of the catalyst (or the reaction rate), R is the radius of the catalyst particles, c is the concentration of the reactant and D_e is the reactant effective diffusivity in the porous catalyst at the chosen reaction temperature.

Many other conditions must be satisfied in order to acquire accurate values of the catalyst activity. The first difficulty to be overcome is the rapid initial deactivation by coke deposits, which occurs during the transformation of highly reactive molecules over strong acid sites of the catalyst. To suppress this deactivation, pulse reactors can be used but accurate activity data can only be obtained for first order monomolecular reactions. With flow reactors, an accurate estimation of the initial activity requires extrapolation at zero TOS of measurements carried out at relatively short intervals of TOS. While, with an on-line analysis, the interval is determined by the time of this analysis, hence is generally too long. The use of a multiposition valve to stock the samples allows overcoming this inconveniency.[159] Furthermore, the choice of operating conditions limit the coke deactivation (e.g. low reactant pressure, adequate temperature and vector gas, etc.), can also allow getting exact values of the initial activity.

The reactant(s) as well as the feed diluents must be free of impurities having either inhibiting or promoting effects. For example, alkene feed impurities promote the cracking or the isomerisation of alkanes, which can be attributed to a change of the reaction mechanism from a monomolecular to a bimolecular one.[160] Compounds with inhibiting or promoting effects can also result from the transformation of the pure reactant(s). This situation can be observed in alcohol dehydration, owing to a competition between alcohol and the water product for the chemisorption over the acid sites.[161]

4.2 Toluene disproportionation (TDP)

The industrial demand of the smallest para isomer being largely predominant, the scientific community was importantly concerned in developing acid catalysts with a high selectivity to this isomer. The mechanism of TDP over most of the acid catalysts is proposed in Scheme I.6, leads to an equimolar mixture of benzene and xylenes, often in proportion close to that of the thermodynamic equilibrium (~25, 50, and 25% of *o*-, *m*-, and *p*-).

MFI zeolite is a shape selective zeolite for this process that features a pore aperture size close to xylene molecules. An additional advantage of MFI zeolite is the limited rate of coke formation and deactivation due to its tridimensional pore structure with regular channels of similar diameter.[163] Furthermore, as the para selectivity of MFI zeolites was often limited, the researchers were focused on the development of efficient methods for improving their para xylene selectivity while maintaining their activity and stability.[164,165]

Kinetic studies of TDP with monitoring the effect of operating conditions and identification of the active acid sites were also carried out.[165] In general, Brønsted acid sites were proposed as active sites.[164,166] Sometimes, the strength, hence the activity of these protonic sites enhanced in presence of EFAL Lewis acid sites.[166] The effect of the operating conditions such as: toluene pressure, temperature, and nature of carrier gas (H_2 or N_2) was also carried out in TDP on large pore zeolites: MOR, FAU (Y), *BEA, *i.e.* on non-shape selective zeolites. As with MFI zeolites, the protonic sites were also the active sites of TDP,[167,168] EFAL Lewis sites contributed to increase their strength and their activity.[168] Moreover, a second order reaction model with toluene inhibition was shown to account for the effect of toluene pressure on the TDP rate.[167]

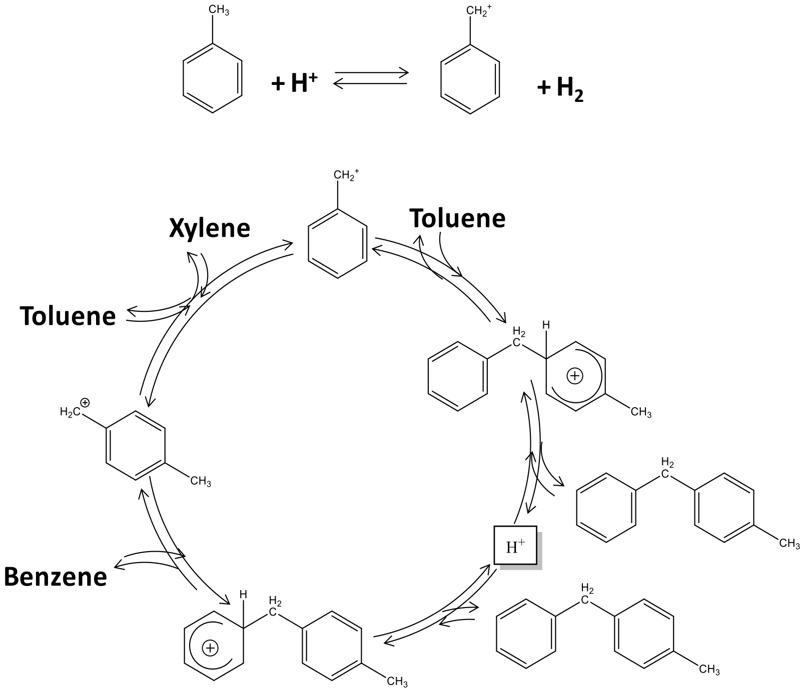

Scheme I.6. Mechanism of toluene disproportionation.[162]

As with MFI catalysts,[166] the effect of the nature of the carrier gas (H_2, N_2, etc.) on the activity and deactivation by coking of H-MOR catalysts was studied.[167,169] In both cases, hydrogen improves the catalyst stability but inhibits the TDP. To explain these observations, two proposals were advanced over H-MOR and H-MFI catalysts, respectively: 1) Hydrogen reacts with the diphenylmethane carbocation intermediates of both disproportionation and coke formation, provoking their desorption and then lowering the rate of these two reactions.[167,169] In favour of this proposal, it can be noted that this reaction of H_2 with diphenylmethane intermediates is the reverse step of their formation (Scheme I.6); 2) The second proposal leans on the similar ranking found for the molecular size of the carrier gases: Ar> N_2> He >H_2 and the corresponding activities of H-MFI catalyst. This observation was related to a physical effect on the residence time of toluene within the micropores more than the chemical effect.[166] While the proposal is valid for the inert gases, a chemical inhibiting effect of hydrogen gas is attained by the formation of coke during TDP (proposal 1), but also during its partial removal by stripping from the spent catalyst.[170]

The acid-catalyzed toluene disproportionation including bulky diphenylmethane intermediates and leading to different sizes of products (*o*-, *m*-, *p*-xylenes) is an appropriate test reaction for characterising the microporous system of zeolites. Indeed its rate can be negatively affected by steric constraints limiting the formation of the bimolecular diphenylmethane inside the zeolite micropores while the xylene distribution is determined by the average micropores of 10-MR zeolites such as MFI. Hence, information can be obtained on either the size of the void available within the micropore system for the diphenyl intermediates and/or, for estimating the micropore size.[171] This reaction is less frequently used for specifying the characteristics of the active acid sites. The initial activities of H-MOR before and after dealumination, by dry air or wet air treatment at 773 K, were compared in a flow reactor. The dealumination had a positive effect on the activity (more pronounced after wet treatment) despite the decrease in the concentration of protonic sites, indicating an increase in the acid strength of the remaining acid sites.[169] However, information on the acid strength is generally obtained by coupling TDP with poisoning experiments using a base desorbed at different temperatures.[172]

4.3 *n*-Hexane (*n*-C_6) cracking

Alkane cracking catalysed by solid acids, was firstly proposed to occur via a chain mechanism including surface carbenium ions (R^+, R_i^+) as intermediates.[173,174] This chain mechanism involves two steps: hydride transfer from the alkane reactant (RH) to a pre-existing carbenium ion R_i^+, followed by β-scission of the resulting carbenium ion R^+:

$$RH + R_i^+ \rightleftarrows R^+ + R_iH \qquad \text{hydride transfer} \qquad (1)$$

$$R^+ \rightleftarrows R_{i'}^+ + A^= \qquad \beta\text{-scission} \qquad (2)$$

The alkane cracking is much slower than the alkene cracking, by approximately three orders of magnitude,[175] which it exposes to a rapid protonation step followed by a β-scission. Therefore, hydride transfer in step 1 of the mechanism can be considered as the rate limiting step and the chain cracking mechanism as bimolecular (B). In steady-state, the carbenium ion R^+ in step 1 results directly as product from step 2 ($R_{i'}^+$) but also indirectly from protonation of its alkene product $A^=$. As a result, in each cycle of the chain mechanism, two carbenium ions can be created whereas in step 1, only one is consumed. The distribution of the cracking products relies significantly on the stability of the carbenium ions which are involved in their formation. This explains why in *n*-hexane cracking the formation of methane and ethane, which implies highly unstable primary carbenium ions, is very low in comparison with largely predominant C_3 products.[176] Moreover, as could be expected from the rapid rearrangement of the C_6 carbenium ion intermediates, the bimolecular alkane cracking (C) is accompanied by the production of isomers (I). Hence, in *n*-hexane transformation on a USHY zeolite at 400 °C, the initial I/C ratio is equal to ~0.35.[177] Similar cracking product distributions were obtained from *n*-hexane and from 2-methylpentane. The reaction steps of Figure I.14 allow to explain these observations.

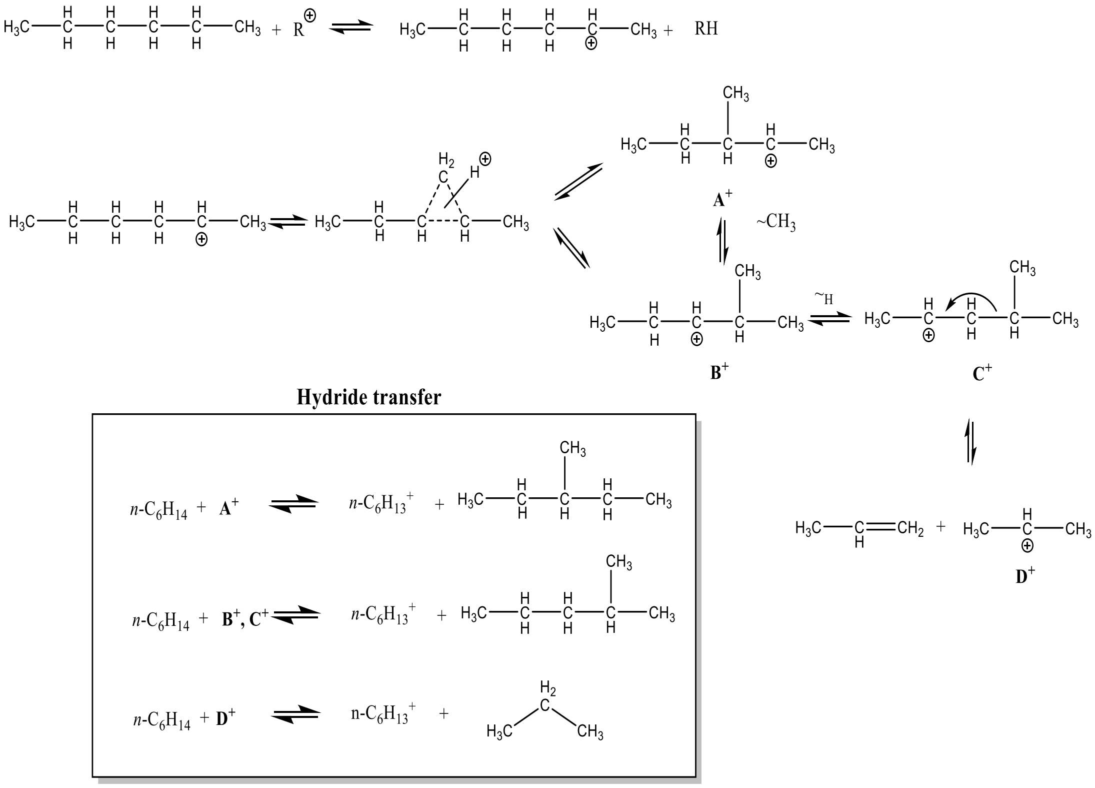

Figure I.14. Bimolecular mechanism of *n*-hexane cracking through carbenium ion intermediates.[162]

To complete this bimolecular mechanism, the origin of the carbenium ions R_i^+ responsible for the first initiation step has to be specified. Several possibilities were established, all being related to the well-known very fast protonation of alkenes over Brønsted acid sites. These carbenium ions can come from the protonation of olefinic impurities of the feed[178,179] of alkenes resulting from the reduction of the alkanes over the catalyst's redox sites[180] or from thermal cracking of alkane reactant at high temperatures. The last possibility which was advanced was the direct formation from the alkane reactant over acid sites at high temperatures, either via hydride abstraction by a Lewis acid site,[181,182] or by dehydrogenation or cracking of the carbonium ions resulting from the protonation of the alkane reactants.[176]

Haag and Dessau[176] were the first to suggest that this protonation could not only be the initiation step of the classical chain mechanism, but also the first step of a new cracking mechanism. Three successive monomolecular steps were proposed to involve this mechanism, as shown in Figure I.15: i) Formation of penta-coordinated carbonium ions through protonation of the alkane reactant molecules; ii) scission of these formed carbonium ions into carbenium ions and either H_2 or alkane molecules; iii) formation of alkenes from the carbenium ions. This monomolecular mechanism (M) was observed to predominate at high T and low olefin concentration (*i.e.* low alkane pressure and low conversion), while it was the opposite with the bimolecular chain mechanism.[176,183] The pore structure has also an important effect: the bimolecular mechanism was predominant within the large pores of H-FAU and of amorphous silica alumina catalysts, while the monomolecular mechanism was largely favoured within the smaller pores of H-MFI due to their steric constraints.[176,183,184]

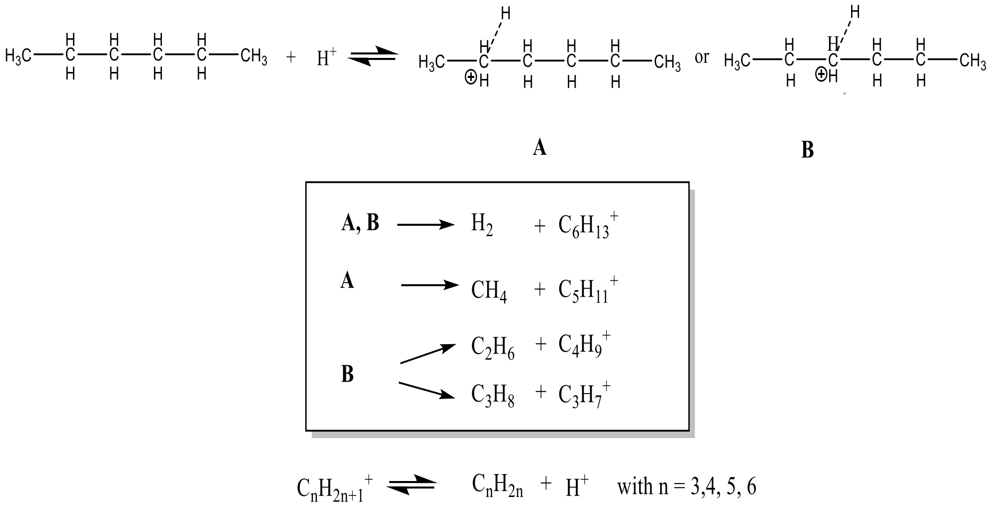

Figure I.15. Monomolecular mechanism of *n*-hexane cracking through carbonium ion intermediates.[162]

The stoichiometry of alkane monomolecular cracking reveals that for each cracked molecule, one alkane molecules and one alkene (or one H_2 molecule) were formed. While, contrarily to the alkane products, alkene products undergo very fast secondary transformations, hence, leading to an alkene/alkane ratio generally lower than 1. That is why, except at very low conversions (<< 1%), the distribution of alkane is diagnostically more useful than that of the alkene distribution.[176] Indeed, while the monomolecular mechanism leads to C_1, C_2, C_3, C_4, C_5 alkanes (and H_2) with the C_1-C_4 produced in strictly parallel reactions as observed in Figure

I.16a, essentially C_3 and C_4 (rich in isobutane) are formed via the chain mechanism. As a result, these paths can be easily discriminated by the formation (or not) of non-classical products, *i.e.* hydrogen, methane and ethane, their relative significance as well as the kinetic characteristics.

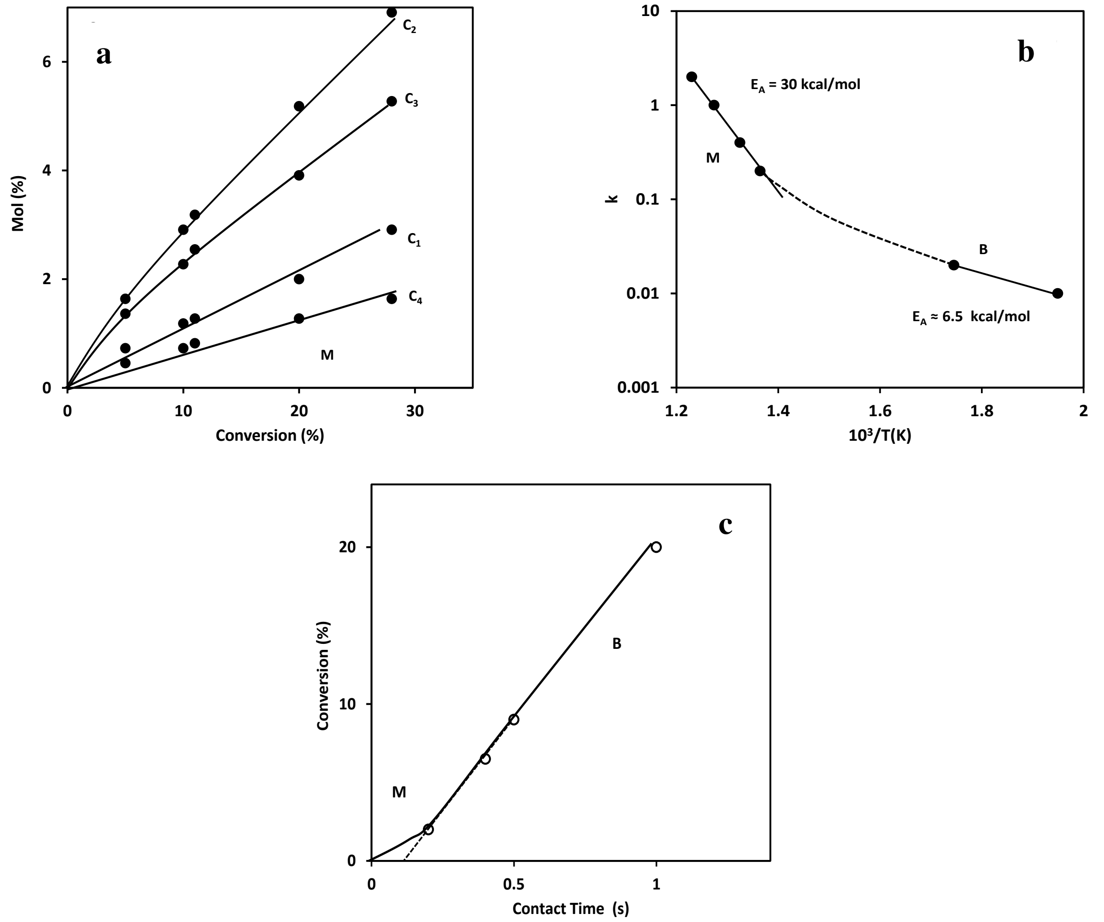

Figure I.16. *n*-hexane cracking on H-MFI (Si/Al = 35): a) Yield in alkane products (T = 811 K, $P_{n\text{-C6}}$ = 0.013 bar) b) T dependence of first-order rate constant ($P_{n\text{-C6}}$ = 0.2 bar), c) demonstration of an autocatalytic process (T = 643 K, $P_{n\text{-C6}}$ = 0.2 bar) (drawn from [183]).

These characteristics were established over an H-MFI catalyst under conditions favouring largely either the mono or the bimolecular paths, *i.e.* by operating at high or low temperatures, respectively. A reaction order of one was found in both cases, which was related to the low and high values of the olefin concentration and of the olefin chemisorption equilibrium constant at high and low temperatures, respectively.[183] However, the large difference in activation energies obtained for the mono and bimolecular paths (30 and 6.5 kcal mol^{-1}, respectively)[183] was, as could be expected, from the very different limiting steps, (Figure I.16b). It should be underlined that although the limiting conditions for monomolecular and bimolecular paths can be easily realised, experiments were often carried out under intermediate conditions, with as a consequence a duality of mechanisms. An autocatalytic-type behaviour (Figure I.16c) is then obtained due to a progressive increase with contact time (hence with conversion) of the relative contribution of the chain mechanism B in the product formation.[183] At very low contact time, the monomolecular pathway is only responsible for the cracking process, while at high contact time, the olefins produced by this mechanism initiate bimolecular cracking.

As was confirmed by Haag *et al.*,[183] *n*-hexane monomolecular cracking can be considered as a quasi-ideal test reaction for characterising the strong acid sites content. As this molecule is linear as well as most of the products, this test reaction is easy to be carried out without diffusion limitations even along the zeolite micropores, reproducible and requires only a little amount of catalyst. Furthermore, the operating of this process at low reactant pressure allows limiting deactivation by coking.[183] In principle, the rate constant k can be determined at any appropriate temperature. While, comparing different catalysts from experiments carried out at different temperatures is not easy, which led Mobil[175,183,185] to propose a standard value of T (538 °C) to calculate the k values. A suitable choice of the contact time allowed an accurate measurement of k values varying by four orders of magnitude.[185] The alpha (α) value is the ratio between these k values and that of a standard SiO_2-Al_2O_3 cracking catalyst,[185] which was used for comparing the acidity (concentration and strength) of series of catalysts, particularly of zeolites. It should be noticed that the frequency value of the acid sites would be a valuable indicator of the average acid strength of the catalysts.

Guisnet et Pinard listed the main conclusions observed from the utilization of *n*-hexane cracking as test reaction of the acid content of solid catalysts.[162] They remarked that essentially zeolites have been used due to the relatively high acid strength necessary for catalysing this reaction. Part of the conclusions agrees with the characteristics of the cracking mechanisms, *i.e.* their monomolecular or bimolecular pathways, the nature of proposed chemisorbed intermediates: radicals, carbenium or carbonium ions, and the steps which are involved. A bimolecular chain mechanism with carbenium intermediates was firstly proposed, the difficulty being to comprehend the initiation step, *i.e.* how the first carbenium ions could be formed. As underlined by Weisz,[180] Haag and co-workers, in absence of alkenes in the reaction medium, the creation of the first carbenium ions was a result of the protolysis of *n*-hexane over protonic sites strong enough for catalysing this step at the chosen temperature.[175] Furthermore, they proposed that this protolysis was also the first step of a monomolecular mechanism, producing thus a comprehensive overall picture of alkane cracking over acid catalysts (Figure I.17).

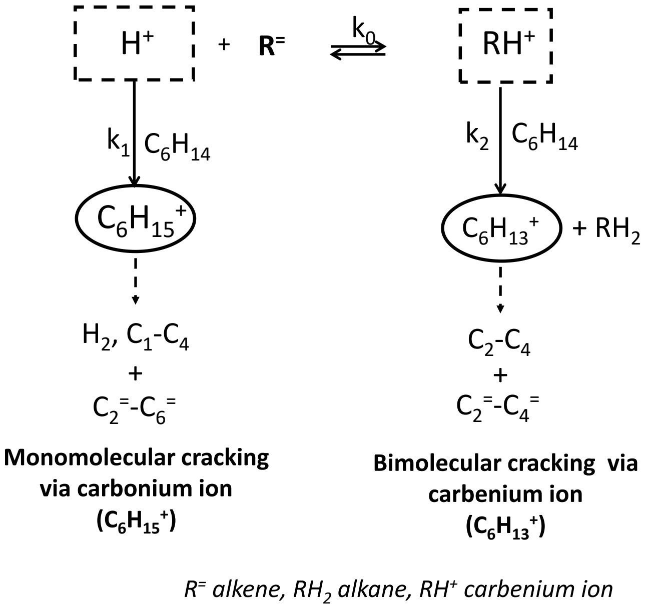

Figure I.17. Dual mechanism of *n*-hexane cracking.[183]

Another significant part of the conclusions results from the comparison of the turnover frequency (TOF values) in *n*-hexane cracking of the protonic acid sites of different amorphous silica alumina and zeolite catalysts with the demonstration of: i) the "superactivity" of the H^+ sites of different zeolites such as H-FAU and H-MOR:[185] their activity can be more than 10.000 times that of the H^+ sites of amorphous silica-alumina; ii) the significant influence of the constrained space within the zeolite micropores on the catalytic activity and selectivity (Shape Selectivity), owing to the location of most of the protonic sites within this microporous system;[186,187] iii) the effect of zeolite dealumination, either via isomorphic substitution of FAL by Si,[183,188,189] e.g. by treatment with AHFS, or with removal of aluminium framework and formation of EFAL species, namely by steaming,[182,190] with finally the quantification of the respective roles of framework and extraframework Al species on the activity, hence on the acidity. Therefore, both cracking mechanism (M and B) can be considered as suitable model reactions for specifying the characteristics of the solid catalysts acid sites: nature, strength, density and location, which determine their activity and selectivity.

Guisnest et Pinard were focused to the influence of dealumination treatments (point iii) on the zeolite activity on *n*-hexane cracking.[162] The steaming of zeolites was shown to extract Al atoms from the framework, with therefore a stability increase and a creation of EFAL, which mainly deposited within the micropores, can be preferentially removed by a subsequent acid treatment. Moreover, dealumination by AHFS leads to samples containing a minimum amount of dislodged aluminum. Furthermore, samples with different Si/Al ratios and free with any

EFAL species can also be directly synthesized. Series of zeolite catalysts varying largely by the amounts of framework and extraframework species can thus be prepared; their characterisation with model reactions leads to the comprehension of the individual and combined roles played by FAL and EFAL species on the acidity and activity of zeolite catalysts.

With carefully synthesized H-MFI samples (*i.e.* without EFAL species), a constant activity per framework Al, therefore per protonic acid site has been observed, which reveals an identical strength of all the sites.[191] While, with H-FAU (Y) zeolites in absence of any EFAL species, the situation was not the same, the samples containing less than 35 FAL atoms per unit cell having just strong acid sites, those with more FAL atoms per unit cell containing low, intermediate and strong acid sites,[192] hence an average lower activity.[190] This effect of the zeolite composition was attributed to the heterogeneity of the acid sites and to the elevation of their strength with the reduction in the number of next nearest Al neighbours, this strength becoming maximal for isolated FAL.[193]

Aditionally, the production of EFAL species by mild steaming of zeolites was shown to enhance significantly the acidity of their protonic sites. This enhancement in acid strength, firstly demonstrated with H-FAU zeolites, was related to an inductive influence of these species with Lewis acidity on the hydroxyl groups.[194] Many publications on the FAU zeolite [188,189,195] and other large pore zeolites: H-MOR[195,196] and H-*BEA[197] confirm this positive effect of EFAL species produced by mild steaming, on the activity of the protonic sites, hence on their acid strength. However, after treatment under severe conditions, the activity of H-FAU zeolites in *n*-heptane cracking was shown to be proportional to the number of framework Al species, suggesting the absence of interaction between EFAL species and protonic sites.[190]

A specific attention was devoted to the favourable effect of EFAL species created by mild steaming of the H-MFI zeolites on their activity in *n*-hexane cracking. One of the first articles, published by Mobil scientists,[198] demonstrates that like with the other zeolites, severe steaming reduces the catalytic activity. This loss in activity (estimated by the α value) was shown to be proportional to the tetrahedral Al (FAL) eliminated from the zeolite framework, which suggests that EFAL species formed by severe steaming do not interact with the protonic sites. Moreover, despite a decrease in FAL content, mildly steamed H-MFI reveals a 4-fold or greater activity in n-C_6 cracking at 538 °C (α test). The activity of the enhanced sites was estimated to be 45-75 times greater than that of the protonic sites which do not interfere with EFAL species.[198] This large difference between the activity of “enhanced’’ and normal protonic sites was also demonstrated in *n*-C_5 cracking over MFI zeolites.[199] In order to understand the formation of enhanced sites, a series of H-MFI zeolites with various Si/Al ratios were submitted to mild steaming.[198] As shown in Figure I.18a, the shape of the enhancement curve as a function of the aluminum content of the starting samples was similar to that of the curve displaying the increase in their number of paired Al sites deduced from a random siting model in Figure I.18b.

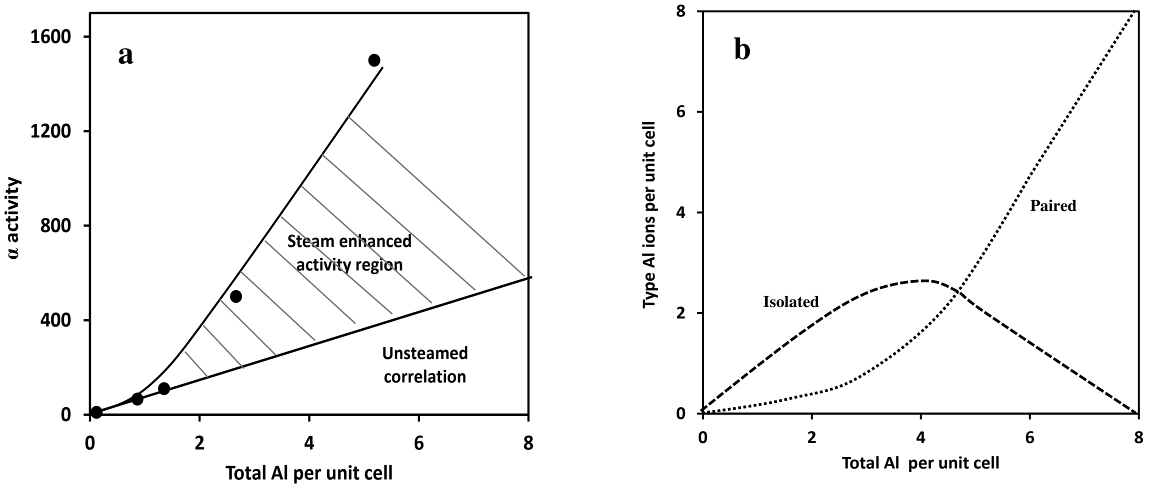

Figure I.18. Comparison of the change as a function of the concentration of Al per unit cell, of the α activity (a) and of the number of paired Al sites (b). (drawn from [198]).

This similarity proves that, as was proposed before,[194] paired Al framework atoms play a critical role in the production of the enhanced acid sites. In addition, while the enhance in activity by mild steaming was often explained by an elevation in acidity of the protonic sites owing to their interaction with EFAL species, some other explanations were also advanced: presence of partially distorted octahedral Al atoms on the outer surface of zeolite crystals,[200] polarisation of the alkane molecules[201] or their dehydrogenation by EFAL Lewis sites[202] and increase of the diffusion rates caused by mesopores and other structural defects created by steaming.[203]

5. Objective

Zeolites contribute largely as catalysts in industrial field. Yet, their efficiency importantly hampered by diffusion limitation. In order to overcome this inconvenience, post modification strategies have been developed during the last 20 years. Concerning mordenite, several post-synthetic modification strategies based on acid and alkaline treatment have been described. Yet, these studies are mostly limited to a very narrow range of conditions (e.g. Si/Al ratio) and the impact of the post-synthetic modifications on catalytic key parameters has scarcely been reported. The objective of this PhD thesis was thus to investigate the impact of different routes of post synthetic modification of mordenite on the catalytic performance (activity, selectivity, and stability). As such, known protocols based on alkaline and acid treatments have been adapted. Thorough characterization of texture and chemical properties allowed to deduce the impact of the modification strategy on the observed catalytic activities, selectivities, and stabilities for the *n*-hexane cracking and toluene disproportionation. Moreover, two new post-synthetic modification strategies have been developed, which allow to substantially wider the range of possible mordenite post-synthetic modification approaches.

Firstly, the pyridine assisted desilication of mordenite has been elaborated as new process, which allows to develop new textural features and for the development of EFAL in situ (chapter III).

Moreover, mordenite etching in pyridine media has been disclosed as very attractive post-synthetic modification strategy, which allows for unselective removal of Si and Al and to superior catalytic outputs (chapter IV).

Finally, a rigorous comparison of textural, chemical and catalytic properties has been drawn, obtained through the comparison the treatment of a wide range of mordenites with varying Si/Al ratios on the already described and new post-synthetic modification strategies. The comparison of all these samples allowed ultimately to deduce the real impact of hierarchization, acidity, presence of EFAL and crystallinity on the catalytic outputs (chapter V).

Table I.1. Different industrial applications of mordenites.[5,12,14]

	Process	Feed	Products or goal	Catalyst
Refining	Hydrocracking	Vacuum gasoils	Gasoline	Ni/MFI-MOR
	Dewaxing	Middle distillates and lubricants	Middle distillates Cold flow Properties↑	Ni/MFI-MOR
	Hydroisomerization	nC4	iC4$^{=}$	Pt H-MOR
		nC5, nC6	iC5$^{=}$, iC6$^{=}$	Pt H-MOR
Petrochemical	Xylene isomerization	C8 aromatic	Paraxylene	Pt H-MOR
	Transalkylation	Toluene-trimethylbenzene	Xylene	H-MOR
		Benzene-diisopropylbenzenes	Cumene	H-MOR
		Benzene-diethylbenzenes	Ethylbenzene	H-MOR
	Benzene alkylation	Propene	Cumene	H-*BEA/H-MOR/H-MWW
	Biphenyl alkylation	Propene	Cumene	H-*BEA/H-MOR/H-MWW
	Toluene disproportionation	Toluene	Xylene-benzene	HMOR

Table I.2. Scientific literature of desilication in presence of CTAB.

Year/ Country	Catalyst	(R^{p}/ R^{m})^{1}	Reacted by	H. T^{2}	$[H^{+}]^{p}$/ $[H^{+}]^{m}$	A^{p}/ A^{m}	V_{micro}^{p}/ V_{micro}^{m}	V_{meso}^{p}/ V_{meso}^{m}	Hysteresis shape	Catalytic test	Conclusion	Ref.
2012/CN	MFI (ZSM-5)	20/x	1.50 M NaOH^{D} 40 °C/ 1h 0.27 M CTAB 1h	2 times 110 °C 24 h	915/785^{TPD}	407/435^{BET}	Total volume (0.19/0.40)		H3	Dehydration of methanol to DME^{3} 190 °C-300 °C	ZSM-5/MCM-41Composite ↑Activity (86%) Selectivity (100%). Lifetime > 7 days at 210 °C	204
2012/USA	MFI (ZSM-5)	46/28	0.05 M NaOH^{S} 0.01 M CTAB	100 °C 24 h	310/280^{TPD}	388/583^{BET}	0.15/0.14	0.27/0.53	H3	-	↑ Surface area. = Crystallinity & V_{micro}	96
2013/DE	MFI (ZSM-5)	51/25	0.50 M NaOH^{S} 0.05 M CTAB	80 °C 24 h	-	55/439^{ext}	0.15/0.08	0.09/0.61	H2(b)	MTO^{4}-400 °C	↑Conversion & lifetime ↑Deactivation/reactivation	205
2013/DE	MFI (ZSM-5)	51/25	0.50 M NaOH^{D} 0.05 M CTAB	80 °C 24 h	-	55/439^{ext}	0.15/0.08	0.08/0.59	H2(b)	MTO-400 °C	Catalytic lifetime > 40 h	77
2004/JP	MFI (ZSM-5)	39/1240	0.20 M NaOH^{D} 0.02 M CTAB 80 °C/ 5h	80 °C 24 h	-	-	-	-	H3	Cracking of cumene-350 °C	ZSM-5/MCM-41 Composite. ↑ Yield of benzene	206
2015/CN	MEL (ZSM-11)	53/40	0.50 M NaOH^{S} 0.05 M CTAB 75 °C/ 0.25 h	no	151/165	112/281^{ext}	0.11/0.10	0.30/0.69	H3	Alkylation of C_6H_6 with DME -450 °C	↑Catalytic perforance, selectivity & lifetime	113
2018/NO	TON (ZSM-22)	49/48	0.50 M NaOH^{S} 0.05 M CTAB (0.10 M HCl 65 °C/ 6 h)^{5}	80 °C 24 h	-	33/114^{ext}	0.07/0.08	0.07/0.45	H3	-	Rod-like crystallites. Well-defined mesopores < 2 nm	207
2014/DE	DDR (ZSM-58)	44/31	0.2 M NaOH^{D} 0.05 M CTAB 95 °C/ 1h	80 °C 24 h	208/262^{TPD}	20/384^{ext}	0.14/0.11	0.03/0.28	H3	-	↑S_{BET} & V_{meso} . ≈V_{micro}	208
2014/CN	MWW (MCM-49)	11/11	0.6 M NaOH^{D} 70 °C/ 1h 0.3 M CTAB 70 °C/ 0.5 h	110 °C 22 h	-	117/148^{ext}	0.18/0.52	0.36/0.52	-	Catalytic degradation of LDPE^{6} & PP^{7}	↑ Conversion 33%	209
2015/CN	MWW (MCM-49)	11/11	0.27 M CTAB^{S} 70 °C/ 1 h	no	300/340^{py}	118/111^{ext}	0.17/0.18	0.35/0.33	-	Acylation of AN^{8} with AA^{9} 110°C	C_i and C_f > 35% . = Selectivity	112
2015/CN	MWW (MCM-49)	11/10	0.60 M NaOH^{S} 0.27 M CTAB 85 °C/ 1 h	no	300/410^{TPD}	118/361^{ext}	0.15/0.08	0.35/0.57	H3	Acylation of AN with AA-110°C	C_i and C_f > 35%	111

Continuation of **Table I.2.** Scientific literature of desilication in presence of CTAB.

Year/ Country	Catalyst	(R^p/ R^m)[1]	Reacted by	H.T[2]	$[H^+]^p$/ $[H^+]^m$	A^p/ A^m	V_{micro}^p/ V_{micro}^m	V_{meso}^p/ V_{meso}^m	Hysteresis shape	Catalytic test	Conclusion	Ref.
2004/RU	MOR	49/46	0.3 M NaOH^D x M CTAB	100 °C	365/322^{TPD}	-	0.16/0.14	0.08/0.25	H3	Transalkylation of BP[10] with DIPB[11]-220 °C	↑Catalytic performance, selectivity & stability	210
2011/RU	MOR	48/67	0.65 M NaOH^D x M CTAB	100 °C	153/155^{py}	-	0.18/0.09	0.06/0.37	H3	Alkylation of NP[12] with cyclohexane-160°C	↑↑ Catalytic performance Yield of Alkylnaphtalene >80%	211
2012/RU	MOR	48/40	0.50 M NaOH^D x M CTAB	100 °C	153/160^{py}	-	0.16/0.15	0.03/0.17	H3	Disproportionation of cumene	↑catalytic performance. ↑ Accessibility	114
2013/RU	MOR	48/26	0.15 M NaOH^S x M CTAB	150 °C 10 h	-	-	0.16/0.02	0.08/0.58	H3	-	Intramesopores of 3-20 nm Intermesopores > 30 nm	108
2007/RU	*BEA	42/31	0.75 M NaOH^D x M CTAB	100 °C	189/177^{py}	-	0.15/0.13	0.07/0.25	H3	Adsorption of DTBPy[13] -150 °C	↑ Accessibility of bulky groups Preservation of acidity	100
2010/FR	FAU (CBV-720)	16/16	0.09 M TMAOH[14]^D 0.04 M CTAB	150 °C 20 h	720/670^{TPD}	722/805^{BET}	0.19/0.10	0.21/0.51	H1	-	↑Mesoporosity, Same Crystallinity	95
2011/-	FAU (CBV-720)	15/15	0.37 M NH$_4$OH^S 0.03 M CTAB	150 °C 10 h	-	128/704^{ext}	0.30/0.21	0.16/0.50	H1	FCC[15]-526 °C	↑Selectivity & diffusion Coke formation ↓	94
2013/PL	FAU (CBV-720)	15/x	0.09 M TMAOH^S 0.02 M CTAB	150 °C 16 h	-	72/747^{ext}	0.23/0.05	0.04/0.58	H1	QE-TPDA of n-alkanes	Creation of mesopores Preservation of structure	212
2017/ES	FAU (CBV-720)	16/16	0.54 M NH$_4$OH^S 0.03 M CTAB	150 °C 48 h	190/123	-	0.30/0.22	0.26/0.40	H2(b)	Creation of mesopores controlled by Temperature & time. Crystals expanded to accommodate mesopores without any desilication. Accessibility ↑ for longer treatment times		104
2014/CN	FAU	4.9/5.5	0.0006 M HLA[16] 100 °C/ 2h 0.16 M NaOH^S 0.06 M CTAB	150 °C 24 h	-	39/377^{ext}	0.35/0.23	0.05/0.30	H3	Acetylization of cyclohexane with PE[17] -120 °C	↑catalytic performance	213

Continuation of **Table I.2.** Scientific literature of desilication in presence of CTAB.

Year/ Country	**Catalyst**	**(R^p/ R^m)^1**	**Reacted by**	**H.T^2**	**[H^+]^p/ [H^+]^m**	**A^p/ A^m**	**$V_{micro}{}^p$/ $V_{micro}{}^m$**	**$V_{meso}{}^p$/ $V_{meso}{}^m$**	**Hysteresis shape**	**Catalytic test**	**Conclusion**	**Ref.**
2016/CN	FAU	03/x	0.01 M CA^{18} 0.18 M NH_4OH^S 0.06 M CTAB	150 °C 10 h	-	73/393^{ext}	0.26/0.18	0.12/0.31	H2	FCC-500 °C	↑Conversion with (Ni or Vn). Coke formation ↓. Desorption of oil molecules↑.	214
2018/FR	FAU		0.025-0.25 M NaOH	115 °C 20 h	0.65^{TPD}	937/926	0.37/0.22	0.06/0.41	-	-	Large mesopore volume with high acidity	109
2011/RU	FER	34/31	1.2 M NaOH^D x M CTAB	110 °C 24h	359/167^{py}	-	0.11/0.07	0.01/0.15	-	Conversion of 1-Butene-350 °C	↑Catalytic performance. Yield of isobutene> 40%	215
2018/FR	FER	9.2/5.2	0.50 M NaOH^S 0.04 M CTAB	130 °C 24 h	-	390/406^{BET}	0.14/0.10	0.04/0.27	H3	-	Inter & Intracrystalline mesopores	216

^{m} Modified material; ^{p} Parent zeolite ; ^{py} Amount of Brønsted acid by adsorption of pyridine at 150 °C; ^{TPD} Measurment of acidity by Ammonia-temperature programmed desorption ; ^{BET} Measured by BET method; ^{ext} External surface area measured by t-plot; ^{S} Surfactant-templating process; ^{D} Dissolution-reassembly process.

[1] Global silicon aluminum ratio; [2] Hydrothermal treatment; [3] Dimethylether; [4] Methanol to olefin; [5] Acid leaching conditions after hydrothermal treatment; [6] Low density polyethylene; [7] Polypropylene; [8] Anisole; [9] Acetic anhydride; [10] Biphenyl; [11] 1,4-diisopropylbenzene; [12] Naphtalene; [13] 2,6-di-tert-butylpyridine; [14] Tetramethylammonium hydroxide; [15] Fluid catalytic cracking; [16] Lactic acid; [17] Pentaerythritol; [18] Citric acid.

Table I.3. Scientific literature of desilication assisted by microwave heating.

Year/ Country	**Catalyst**	**(R^p/ R^m)^1**	**Reacted by**	**$[H^+]^p$/ $[H^+]^m$**	**A_{ext}^p/ A_{ext}^m**	**V_{micro}^p/ V_{micro}^m**	**V_{meso}^p/ V_{meso}^m**	**Hysteresis shape**	**Catalytic test**	**Conclusion**	**Ref.**
2009/ES	MFI (ZSM-5)	37/24	0.2 M NaOH 65 °C/ 5 min	-	40/204	0.17/0.12	0.11/0.37	H3	-	Development of mesopores much faster than conventional (10 nm)	117
2015/KR	MFI (ZSM-5)	91/64^2	0.05 M NaOH 100 °C/ 20 min	-	84/151	0.14/0.08	0.07/0.18	-	Butylation of phenol-130 °C	Production of narrow sized pores attributed to shape selectivity for less bulky products	123
2015/SA	MTW (ZSM-12)	-	0.3 M NaOH 85 °C/ 10 min	-	40/380	0.17/0.00	0.09/0.53	H3	Methylation of 2-methyl naphthalene-450 °C	↓of conversion with ↑of mesoporosity and ↓of microporosity	124
2016/SA	MTW (ZSM-12)	-	0.3 M NaOH 85 °C/ 10 min	561/415 ^{TPD}	40/380	0.17/0.00	0.09/0.53	H3	Cracking of n-heptane-650 °C	Formation of mesopores in the expense of micropores. ↑conversion, selectivity & P/E ratio	125
2014/SA	MTT (ZSM-23)	76/66	0.2 M NaOH 85 °C/ 10 min 0.3 M HNO_3 80 °C/ 10 min	-	29/34	0.00/0.02	0.00/0.10	H3	Cracking of *n*-hexane-650 °C	↑micropores and mesopores. ↑conversion and selectivity to produce propylene	126
2011/PT	MOR	9.5/8.8	0.2 M NaOH 85 °C/ 15 min	-	24/96	0.20/0.19	0.05/0.12	H3	Isomerization of m-Xylene-350 °C	Enlargement of micropores. Catalytic behavior near to the parent	127

^{m} Modified material; ^{p} Parent zeolite; ^{py} Amount of Brønsted acid by adsorption of pyridine at 150 °C; ^{TPD} Measurment of acidity by Ammonia-temperature programmed desorption.
^{1} Global silicon aluminum ratio; ^{2} Measurement of SiO_2/Al_2O_3.

Table I.4. Scientific literature of regular etching and etching assisted by NH_4F.

Year/ Country	Catalyst	$(R^p/$ $R^m)^1$	Reacted by	$[H^+]^p/$ $[H^+]^m$	$A_{ext}^p/$ A_{ext}^m	$V_{micro}^p/$ V_{micro}^m	$V_{meso}^p/$ V_{meso}^m	Hysteresis shape	Catalytic test	Conclusion	Ref.
2003/PL	MFI (ZSM-5)	-	5 M HF (acetone) 10 min	-	-	-	-	-	Uptake of *n*-hexane 25 °C	Template in the non-calcined pores is confined to etching just crystal surface, preserve shape and size of the crystals. ↑↑Diffusion coefficient by removing of mechanical barriers on the suface of crystals.	132
2013/FR	MFI (ZSM-5)	19/19	0.5 M HF 4.5 M NH_4F	$643/614^{py}$	09/16	0.18/0.18	0.02/0.04	H3	Isomerization of *m*-xylene-350 °C	Selective dissolution of defect zones & deep penetration in the crystals leading to easier access to the micropores. ↑ Diffusion & Conversion	128
2014/FR	MFI (ZSM-5)	19/20	0.3 M HF 0.2 M HCl 4.5 M NH_4F	$617/596^{py}$	09/14	0.18/0.20	0.02/0.03	H3	Conversion of methylcyclohexane 450 °C	Formation of macropores without changing the physio-chemical properties of its parent. ↑Lifetime & coke content with less toxicity by allowing many coke precursors to diffuse out of the micropores.	144
2016/CN	MFI (ZSM-5)	$26/32^2$	0.5 M HF 25 °C/ 45 min	$597/431^{py}$	72/82	0.11/0.10	0.05/0.06	H3	MTO^3-400 °C	↓ Crystal size & mesopores with ↑ [HF]. ↑Yield of liquid hydrocarbons. ↑Lifetime > 25 h	133
2017/CN	MFI (ZSM-5)	13/13	0.5 M HF 4.5 M NH_4F 25 °C/ 10 min	$597/595^{TPD}$	66/92	0.02/0.02	0.04/0.07	H3	MTO-400 °C	↑V_{meso} with = V_{micro} & acidity. Conversion, lifetime & yield of hydrocarbons. Good performance in regeneration	145
2018/CN	MFI (ZSM-5)	-	0.5 M HF 4.5 M NH_4F 25 °C/ 10 min	-	-	0.15/0.17	0.09/0.18	H3	Cracking of *n*-hexane-650 °C	↑BET& mesopores / = microporsity & acidity. Catalytic activity ↑ as coke ↓ coke. Introduction of phosphorous leads to high & stable catalytic activity & higher selectivity on olefins.	146
2018/SA	ZSM-22	59/62	3.5 M HF Ice bath 30 min	$1370/1970^{TPD}$	56/26	0.04/0.02	0.10/0.14	H3	Steam cracking of *n*-hexane -650 °C	↑Mesoporosity & ↓Microporosity. ↑ Conversion & lifetime	135
2007/CZ	MFI (Silicate-1)	-	2 M HF 3 min	-	-	-	-	-	-	Sharp slits along grain boundaries for polycrystalline layers &along contact faces of both individual single crystals for large crystal twins	217
1986/CA	MOR	7.9/9.1	0.12 M HF	$4.4/10^{py4}$	319/331	-	-	-	Conversion of cumene	Flouride enhanced strong lewis & weak bronsted. ↑ External surface & catalytic lifetime	130
1987/DU	MOR	-	0.5 M NH4F (1 wt.% F)	> 0	-	-	-	-	Oxidation of methane < 400 °C	Presence of superacid sites after fluorination that ↑ activity & selectivity of hydrocarbons & methanol. Activity ↓ in deep fluorination	218

Continuation of **Table I.4.** Scientific literature of regular etching and etching assisted by NH_4F.

Year/ Country	**Catalyst**	**(R^p/ R^m)^1**	**Reacted by**	**[H^+]^p/ [H^+]^m**	**$A_{ext}{}^p$/ $A_{ext}{}^m$**	**$V_{micro}{}^p$/ $V_{micro}{}^m$**	**$V_{meso}{}^p$/ $V_{meso}{}^m$**	**Hysteresis shape**	**Catalytic test**	**Conclusion**	**Ref.**
1998/KP	MOR	05/14	0.5 M HF 25 °C/ 240 h (polyethylen)	9.9/3.4^{py}	15/64	0.18/0.18	0.03/0.11	H2	-	↑Dealumination time leads to partial destruction of structure by simultaneous removal of Si & Al	131
2016/BG	MOR	9.7/8.9	0.1 M HF x M NH_4F 25 °C/ 15 min	≈	-	≈	> 0	H3	Conversion of m-xylene-250 °C	↑↑ Catalytic test due to formation of secondary system of large mesopores that improve access to the microopore with preservation of acidity & composition.	150
2017/HU	MOR	≈	0.5 M HF x M NH_4F	186/218^{TPD5}	-	0.16/0.18	-	-	Conversion of glycerol-100 °C	Best catalytic performance with optimal Br/L acid sites ratio. ↑ in the accessibility with zirconia. Zr-MOR is a highly active, cost effective, stable & reusable.	151
1995/USA	*BEA	19.8/17.8	0.17 M NH4F (0.3 wt.% F)	> 0	-	-	-	-	Cracking of *n*-hexane-350 °C	Low level fluorination that ↑the acidity of Brønsted acid sites through an inductive effect by F, leading to ↑ in the catalytic activity.	219
2014/FR	FER	08/09	0.25 M HF 13.5 M NH_4F	≈	18/55	0.15/0.15	0.07/0.33	-	-	Rectangular shape of mesopores leads to ↑access to 8 & 10-MR pore system. Similar composition & acid properties to its parent.	147
2016/CN	CHA (SAPO-34)	-	0.05 M HF 13.5 M NH_4F 25 °C/ 60 min	≈	13/06	0.26/0.26	0.01/0.04	H3	MTO-400 °C	Large meso-macropores rely on organic template used. ↑Selectivity attributed to the enhanced diffusion, the retained microporsity & appropriate acidity.	149
2016/FR	CHA (SAPO-34)	13/22^6	HF-NH_4F 25 °C/ 30 min	296/120DA	-	0.29/0.21	> 0	H3	MTO-400 °C	↓V_{micro} with ↑S_{BET}& V_{meso} due to direct dissolution of defected zones enriched with silicon makes better access to all microprosity	148
-/SE	IZM-2-50^7	50/51	0.5 M HF Icebath 15 min	≈	115/176	0.1/0.09	0.21/0.67	H3	-	De-agglomeration of zeolite with a preservation of crystallinity, composition and higher external surface	134

^{m} Modified material; ^{p} Parent zeolite; ^{py} Amount of Brønsted acid by adsorption of pyridine at 150 °C; ^{TPD} Measurment of acidity by Ammonia-temperature programmed desorption; ^{DA} Deuterated acetonitrile
^{1} Global silicon aluminum ratio; ^{2} Measurement of SiO_2/Al_2O_3; ^{3} Methanol to olefin; ^{4} Amount of Brønsted acid by adsorption of pyridine at 400 °C; ^{5} ($\times 10^2$) but it is a strange value; ^{6} (Al + P/Si), ^{7} IFPEN zeolitic material no. 2 (unknown structure).

Bibliographic references

[1] F. Cronstedt, in: Akademibokhandeln Stockholm, 1756, 120.

[2] A. Dwyer, An introduction to zeolite molecular sieves, John Wiley & Sons, Chichester, 1988.

[3] M. E. Davis, Ordered porous materials for emerging applications, Nature 417 (2002) 813–821.

[4] H. O. Pastore, S. Coluccia, L. Marchese, POROUS ALUMINOPHOSPHATES : From molecular sieves to designed acid catalysts, Annu. Rev. Mater. Res. 35 (2005) 351–395.

[5] M. Guisnet, F. R. Ribeiro, Les zéolithes un nanomonde au service de la catalyse, 6th Ed., 2006.

[6] A. Corma, A. Martinez, Zeolites and zeotypes as catalysts, Adv. Mater. 7 (1995) 137–144.

[7] A. Thangaraj, M. J. Eapen, S. Sivasanker, P. Ratnasamy, Studies on the synthesis of titanium silicalite, TS-1, Zeolites 12 (1992) 943–950.

[8] E. M. Flanigen, White Plains, Zeolites and molecular sieves: An historical perspective, in: Introduction to zeolite science and practice, H. van Bekkum, E.M. Flanigen, P.A. Jacobs and J.C. Jansen (Eds.), Elsevier, Stud. Surf. Sci. Catal., 2001, 11–38.

[9] D. W. Breck, Zeolite molecular sieves: Structure, chemistry, and use, John Wiley & Sons, 1974, 634.

[10] R. W. Broach, Zeolite types and structures, in: Zeolites in industrial separation and catalysis, S. Kulprathipanja (Ed.), WILEY-VCH Verlag GmbH & Co., 2010, 27–60.

[11] R. M. Barrer, Synthesis and reactions of mordenite, J. Chem. Soc. (1948) 2158–2163.

[12] R. F. Lobo, Introduction to the structural chemistry of zeolites, in: Handbook of zeolite science and technology, S. Auerbach, K. A. Carrado, P. Dutta (Eds.), Marcel Dekker, New York, 2003.

[13] C. Baerlocher, L. B. McCusker, Atlas of zeolite framework types, 6th Ed., Elsevier, 2007, 218, 219.

[14] M. Guisnet, J. -P. Gilson, Zeolites for cleaner technologies, Catalytic science series, 3, 2001.

[15] M. Elanany, M. Koyama, M. Kubo, E. Broclawik, A. Miyamoto, Periodic density functional investigation of Lewis acid sites in zeolites: relative strength order as revealed from NH_3 adsorption, Appl. Surf. Sci. 246 (2005) 96–101.

[16] T. Chen, A. Men, P. Sun, J. Zhou, Z. Yuan, Z. Guo, J. Wang, D. Ding, H. Li, Lewis acid sites on dehydroxylated zeolite HZSM-5 studied by NMR and EPR, Catal. Today 30 (1996) 189–192.

[17] A. Corma, Inorganic solid acids and their use in acid-catalyzed hydrocarbon reactions, Chem. Rev. 95 (1995) 559–614.

[18] J. A. Ryder, A. K. Chakraborty, A. T. Bell, Density functional theory study of proton mobility in zeolites: Proton migration and hydrogen exchange in ZSM-5, J. Phys. Chem. B 104 (2000) 6998–7011.

[19] R. Gounder, E. Iglesia, The catalytic diversity of zeolites: confinement and solvation effects within voids of molecular dimensions, Chem. Commun. 49 (2013) 3491–3509.

[20] A. Auroux, Acidity and basicity: Determination by adsorption microcalorimetry, H. G. Karge, J. Weitkamp (Eds.), Springer-Verlag Berlin Heidelberg, Mol. Sieves, 6, 2008, 45–152.

[21] D. J. Parillo, R. J. Grote, Characterization of acidity in H-ZSM-5, H-ZSM-12, H-mordenite, and H-Y using microcalorimetry, J. Phys. Chem. 97 (1993) 8786–8792.

[22] D. B. Lukyanov, T. Vazhnova, N. Cherkasov, J. L. Casci, J. J. Birtill, Insights into Brønsted acid sites in the zeolite mordenite, J. Phys. Chem. 118 (2014) 23918–23929.

[23] W. J. Mortier, J. J. Pluth, J. V. Smith, Positions of cations and molecules in zeolites with the mordenite-type framework. II Dehydrated hydrogen ptilolite. Mater. Res. Bull. 10 (1975) 1319–1326.

[24] M. Brändle, J. Sauer, Acidity differences between inorganic solids induced by their framework structure. A combined quantum mechanics/molecular mechanics ab initio study on zeolites, J. Am. Chem. Soc. 120 (1998) 1556–1570.

[25] A. Simperler, R. G. Bell, M. D. Foster, A. E. Gray, D. W. Lewis, M. W. Anderson, Probing the acid strength of Brønsted acidic zeolites with acetonitrile: An atomistic and quantum chemical study, J. Phys. Chem. B 108 (2004) 7152–7161.

[26] T. Bucko, L. Benco, T. Demuth, J. Hafner, Ab initio density functional investigation of the (001) surface of mordenite, J. Chem. Phys. 117 (2002) 7295–7305.

[27] D. B. Lukyanov, T. Vazhnova, J. L. Casci, J. J. Birtill, On the catalytic properties of Brønsted acid sites located in the small and large channels in zeolite mordenite. Book of Abstracts 1:13th International Congress on Catalysis, Paris, 2004, 219.

[28] V. L. Zholobenko, M. A. Makarova, J. Dwyer, Inhomogeneity of Brønsted acid sites in H-mordenite, J. Phys. Chem. 97 (1993) 5962–5964.

[29] H. G. Karge, V. J. Dondur, Investigation of the distribution of acidity in zeolites by temperature-programmed desorption of probe molecules. I. Dealuminated mordenites, J. Phys. Chem. 94 (2) (1990) 765–772.

[30] A. Jacobs, W. J. Mortier, An attempt to rationalize stretching frequencies of lattice hydroxyl groups in hydrogen-zeolites, Zeolites 2 (1982) 226–230.

[31] S. Devautour, F. Henn, J. C. Giuntini, J. V. Zanchetta, J. Vander-Schueren, TSDC relaxation map analysis in a Na-mordenite zeolite, Solid State Ionics 122 (1999) 105–111.

[32] O. Marie, P. Massiani, F. Thibault-Starzyk, Infrared evidence of a third Brønsted site in mordenites, J. Phys. Chem. B 108 (2004) 5073–5081.

[33] A. Alberti, Location of Brønsted sites in mordenite, Zeolites 19 (1997) 411–415.

[34] A. Martucci, G. Cruciani, A. Alberti, C. Ritter, P. Ciambelli, M. Rapacciuolo, Location of Brønsted sites in D-mordenites by neutron powder diffraction, Microporous Mesoporous Mater. 35–36 (2000) 405–412.

[35] H. Huo, L. Peng, Z. Gan, C. P. Grey, Solid-state MAS NMR studies of Brønsted acid sites in zeolite H-mordenite, J. Am. Chem. Soc. 134 (2012) 9708–9720.

[36] M. Bevilacqua, G. A. Busca, Study of localization and accessibility of Brønsted and lewis acid sites of H-mordenite through the FT-IR spectroscopy of adsorbed branched nitriles, Catal. Commun. 3 (2002) 497–502.

[37] T. Vazhnova, D. B. Lukyanov, Fourier Self-Deconvolution of the IR spectra as a tool for investigation of distinct functional groups in porous materials: Brønsted acid sites in zeolites, Anal. Chem. 85 (2013) 11291–11296.

[38] A. Corma, Microporous to mesoporous molecular sieve materials and their use in catalysis, Chem. Rev. 97 (1997) 2373–2420.

[39] G. F. Froment, J. D. Meyer, E. G. Derouane, Deactivation of zeolite catalysts by coke formation, J. Catal. 124 (1990) 391– 400.

[40] G. F. Froment, Coke formation in catalytic processes: Kinetics and catalyst deactivation, Stud. Surf. Sci. Catal. 111 (1997) 53–68.

[41] R. Baur, R. Krishna, The effectiveness factor for zeolite catalysed reactions, Catal. Today. 105 (2005) 173–179.

[42] A. Taguchi, F. Schüth, Ordered mesoporous materials in catalysis, Microporous Mesoporous Mater. 77 (2005) 1–45.

[43] C. T. Kresge, M. E. Leonowicz, W. J. Roth, J. C. Vartuli, J. S. Beck, Ordered mesoporous molecular sieves synthesized by a liquid-crystal template mechanism, Nature 359 (1992) 710–712.

[44] V. Meynen, P. Cool, E. F. Vansant, Synthesis of siliceous materials with micro-and mesoporosity, Microporous Mesoporous Mater. 104 (2007) 26–38.

[45] R. Mokaya, Alumination pathways to mesoporous aluminosilicates with high-temperature hydrothermal stability, Chem. Phys. Chem. 3 (2002) 360–363.

[46] C. C. Freyhardt, M. Tsapatsis, R. F. Lobo, K. J. B. Jr, M. E. Davis, A high-silica zeolite with a 14-tetrahedral-atom pore opening, Nature 381 (1996) 295–298.

[47] R. F. Lobo, The promise of emptiness, Nature 443 (2006) 757–758.

[48] E. Koohsaryan, M. Anbia, Nanosized and hierarchical zeolites: A Short Review, Chin. J. Catal. 37 (2016) 447–467.

[49] J. C. Groen, J. A. Moulijn, J. Perez-Ramirez, Desilication: on the controlled generation of mesoporosity in MFI zeolites, J. Mater. Chem. 16 (2006) 2121–2131.

[50] M. Ogura, E. Kikuchi, M. Matsukata, MFI zeolite with uniform mesopores created by alkali treatment, in: Zeolites and mesoporous materials at the dawn of the 21st century, A. Galarneau, F. Fajula, F. Di Renzo, J. Vedrine (Eds.), Elsevier, Stud. Surf. Sci. Catal. 130, 2001, 216.

[51] J. Perez-Ramirez, C. H. Christensen, K. Egeblad, C. H. Christensen, J. C. Groen, Hierarchical zeolites: Enhanced utilisation of microporous crystals in catalysis by advances in materials design, Chem. Soc. Rev. 37 (2008) 2530–2542.

[52] W. Schmidt, Solid catalysts on the nanoscale: Design of complex morphologies and pore structures, ChemCatChem 1 (2009) 53–67.

[53] R. Chal, C. Gérardin, M. Bulut, S. Van Donk, Overview and industrial assessment of synthesis strategies towards zeolites with mesopores, ChemCatChem 3 (2011) 67–81.

[54] K. R. Kloestra, H. Van Bekkum, J. C. Jansen, Mesoporous material containing framework tectosilicate by pore-wall recrystallization, Chem. Commun. - (1997) 2281–2282.

[55] A. H. Janssen, I. Schmidt, C. J. H. Jacobsen, A. J. Koster, K. P. De Jong, Exploratory study of mesopore templating with carbon during zeolite synthesis, Microporous Mesoporous Mater. 65 (2003) 59–75.

[56] M. Choi, K. Na, J. Kim, Y. Sakamoto, O. Terasaki, R. Ryoo, Stable single-unit-cell nanosheets of zeolite MFI as active and long-lived catalysts, Nature 461 (2009) 246–250.

[57] Y. Liu, W. Z. Hang, T. J. Pinnavaia, Steam-stable MSUS aluminosilicate mesostructures assembled from zeolite ZSM-5 and zeolite Beta seeds, Angew. Chem., Int. Ed. 40 (2001)1255–1258.

[58] L. Tosheva, V. P. Valtchev, Nanozeolites: Synthesis, crystallization mechanism, and applications, Chem. Mater. 17 (2005) 2494–2513.

[59] S. Moreno, G. Poncelet, Dealumination of small- and large-port mordenites: A comparative study, Microporous Mater. 12 (1997) 197–222.

[60] Y. Hong, J. J. Fripiat, Microporous characteristics of H-Y, H-ZSM-5 and H-mordenite dealuminated by calcination, Microporous Mater. 4 (1995) 323–334.

[61] R. Giudici, H. Kouwenhoven, R. Prins, Comparison of nitric and oxalic acid in the dealumination of mordenite, Appl. Catal., A 203 (2000) 101–110.

[62] A. W. O'Donovan, C. T. O'Connor, K. R. Koch, Effect of acid and steam treatment of Na- and H-mordenite on their structural, acidic and catalytic properties, Microporous Mater. 5 (1995) 185–202.

[63] B. Tang, W. Dai, X. Sun, N. Guan, L. Li, M. Hungerb, A procedure for the preparation of Ti-Beta zeolites for catalytic epoxidation with hydrogen peroxide, Green Chem. 16 (2014) 2281–2291.

[64] A. Pradhan, S. J. Jong, W. H. Chen, J. F. Wu, T.C. Tsai, S. B. Liu, Influences of zeolite structure on formation and location of coke: A^{129}Xe and ^{13}C CP-MAS NMR study, Appl. Catal., A 159 (1997) 187–209.

[65] M. F. Wilson, I. P. Fisher, J. F. Kriz, Hydrogenation and extraction of aromatics from oil sands distillates and effects on cetane improvement, Energy Fuels 1 (1987) 540–544.

[66] M. M. L. Ribeiro Carrott, P. A. Russo, C. Carvalhal, P. J. M. Carrott, J. P. Marques, J. M. Lopes, I. Gener, M. Guisnet, F. Ramoa Ribeiro, Microporous Mesoporous Mater. 81 (2005) 259–267.

[67] R. Szostak, Secondary synthesis methods, in: Introduction to zeolite science and practice, H. Van Bekkum, E. M. Flanigen, P. A. Jacobs, J. C. Jansen (Eds.), Elsevier, Stud. Surf. Sci. Catal. 137, 2001, 261–298.

[68] R. López-Fonseca, B. de Rivas, J. I. Gutiérrez-Ortiz, A. Aranzabal, J. R. González-Velasco, Enhanced activity of zeolites by chemical dealumination for chlorinated VOC abatement, Appl. Catal., B 41(2003) 31–42.

[69] A. Corma, M. J. Diaz-Cabanas, J. Martinez-Triguero, F. Rey, J. Rius, A large-cavity zeolite with wide pore windows and potential as an oil refining catalyst, Nature 418 (2002) 514–517.

[70] A. H. Janssen, A. J. Koster, K. P. de Jong, On the shape of the mesopores in zeolite Y: A three-dimensional transmission electron microscopy study combined with texture analysis, J. Phys. Chem. B 106 (2002) 11905–11909.

[71] L. Teyssier, M. Thomas, C. Bouchy, J. A. Martens, E. Guillon, Liquid chromatography method for quantification of surface connected mesoporosity in ultrastable Y zeolites, Microporous Mesoporous Mater. 100 (2007) 6–11.

[72] H. -M. Kao, Y. -C. Chen, C. -C. Ting, P. T. Chen, J. -C. Jiang, Characterization of extraframework aluminium in H-mordenite dealuminated with ammonium hexaflourosilicate, Catal. Today 97 (2004) 13–23.

[73] Q. L. Wang, M. Torrealba, G. Giannetto, M. Guisnet, G. Perot, M. Cahoreau, J. Caisso, Dealumination of Y-zeolite with ammonium hexaflourosilicate: A SIMS-XPS study of the aluminium distribution, Zeolites 10 (1990) 703–706.

[74] G. Garralon, V. Fornes, A. Corma, Faujasites dealuminated with ammonium hexafluorosilicate: Variables affecting the method of preparation, Zeolites 8 (1988) 268–272.

[75] J. M. Silva, M. F. Riberio, F. R. Ribeiro, E. Benazzi, N. S. Gnep, M. Guisnet, Influence of the treatment of mordenite by ammonium hexaflourosilicate on physiochemical and catalytic properties, Zeolites 16 (1996) 275–280.

[76] J. C. Groen , T. Sano , J. A. Moulijn, J. Pérez-Ramírez, Alkaline-mediated mesoporous mordenite zeolites for acid-catalyzed conversions, J. Catal. 251 (2007) 21–27.

[77] F. Schmidt, M. R. Lohe, B. Büchner, F. Giordanino, F. Bonino, S. Kaskel, Improved catalytic performance of hierarchical ZSM-5 synthesized by desilication with surfactants, Microporous Mesoporous Mater. 165 (2013) 148–157.

[78] D. Verboekend, J. Perez-Ramirez, Design of hierarchical zeolite catalysts by desilication, Catal. Sci. Technol. 1 (2011) 879–890.

[79] S. Abelló, A. Bonilla, J. Pérez-Ramírez, Mesoporous ZSM-5 zeolite catalysts prepared by desilication with organic hydroxides and comparison with NaOH leaching, Appl. Catal., A 364 (2009) 191–198.

[80] L. Zhao, B. Shen, J. Gao, C. Xu, Investigation on the mechanism of diffusion in mesopore structured ZSM-5 and improved heavy oil conversion, J. Catal. 258 (2008) 228–234.

[81] M. Ogura, S. Shinomiya, J. Tateno, Y. Nara, M. Nomura, E. Kikuchi, M. Matsukata, Alkali-treatment technique-new method for modification of structural and acid-catalytic properties of ZSM-5 zeolites, Appl. Catal., A 219 (2001) 33–43.

[82] A. Čižmek, B. Subotić, R. Aiello, F. Crea, A. Nastro, C. Tuoto, Dissolution of high-silica zeolites in alkaline solutions I. Dissolution of silicalite-1 and ZSM-5 with different aluminum content, Microporous Mater. 4 (1995) 159–168.

[83] J. C. Groen, L. A. A. Peffer, J. A. Moulijn, J. Pérez-Ramírez, Mechanism of hierarchical porosity development in MFI zeolites by desilication: The role of aluminium as a pore-directing agent, Chem. - Eur. J. 11 (2005) 4983–4994.

[84] J. C. Groen, J. A. Moulijn, J. Pérez-Ramírez, Decoupling mesoporosity formation and acidity modification in ZSM-5 zeolites by sequential desilication-dealumination, Microporous Mesoporous Mater. 87 (2005) 153–161.

[85] J. M. Cruz, A. Corma, V. Fornés, Framework and extra-framework aluminium distribution in $(NH4)_2F_6Si$-dealuminated Y zeolites: Relevance to cracking catalysts, App. Catal. 50 (1989) 287–293.

[86] J. Lynch, F. Raatz, C. Delalande, Defects in AHFS-dealuminated Y zeolite: A crucial factor for mesopores formation in the following base treatment procedure, Stud. Surf. Sci. Catal. 39 (1998) 547–557.

[87] S. Van Donk, A. H. Janssen, J. H. Bitter, K. P. de Jong, Generation, characterization, and impact of mesopores in zeolite catalysts, Catal. Rev. 45 (2003) 297–319.

[88] Y. Tao, H. Kanoh, L. Abrams, K. Kaneko, Mesopore-modified zeolites: preparation, characterization, and applications, Chem. Rev. 106 (2006) 896–910.

[89] D. Verboekend, T. C. Keller, M. Milina, R. Hauert, J. Pérez-Ramírez, Hierarchy brings function: mesoporous clinoptilolite and L zeolite catalysts synthesized by tandem acid-base treatments, Chem. Mater. 25 (2013) 1947–1959.

[90] C. Li, L. Guo, P. Liu, K. Gong, W. Jin, L. Li, X. Zhu, X. Liu, B. Shen, Defects in AHFS-dealuminated Y zeolite: A crucial factor for mesopores formation in the following base treatment procedure, Microporous Mesoporous Mater. 255 (2018) 242–252.

[91] D. Verboekend, S. Mitchell, M. Milina, J. C. Groen, J. Pérez-Ramírez, Full compositional flexibility in the preparation of mesoporous MFI zeolites by desilication, J. Phys. Chem. C 115 (2011) 14193–14203.

[92] D. Verboekend, J. Pérez-Ramírez, Desilication mechanism revisited: Highly mesoporous all-silica zeolites enabled through pore-directing agents, Chem. - Eur. J. 17 (2011) 1137–1147.

[93] J. Y. Ying, J. García-Martínez, Mesostructured zeolitic materials, and methods of making and using the same, US Patent 20050239634 (2005).

[94] J. García-Martínez, M. Johnson, J. Valla, K. Li, J. Y. Ying, Mesostructured zeolite Y-high hydrothermal stability and superior FCC catalytic performance, Sci. Technol. 2 (2012) 987–994.

[95] R. Chal, T. Cacciaguerra, S. Van Donk, C. Gerardin, Pseudomorphic synthesis of mesoporous zeolite Y crystals, Chem. Commun. 46 (2010) 7840–7842.

[96] W. C. Yoo, X. Zhang, M. Tsapatsis, A. Stein, Synthesis of mesoporous ZSM-5 zeolites through desilication and re-assembly processes, Microporous Mesoporous Mater. 149 (2012) 147–157.

[97] Y. Goto, Y. Fukushima, P. Ratu, Y. Imada, Y. Kubota, Y. Sugi, M. Ogura, M. Matsukata, Mesoporous material from zeolite, J. Porous Mater. 9 (2002) 43–48.

[98] I. I. Ivanova, E. E. Knyazeva, Micro-mesoporous materials obtained by zeolite recrystallization: synthesis, characterization and catalytic applications, Chem. Soc. Rev. 42 (2013) 3671–3688.

[99] I. I. Ivanova, E. E. Knyazeva, Method of hydrocarbon conversion, micro-mesoporous catalyst for its realization and method of catalyst preparation, RU Patent 2288034 (2006).

[100] V. V. Ordomsky, V. Y. Murzin, Y. V. Monakhova, Y. V. Zubavichus, E. E. Knyazeva, N. S. Nesterenko, I. I. Ivanova, Nature, strength and accessibility of acid sites in micro/mesoporous catalysts obtained by recrystallization of zeolite BEA, Microporous Mesoporous Mater. 105 (2007) 101–110.

[101] I. A. Kasyanov, A. Maerle, I. I. Ivanova, V. I. Zaikovskii, Towards understanding of the mechanism of stepwise zeolite recrystallization into micro/mesoporous materials, J. Mater. Chem. A 2 (2014) 16978–16988.

[102] K. Li, J. García-Martínez, M. G. Beaver, Introduction of mesoporosity into low silica zeolites, US Patent 2013106816 A1 (2013).

[103] J. García-Martínez, J. M. Marvin, J. Valla, Mesoporous framework-modified zeolites, US Patent 13/440781 (2012).

[104] A. Sachse, A. Grau-Atienza, E. O. Jardim, N. Linares, M. Thommes, J. Garcia-Martinez, Development of intracrystalline mesoporosity in zeolites through surfactant-templating, Crys. Growth Des. 17 (8) (2017) 4289–4305.

[105] J. M. Thomas, R. K. Leary, A major advance in characterizing nanoporous solids using a complementary triad of existing techniques, Angew. Chem., Int. Ed. 53 (2014) 12020–12021.

[106] J. García-Martínez, C. Xiao, K. A. Cychosz, K. Li, W. Wan, X. Zou, M. Thommes, Evidence of intracrystalline mesostructured porosity in zeolites by advanced gas sorption, electron tomography and rotation electron diffraction, ChemCatChem 6 (2014) 3110–3115.

[107] N. Linares, A. Sachse, E. Serrano, A. Grau-Atienza, E. O. De Oliveira Jardim, J. Silvestre-Albero, M. A. L. Cordeiro, F. Fauth, G. Beobide, O. Castillo, J. García-Martínez, In situ time-resolved observation of the development of intracrystalline mesoporosity in USY zeolite, Chem. Mater. 28 (2016) 8971–8979.

[108] I. I. Ivanova, I. A. Kasyanov, A. A. Maerle, V. I. Zaikovskii, Mechanistic study of zeolites recrystallization into micro-mesoporous materials, Microporous Mesoporous Mater. 189 (2013) 163–172.

[109] D. Mehlhorn, J. Rodriguez, T. Cacciaguerra, R. -D. Andrei, C. Cammarano, F. Guenneau, A. Gedeon, B. Coasne, M. Thommes, D. Minoux, C. Aquino, J. -P. Dath, F. Fajula, A. Galarneau, Relevation on the complex nature of mesoporous hierarchical FAU-Y zeolites, Longmuir 34 (2018) 11414–11423.

[110] V. Meynen, P. Cool, E. F. Vansant, Verified syntheses of mesoporous materials, Microporous Mesoporous Mater. 125 (2009) 170–223.

[111] H. Wei, S. Xie, N. Gao, K. Liu, X. Liu, W. Xin, X. Li, S. Liu, L. Xu, Alkali treatment upon MCM-49 zeolite with various contents of HMI in the presence of CTAB and application in anisole acylation with acetic anhydride, App. Catal., A 495 (2015) 152–161.

[112] H. Wei, S. Xie, K. Liu, W. Xin, X. Li, S. Liu, S. Gu, S. Liu, L. Xu, CTAB Modification of MCM-49 Zeolite Containing HMI and its acylation of anisole, Chin. J. Catal. 36 (2015) 1766–1776.

[113] H. Liu, S. Xie, W. Xin, S. Liu, L. Xu, Hierarchical ZSM-11 zeolite prepared by alkaline treatment with mixed solution of NaOH and CTAB, Catal. Sci. Technol. 6 (2015) 1328–1342.

[114] V. V. Ordomsky, I. I. Ivanova, E. E. Knyazeva, V. V. Yuschenko, V. I. Zaikovskii, Cumene disproportionation over micro/mesoporous catalysts obtained by recrystallization of mordenite, J. Catal. 295 (2012) 207–216.

[115] I. Grosse, K. Estel, Thin surfactant layers at the solid interface, Colloid Polym. Sci. 278 (2000) 1000–1006.

[116] D. Verboekend, G. Vile, J. Perez-Ramirez, Mesopore formation in USY and Beta zeolites by base leaching: selection criteria and optimization of pore-directing agents, Cryst. Growth Des. 12 (2012) 3123–3132.

[117] S. Abello, J. Perez-Ramirez, Accelerated generation of intracrystalline mesoporosity in zeolites by microwave-mediated desilication, Phys. Chem. Chem. Phys. 11 (2009) 2959–2963.

[118] C. S. Cundy, Microwave techniques in the synthesis and modification of zeolite catalysts. A review, Collect. Czech. Chem. Commun. 63 (1998) 1699–1723.

[119] C. Gabriel, S. Gabriel, E. H. Grant, B. S. J. Halstead, D. M. P. Mingos, Dielectric parameters relevant to microwave dielectric heating, Chem. Soc. Rev. 27 (1998) 213–225.

[120] A. Fini, A. Breccia, Chemistry by microwaves, Pure Appl. Chem. 71 (1999) 573–579.

[121] C. C. Pavel, W. Schmidt, Generation of hierarchical pore systems in the titanosilicate ETS-10 by hydrogen peroxide treatment under microwave irradiation, Chem. Commun. 0 (2006) 882–884.

[122] C. C. Pavel, S. -H. Park, A. Dreier, B. Tesche, W. Schmidt, Structural defects induced in ETS-10 by postsynthesis treatment with H_2O_2 solution, Chem. Mater. 18 (2006) 3813–3820.

[123] Z. Hasan, J. Wong Jun, C. -U. Kim, K. -E. Jeong, S. -Y. Jeong, S. H. Jhung, Desilication of ZSM-5 zeolites for mesoporosity development using microwave irradiation, Mater. Res. Bull. 61 (2015) 469–474.

[124] M. A. Sanhoob, O. Muraza, T. Tago, T. Taniguchi, G. Watanabe, T. Masuda, Development of mesoporous ZSM-12 zeolite and its application in alkylation of 2-methylnaphthalene, Res. Chem. Intermed. 42 (2016) 6437–6448.

[125] O. Muraza, M. A. Sanhoob, M. A. B. Siddiqui, Fabrication of desilicated MTW zeolite and its application in catalytic cracking of *n*-heptane, Adv. Power Tech. 27 (2016) 372–378.

[126] O. Muraza, I. A. Bakare, T. Tago, H. Konno, T. Taniguchi, A. M. Al-Amer, Z. H. Yamani, Y. Nakasaka, T. Masuda, Selective catalytic cracking of *n*-hexane to propylene over hierarchical MTT zeolite, Fuel 135 (2014) 105–111.

[127] V. Piaxao, R. Monteiro, M. Andrade, A. Fernandes, J. Rocha, A. P. Carvalho, A. Martins, Desilication of MOR zeolite: Conventional versus microwave assisted heating, Appl. Catal., A 402 (2011) 59–68.

[128] Z. Qin, L. Lakiss, J. -P. Gilson, K. Thomas, J. -M. Goupil, C. Fernandez, V. Valtchev, Chemical equilibirium controlled etching of MFI-type zeolite and its influence on zeolite structure, acidity, and catalytic activity, Chem. Mater. 25 (2013) 2759–2766.

[129] F. Thibault-Starzyk, I. Stan, S. Abello, A. Bonilla, K. Thomas, C. Fernandez, J. -P. Gilson, J. Perez-Ramirez, Quantification of enhanced acid site accessibility in hierarchical zeolites-the accessibility index, J. Catal. 264 (2009) 11−14.

[130] A. K. Ghosh, R. A. Kydd, Acidity and activity of fluorinated mordenites, J. Catal. 103 (1987) 399−406.

[131] K. -H. Lee, B. -H. Ha, Characterization of mordenites treated by HCl/steam or HF, Microporous Mesoporous Mater. 23 (1998) 211–219.

[132] J. Wloch, Effect of surface etching of ZSM-5 zeolite crystals on the rate of *n*-hexane sorption, Miroporous Mesoporous Mater. 62 (2003) 81–86.

[133] F. Meng, Y. Wang, S. Wang, Methanol to gasoline over zeolite ZSM-5: Improved catalyst performance by treatment with HF, RCS Adv. 6 (2016) 58586–58593.

[134] Y. Li, H. Zheng, Y. Yun, D. Bernin, M. Edén, X. Zou, F. Gao, Deagglomeration of IZM-2 zeolite crystals by post-synthetic treatment, Microporous Mesoporous Mater. 225 (2016) 185–191.

[135] A. K. Jamil, O. Muraza, M. H. Ahmed, A. Zainalabdeen, K. Muramoto, Y. Nakasaka, Z. H. Yamani, T. Yoshikawa, T. Masuda, Hydrothermally stable acid-modified ZSM-22 zeolite for selective propylene production via steam-assisted catalytic cracking of *n*-hexane, Microporous Mesoporous Mater. 260 (2018) 30–39.

[136] K. W. Kolasinski, The composition of fluoride solutions, J. Electrochem. Soc.152 (2005) J99–J104.

[137] D. M. Knotter, The chemistry of wet etching, in: Handbook of cleaning in semiconductor manufacturing: Fundamental and applications, K. A. Reinhardt, R. F. Reidy (Eds.), John Wiley & Sons, Inc.: Hoboken, NJ, USA, Chapter 3, 95–141.

[138] J. R. Schlup, R.W. Vaughan, Nuclear magnetic resonance investigation of fluorinated oxide catalysts: II. Fluorinated alumina and aluminosilicates, J. Catal. 99 (1986) 304–315.

[139] G. A. C. M. Spierings, Wet chemical etching of silicate glasses in hydrofluoric acid based solutions, J. Mater. Sci. 28 (1993) 6261–6273.

[140] J. S. Judge, A study of the dissolution of SiO_2 in acidic fluoride solutions, J. Electrochem. Soc. 118 (1971) 1772–1775.

[141] D. M. Knotter, Etching mechanism of vitreous silicon dioxide in HF-based solutions, J. Am. Chem. Soc. 122 (2000) 4345–4351.

[142] K. W. Kolasinski, The mechanism of Si etching in fluoride solutions, Phys. Chem. Chem. Phys. 5 (2003) 1270–1278.

[143] F. Meunier, C. D. Verboekend, J. -P. Gilson, J. C. Groen, J. Pérez-Ramírez, Influence of crystal size and probe molecule on diffusion in hierarchical ZSM-5 zeolites prepared by desilication, Microporous Mesoporous Mater. 148 (2012) 115–121.

[144] F. Ngoye, L. Lakiss, Z. Qin, S. Laforge, C. Canaff, V. Valtchev, K. Thomas, A. Vicente, J. -P. Gilson, Y. Pouilloux, C. Fernandez, L. Pinard, Mitigating coking during methylcyclohexane transformation on HZSM-5 zeolites with additional porosity, J. Catal. 320 (2014) 118–126.

[145] F. Meng, X. Wang, S. Wang, Y. Wang, Fluoride-treated HZS-5 as a highly stable catalyst for the reaction of methanol to gasoline, Catal. Today 298 (2017) 226–233.

[146] Y. Ji, H. Yang, W. Yan, Catalytic Cracking of *n*-hexane to Light Alkene over ZSM-5 Zeolite: Influence of Hierarchical Porosity and Acid Property, Mol. Catal. 448 (2018) 91−99.

[147] X. Chen, T. Todorova, A. Vimont, V. Ruaux, Z. Qin, J. -P. Gilson, V. Valtchev, In situ and post-synthesis control of physiochemical properties of FER-type crystals, Microporous Mesoporous Mater. 200 (2014) 334–342.

[148] X. Chen, A. Vicente, Z. Qin, V. Ruaux, J. -P. Gilson, V. Valtchev, The preparation of hierarchical SAPO-34 crystals via post-synthesis fluoride etching, Chem. Commun. 52 (2015) 3512–3515.

[149] X. Chen, D. Xi, Q. Sun, N. Wang, Z. Dai, D. Fan, V. Valtchev, J. Yu, A top-down approach to hierarchical SAPO-34 zeolites with improved selectivity of olefin, Microporous Mesoporous Mater. 234 (2016) 401–408.

[150] Y. Kalvachev, T. Todorova, D. Nihtianova, H. Lazarova, M. Popova, Fluoride etching of mordenite and its influence on catalytic activity, J. Mater. Sci. 52 (2017) 5297–5308.

[151] M. Popova, H. Lazarova, Y. Kalvachev, T. Todorova, A. Szegedi, P. Shestakova, G. Mali, V. D. B.C. Dasireddy, B. Likozar, Zr-modified mordenite as heterogeneous catalyst for glycerol esterification, Catal. Commun. 100 (2017) 10–14.

[152] H. G. Karge, Concepts and analysis of acidity and basicity, in: Handbook of heterogeneous catalysis, G. Ertl, H. Knözinger, F. Schüth, J. Weitkamp (Eds.), Wiley-VCH, 8, 2008, 1096–1122.

[153] L. Damjanovic, A. Auroux, Determination of acid/base properties by temperature programmed desorption (TPD) and adsorption calorimetry, in: Zeolite characterization and catalysis, A. W. Chester, E.G. Derouane (Eds.), Springer, 3, 2009, 107–167.

[154] E. Brunner, H. Pfeifer, NMR spectroscopic techniques for determining acidity and basicity. Mol. Sieves, H. G. Karge, J. Weitkamp (Eds), Springer, 6, 2008, 1–43.

[155] M. Guisnet, Model reactions for characterizing the acidity of solid catalysts, Acc. Chem. Res. 23 (1990) 392–398.

[156] M. Guisnet, P. Magnoux, Deactivation by coking of zeolite catalysts. Prevention of deactivation. Optimal conditions for regeneration, Catal. Today 36 (1997) 477–483.

[157] J. M. Smith, Chemical engineering kinetics, McGraw-Hill Book Company 1970, 362.

[158] P. B. Weisz, Diffusivity of porous particles, Z. Phys. Chem. 11 (1957) 1–15.

[159] M. T. Tran, N. S. Gnep, G. Szabo, M. Guisnet, Isomerization of *n*-butane over H-mordenites under nitrogen and hydrogen: Influence of the acid site density, J. Catal. 174 (1998) 185–190.

[160] N. Lohitharn, J. G. Goodwin Jr, *n*-Butane isomerization on sulfated zirconia: How olefins affect surface intermediate concentration, J. Catal. 245 (2007) 198–204.

[161] H. Knözinger, Dehydration of alcohols on aluminum oxide, Angew. Chem., Intern. Edt. 7 (1968) 791–805.

[162] M. Guisnet, L. Pinard, Characterization of acid-base catalysts through model reactions, Catal. Rev. 60 (2018) 337–436.

[163] M. Guisnet, Modes of coke formation and deactivation, in: Deactivation and Regeneration of zeolite catalysts. Catalytic Science series. M. Guisnet, F. R. Ribeiro (Eds), Imperial College Press. Chapter 7, 9, 2011, 115−137.

[164] W. W. Kaeding, C. Chu, L. B. Young, S. A. Butter, Shape-selective reactions with zeolite catalysts. II. Selective disproportionation of toluene to produce benzene and *p*-xylene, J. Catal. 69 (1981) 392–398.

[165] J. Das, T. S. Bhat, A. B. Halgeri, Selective disproportionation over pore-size controlled MFI zeolite, Ind. Eng. Chem. Res. 33 (1994) 246–250.

[166] G. Schulz-Ekloff, N. I. Jaeger, C. Vladov, L. Petrov, Effects of carrier gases in the toluene disproportionation on HZSM-5 zeolite, Appl. Catal. 33 (1987) 73–81.

[167] N. S. Gnep, M. Guisnet, Toluene disproportionation over mordenites, II Kinetic study, Appl. Catal. 1 (1981) 329–342.

[168] N. P. Rhodes, R. Rudham, Catalytic studies with dealuminated Y zeolite. Part 2. Disproportionation of toluene, J. Chem. Soc. Faraday Trans. 90 (1994) 809–814.

[169] N. S. Gnep, M. L. Martin de Armando, C. Marcilly, B. H. Ha, M. Guisnet, Toluene disproportionation and coke formation on mordenites: Effect of catalyst modifications and of operating conditions, Stud. Surf. Sci. Catal. 6 (1980) 79–89.

[170] T. -C. Tsai, Reactivation of acidic sites in mordenite used in toluene disproportionation, Appl. Catal., A 301 (2006) 292–298.

[171] N. S. Gnep, J. Tejada, M. Guisnet, Mise au point d'une réaction simple de caractérisation du réseau poreux des zéolithes de taille de pore intermédiaire, Bull. Soc. Chim. Fr. 1 (1982) 5–11.

[172] V. R. Choudhary, Titration of active sites on zeolites by selective poisoning of stronger acid sites, Zeolites 7 (1987) 272–276.

[173] B. C. Gates, J. R. Katzer, G. C. A. Schuit, in: Chemistry of catalytic processes, McGraw Hill Book Co. 1979, 29.

[174] H. Pines, The chemistry of catalytic hydrocarbon conversions, Academic Press, N.Y. 1981.

[175] W. O. Haag, R. M. Lago, P. B. Weisz, The active site of acidic aluminosilicate catalysts, Nature 309 (1984) 589–591.

[176] W. O. Haag, R. M. Dessau, Duality of mechanism for acid-catalyzed paraffin cracking, in: Proceedings of the 8th international congress on catalysis, Verlag Chemie-Dechema, Heidelberg, Berlin, 2, 1984, 305–316.

[177] G. Bourdillon, M. Guisnet, C. Gueguen, Catalytic characterization of H-offretite, Zeolites. 6 (1986) 221–224.

[178] W. F. Pansing, The catalytic cracking of hexadecane; effects of impurities, olefins, and steam, J. Phys. Chem. 69 (1965) 392–399.

[179] D. M. Anufriev, P. N. Kuznetsov, K. G. Ione, Transformation of hydrocarbons on zeolites of type Y: I. Promoting effect of olefins on the rate of catalytic cracking of paraffins, J. Catal. 65 (1980) 221–226.

[180] P. B. Weisz, Some classical problems of catalytic science: resolution and implications, Microporous Mesoporous Mater. 35–36 (2000) 1–9.

[181] J. Abbot, Cracking reactions of C_6 paraffins on HZSM-5, Appl. Catal. 57 (1990) 105–125.

[182] V. L. Zholobenko, L. M. Kustov, V. B. Kazansky, E. Loeffer, U. Lohse, G. Oehlmann, On the nature of the sites responsible for the enhancement of the cracking activity of HZSM-5 zeolites dealuminated under mild steaming conditions: Part 2, Zeolites 11 (1991) 132–134.

[183] W. O. Haag, R. M. Dessau, R. M. Lago, Kinetics and mechanisms of paraffin cracking with zeolite catalysts, Stud. Surf. Sci. Catal. 60 (1991) 255–265.

[184] A. F. H. Wielers, M. Vaarkamp, M. F. M. Post, Relation between properties and performance of zeolites in paraffin cracking, J. Catal.127 (1991) 51–66.

[185] P. B. Weisz, J. N. Miale, Superactive crystalline aluminosilicate hydrocarbon catalysts, J. Catal. 4 (1965) 527–529.

[186] V. J. Frillette, W. O. Haag, R. M. Lago, Catalysis by crystalline aluminosilicates: Characterization of intermediate pore-size zeolites by "Constraint Index", J. Catal. 67 (1981) 218−222.

[187] W. O. Haag, R. M. Lago, P. B. Weisz, Transport and reactivity of hydrocarbon molecules in a shape-selective zeolite, Faraday Discuss. Chem. Soc. 72 (1981) 317−330.

[188] O. P. Fritz, J. H. Lunsford, The effect of sodium poisoning on dealuminated Y-Type zeolites, J. Catal. 118 (1989) 85–98.

[189] F. Lonyi, J. H. Lunsford, The development of strong acidity in hexafluorosilicate-modified Y-type zeolites, J. Catal. 136 (1992) 566–577.

[190] Q. L. Wang, G. Giannetto, M. Guisnet, Dealumination of zeolites III. Effect of extra-framework aluminum species on the activity, selectivity and stability of Y zeolites in *n*-heptane cracking, J. Catal. 130 (1991) 471–482.

[191] R. Carvajal, P. -J. Chu, J. H. Lunsford, The role of polyvalent cations in developing strong acidity: A study of lanthanum-exchanged zeolites. J. Catal. 125 (1990) 123−131.

[192] R. Beaumont, D. X. Barthomeuf, Aluminum-deficient and ultrastable faujasite-type zeolites. I Acidic and structural properties, J. Catal. 26 (1972) 218–225.

[193] S. J. Decanio, J. R. Sohn, P. O. Fritz, J. H. Lunsford, Acid catalysis by dealuminated zeolite-Y: I. Methanol dehydration and cumene dealkylation, J. Catal. 101 (1986) 132–141.

[194] J. H. Lunsford, Surface interactions of NaY and decationated Y zeolites with nitric oxide as determined by electron paramagnetic resonance spectroscopy, J. Phys. Chem. 72 (1968) 4163–4168.

[195] C. Mirodatos, D. Barthomeuf, Superacid sites in zeolites, J. Chem. Soc. Chem. Commun. 0 (1981) 39–40.

[196] Y. Hong, V. Gruver, J. J. Fripiat, Role of Lewis acidity in the isomerization of *n*-pentane and *o*-xylene on dealuminated H-mordenites, J. Catal. 150 (1994) 421–429.

[197] J. P. Marques, I. Gener, J. M. Lopes, F. R. Ribeiro, M. Guisnet, *n*-Heptane cracking on dealuminated HBEA zeolites, Catal. Today 107–108 (2005) 726–733.

[198] R. W. Lago, W. O. Haag, R. J. Mikovsky, D. H. Olson, S. D. Hellring, K. D. Schmitt, G. T. Kerr, The nature of the catalytic sites in HZSM-5-Activity enhancement, Stud. Surf. Sci. Catal. 28 (1986) 677–684.

[199] S. Schallmoser, T. Ikuno, M. F. Wagenhofer, R. Kolvenbach, G. L. Haller, M. Sanchez-Sanchez, J. A. Lercher, Impact of the local environment of Brønsted acid sites in ZSM-5 on the catalytic activity in *n*-pentane cracking, J. Catal. 316 (2014) 93–102.

[200] T. Masuda, Y. Fujikata, S. R. Mukai, K. Hashimoto, Changes in catalytic activity of MFI-type zeolites caused by dealumination in a steam atmosphere, Appl. Catal., A 172 (1998) 73–83.

[201] V. L. Zholobenko, L. M. Kustov, V. B. Kazansky, E. Loeffler, U. Losher, Ch. Peuker, G. Oehlmann, On the possible nature of sites responsible for the enhancement of cracking activity of HZSM-5 zeolites dealuminated under mild steaming conditions, Zeolites 10 (1990) 304–306.

[202] G. Bourdillon, C. Gueguen, M. Guisnet, Characterization of acid catalysts by means of model reactions. Acid strength necessary for the catalysis of various hydrocarbon reactions, Appl. Catal. 61 (1990) 123–139.

[203] H. H. Kung, B. A. Williams, S. M. Babitz, J. T. Miller, W. O. Haag, R. Q. Snurr, Enhanced hydrocarbon cracking activity of Y zeolites, Top. Catal. 10 (2000) 59–64.

[204] Q. Tang, H. Xu, Y. Zheng, J. Wang, H. Li, J. Zhang, Catalytic dehydration of methanol to dimethyl ether over micro-mesoporous ZSM-5/MCM-41 composite molecular sieves, Appl. Catal., A 413–414 (2012) 36–42.

[205] F. Schmidt, C. Hoffmann, F. Giordanino, S. Bordiga, P. Simon, W. Carrillo-Cabrera, S. Kaskel, Coke location in microporous and hierarchical ZSM-5 and the impact on the MTH reaction, J. Catal. 307 (2013) 238–245.

[206] S. Inagaki, M. Ogura, T. Inami, Y. Sasaki, E. Kikuchi, M. Matsukata, Synthesis of MCM-41-type mesoporous materials using filtrate of alkaline dissolution of ZSM-5 zeolite, Microporous Mesoporous Mater. 74 (2004) 163–170.

[207] P. Campo, P. Beato, F. Rey, M. T. Navarro, U. Olsbye, K. P. Lillerud, S. Svelle, Influenece of post-synthetic modifications on the composition, acidity and textural properties of ZSM-22 zeolite, Catal. Today 299 (2018) 120–134.

[208] T. Biemelt, C. Selzer, F. Schmidt, G. Mondin, A. seifert, K. Pinkert, S. Spange, T. Gemming, S. Kaskel, Hierarchical porous zeolite ZSM-58 derived by desilication and desilication re-assembly, Microporous Mesoporous Mater. 187 (2014) 114–124.

[209] N. Gao, S. Xie, S. Liu, J. An, X. Zhu, L. Hu, H. Wei, X. Li, L. Xu, Catalytic degradation of LDPE and PP over MCM-49 based micro-mesoporous composite, Catal. Lett. 114 (2014) 1296–1304.

[210] I. I. Ivanova, A. S. Kuznetsov, V. V. Yuschenko, E. E. Knyazeva, Design of composite micro/mesoporous molecular sieve catalysts, Pure Appl. Chem. 76 (2004) 1647–1658.

[211] I. I. Ivanova, A. S. Kuznetsov, E. E. Knyazeva, F. Fajula, F. T. -Starzyk, C. Fernandez, J. -P. Gilson, Design of hierarchical structured catalysts by mordenites recrystallization: Application in naphthalene alkylation, Catal. Today 168 (2011) 133–139.

[212] M. Maniko, R. Chal, P. Trens, D. Minoux, C. Geradrin, W. Makowski, Porosity of micro-mesoporous zeolites prepared via pseudomorphic transformation of zeolite Y crystals: A combined isothermal sorption and thermodesorption investigation, Microporous Mesoporous Mater. 170 (2013) 243–250.

[213] W. Q. Jiao, W. H. Fu, X. M. Liang, Y. M. Wang, M. -Y. He, Preparation of hierarchically structured Y zeolite with low Si/Al ratio and its applications in acetalization reactions, RSC Adv. 4 (2014) 58596–58607.

[214] U. J. Etim, B. Xu, Z. Zhang, Z. Zhong, P. Bai, K. Qiao, Z. Yan, Improved catalytic cracking performance of USY in the presence of metal contaminants by post-synthesis modification, Fuel 178 (2016) 243–252.

[215] Y. P. Khitev, Y. G. Kolyagin, I. I. Ivanova, O. A. Ponomareva, F. T.-Starzyk, J. -P. Gilson, C. Fernandez, F. Fajula, Synthesis and catalytic properties of hierarchical micro/mesoporous materials based on FER zeolite, Microporous Mesoporous Mater. 146 (2011) 201–207.

[216] X. Cheng, T. Cacciaguerra, D. Minoux, J. -P. Dath, F. Fajula, C. Gerardin, Generation of parallelpiped-shaped mesopores and structure transformation in highly stable ferrierite zeolite crystals by framework desilication in NaOH solution, Microporous Mesoporous Mater. 260 (2018) 132–145.

[217] L. Brabec, M. Kocirik, Silicalite-1 polycrystalline layers and crystal twins: Morphology and grain boundaries, Mater. Chem. Phys. 102 (2007) 67–74.

[218] K. A. Becker, S. Kowalak, Zeolite catalysts modified with fluorine, Stud. Surf. Sci. Catal. 52(1989)123–132.

[219] R. B. Borade, A. Clearfield, Effect of fluoride ions on the acidic and catalytic properties of beta zeolite, J. Chem. Faraday Trans. 91 (1995) 539–547.

Chapter II: Description of characterization techniques and catalytic tests

1. Techniques used for the physico-chemical characterization of materials

1.1 X-ray diffraction (XRD)

1.1.1 Principle

The X-ray powder diffraction patterns were obtained to identify characteristic peaks of parent and modified mordenite zeolites. XRD peaks were integrated to estimate the percentage of crystallinity of modified mordenites. The Debye-Scherrer method through using the full width at half maximum (FWHM) allows to calculate the modification of the crystals size during the modification. In addition to that, the associated XRD software (HighScore Plus) was used to determine the Miller indices of samples.

Crystalline bodies can be considered as assemblies of atomic planes, called reticular planes, separated by a characteristic distance, the inter-reticular distance (d_{hkl}). When an X-ray beam irradiates a crystalline sample, it is reflected by a family of planes with a Miller's index (h k l) encountered at a certain angle, called the Bragg angle (θ). The X-rays diffracted during the angular scanning of the surface of the sample are collected by an X'Celerator detector. Therefore, each diffracted peak corresponds to an angle θ which can be connected to the inter-reticular distance according to the Bragg's law:

$$2d_{hkl} \times sin\theta = n \times \lambda \qquad \text{Equation II.1}$$

Where,

d is the distance between two Miller index planes;

λ is the X-ray wavelength;

n is the diffraction order;

and θ is the incident angle of the X-ray beam (Bragg's angle).

1.1.2 Experimental procedure

All the XRD patterns were collected on a D5005 BRUKER AXS diffractometer by using a CuK_α radiation (λ=1.5406 Å) as an incident beam, obtained by summiting a copper anode to a tension of 40 kV and an intensity of 30 mA. A graphite monochromator was used to eliminate the CuK_β radiation and the eventual fluorescence.

The acquisition method ranged from 5 to 60 ° 2θ on all the samples including the parent and the modified materials.

1.1.3 Debye-Scherrer method and Williamson-Hall analysis

As mentioned before, the Debye-Scherrer method was used to estimate the crystalline coherent size (CCS). The corresponding Debye-Scherrer equation (Equation II.2) was applied to the six most intense peaks in case of the mordenite zeolite these were centered at 6.51, 9.77, 13.45, 22.20, 25.63, and 27.67 ° 2θ (corresponding to Miller index 1 1 0, 2 0 0, 1 1 1, 1 5 0, 2 0 2, and 5 1 1, respectively).

$$D = \frac{K\lambda}{FWHM.\cos\theta} \qquad \text{Equation II.2}$$

Where,

D (Å) is the CCS;

K is the shape factor (typically 0.9);

λ (Å) is the incident x-ray radiation wavelength;

FWHM (rad) is the full width at half maximum of the peak;

and θ (rad) is the incidence angle or Bragg's angle.[1]

Beside the CCS, the second main property extracted from peak width analysis is lattice strain. It is a measurement of the distribution of lattice constants resulting from crystal imperfections, such as lattice dislocation, stacking faults, coherency stresses, etc.[2] By applying the below Williamson-Hall equation (Equation II.3), a plot is drawn with 4sinθ along the *x*-axis and FWHMcosθ along the *y*-axis. The CCS was determined from the *y*-intercept and the strain (ε) from the slope of the linear fit of the data.[2]

$$FWHM \cos\theta = \frac{K\lambda}{D} + 4\varepsilon sin\theta \qquad \text{Equation II.3}$$

1.2 Induced Coupled Plasma - Atomic Emission Spectroscopy (ICP-AES)

The compositional weight of Si, Al, and Na, allowed for the determination of the global Si/Al (Si/Al_{global}) ratio of the mordenite samples before and after modification. The elemental analysis was achieved by atomic emission spectrometry (ICP-AES).

1.2.1 Principle

Inductive plasma emission spectrometry (ICP-AES) is based on the formation of plasma in a rare gas stream. The liquid sample is nebulized then transferred to the plasma (argon). It undergoes various stages of decomposition, atomization, and ionization, leading to the excitation of atoms and ions. After excitation, the light is emitted with a characteristic wavelength by the atoms contained in the sample. This light is then transmitted through the optical system to a detector which allows dosing. A prior calibration of the element makes it possible to quantify it.

1.2.2 Experimental procedure

The analysis was carried out in argon plasma using a Perkin-Elmer OPTIMA 2000DV spectrometer. The sample was diluted in aqueous solution and then vaporized using plasma to measure the emission intensity of a radiation characteristic of the element to be tested.

1.3 Nitrogen physisorption

The textural properties were characterized by nitrogen physisorption, which allowed to obtain the BET surface area, external surface area, micro- and meso-pore volume and pore size distribution.

1.3.1 Experimental procedure

The experimental data on the nitrogen adsorption-desorption isotherms were obtained by using a Micromeritics 3 Flex surface characterization apparatus. The samples were first outgased for 1 h at 90 °C then at 350 °C overnight. Nitrogen isotherms were recorded at -196 °C.

1.3.2 Isotherm classification

In the 2005, physisorption isotherms were grouped into 8 types by the International Union of Pure and Applied Chemistry (IUPAC).[3] IUPAC further classified the shape of hysteresis loops. As such, 6 hysteresis types have been defined. The proposed updated classification of physisorption isotherms is shown in Figure II.1 and hysteresis loops classification in Figure II.2.

The adsorption isotherms classified into:

Reversible Type I isotherms are given by microporous solids having relatively small external surfaces (e.g., some activated carbons, molecular sieve zeolites and certain porous oxides). A Type I isotherm is concave to the p/p_0 axis and the adsorbed amount approaches a limiting value. This limiting uptake is governed by the accessible micropore volume rather than by the internal surface area. At very low p/p_0, a steep uptake is due to enhanced adsorbent-adsorptive interactions in narrow micropores (micropores of molecular dimensions), resulting in micropore filling at very low p/p_0. For nitrogen and argon adsorption at 77 K and 87 K, **Type I (a) isotherms** are given by microporous materials having mainly narrow micropores smaller than 1 nm, while **Type I (b) isotherms** are found with materials having pore size distributions over a broader range including wider micropores and possibly narrow mesopores that can reach 2.5 nm (e.g. activated carbons). Mesoporous materials with pore sizes between 2 and 2.5 nm are thus included in the Type I (b) isotherms.

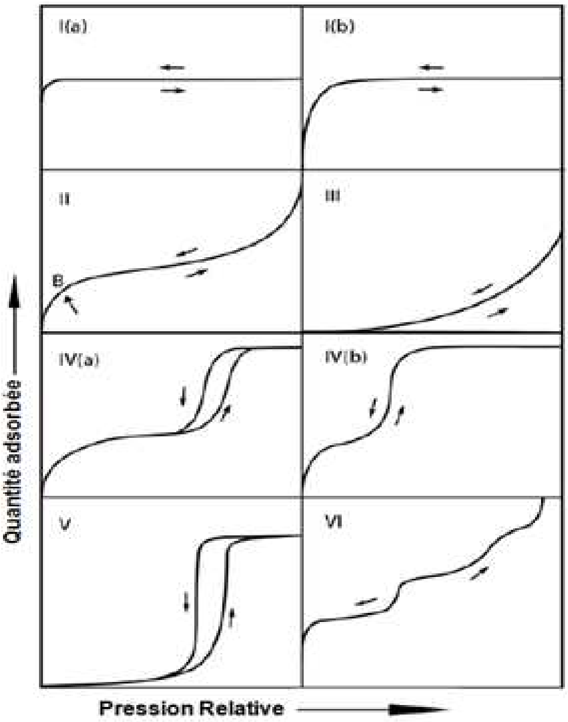

Figure II.1. Classification of physisorption isotherms by IUPAC.[3]

Reversible Type II isotherms are given by the physisorption of most gases on nonporous or macroporous adsorbents. The shape is the result of unrestricted monolayer-multilayer adsorption up to high p/p_0. If the knee is sharp, the Point B (beginning of the middle almost linear section) usually corresponds to the completion of the monolayer coverage. A more gradual curvature (*i.e.* a less distinctive Point B) is an indication of a significant amount of overlap of monolayer coverage and the onset of multilayer adsorption. The thickness of the adsorbed multilayer generally appears to increase without limit when $p/p_0 = 1$.

Type III has no Point B and therefore no identifiable monolayer formation; the adsorbent-adsorbate interactions are now relatively weak, and the adsorbed molecules are clustered around the most favorable sites on the surface of a nonporous or macroporous solid. In contrast to a Type II isotherm, the amount adsorbed remains finite at the saturation pressure (*i.e.* at $p/p_0 = 1$).

Type IV isotherms are given by mesoporous adsorbents. The adsorption behavior in mesopores is determined by the adsorbent adsorptive interactions and also that between the molecules in the condensed state. In this case, the initial monolayer-multilayer adsorption on the mesopore walls, as Type II isotherm, is followed by pore condensation. A typical feature of Type IV isotherms is a final saturation plateau, of variable length.

In the case of a **Type IV (a) isotherm**, capillary condensation is accompanied by hysteresis. This occurs when the pore width exceeds a certain critical width, which is dependent on the adsorption system and temperature (e.g. for nitrogen and argon adsorption in cylindrical pores at 77 K and 87 K, respectively, hysteresis starts to occur for pores wider than ~ 4 nm).[4-6] With adsorbents having mesopores of smaller width, completely reversible Type IV (b) isotherms are observed. In principle, **Type IV (b) isotherms** are also given by conical and cylindrical mesopores that are closed at the tapered end.

Type V has very similar shape to that of Type III at low p/p_0, which can be attributed to relatively weak adsorbent-adsorbate interactions. At higher p/p_0, molecular clustering is followed by pore filling. For instance, Type V isotherms are observed for water adsorption on hydrophobic microporous and mesoporous adsorbents.

Type VI is a reversible stepwise isotherm which is representative of layer-by-layer adsorption on a highly uniform nonporous surface. The step-height now represents the capacity for each adsorbed layer, while the sharpness of the step is dependent on the system and the temperature. Amongst the best examples of Type VI isotherms are those obtained with argon or krypton at low temperature on graphitised carbon blacks.

1.3.3 Types of hysteresis

Reproducible, permanent hysteresis loops, which are located in the multilayer range of physisorption isotherms, are generally associated with capillary condensation. This form of hysteresis can be attributed to adsorption metastability and/or network effects. Many different shapes of hysteresis loops have been reported, but the main types are shown in Figure II.2. Types H1, H2 (a), H3, and H4 were identified in the original IUPAC classification of 1985, which is now extended in the light of more recent findings. Each of these six characteristic types is fairly closely related to particular features of the pore structure and underlying adsorption mechanism.

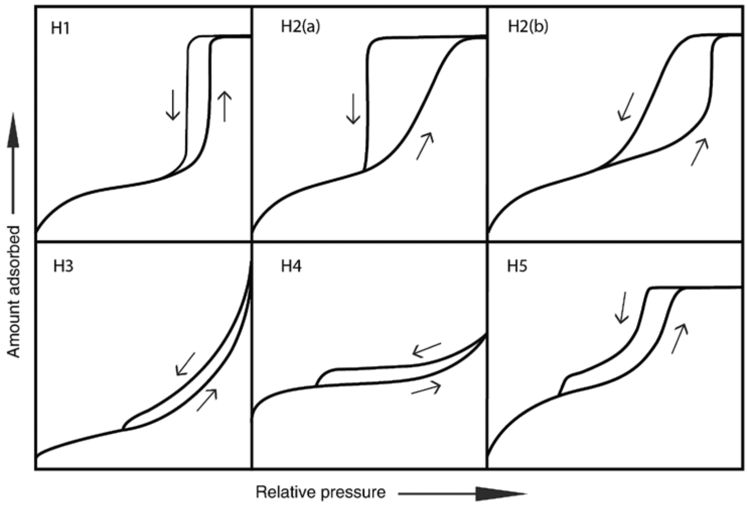

Figure II.2. Classification of hysteresis loops by IUPAC.[3]

The **Type H1** loop is found in materials which exhibit a narrow range of uniform mesopores, as for instance in templated silicas (e.g. MCM-41, MCM-48, SBA-15), some controlled pore glasses, and ordered mesoporous carbons. Usually, network effects are minimal and the steep, narrow loop is a clear sign of delayed condensation on the adsorption branch. However, Type H1 hysteresis has also been found in networks of ink-bottle pores where the width of the neck size distribution is similar to the width of the pore/cavity size distribution (e.g. 3DOm carbons [5]).

Hysteresis loops of **Type H2** are given by more complex pore structures in which network effects are important. The very steep desorption branch, which is a characteristic feature of H2(a) loops, can be attributed either to pore-blocking/percolation in a narrow range of pore necks or to cavitation-induced evaporation. H2(a) loops are for instance given by many silica gels, some porous glasses (e.g. vycor) as well as some ordered mesoporous materials (e.g. SBA-16 and KIT-5 silicas). The Type H2(b) loop is also associated with pore blocking, but the size distribution of neck widths is now much larger. Examples of this type of hysteresis loops have been observed with mesocellular silica foams and certain mesoporous ordered silicas after hydrothermal treatment.

Type H3 loops have two distinctive features: (i) the adsorption branch resembles a Type II isotherm (ii) the lower limit of the desorption branch is normally located at the cavitation-induced p/p_0. Loops of this type are given by non-rigid aggregates of plate-like particles (e.g., certain clays) but also if the pore network consists of macropores which are not completely filled with pore condensate.

The **H4 Type** loop is somewhat similar, but the adsorption branch is now a composite of Types I and II, the more pronounced uptake at low *p/p0* being associated with the filling of micropores. H4 loops are often found with aggregated crystals of zeolites, some mesoporous zeolites, and micro-mesoporous carbons.

Although the **Type H5** loop is unusual, it has a distinctive form associated with certain pore structures containing both open and partially blocked mesopores (e.g. plugged hexagonal templated silicas).

1.3.4 Specific surface area – BET surface area

The Brunauer, Emmett, and Teller equation (BET),[7] which is an extension of the Langmuir equation,[8] was used to evaluate the specific surface area of the zeolitic materials. Subsequently, the values obtained for the "specific surface" via the BET equation are designated by BET surface (S_{BET}).

In order to otain the value of the BET surface firstly the amount of gas needed to form the monolayer volume (v_m) was calculated. Equation II.4 was used to calculate the monolayer volume (v_m):

$$\frac{\frac{P}{P_0}}{v\left(1-\frac{P}{P_0}\right)} = \frac{C-1}{v_m.C} \cdot \frac{P}{P_0} + \frac{1}{v_m.C} \qquad \text{Equation II.4}$$

Where,

P = pressure at equilibrium (mmHg), on zeolites: $P/P_0 < 0.1$;

P_0 = saturation pressure (mmHg);

v = volume of adsorbed gas (mL g^{-1});

v_m = quantity of monolayer gas (mL g^{-1});

and C = BET constant.

As indicated by several authors[9] the BET equation is not suited for samples containing micropores. Hence the external surface was calculated through the t-plot method as specified below.

The BET constant (C) relies on the molar heat of adsorption of the first layer on the surface of the material (E_l) and the molar heat of liquefaction of the adsorbate (E_L). Strong adsorbent-adsorbate interactions are characterized by a high value of the C constant. The exponential equation of this constant is given by equation below:

$$C = exp\left(\frac{E_l - E_L}{RT}\right) \quad \text{Equation II.5}$$

Once v_m was calculated, the BET surface was obtained by using the following equation:

$$S_{BET} = v_m . \sigma(N_2). N_A \quad \text{Equation II.6}$$

Where,

S_{BET} = BET surface (m^2 g^{-1});

v_m = volume of monolayer gas (mL g^{-1});

σ (N_2) = Nitrogen surface area (16.2 x 10^{-20} m^2);

and N_A = Avogadro's number (6.022 x 10^{23} mol^{-1}).

1.3.5 Description of pores

The samples pore size distribution volume is classified according to IUPAC into three different categories:[10]

i. Macropores: greater than 50 nm (not detected with nitrogen physisorption);
ii. Mesopores: between 2 and 50 nm;
iii. Micropores: less than 2 nm;

In addition, micropores can be divided into ultra-micropores (less than 0.8 nm) and super-micropores (between 0.8 and 2 nm).

1.3.5.1 Total pore volume

The total pore volume is determined through the nitrogen volume achieved at a relative pressure (*p/p₀*) of 0.97. It is calculated with equation II.7:

$$V_{Total} = \frac{M.V_{ads}}{V_M.\rho_{liq}} \quad \text{Equation II.7}$$

Where,

V_{total} = total pore volume (cm^3 g^{-1});

M = molar weight of nitrogen gas (28 g mol^{-1});

V_M = molar volume (22414 cm^3 mol^{-1});

and ρ_{liq} = density of liquid nitrogen (0.808 cm^3 g^{-1}).

1.3.5.2 t-plot

The t-plot method was used to calculate the micropore volume. Figure II.3 shows different types of t-plots, which represents graphically the adsorbed volume (V_{ads}) against the statistical thickness of the adsorbed layer (*t*). For nonporous materials (a), a straight line passes through or very close to the origin. In mesoporous materials (b), the plot shows a deviation from the straight line at high nitrogen relative pressures, whereas for materials possessing micropores (c), the deviation takes place at low nitrogen relative pressures.[11-13] For hierarchical zeolites that possess both micro- and mesopores, their t-plot is a combination of the one for purely microporous (d).

Different mathematical models (such as Halsey, Harkins-Jura, Broekhoff-de Boer) were developed to calculate the statistical thickness of the adsorbed layer (*t*), depending on the studied solids.[11-13] In our case, the Harkins-Jura isotherm was used (equation II.8).[14]

$$t = \sqrt{\frac{13.99}{0.034 - log\left(\frac{P}{P_0}\right)}} \qquad \text{Equation II.8}$$

Where,

t = thickness of the adsorbed layer (Å);

P = pressure at equilibrium (mmHg);

and P_0 = saturation pressure (mmHg).

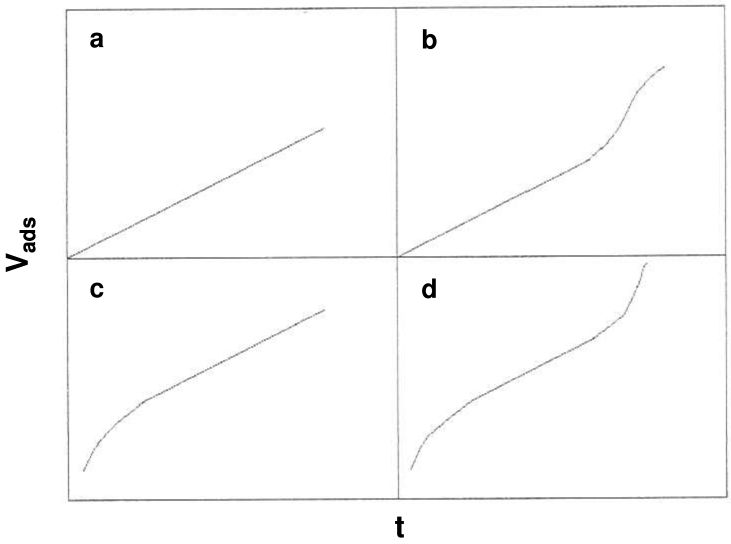

Figure II.3. Different types of *t*-plots: (a) nonporous solid; (b) mesoporous solid; (c) microporous solid, and (d) micro- and mesoporous solid.

In microporous solids (c, d), at low relative pressures (low *t* values) and after the complete filling of the micropores volume that occurs, a linear region appears in the plot. It is possible then to determine the micropore volume (V_{micro}) from the intercept with the y-axis and the external surface (S_{ext}) from the slope of the straight line, as shown in Figure II.5. As said before, it should be taken into consideration that the value of external surface includes both the external surface of crystallites and the mesopore area.

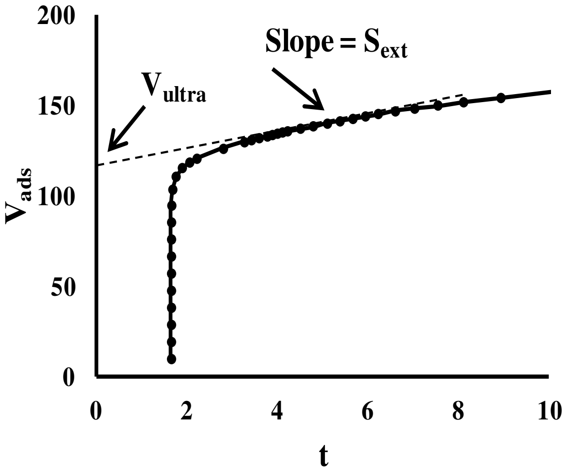

Figure II.4. *t*-plot example for mordenite zeolite (Si/Al = 20).

1.3.5.3 Mesopore volume (2 < Ø < 50 nm)

The mesopores volume was obtained as the difference between the total pore volume (V_{total}) and the micropore volume (V_{micro}).

1.3.6 Mesopore size distribution

The BJH method (Barret, Joyner, and Halenda)[15] was used to obtain the pore size distribution. This method characterizes the adsorption-capillary condensation process that occurs inside the mesopores.[9] The increase in pressure, in the capillary condensation region (p/p_0 > 0.4), causes the thickening of the layer adsorbed on pore walls, as well as capillary condensation in pores having a core (empty pore space) size r_c defined by the Kelvin equation (equation II.9).

$$ln\left(\frac{P}{P_0}\right) = -\frac{2\gamma V_M \cos\theta}{RTr_c} \qquad \text{Equation II.9}$$

Where,

P = pressure at equilibrium (mmHg);

P_0 = saturation pressure (mmHg);

γ = surface tension (N_2: 8.85 m.Nm^{-1});

V_M= molar volume (N_2: 22414 cm^3.mol^{-1});

θ = contact angle;

R = gas constant;

T = temperature (K);

and r_c = radius for cylindrical pores.

It is possible to calculate the contribution of a thickness of the adsorbed film to the total adsorption and the core volume, by assuming the pore geometry. Therefore, from these results and from the assumed pore geometry it is rational to transform the core volume and core size into pore volume and pore size respectively. Finally, the mesopore size distribution can be determined by following the isotherm step by step in the range $0.4 < p/p_0 < 0.97$.

1.4 Mercury porosimetry

Since mercury does not wet most substances and will not spontaneously penetrate pores by capillary action, it must be forced into the pores by the application of external pressure. The required equilibrated pressure is inversely proportional to the size of the pores, only slight pressure being required to intrude mercury into large macropores, whereas much greater pressures are required to force mercury into small pores. Mercury porosimetry analysis is the progressive intrusion of mercury into a porous structure under stringently controlled pressures. From the pressure versus intrusion data, the instrument generates volume and size distributions using the Washburn equation. Clearly, the more accurate the pressure measurements, the more accurate the resulting pore size data.[16]

1.4.1 Principle

It is the non-wetting property of Hg combined with its high surface tension that almost uniquely qualifies it for use in probing pore space. There is tension that acts tangentially to the interface, at each surface interface with a liquid. This is termed ‘surface tension’ and acts like an elastic membrane contacting the surface until the surface forces are in equilibrium with the forces leading to increase the surface area of the interface. Surface tension, then, can be defined as the force per unit length acting along the surface of a liquid at right angles to a line that separates the two phases. If mercury is placed in contact with a pore opening, the surface tension of the mercury acts along the line of contact with the opening equal in length to the perimeter of the opening and creating a force-resisting entry.[16]

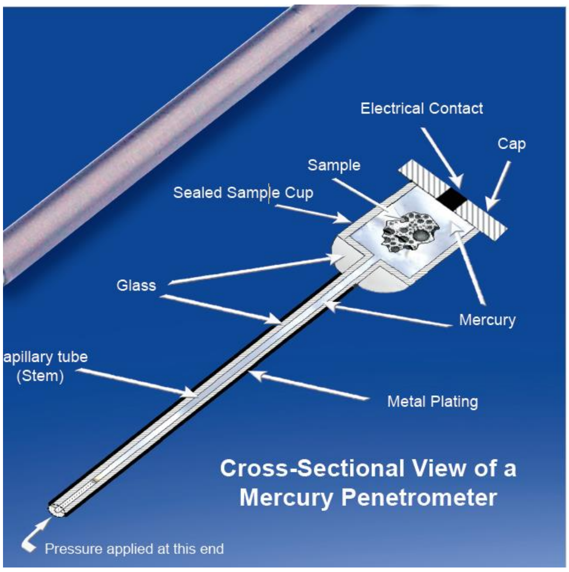

Figure II.5. Cross-sectional view of a mercury penetrmeter.[16]

The magnitude of resisting force is proportional to the length of the line of contact, the surface tension of mercury, and the cosine of the contact angle. For a pore with a circular opening at the surface, the resisting force is expressed as:

$$f_R = \pi D\gamma\cos\theta \qquad \text{Equation II.10}$$

Where,

f_R = resisting force;

D = length of the line of contact;

γ = surface tension of mercury;

and θ = contact angle.

An externally applied pressure tending to force mercury into the opening acts over the surface of the interface bridging the opening. The externally applied force, therefore, is the product of the pressure and area over which the pressure is applied. For a pore of circular cross-section:

$$f_{EXT} = PA = P\gamma D^2/4 \qquad \text{Equation II.11}$$

Where,

f_{EXT} = external applied pressure;

P = pressure;

and A = area.

At equilibrium, just before the resistive force is overcome, the equation is:

$$-\pi D\gamma cos\theta = \pi D^2 P/4 \qquad \text{Equation II.12}$$

Therefore, at any pressure, the pores into which mercury has intruded have diameters greater than:

$$D = -4\gamma cos\theta/P \qquad \text{Equation II.13}$$

By measuring the volume of mercury that intrudes into the sample material with each pressure change, the volume of pores in the corresponding size class is known. The volume of mercury that enters pores is measured by a mercury penetrometer (an electrical capacitance dilatometer). These devices are very sensitive and can detect a change in mercury volume of under 0.1 μL. The penetrometer is constructed of glass (an insulator) and filled with mercury (a conductor). The stem of the penetrometer is a capillary that acts as a reservoir for the analytical volume of mercury. The stem is plated with metal (a conductor). The two conductors, mercury, and the metal plating are separated by glass, thus forming a coaxial capacitor. As pressure forces mercury out of the capillary and into the sample, the mercury inside the capillary decreases and so is the capacitance. The decrease in capacitance, therefore, is proportional to the volume of mercury leaving the capillary with each change in pressure.[16]

1.5 Transmission Electron Microscopy (TEM)

The TEM technique was also used to observe the morphology of the crystals of the parent and modified mordenite zeolites.

1.5.1 Experimental procedure

The morphology of the samples was determined by TEM using a Philips CM 120 microscope equipped with a LaB_6 filament. To prepare the sample, a small drop of a suspension in ethanol was put on a gold grid (Au) and after that the solvent was evaporated.

1.6 Infrared spectroscopy

The infrared spectroscopy experiments were done using a Fourrier Transform Infrared spectroscopy (FT-IR) apparatus. In the work reported, this technique was used for the following intents:

- To study the hydroxyl (OH) stretching vibrations bands in the range of 3500 to 3800 cm^{-1} IR region.
- To use the probe molecule pyridine, for the quantification of the samples acid site density.

1.6.1 Stretching vibration bands of hydroxyl groups (OH)

In general, the hydroxyl groups of zeolites and acid catalysts are related to the Brønsted acidity. Their vibrations generate IR adsorption bands in the regime of 3500 and 3800 cm^{-1}. The quantification of the density of the hydroxyl group acidity is not possible, because when the density of Brønsted acid sites increases, the O-H bond weakens thus decreasing the OH frequency.[17] Furthermore, the O-H bond also depends on the location of the hydroxide group, which is affected by the pore structure and the presence of an extra-framework phase. Therefore, the comparison of these groups between zeolites is not possible, as well as between OH groups in case located on different environments inside the same sample.[17]

1.6.1.1 Experimental procedure

All the experiments were done in a quartz IR cell equipped with CaF_2 windows, connected to vacuum as well as precised atmospheric systems, in addition to a temperature controlled oven. Prior to any analysis, the catalyst was pressed into a self-supported 2 cm^2 wafer (0.5 ton) that weighted between 10 and 30 mg. After that, the sample was placed in the IR cell and exposed to calcination overnight at 450 °C under air flow (60 cm^3 min^{-1}). The sample was then outgased (10^{-5} bar) during 1 h at 200 °C, after which finally an IR spectrum was taken.

Figure II.6 shows the IR spectra of the region of the mordenite zeolite OH stretching vibration bands, where:

- The two bands at 3731 and 3745 cm^{-1} correspond to the silanol groups (Si-OH). The first band at 3731 cm^{-1} is attributed to the internal Si-OH and the more intense band at 3745 cm^{-1} is attributed to the external Si-OH.[18-19]
- The band at 3684 cm^{-1} is ascribed to the Al-OH hydroxyls. They refer to the EFAL.[20-21]
- The band at 3608 cm^{-1} is ascribed to bridging OH groups that are responsible for the Brønsted acidity.[17,22]
- The band at 3503 cm^{-1} is attributed to OH nests (silanol defects).

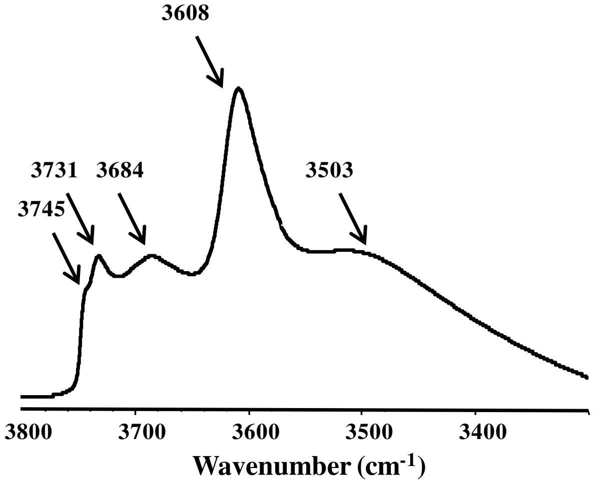

Figure II.6. OH stretching vibration band of mordenite.

1.6.2 Pyridine adsorption followed by IR

Pyridine is widely used as a molecule to probe oxides and zeolites to determine their acidity.[22-25] The interactions between the material's acid sites and the pyridine molecule are responsible for the creation of different bands in the IR spectra. These bands appear between 1400 and 1700 cm^{-1} IR region. The bands at 1490, 1545, and 1640 cm^{-1} are attributed to the formation of pyridinium ions on the Brønsted sites (PyH^+) and those at 1455, 1490, and 1600-1630 cm^{-1} are attributed to the coordination of the pyridine on the Lewis sites (PyL).[17,26] The corresponding spectrum is shown in Figure II.7.

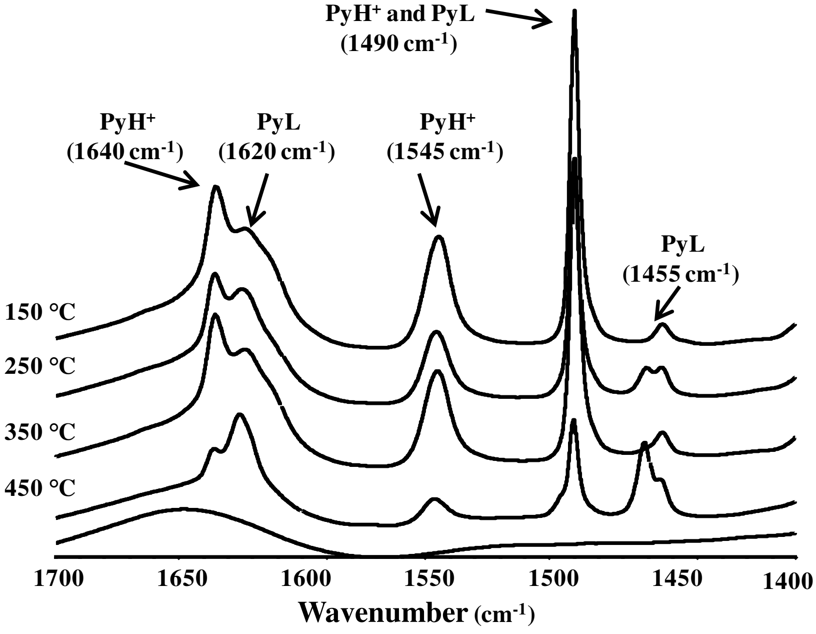

Figure II.7. Pyridine interaction bands (1400-1700 cm^{-1}) of parent mordenite (Si/Al = 20) at different temperatures.

1.6.2.1 Experimental procedure

The first step of all the experiments were the same as mentioned above. Samples were cooled to 150 °C and exposed to 1.5 mbar pyridine pressure during 5 min and then outgassed (10^{-5} bar) in order to eliminate the physisorbed pyridine. The spectrum was then taken at 150°C after 1 hour followed by three other spectra recorded at 250, 350, and 450 °C with 1 hour gap between each one. This procedure at different temperatures allows for further understanding of the acid sites strength. The characteristic spectra of the adsorbed pyridine at each temperature were, consequently, obtained by subtraction with the reference spectrum taken at 200 °C.

THERMO NICOLET 6700 FT-IR spectrometer was used to determine all the spectra between 1000 and 4000 cm^{-1} IR region with a resolution of 2 cm^{-1} and 64 analyses per spectrum.

As mentioned above, the pyridine interaction enables to determine both Brønsted and Lewis acid site densities on this material. This is attained through the correlation between the 1455 and 1545 cm^{-1} band integrated absorbance and, respectively, the Lewis and the Brønsted acid sites density given by a modified Lambert-Beer law, which ultimately results on the following equation:

$$c = \frac{A.S}{\varepsilon.m} \qquad \text{Equation II.14}$$

Where,

c = Brønsted or Lewis acid site density (μmol g^{-1})

A = Wafer surface area (2 cm^2);

ε = molar absorption coefficient ($\varepsilon_L = 1.28$; $\varepsilon_B = 1.13$)[25]

m = wafer weight (g)

and S = area under integrated peak (cm^2 mol^{-1}).

2. Catalytic tests: *n*-hexane cracking

The cracking of *n*-hexane is a reaction which requires high acidity (activation energy E). It is used as a model reaction to characterize the acidity of zeolites.

2.1 Operating conditions

The catalytic tests were carried out in an assembly consisting of a quartz reactor with fixed bed with a descending flow placed in a three-zone furnace. The temperature of the bed is checked by a thermocouple (Chrome-Nickel) placed at the same height where the catalyst is present. The upper part of the reactor is provided with a coil, which makes it possible to prolong the residence time of the reactant in the furnace, thus ensuring its vaporization before reaching the catalytic bed. As for the lower part, it is linked to an automatic storage valve (10 loops) and a 6-way electric valve coupled to a chromatograph. (Figure II.9).

Before each test, the materials are pretreated *in situ* under N_2 at 540 °C overnight. The *n*-hexane (Sigma Aldrich > 99% purity) is then injected with a Metrohm 725 Dosimat infuser after dilution in dinitrogen. The standard operating conditions are shown in Table II.1.

Table II.1. Operating condition of *n*-hexane cracking.

***n*-hexane transformation**	
Reaction temperature (°C)	540
Pressure (bar)	1
Contact time (s)	0.04
N_2/n-C_6 (molar ratio)	9

The reaction products are injected manually into a "VARIAN 450" gas chromatography (GC) equipped with a 50 m Cp-Al_2O_3/Na_2SO_4 capillary column of 0.32 mm internal and a flame ionization detector (FID). The temperature program of the furnace of the column and the conditions of analysis (detector and injector) are presented in the following diagram:

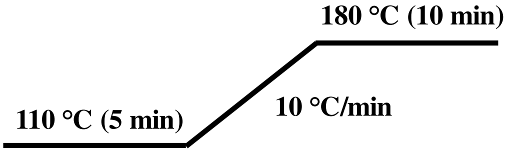

Injector: 200 °C / Split : 200
Vector gas: H_2
FID detector: 250 °C

Figure II.8. Oven temperature program and analysis conditions of the GC.

2.2 Pilot plant flowsheet

All the reactor outlet lines, as well as the storage and injection valves, are heated to 200 °C in order to avoid condensation of the products. The overall layout of the assembly is shown in Figure II.9.

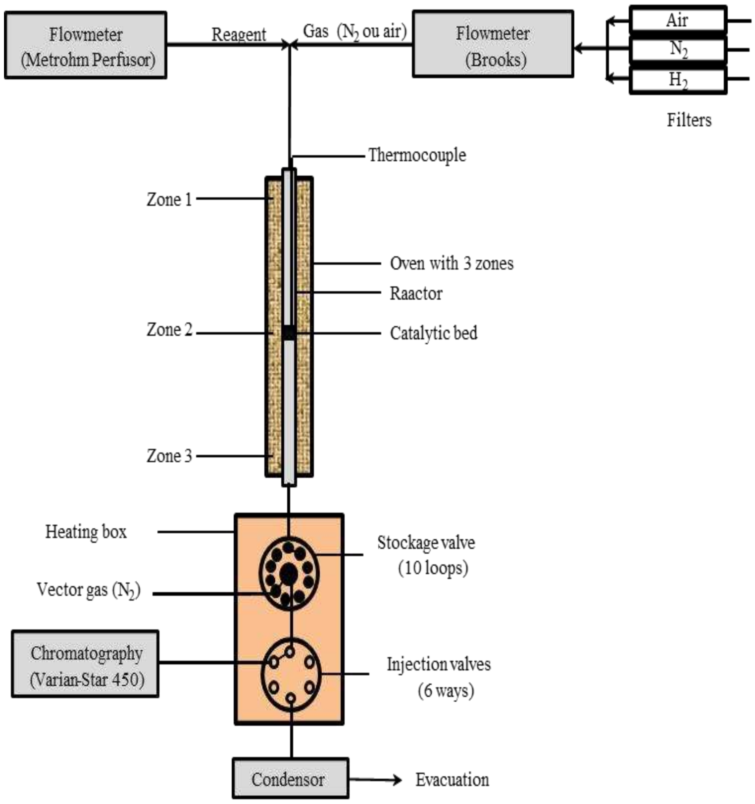

Figure II.9. Pilot plant flowsheet.

2.3 Results exploitation

The *n*-hexane cracking chromatograms allowed determining the following parameters: *n*-hexane conversion, catalyst activity, TOF, and products mass and molar yield. One example of these chromatograms is present in Figure II.10.

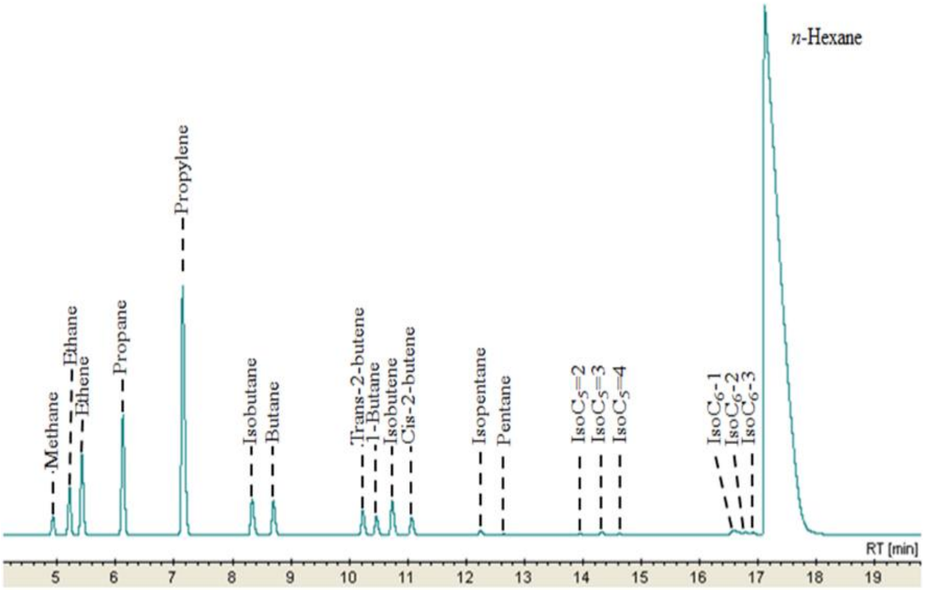

Figure II.10. Example of *n*-hexane cracking chromatogram.

2.3.1 *n*-Hexane conversion (x)

The conversion (x) of *n*-hexane defined by the ratio between the amount of reactant before and after reaction, is given by the following equation:

$$x = \left(1 - \frac{a_{nCx}}{\sum_i a_i}\right) * 100 \qquad \text{Equation II.15}$$

Where,

x = *n*-hexane conversion (%);

a_{nCx} = *n*-hexane (nC_x) peak area;

and a_i = all the peaks areas.

2.3.2 Catalyst activity (a)

The equation below allows the calculation of the catalyst activity:

$$a = \frac{D_{nCx}}{m} * \frac{x}{100} \qquad \text{Equation II.16}$$

Where,

a = catalyst activity (mol g_{cat}^{-1} h^{-1});

D_{nCx} =*n*-hexane liquid flow (mol h^{-1});

m = catalyst weight (g);

x = *n*-hexane conversion (%).

2.3.3 Turn-Over-Frequency (TOF)

The TOF represents the activity per Brønsted acid site and is given by the following equation:

$$TOF = \frac{a}{n_{H^+}} x1000000 \qquad \text{Equation II.17}$$

Where,

TOF = Turn-Over-Frequency (h^{-1});

a = catalyst activity (mol g_{cat}^{-1} h^{-1});

n_{H^+}= catalyst Brønsted acid site density (mol g_{cat}^{-1}), determined by pyridine adsorption followed by IR at 150 °C.

2.3.4 Products mass and molar yield (Y)

The mass yield of a certain product is given by the following equation:

$$Y_i = \frac{a_j}{\sum_i a_i} * 100 \qquad \text{Equation II.18}$$

Where,

Y_i = product mass yield (wt.%);

a_j = product peak area;

and a_i = areas of all peaks.

The molar yield is calculated using the following relation:

$$Y_i = \frac{n_j}{\sum_i n_i} * 100 \qquad \text{Equation II.19}$$

Where,

Y_i = product molar yield (mol %);

n_j = product molar weight given by: n = a_j / M, with M molar mass of the product;

and n_i = summation of molar weights of all products.

3. Catalytic tests: Toluene disproportionation

The TDP is a further reaction used as a model reation to characterize the acidity of zeolites. Additionally, TDP is one of the industrial applications of mordenite.

3.1 Experimental part

The setup of TDP is the same as for the *n*-hexane cracking (Figure II.9). The upper part of reactor is provided with a coil and the lower part is linked to an automatic storage valve (10 loops) and a 6-way electric valve. Prior each test, each sample is subjected to pretreatment in situ under N_2 (100 mL min^{-1}) at 450 °C overnight. The nitrogen is replaced by the carrier gas H_2 of 50 mL min^{-1} before injection of toluene by a Metrohm 725 Dosimat infusor with flow rate 0.06 mL h^{-1}. The standard operating conditions are summarized in Table II.2.

Table II.2. Operating conditions of toluene disproportionation.

Toluene disproportionation	
Reaction temperature (°C)	450
Pressure (bar)	1
Contact time (s)	0.12
H_2/n-C_7 (molar ratio)	4

The reaction products are injected manually into a "SCION 456 GC" equipped with an FID and a 60 m BR wax capillary column of internal diameter 0.25 mm. The temperature program of the furnace, the column and the conditions of analysis (detector and injector) are presented in the following diagram:

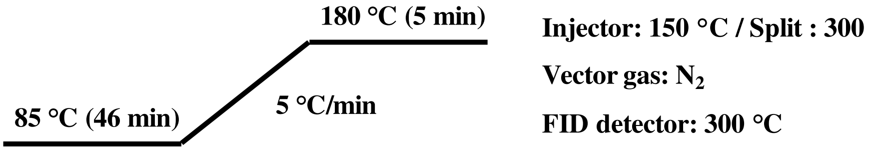

Figure II.11. Oven temperature program and analysis conditions of the GC.

3.2 Exploitation of results

The toluene disproportionation chromatograms permitted determining parameters mentioned before. One example of these chromatograms is present in Figure II.12.

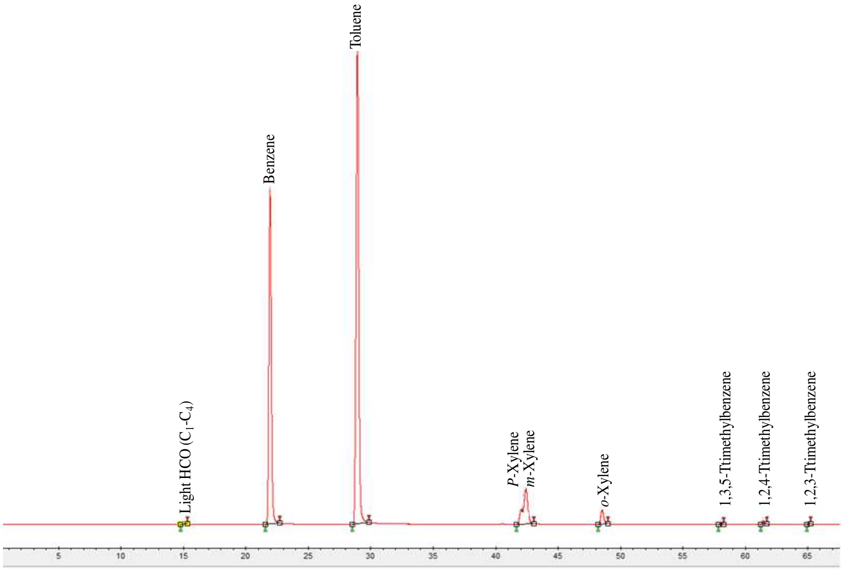

Figure II.12. Example of typical chromatogram achieved in toluene disproportionation.

4. Analysis of coking kinetics by microgravimetry

The evolution of the carbonaceous deposits as a function of time is followed by the continuous measurement of the weight gain of the catalyst, resulting from the non-desorbable products, under the operating conditions, which are considered as coke molecules. The measurements are made by microbalance (Sartarious 4433, accuracy 0.01 mg) during the conversion of propene in static mode. (Figure II.13)

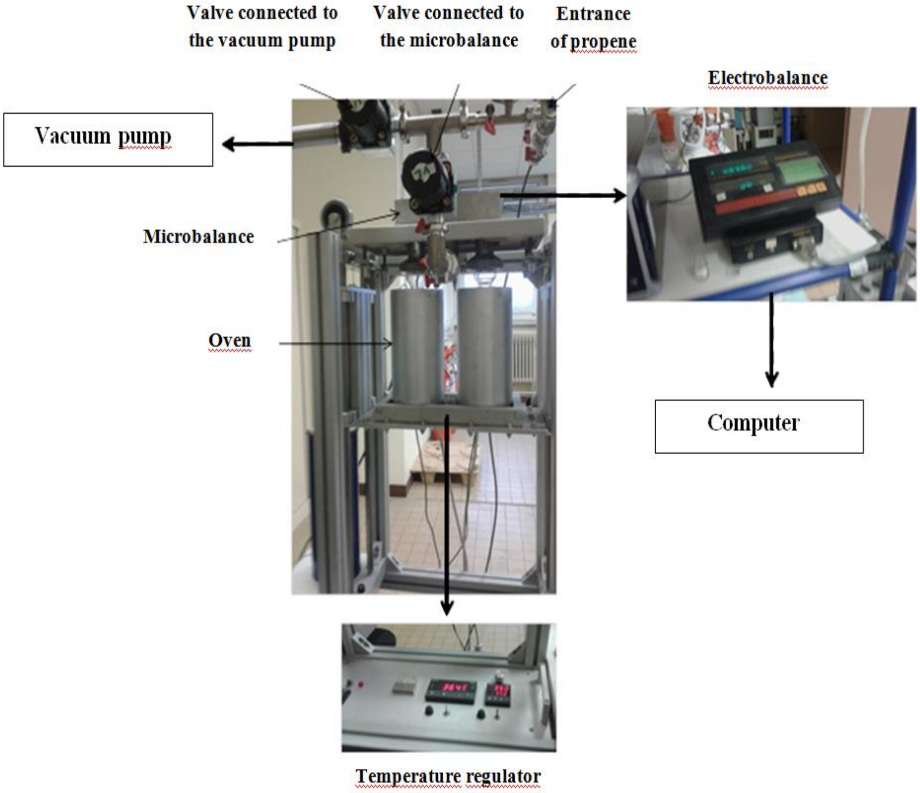

Figure II.13. The main components of the microbalance apparatus.

4.1 Experimental part

Samples of 50 mg are activated under a secondary dynamic vacuum of about 10-16 KPa, at a temperature of 350 °C for 12 hours. After activation, the zeolites lose about 15% of their masses, due to desorption of water. The coking reaction is carried out at the same temperature as the activation, introducing the propene at the desired pressure. The weight gain is considered as the amount of coke formed after a given time. The variation of this weight gain, due to molecules that do not desorb from the zeolite, under the reaction conditions, allows us to have kinetics of coking. In this study, we performed the conversion reaction of propene under 0.1 bar. The decrease in propene pressure is negligible during the coking reaction.

Bibliographic references

[1] A. L. Patterson, The Scherrer formula for X-ray particle size determination, Phys. Rev. 56 (1939) 978–982.

[2] V. D. Mote, Y. Purushotham, B. N. Dole, Williamson-Hall analysis in estimation of lattice strain in nanometer-sized ZnO particles, J. Theor. Appl. Phys. 6 (2012) 6

[3] M. Thommes, K. Kaneko, A. V. Neimark, J. P. Olivier, F. Rodriguez-Reinoso, J. Rouquerol, K. S. W. Sing, Physisorption of gases, with special reference to the evaluation of surface area and pore, IUPAC technical report. Pure Appl. Chem. 87 (2015) 1051–1069.

[4] S. Lowell, J. Shields, M. A. Thomas, M. Thommes, Characterization of porous solids and powders: Surface area, pore size and density, Springer, 2004.

[5] M. Thommes, K. A. Cychosz, Physical adsorption characterization of nanoporous materials: Progress and challenges, Adsorption 20 (2014) 233–250.

[6] J. Landers, G. Y. Gor, A. V Neimark, Density functional theory methods for characterization of porous materials, Colloids Surf., A 437 (2013) 3–32.

[7] S. Brunauer, P.H. Emmett, E. Teller, Adsorption of gases in multimolecular layers, J. Am. Chem. Soc. 60 (1938) 309–319.

[8] I. Langmuir, The constitution and fundamental properties of solids and liquids. Part I. Solids, J. Am. Chem. Soc. 38 (1916) 2221–2295.

[9] A. Corma, A.V. Orchillés, Current views on the mechanism of catalytic cracking, Microporous Mesoporous Mater. 35 (2000) 21–30.

[10] G. Caeiro, R. H. Carvalho, X. Wang, M. A. N. D. A. Lemos, F. Lemos, M. Guisnet, F. Ramôa Ribeiro, Activation of C2–C4 alkanes over acid and bifunctional zeolite catalysts, J. Mol. Catal. A: Chem. 255 (2006) 131–158.

[11] G. Leofanti, M. Padovan, G. Tozzola, B. Venturelli, Surface area and pore texture of catalysts, Catal. Today 41 (1998) 207–219.

[12] B. C. Lippens, J. H. de Boer, Studies on pore systems in catalysts, J. Catal. 4 (1965) 319–323.

[13] S. Storck, H. Bretinger, W. F. Maier, Characterization of micro- and mesoporous solids by physisorption methods and pore-size analysis, Appl. Catal., A 174 (1998) 137–146.

[14] P. Hudec, A. Smiešková, Z. idek, P. Schneider, O. Ŝolcová, Determination of microporous structure of zeolites by t-plot method—State-of-the-art, Stud. Surf. Sci. Catal. 142 (2002) 1587–1594.

[15] E. P. Barrett, L.G. Joyner, P. P. Halenda, The Determination of pore volume and area distributions in porous substances. I. Computations from nitrogen isotherms, J. Am. Chem. Soc. 73 (1951) 373–380.

[16] Mercury intrusion porosimetry theory, Micromeritics Instrument Corporation, Norcross, GA 30093-1877, USA.

[17] F. Thibault-starzyk, Groupe français des zéolithes, Les matériaux micro et mésoporeux : Caractérisation, EDP Sciences, Les Ulis, France, 2004.

[18] J. Marques, I. Gener, P. Ayrault, J. Bordado, J. Lopes, F. Ramôa Ribeiro, M. Guisnet, Infrared spectroscopic study of the acid properties of dealuminated BEA zeolites, Microporous Mesoporous Mater. 60 (2003) 251–262.

[19] S. G. Hegde, R. Kumar, R. N. Bhat, P. Ratnasamy, Characterization of the acidity of zeolite Beta by FT-IR spectroscopy and TPD of NH3, Zeolites 9 (1989) 231–237.

[20] E. Loeffler, U. Lohse, C. Peuker, G. Oehlmann, L. M. Kustov, V. L. Zholobenko, V. B. Kazansky, Study of different states of nonframework aluminum in hydrothermally dealuminated HZSM-5 zeolites using diffuse reflectance IR spectroscopy, Zeolites 10 (1990) 266–271.

[21] C. Baerlocher, L.B. McCusker, D.H. Olson, Atlas of Zeolite Framework Types, 6th edition, Elsevier, 2007.

[22] M. Maache, A. Janin, J. C. Lavalley, J. F. Joly, E. Benazzi, Acidity of zeolites Beta dealuminated by acid leaching: An FT-IR study using different probe molecules (pyridine, carbon monoxide), Zeolites 13 (1993) 419–426.

[23] E. P. Parry, An infrared study of pyridine adsorbed on acidic solids. Characterization of surface acidity, J. Catal. 2 (1963) 371–379.

[24] H. Knöuzinger, Specific poisoning and characterization of catalytically active oxide surfaces, Adv. Catal. 25 (1976) 184–271.

[25] M. Guisnet, P. Ayrault, J. Datka, Acid properties of dealuminated mordenites studied by IR spectroscopy. 2. Concentration, acid strength and heterogeneity of OH groups, Pol. J. Chem. 71 (1997) 1455–1461.

[26] F. Bauer, H. G. Karge, Characterization of coke on zeolites, characterization II, Mol. Sieves, Springer-Verlag Berlin Heidelberg 5, 2007, 249–364.

Chapter III: Pyridine assisted desilication of mordenite

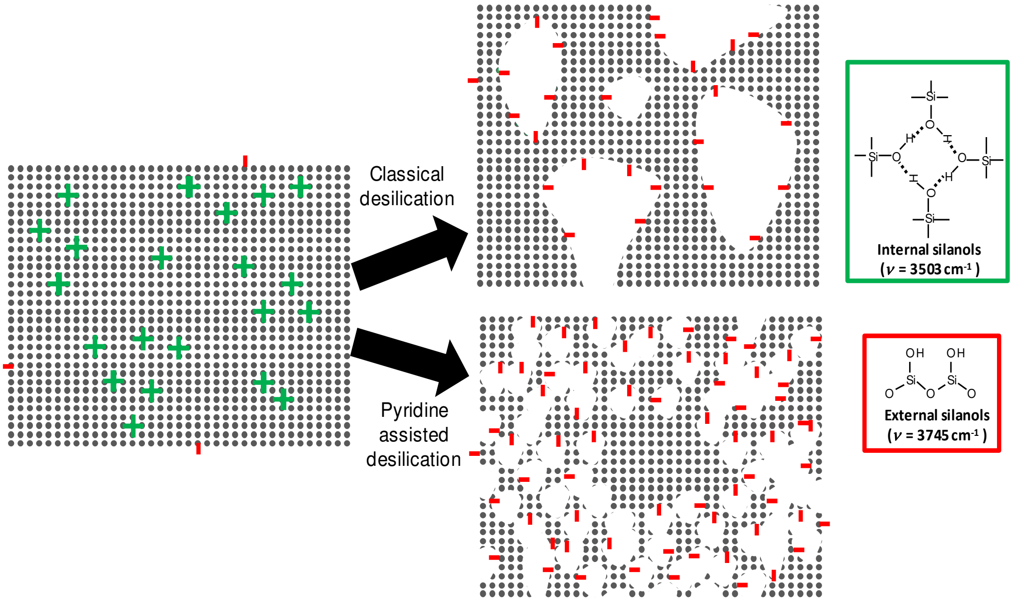

Based on publication accepted in Applied Catalysis A

doi.org/10.1016/j.apcata.2019.117139, 2019

Hussein Issa, Joumana Toufaily, Tayssir Hamieh, Alexander Sachse, Ludovic Pinard

1. Introduction

Among zeolite hierarchization strategies the by far most attractive is based on desilication, due to its simplicity and cost efficiency.[1] During the desilication process molecular silica species are removed from the zeolite structure, which allows to form inner cavities of mesoporous sizes.

Desilication of mordenite in alkaline solutions has been described in a number of contributions and allows for improving catalytic efficiency in the liquid phase alkylation of benzene,[1,2] oligomerization of pentene,[3] transformation of *m*-xylene,[4] and in the pyrolysis of lignocellulosic biomass.[5]

As already stated in the first chapter, the presence of the surfactants allows for a reprecipitation of the dissolved silica around surfactant micelles yielding a mesoporous MCM-41 like phase, which feature catalytically active zeolite fragments in the mesopore walls. This strategy was coined as recrystallization.

The use of amines, such as piperidine and hexamethylenediamine during alkaline zeolite treatment has recently been described for ZSM-5 by Wang *et al.*[6] The authors observed that the use of theses additives has an important effect on the zeolite structure. Indeed, it was inferred that the use of such diamines protects the zeolite from uncontrolled desilication, allowing thus the formation of controlled mesoporosity and reducing the loss of microporosity during the alkaline treatment. A similar behavior has been observed for the ZSM-5 desilication using quaternary ammonia salts, such as tetramethylammonium, during alkaline treatment.[7] The idea behind the use of pyridine during desilication is to selectively protect the active sites in the zeolites during the basic attack of the framework.

2. Experimental section

Four series of catalyst (D, DC, DP, and DPc) were prepared from a commercial protonic mordenite (M20; Süd Chemie). Table III.1 summarizes the operating conditions used for the post-treatments and obtained yields.

The D_x series corresponds to a regular desilication by NaOH with 0.2 or 0.6 M at 85 °C for 1 h (the subscript x indicates the concentration) under stirring. The DC samples have been prepared through desilication in presence of CTAB (0.27 M). DP and DPc samples are obtained through the alkaline treatment assisted by pyridine. In the all treatments, each gram of mordenite zeolite is subjected to 15 cm^3 of alkaline solution. The pyridine is either added in excess to the basic solution (DP series), or previously chemisorbed on M20 (DPc). The amount of pyridine added to the alkaline solution were 1650, 8250, and 16500 µmol g^{-1}, which correspond to ca 3, 15, and 30 times the number of Brønsted acid sites probed on M20 by pyridine at 150 °C. The chemisorption of pyridine was carried out in a fixed bed reactor at 150 °C with a nitrogen gas flow saturated in pyridine for 1 h. After 1 h of stripping under nitrogen in order to remove physisorbed species, the number of pyridine chemisorbed was measured and amounts to 550 µmol g^{-1}. For all of the treatments, reactions were quenched in an ice bath followed by a mild acid leaching through the adding a few drops of concentrated HCl (6 M) and stirring at room temperature for 1 h.

Table III.1. Composition of alkaline solution for desilication: regular, CTAB and pyridine assisted desilication and yield of the post-synthesis treatments.

Series	Catalyst	[NaOH]	[CTAB]	[Pyridine]	Yield^{a}
		(M)		µmol g$_{zeolite}^{-1}$	(%)
D (*Regular*)	$\mathbf{D_{0.2}}$	0.2			73
	$\mathbf{D_{0.6}}$	0.6			66
DC (*with CTAB*)	$\mathbf{D_{0.2}C}$	0.2	0.27		76
	$\mathbf{D_{0.6}C}$	0.6	0.27		61
DPc (*with chemisorbed py*)	$\mathbf{D_{0.6}\,P_{550}}$	0.6		550	68
DP (*with excess of py*)	$\mathbf{D_{0.6}\,P_{1650}}$	0.6		1650	77
	$\mathbf{D_{0.6}\,P_{8250}}$	0.6		8250	76
	$\mathbf{D_{0.6}\,P_{16500}}$	0.6		16500	72
P (*blank*)	$\mathbf{P_{8250}}$			8250	91
	$\mathbf{P_{550}}$			550	88

[a] *Calculated from the weight before and after post-treatment.*

The catalysts were recovered by centrifugation, washed with deionized water, dried and calcined at 550 °C for 4 h (heating rate 5 °C min^{-1}). The protonic form of the catalyst was obtained after three consecutive exchanges with a 1 M solution of NH_4NO_3 using the proportion of 50 cm^{3} g^{-1} of zeolite. The exchange was carried out at 85 °C for 1 h. After a careful wash up to pH 7 the solids were dried at 80 °C during 12 h and then calcined 550 °C for 4 h.

The samples P_{8250} and P_{550} were obtained through blank treatments and correspond to treatments in which the alkaline treatment was suppressed.

3. Results and discussion

3.1 Textural properties

Pyridine assisted desilication was carried out by following two approaches: (*i*) the addition of pyridine during desilication (DP series) and (*ii*) the pre-adsorption of pyridine through chemisorption by interacting with the BAS of the zeolite prior to desilication (DPc series). It is to note that the concentration of NaOH was kept constant for each experiment (0.6 M). The textural, chemical and catalytic properties of the modified zeolites were compared with the parent mordenite (Tables III.2 and III.3). Samples were further compared to blank experiments, in which no pyridine was added (D series), CTAB was added (DC series) or in which no NaOH was used (P series).

Table III.2. Textural properties of parent zeolite (M20) and after desilication by NaOH (D) in the presence of CTAB (DC) or assisted by pyridine (DPc and DP); P: blank samples.

Series	Catalyst	Crystallinity[a] (%)	CCS[b] (nm)	Strain[c]	V_{micro}[d] (cm^3 g^{-1})	V_{meso}[e] (cm^3 g^{-1})
M	**M20**	100	66.4	7.3	0.18	0.11
D	**$D_{0.2}$**	93	55.7	9.1	0.16	0.13
	$D_{0.6}$	60	56.3	8.9	0.09	0.54
DC	**$D_{0.2}C$**	98	57.8	8.2	0.18	0.15
	$D_{0.6}C$	68	48.7	10.5	0.09	0.36
DPc	**$D_{0.6}\,P_{550}$**	67	48.6	10.9	0.09	0.66
DP	**$D_{0.6}\,P_{1650}$**	66	55.8	9.8	0.08	0.58
	$D_{0.6}\,P_{8250}$	59	58.1	9.9	0.10	0.72
	$D_{0.6}\,P_{16500}$	42	58.7	9.8	0.11	0.54
P	**P_{8250}**	92	55.4	9.6	0.16	0.11
	P_{550}	87	53.6	9.6	0.16	0.13

[a]Measured by XRD analysis; [b,c] Coherent crystal size and strain estimated by Scherrer method [d]Estimated by t-plot method; [e]Mesopore volume = V_{total}-V_{micro} (V_{total}: determined from the adsorbed volume at P/P_0= 0.96).

The morphology of the parent mordenite consists out of aggregates of crystals (50-100 nm) that are probably due to the steaming process applied during the preparation of this sample by the supplier (Figure III.1). The nitrogen adsorption and desorption isotherms at 77 K of the sample is of type I, which is expected for a purely microporous material (Figure III.2) and features a microporous volume of 0.18 cm^3 g^{-1}

First classical desilication using aqueous NaOH was studied on the parent MOR. Here for NaOH solutions of various concentration ranging from 0.2 to 0.6 M were tested and abbreviated by $D_{0.2}$ and $D_{0.6}$. An important part of the zeolite dissolves during the alkaline treatment and the higher the concentration of the base, the lower the materials yield (Table III.1). As can be inferred from the nitrogen adsorption and desorption isotherm, the treatment using the 0.2 M solution hardly impacts the shape of the isotherm, which indicates that no textural modification was developed during the treatment (Figure III.2).

This finding was further confirmed by the electron microscopy images, which present identical textural features compared to the parent mordenite (Figure III.1). The isotherm of the desilicated mordenite achieved through a treatment with a 0.6 M NaOH solution is of type IV and presents an important gas uptake in the high relative pressure region ($p/p_0 > 0.5$) and features an H3 hysteresis loop, which is characteristic for a large size distribution of mesopores (Figure III.3). During the treatment microporosity was affected and reduced to 0.09 $cm^3\ g^{-1}$ (Table III.2). Indeed, the micrographs of this sample present electron clear regions within the mordenite crystals, which allows to conclude the formation of mesopores of a wide size distribution (Figures III.1 and III.3).

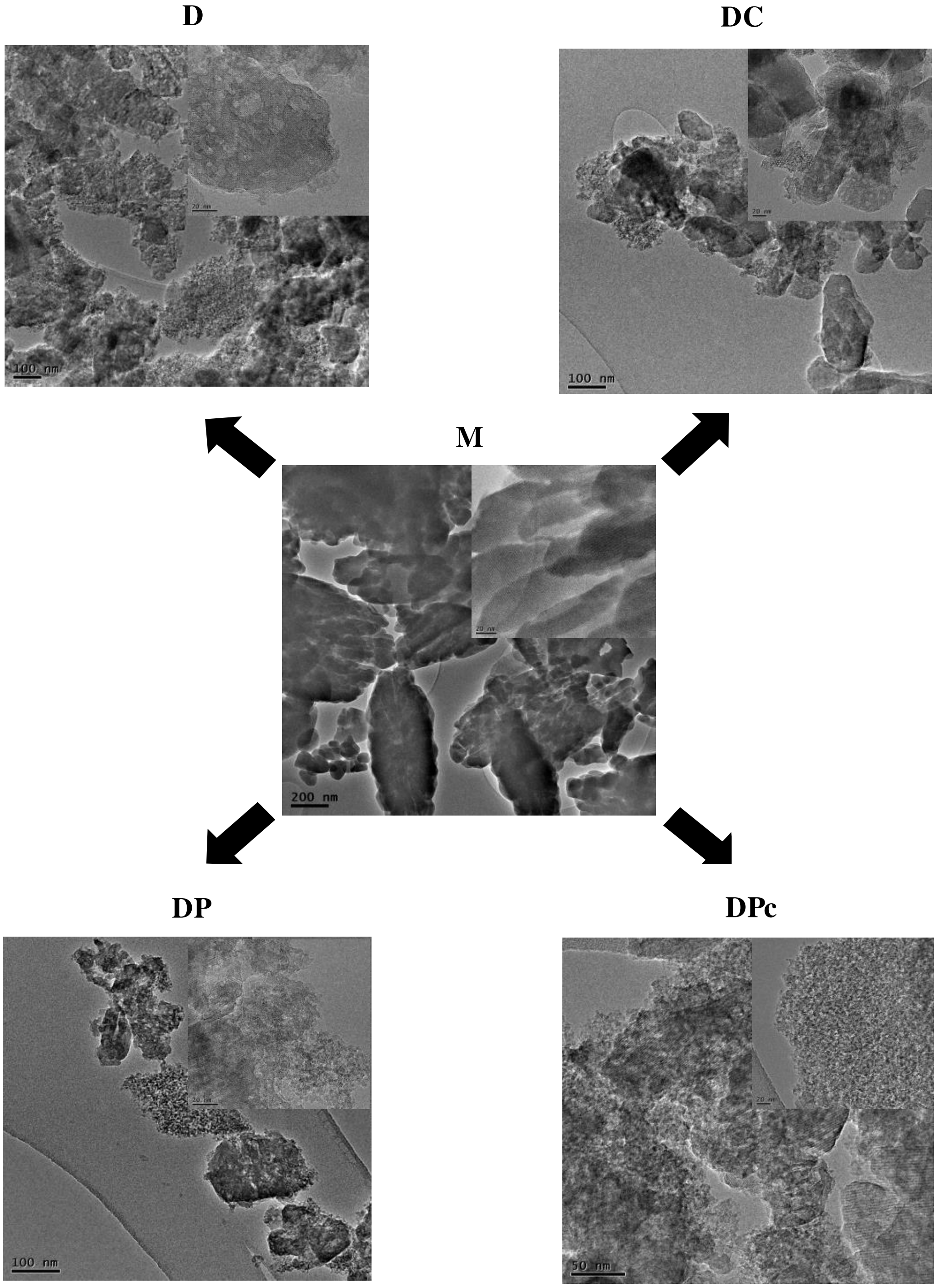

Figure III.1. TEM images of M20 and one material for each series: D, DC, DP, and DPc.

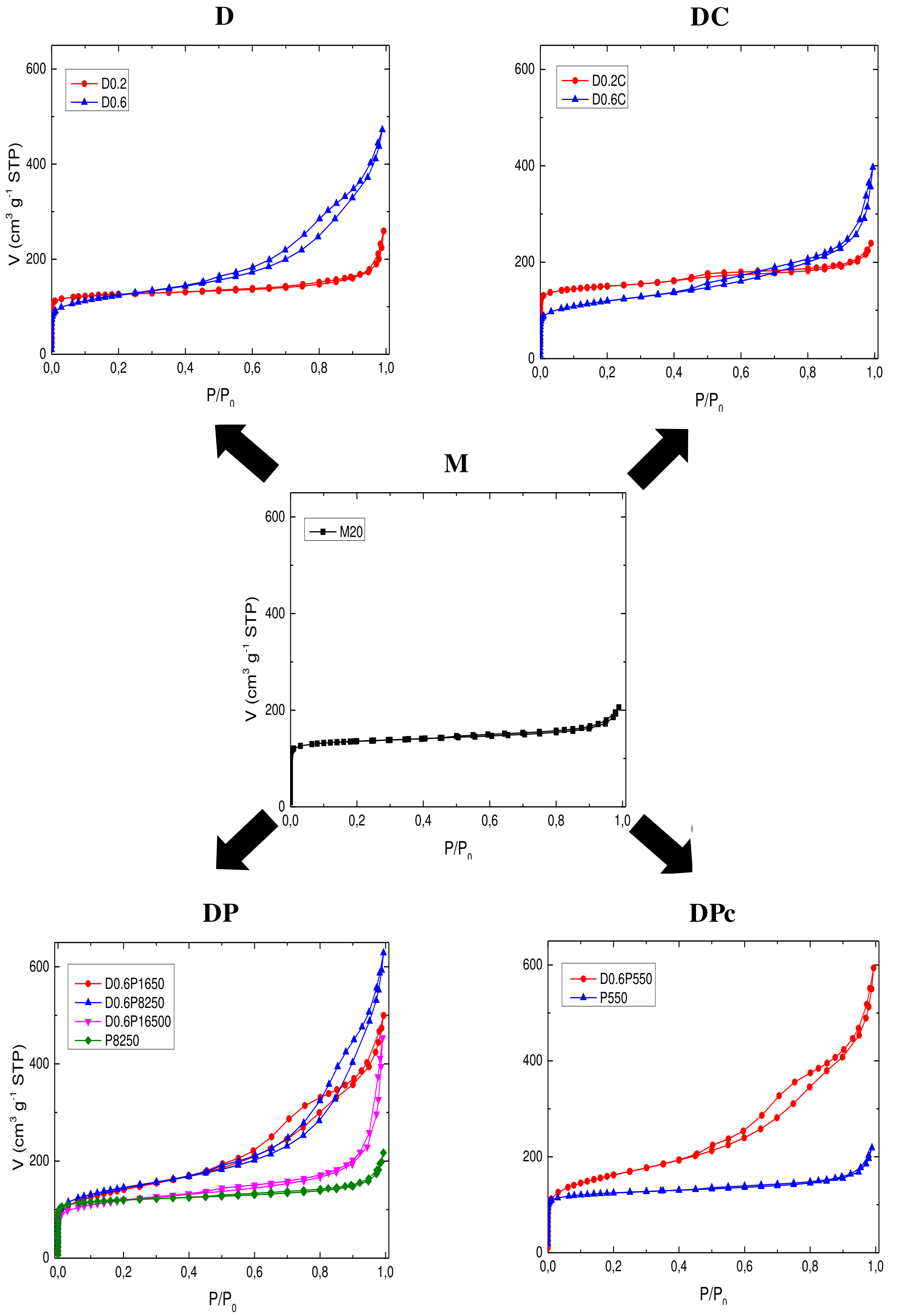

Figure III.2. Comparison of the nitrogen adsorption and desorption isotherms at -196 °C of the parent mordenite (M20) and the four series: D, DC, DP, and DPc.

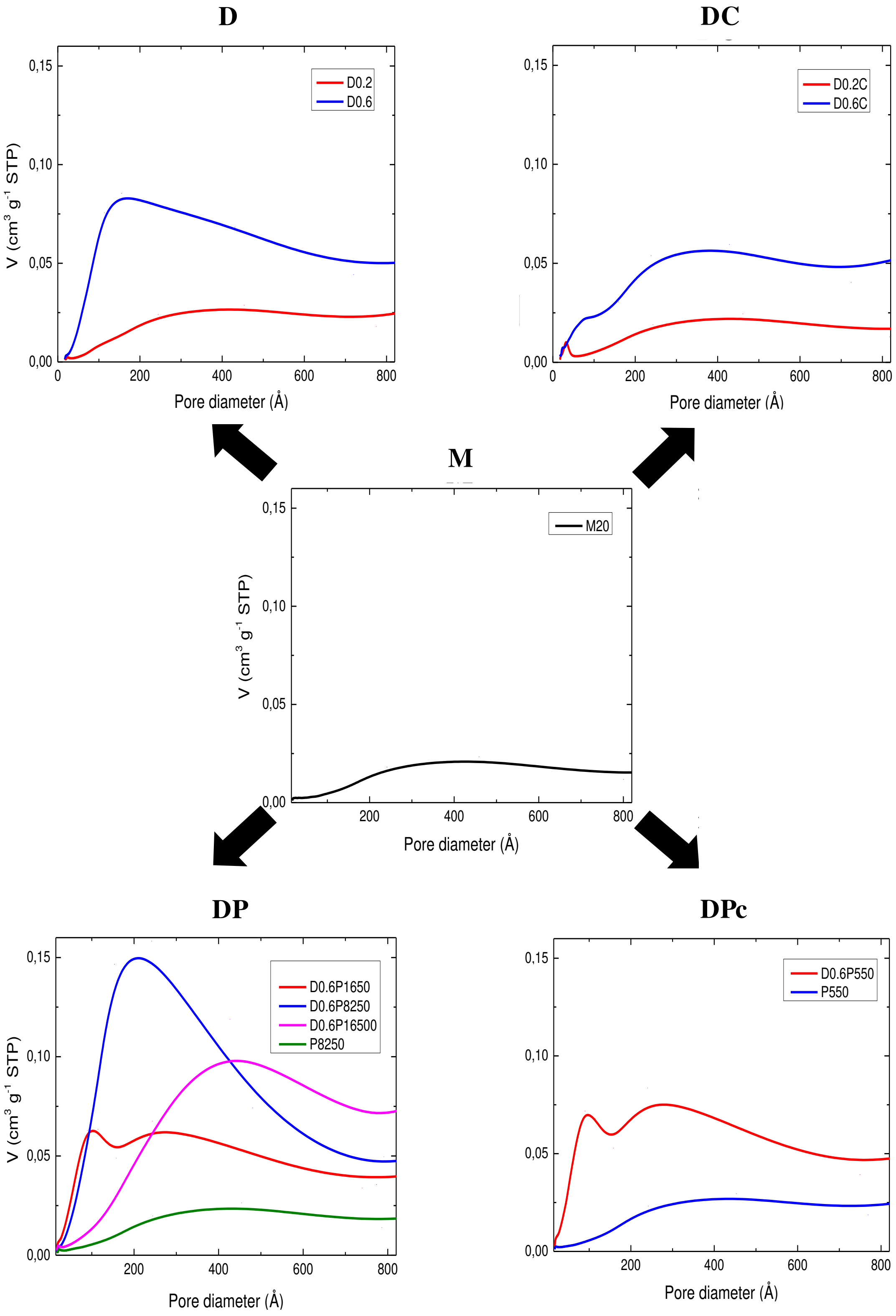

Figure III.3. BJH pore size distribution plots derived from the adsorption branch for the four catalyst series: D, DC, DP, and DPc.

With the aim to preserve the acidity of the parent mordenite during the desilication step, a pyridine pre-adsorption on M20 was performed, followed by a temperature treatment at 150 °C in order to remove eventually physisorbed pyridine. The amount of chemisorbed pyridine by this strategy was quantified through thermogravimetric analysis (TGA) and amounts to 550 µmol g^{-1}. The pyridine pre-adsorbed sample was then subjected to alkaline treatment using a 0.6 M aqueous NaOH solution. The presence of chemisorbed pyridine has only little impact on the synthesis yield (Table III.1). In addition, pyridine remains adsorbed within the sample throughout the alkaline treatment, as revealed by TGA (Figure III.4).

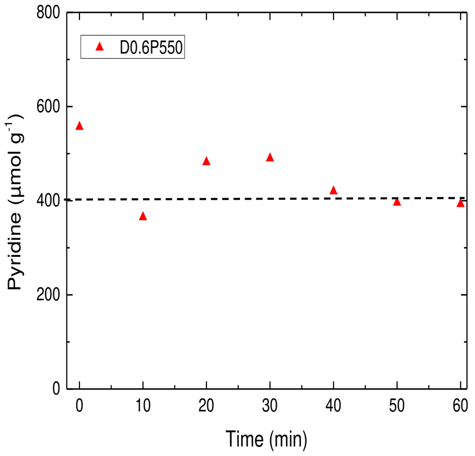

Figure III.4. Pyridine content of DPc during desilication.

It is interesting to notice that the shape of the isotherm of this sample is similar to the one obtained by usual desilication yet featuring the striking difference of a sharp uptake in the very high relative pressure region close to saturation and achieving a mesoporous volume of 0.66 cm^3 g^{-1} (Figure III.2). The difference in texture was further inferred from the TEM images, which allow to observe next to the development of intracrystalline mesoporosity smaller particles of sizes below 10 nm that feature zeolite crystallinity (Figure III.1). Indeed, the important nitrogen uptake at very high relative pressures is characteristic for the condensation in interparticular porosity.[8] Interestingly, merely a minor reduction of the FWHM of the XRD peaks is observed, and coherent crystal sizes obtained through applying Williamson-Hall analysis are of 66 and 48 nm for M20 and chemisorbed pyridine assisted mordenite desilication (DP_{550}), respectively (Table III.2). Yet, the intensity of the XRD peaks importantly decreases, indicating the reduction of diffraction efficiency (Figure III.5). It can hence be assumed that the small sizes of the zeolite particles contain insufficient diffraction planes to allow for the observation of XRD peaks, which explains the important reduction of crystallinity.[9]

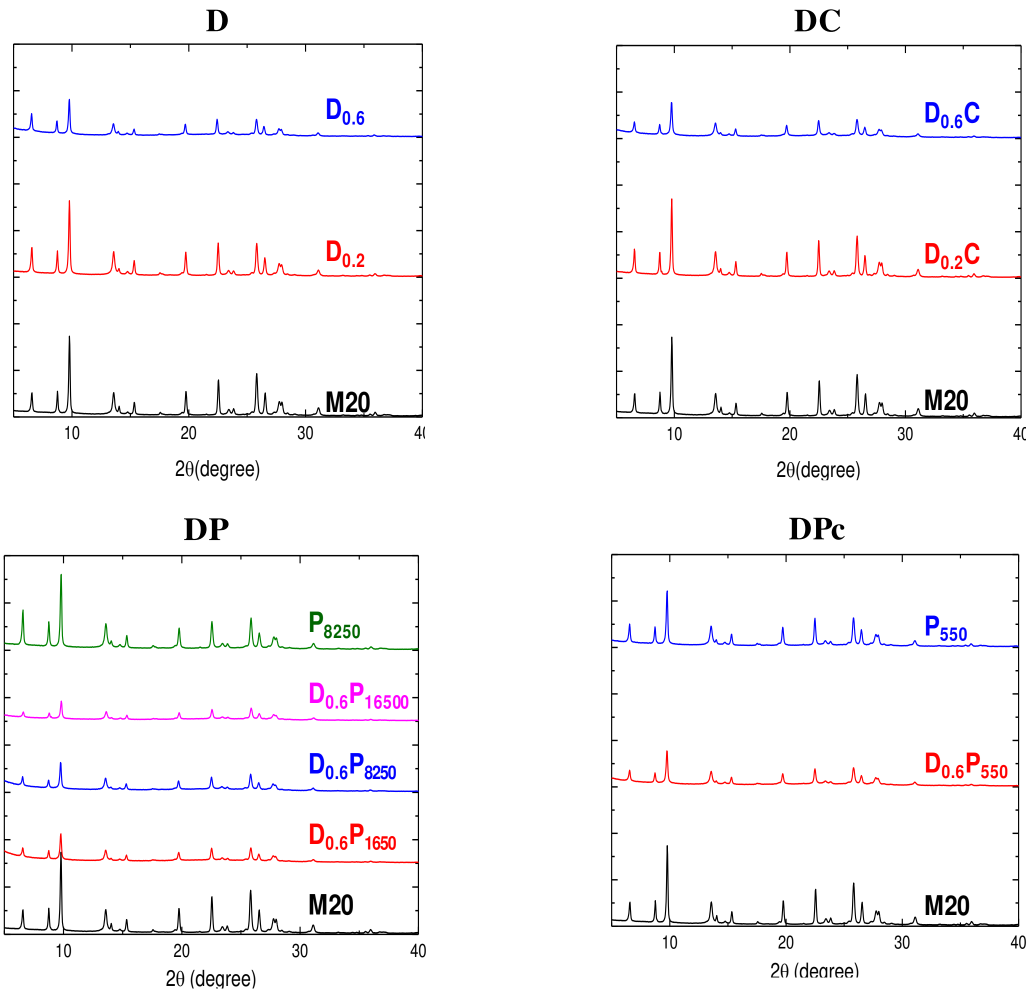

Figure III.5. XRD patterns of the M20 and the four modified catalyst series.

Though the developed pyridine pre-adsoprtion strategy followed by alkaline treatment allows for importantly impacting the textural properties it features as major drawback the limitation of the maximal pyridine content to its chemisorption capacity. In order to further increase the amount of pyridine during alkaline treatment, an excess of pyridine with respect to the number of acid sites was added directly to the aqueous NaOH solution, *i.e.* an excess of 3, 15 and 30 times the amount of pyridine compared to the BAS. From the nitrogen physisorption of the obtained samples important differences in the textural properties of the achieved materials can be deduced (Figure III.2). The sample achieved with the lowest amount of pyridine ($D_{0.6}$ P_{1650}, Table III.1) features an isotherm that is very similar to the one of the sample achieved by the pyridine pre-adsorption strategy with comparable microporous and mesoporous volume. Additionally, from the TEM images very similar morphological features can be observed (Figure III.1), which indicates that the direct addition of pyridine to the desilication solution has a similar effect as pre-adsorption of pyridine. Increasing the amount of pyridine in the desilication solution has important implications as far as texture is concerned as can be observed from the nitrogen adsorption isotherms. Indeed, for the sample treated with the highest amount of pyridine ($D_{0.6}P_{16500}$, Table III.1) the shape of the isotherm has completely changed, as merely the sharp uptake at very high relative pressure is observed, which indicates the absence of intracrystalline mesoporosity. This is confirmed by the TEM images for which a much greater part of smaller aggregated particles can be observed (Figure III.1). This is further indicated form the overall crystallinity (Table III.2 and Figure III.5) that reduces substantially for samples with increasing amount of pyridine in the synthesis mixture.

In order to size the impact of pyridine during the alkaline treatment a blank experiment was conducted in which the parent zeolite was added to an aqueous solution that merely contained 8250 µmol g^{-1} of pyridine (P_{8250}, Table III.1). The achieved sample presents textural properties like the parent zeolite, the only difference is the microporous volume that is slightly reduced, which indicates that the microporosity might be partially blocked (see part 3.2).

For the sake of comparison, desilication was carried out in the presence of CTAB (DC series, Table III.1). In earlier works it has been described that depending on the synthesis conditions the addition of quaternary amines can lead to the protection of zeolites from extensive desilication and through applying harsher conditions to the recrystallization of mordenite.[10-12] For the applied synthesis conditions recrystallisation into an amorphous mesoporous phase can be observed by TEM (Figure III.1), yet the overall amount of recrystallized material is very low as indicated by the absence of capillary condensation in the N_2 adsorption isotherm at p/p_0 between 0.4 and 0.5 (Figure III.2).

3.2 Chemical properties

Figure III.6 compares the hydroxyl stretching vibration of IR spectra before and after adsorption of pyridine at 150 °C, on all catalysts. M20 exhibits a band at 3607 cm^{-1}, which is assigned to the bridged hydroxyl groups (SiOHAl). The less intense bands at 3745, 3733, and 3684 cm^{-1} are due to stretching vibrations of external and internal silanols Si-OH, and OH linked to EFAL, respectively. The broad band centered at 3503 cm^{-1}, it related to the presence of hydroxyl nests.[13] The presene of hydroxyl nests in the parent zeolite can be explained according to what was described by Barrer and Maki.[14]

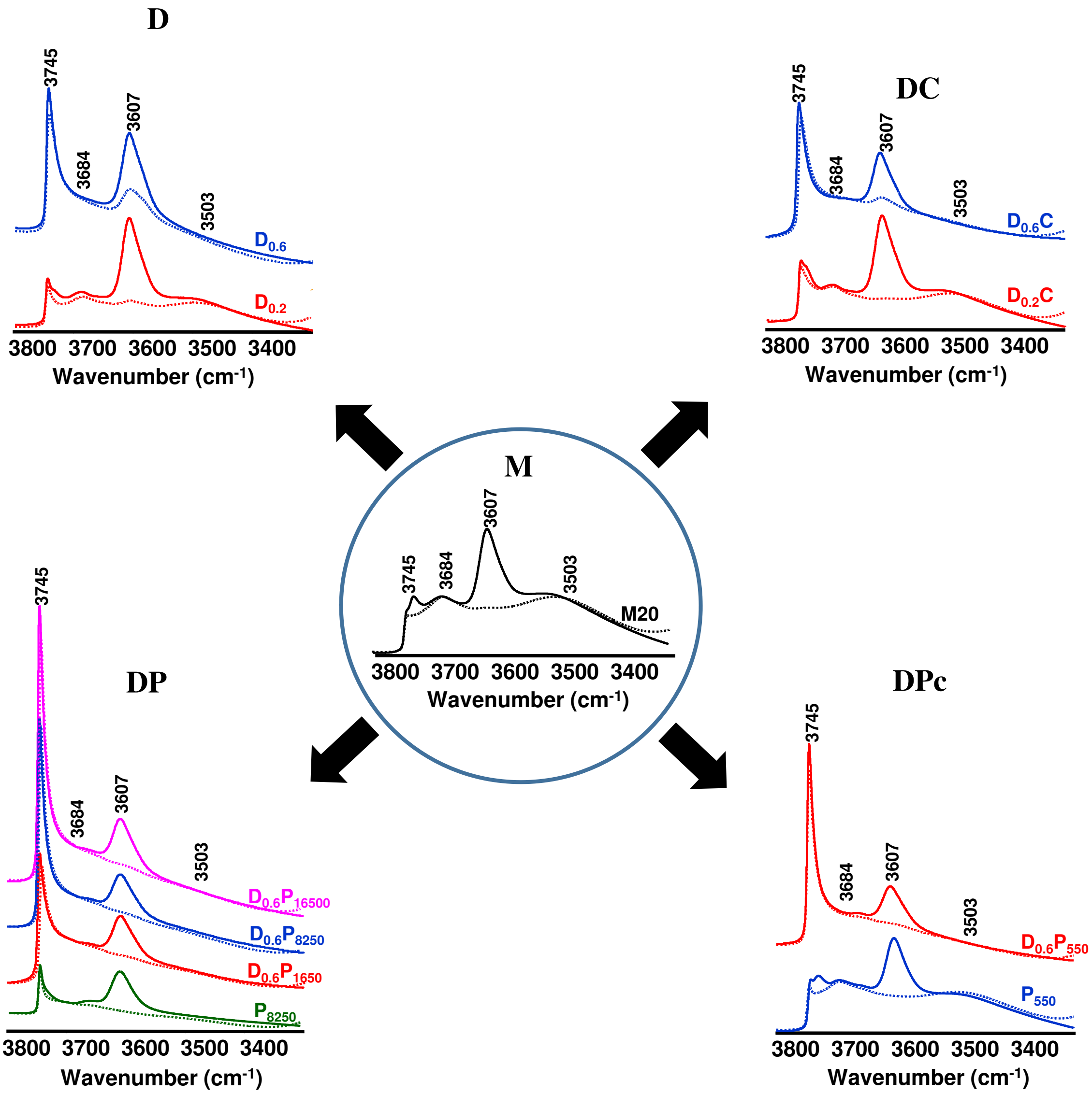

Figure III.6. Comparison of IR spectra before and after pyridine adsorption at 150 °C of M20 and the four catalyst series: D, DC, DP, and DPc.

They observed that the calcination of a zeolite in its ammonium form, leads to the dislodgment of aluminum atoms, leaving four OH groups saturating the four Si atoms previously connected to the aluminum. The developed hydroxyl nests are stabilized by a network of hydrogen atoms, in which each Si-OH group is bonded via a hydrogen bond to an oxygen atom of a neighboring OH group, which leads to a broad band centered at ca. 3500 cm^{-1}.

The chemisorption of pyridine at 150 °C only leads to the disappearance of the band at 3607 cm^{-1}, therefore all the bridged hydroxyl groups are accessible to probe molecule which means they are located in the 12-MR channels and/or to the intersection between the side pocket constituted of 8-MR and 12-MR channels. It is worth to mention that mordenites featuring a lower Si/Al ratio present BAS at the bottom of site pockets, which are inaccessible to pyridine.[15] The number of acid sites (C_B) probed by pyridine is 552 µmol g^{-1} (Table III.3), while the theoretical value calculated assuming that all aluminum is in the framework would amount to 650 µmol g^{-1}. The observed difference is due to the presence of EFAL species, which is confirmed by the presence of Lewis acid sites (C_L = 47 µmol g^{-1}, Table III.3).

Table III.3. Global Si/Al molar ratio and number of acid sites able to retain pyridine at 150 °C and 450 °C on parent zeolite (M20) and after desilication by NaOH (D) in the presence of CTAB (DC) or assisted by pyridine (DPc and DP); P: blank samples.

Series	**Catalyst**	**Si/Al^a**	**[H$^+$]^b**		**[L]^c**	**Accessibility^d**
			150 °C	**450 °C**	**150 °C**	
		mol/mol		**µmol g^{-1}**		**%**
M	**M20**	20.4	552	109	47	100
D	**$D_{0.2}$**	18.2	491(516)	44	96	95
	$D_{0.6}$	17.1	324(483)	15	40	67
DC	**$D_{0.2}C$**	18.6	531	29	77	100
	$D_{0.6}C$	18.4	329(391)	59	59	84
DPc	**$D_{0.6}P_{550}$**	19.5	328	79	90	100
DP	**$D_{0.6}P_{1650}$**	17.8	376	15	105	100
	$D_{0.6}P_{8250}$	18.6	300	13	87	100
	$D_{0.6}P_{16500}$	18.3	314	22	105	100
P	**P_{8250}**	18.6	338	36	171	100
	P_{550}	17.5	368	88	86	100

[a] Measured by ICP; [b,c] Brønsted and Lewis acidity measured by pyridine adsorbed at 150 and 450 °C; [d] Measured by the intensity of the hydroxyl group before and after the adsorption of pyridine at 150 °C; In brackets the expected acidity.

Indeed, the sum of C_B and 2 times C_L (assuming that EFAL are of the general formula Al_2O_3), corresponds to the value of the theoretical acidity. As a result, we can thus deduce that 15% of the aluminum in M20 is present under the form of extra-framework species. It is to note that the presence of EFAL species does yet not prevent the access of the organic probe molecule to the acid sites. The dislodged Al atoms remain within the micropores/mesopores in the form of cationic (Al^{3+}, AlO^+), neutral or charged species, which can further feature a certain degree of polymerized, or be in the form of hydroxylaluminates (*e.g.* $Al(OH)^{2+}$, $Al(OH)^+_2$, AlOOH, $Al(OH)_3$).[16,17]

On the samples obtained through classical desilication (D series), increasing the alkaline concentration leads to the reduction of the intensity of band related to hydroxyls nest

(3503 cm^{-1}) up to its complete disappearance and concomitantly to the increase of external silanols (band at 3745 cm^{-1}). This hence indicates that silicon extraction takes place at defective sites within the crystal (*i.e.* hydroxyl nests). This has previously been demonstrated for USY and H-ZSM-5 desilication by Quin *et al.*[18] and Holm *et al.*[19], respectively (Scheme III.1).

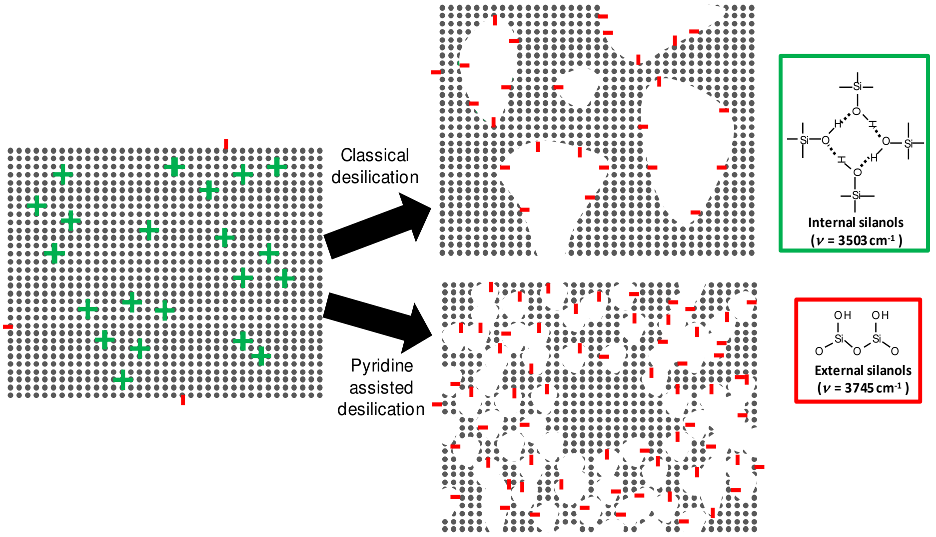

Scheme III.1. Schematic representation of the development of textural features and silanols during classical and pyridine assisted desilication.

After a slight decrease in the bridged hydroxyl band (3607 cm^{-1}), its intensity remains stable; yet the accessibility of the acid sites decreases importantly. For the $D_{0.6}$ sample merely 2/3 of acid sites are accessible to pyridine, which is most likely due to incomplete removal of extraframework silicon (EFSI) or aluminum (EFAL) species during the mild acid leaching process and which are trapped within the zeolite porosity. These extra-framework species are most probably located at the entrance of the pore mouths, which blocks the pore access even to nitrogen (reduction of microporous volume, Table III.2) and hence to a part of the BAS located within the channels, which reduces to 324 µmol g^{-1} for $D_{0.6}$ (Table III.3). Lutz *et al.*[20,21] detected on a modified FAU zeolite an important amount of EFSI species upon alkaline treatment or through combined acid-base treatments. Moreover, Stockenhuber and Lercher[22] evidenced EFSI species within dealuminated Y type zeolite. These silica rich species were located on the outside of the zeolite channels, whereas the EFAL/SI species have been proven to form long-range interaction with BAS.

The addition of CTAB during desilication presents almost no impact as far as acid site accessibility is concerned and similar BAS are observed as for the classical desilication. Hence, the presence of CTAB during the treatment does not modify the desilication process, contrariwise to that what has been observed for the addition of pyridine during the treatment (DP series). It should be mentioned that, in the absence of alkaline treatment (P series), the mere presence of pyridine causes, after calcination, significant changes in the number and nature of acid sites, without any significant modifications of silanol bands (Figure III.6). Whatever the mode of introduction of pyridine though gas phase (P_{550}) or solution (P_{8250}), the number of BAS decreases by 35-40%, while the amount of Lewis acid sites increases (171 and 86 µmol g^{-1} for P_{8250} and P_{550}, respectively). These changes can be ascribed to dealumination occurring during the calcination step in the presence of pyridine in the mordenite structure and chemisorbed on the BAS. The dealumination occurring during calcination of the zeolite containing pyridine is probably analogous to that of the ammonium form used for the ultra-stabilisation process of zeolite Y. This process developed by Mc Daniel and Maher in the late 1970s[23] consists of two major steps: (*i*) a nearly complete exchanged of sodium ions by ammonium and (*ii*) thermal treatment to temperatures higher than 800 °C. The in this way performed thermal deamination allows for partial dealumination of the zeolite and to the formation of EFAL. Therefore, we can assume that the calcination of the chemisorbed pyridine leads then to a selective dealumination process. As such, the total acidity ($C_B + 2C_L = 680$ µmol g^{-1}) of P_{8250} corresponds to that of the parent zeolite (Table III.3), which means that the extra-framework species created during the pyridine combustion do not affect the accessibility to BAS. We can assume that EFAL species are trapped in the side pockets (a location on the outer surface is less likely, due to a need of a migration step). On P_{550}, the total acidity (540 µmol g^{-1}) is slight lower than that of M20.

The most striking difference in the pyridine assisted desilication of mordenite is the important formation of non-acidic external silanol groups (3745 cm^{-1}, Figure III.6). Moreover, the intensity of this band increases with increasing concentration of pyridine used in the desilication solution. The number of BAS is almost equivalent to the blank samples (P series) achieved in the absence of alkaline treatment, hence indicating that the loss of BAS results from the combustion of pyridine during the calcination step. This further suggests that pyridine truly protects BAS during that alkaline desilication step. It indeed seems that the presence of pyridine allows for orienting the hydrolysis of the Si-O-Si bond by protecting aluminum species through filling of the 12-MR channels. Hence the action range of hydroxides (HO^-) is restricted and through increasing the amount of pyridine the attack on external surface is favored (Scheme III.1). This confirms well to the observed morphology of the pyridine assisted desilicated samples (Figure III.1).

4. Catalytic performances

4.1 *n*-Hexane cracking

n-Hexane cracking was chosen to characterize the impact of the presence of pyridine during the alkaline treatment. Figure III.7 compares the conversion of achieved catalysts as a function of the time-on-stream. Though the zeolite framework is considered as "monodimensional" almost no deactivation of the parent catalyst (M20) is observed. The coke content is very low (2.1 wt.%, Table III.4) even after 1 h of reaction, which indicates a low partial pressure of olefins. The cracking mechanism which occurs through the applied operating conditions (540 °C, $P_{n\text{-}C6} = 0.01$MPa) is hence monomolecular. The C_3 cracking product is largely predominant, whilst C_1, C_2, C_4, and C_5 products (Figure III.8a) are formed in small amount with a C_4/C_2 molar ratio close to 1 and a C_5/C_1 molar ratio of 0.7, indicating the occurrence of secondary cracking (Figure III.8b and c). For each cracked molecule one alkane and one alkene are formed (O/P $\approx$1, Table III.4). The distribution of cracking products confirms that the cracking mechanism involves a penta-coordinated carbonium ions, *i.e.* occurrence of a monomolecular mechanism. The turnover rate of BAS (TOF) of the parent zeolite is ca 130 h^{-1}, *i.e.* 2.5 times less than that of an MFI zeolite.[24] This difference can yet not be ascribed to mass transfer limitations as the kinetic diameter of *n*-hexane (4.3 Å) is significantly lower than the size of the 12-MR (6.7 x 7.0 Å), moreover the coherent crystal size (CCS) of the zeolite is small (66.4 nm, Table III.2). Therefore, the strength of protonic acid sites located in the main channels of mordenite is much lower than those located on the channel intersection of the MFI zeolite in spite of a similar void volumes (in MFI channel intersections lead to cage-like voids with a diameter of 0.70 nm). The samples achieved through alkaline treatment with or without the presence of CTAB promotes the formation of olefin (O/P between 1.3-1.5, Table III.4), probably by dehydrogenation reaction (H_2 is not detected), which favors the coke formation and thus the catalyst deactivation. Indeed, the deactivation on mordenite zeolite occurs by pore blocking,[25,26] which means that a low coke content is enough to completely deactivate the catalyst. The deactivation remains nevertheless limited given the low coke content (3.2-6.5 wt.%). After alkaline treatment, TOF values are higher than on the parent zeolite. It is worth to mention that TOF are calculated from the number of acid sites probed by pyridine, yet as discussed before, after the desilication treatment only one part of BAS is accessible to pyridine (approximately 2/3). The inaccessibility of pyridine to BAS does yet not mean that they are inaccessible to *n*-hexane, which features a smaller kinetic diameter. The TOF were hence recalculated considering the accessibility of BAS (*i.e.* those probed by pyridine), therefore the values are decreased and closer to the one obtained on the parent zeolite.

Table III.4. Initial activity (A_0), turnover frequency of acid site probed by pyridine at 150 °C (TOF), residual activity after 1 h reaction (A_{60}/A_0), and coke content for *n*-hexane cracking measured by elemental analysis. O/P molar ratio corresponds to the olefins/paraffins ratio.

Series	**Catalyst**	**A_0 mmol h^{-1} g^{-1}**	**TOF h^{-1}**	**O/P mol/mol**	**A_{60}/A_0**	**Coke %**
M	**M20**	72	131	0.95	0.86	2.1
D	**$D_{0.2}$**	101	206(196)	1.26	0.39	6.5
	$D_{0.6}$	99	304(229)	1.46	0.41	3.2
DC	**$D_{0.2}C$**	66	124	1.38	0.35	5.2
	$D_{0.6}C$	69	208(180)	1.41	0.52	3.2
DPc	**DP_{550}**	165	503	1.35	0.51	2.5
DP	**$D_{0.6}P_{1650}$**	249	663	1.34	0.26	2.8
	$D_{0.6}P_{8250}$	217	722	1.52	0.27	2.5
	$D_{0.6}P_{1650}$	201	641	1.18	0.37	1.8
P	**P_{8250}**	102	301	1.73	0.34	3.9
	P_{550}	106	287	1.49	0.45	-

Between brackets are the expected TOF values w.r.t the expected acidity.

The slight dealumination occurring during the calcination of pyridine on P_{550} and P_{8250} samples is sufficient to improve the catalyst activity by doubling the TOF of protonic sites (Table III.4). The activity on $D_{0.6}P_{1650}$ is the same even at lower conversion obtained by decreasing the contact time (Figure III.9). This means that a kinetic order of 1 for the cracking of *n*-hexane, which agrees with a monomolecular mechanism. The increase in activity of the protonic sites can be related to the presence of EFAL species either by an inductive effect on the hydroxyl groups.[27] Moreover, high O/P molar ratios (1.5-1.7) could be related to hydride abstraction induced by Lewis acid sites.[28,29]

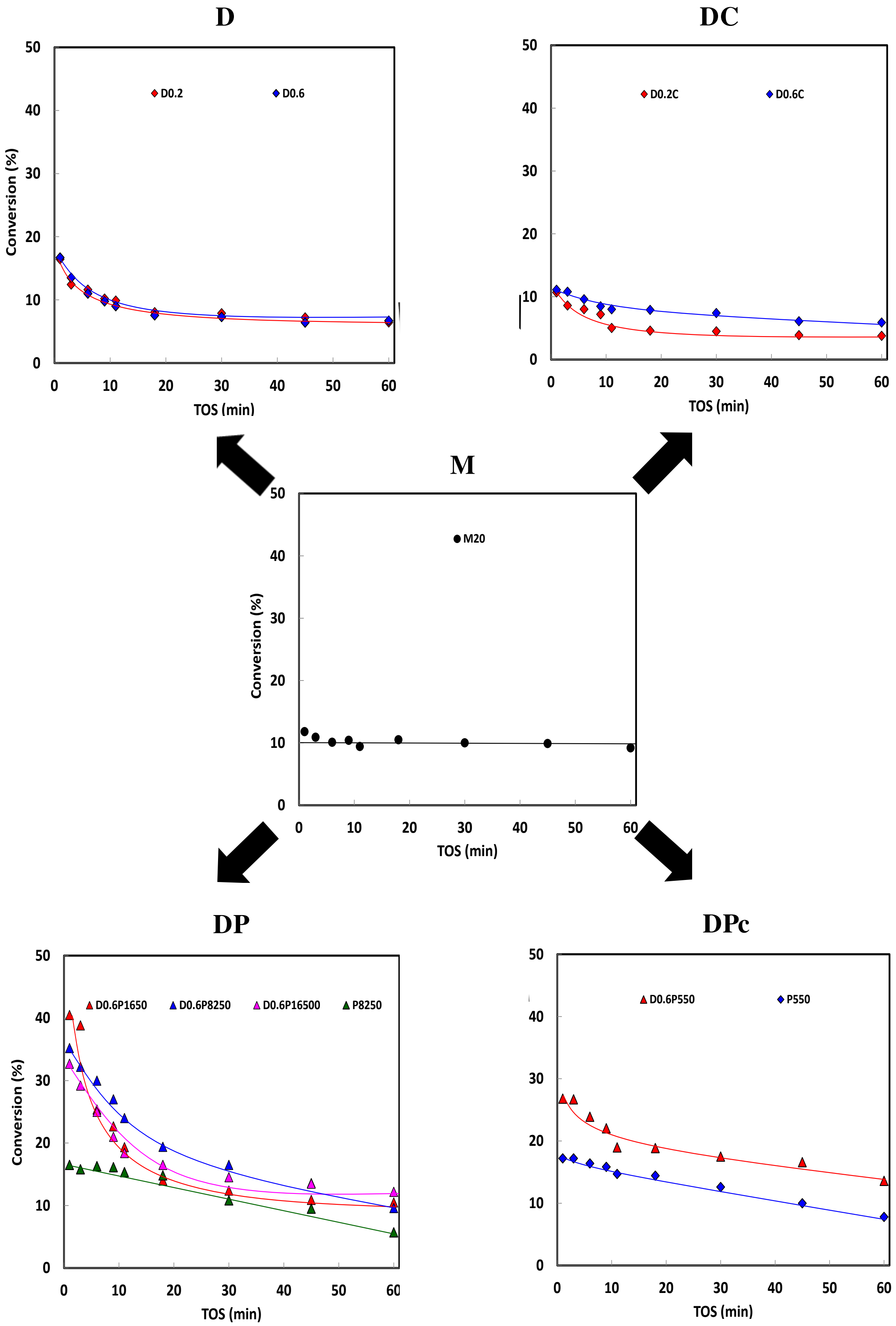

Figure III.7. Conversion of *n*-hexane cracking at 540 °C as a function of time-on-stream obtained on the parent mordenite (M20) and on the four modified series.

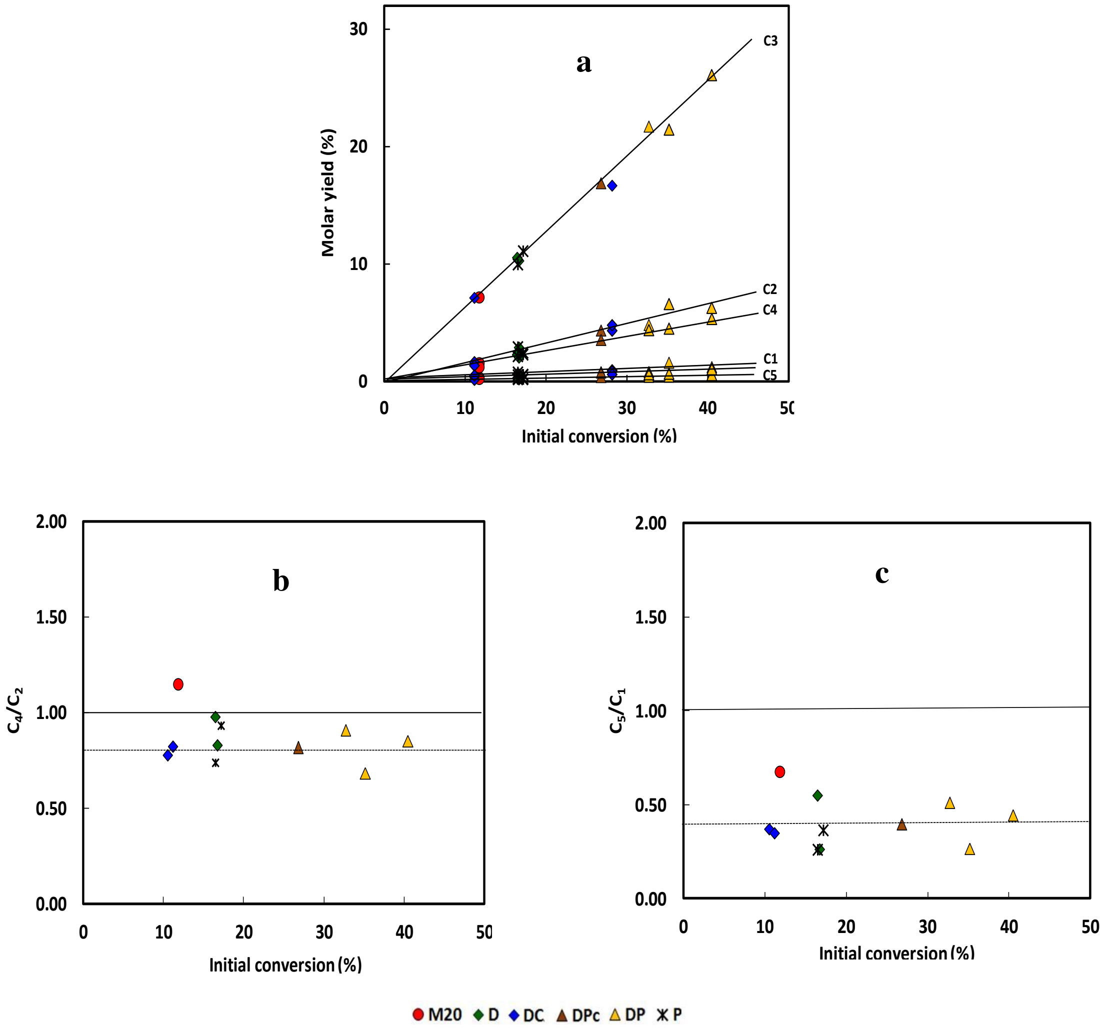

Figure III.8. Molar yields (a), C_4/C_2 (b) and C_5/C_1 (b) ratio as a function of the initial conversion of *n*-hexane cracking for all catalysts.

Yet, the presence of these "super-acid" sites has been contested by Iglesia and co-workers, [30] who suggested that the apparent increased BAS strength would not result from electronic interactions with EFAL species, but rather from a higher solvation effect of the zeolite voids attributable to the occlusion of the void space by extra-framework Al residues. This reasoning is questionable through comparing the TOF values of *n*-hexane cracking obtained by MFI and MOR zeolites, which are present identical void size (see above). The pyridine pre-adsorption followed by alkaline treatment allows a huge improvement of the catalyst activity (by 2-3 times) and in TOF (4-5 times), (Table III.4). As the initial conversion is higher (> 30%), a higher amount of olefins are formed, which lead to catalyst deactivation (Figure III.7). Yet, the coke content remains limited (1.8-2.8 wt.%) in spite of large amount of external silanol and featuring C_1, C_2, C_3 as main cracking product (monomolecular mechanism) and C_4 and C_5 are still formed in strictly parallel reactions (Figure III.8a). A low coke content as well as monomolecular mechanism implies a fast diffusion of olefins, thanks to the improved textural properties generated during of alkaline treatment of pyridine pre-absorbed samples. Thus, the presence of EFAL species combined with shortening of the diffusion path length allows to improve both the catalyst activity and stability.

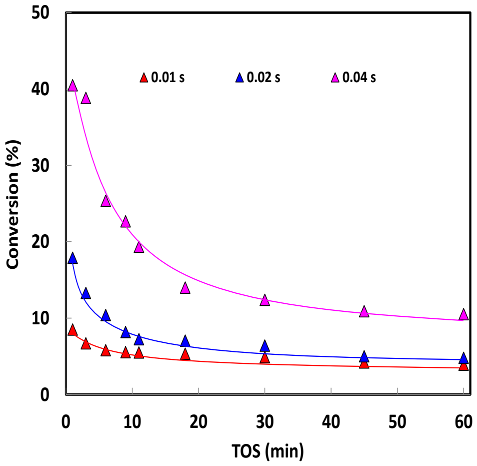

Figure III.9. Conversion as a function of time-on-stream obtained at different contact time (0.01, 0.02, and 0.04 s) on $D_{0.6}P_{1650}$.

4.2 Toluene disproportionation

The disproportionation of toluene is a suitable test reaction for characterizing the micropore structure of the zeolite.[31] The toluene disproportionation yields a mixture of benzene and xylene. The initial molar ratio of xylenes to benzene is significantly lower than unity (*i.e.* 0.2, Table III.5). Benzene, which is smaller, diffuses faster and its desorption is favored, while a large part of the xylenes remains trapped in the micropores and then converted into coke (Table III.5 and Figure III.10), which causes the deactivation of the catalyst (Figure III.11).[15] 1 wt.% of coke is sufficient to completely deactivate the catalyst, which means that the coking mode occurs by pore blocking. Despite the decrease of the concentration of protonic sites, a positive effect of alkaline treatment, more pronounced in presence of pyridine, is observed. As for *n*-hexane cracking, the increase of the TOF value (by 2.5 times) could be due to the presence of EFAL species and a higher coking resistance (4.3 wt.%) to the downsizing of the diffusion path length.

Table III.5. Initial activity (A_0), turnover frequency of acid site probed by pyridine at 150 °C (TOF), residual activity after 1 h reaction (A_{60}/A_0), and coke content for toluene disproportionation measured by elemental analysis. X/B molar ratio corresponds to the xylenes/benzene ratio.

Series	**Catalyst**	**A_0 mmol h^{-1} g^{-1}**	**TOF h^{-1}**	**X/B mol/mol**	**A_{60}/A_0**	**Coke (%)**
M	**M20**	51	92	0.34	0.20	1.0
D	**$D_{0.2}$**	85	173	0.13	0.21	2.0
	$D_{0.6}$	54	167	0.18	0.15	1.1
DC	**$D_{0.2}C$**	93	175	0.18	0.19	1.7
	$D_{0.6}C$	49	149	0.30	0.16	2.0
DPc	**$D_{0.6}$ P_{550}**	56	173	0.15	0.25	2.3
DP	**$D_{0.6}$ P_{1650}**	94	249	0.20	0.16	4.3
	$D_{0.6}$ P_{8250}	83	276	0.22	0.13	-
	$D_{0.6}$ P_{16500}	81	258	0.22	0.11	2.0
P	**P_{8250}**	71	210	0.20	0.07	1.5
	P_{550}	56	151	0.21	0.34	1.4

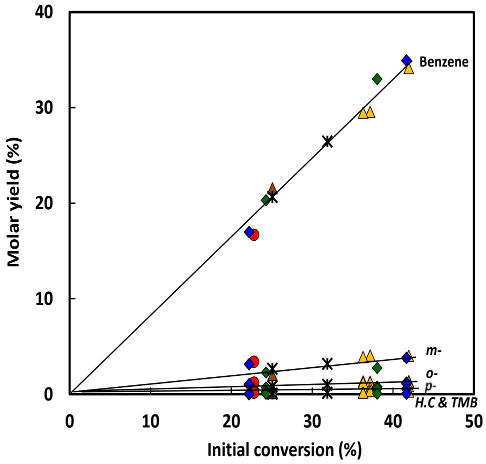

Figure III.10. Molar yields as a function of initial conversion of toluene disproportionation for M20 (red symbol), blank materials (black) and four catalyst series: D (green), DC (blue), DPc (brown) and (DP (yellow).

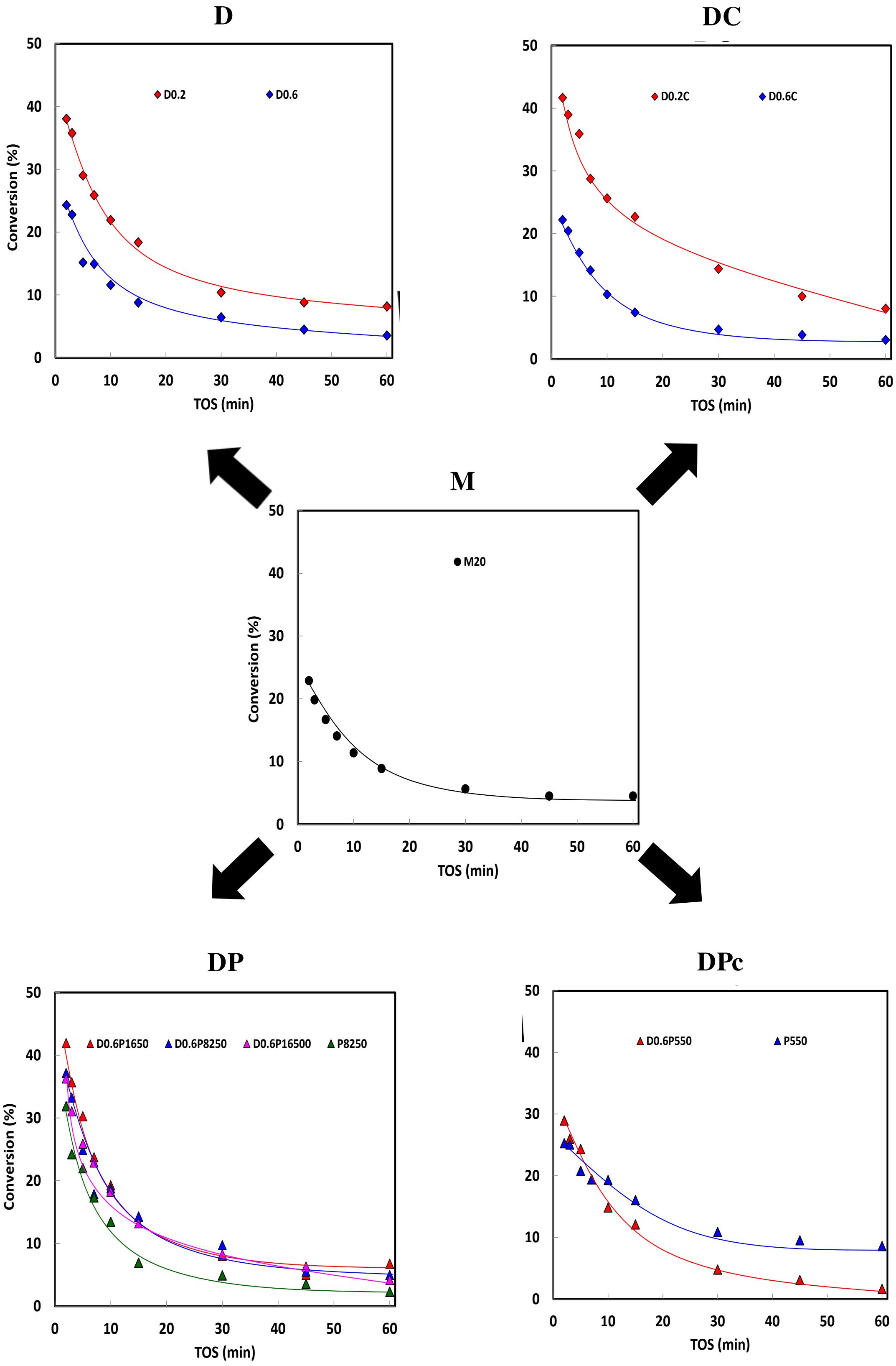

Figure III.11. Conversion of toluene disproportionation as a function of time-on-stream on M20 and the four modified catalysts series.

4.3 Coke formation

The impact of alkaline treatment in the presence or absence of pyridine on coke formation was determined through the mass uptake during the transformation of propene at 350 °C (Table III.6). On the parent zeolite, the coke uptake increases rapidly and reaches 8 wt.% after 2 h (Figure III.12). Despite the decrease in acidity after desilication, the initial coking rate (derivative of the coke uptake curve) is twice as high. The higher coking rate can be ascribed to an increase in strength of the protonic sites due to their interaction with the Lewis acid EFAL species. Indeed, the effect of acidity on the rate of propene transformation into coke was determined at 350 °C over a series of H-FAU(Y) zeolites with different framework Si/Al ratios.[25] For dealuminated samples (Si/Al from 16 to 100) the coking rate was roughly proportional to the concentration of the protonic sites, which can be related to the similarity in strength of the isolated sites of these zeolites. The slightly greater TOF value found for the most dealuminated sample was ascribed to an increase in strength of its protonic sites due to their interaction with Lewis acid EFAL species. As far as the amount of coke uptake after 10 h is concerned, it depends rather on the textural properties of the achieved materials. The presence of mesopores (Table III.3) favor the accumulation (and retention) of carbonaceous compounds.[16, 31-32]

Table III.6. Coke uptake resulting of the propene transformation at 350 °C on the parent zeolite and the four catalysts (initial coking rate and content after 10 h reaction time).

Series	Catalyst	Rate h^{-1}	Coke %
M	**M20**	71	8.6
D	**D$_{0.6}$**	143	12.6
DC	**D$_{0.6}$C**	139	12.4
DP	**D$_{0.6}$ P$_{1650}$**	157	11.2
	D$_{0.6}$ P$_{8250}$	150	11.1
DPc	**D$_{0.6}$ P$_{550}$**	126	10.6

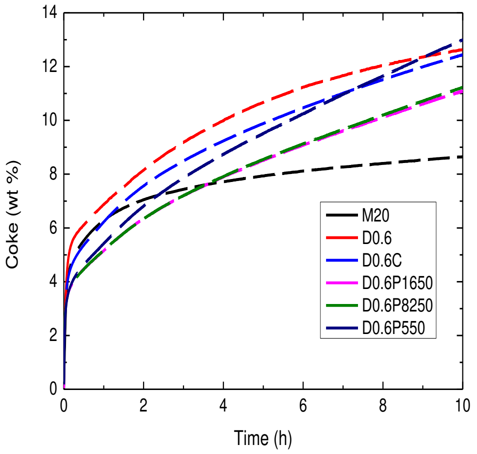

Figure III.12. Coke uptake resulting from propene transformation at 350 °C on the parentzeolite and the four catalyst series: D, DC, DP and DPc.

5. Conclusion

Several agents have been added to alkaline desilication solutions with the aim to tailor, direct and/or protect zeolites during the treatment. In this chapter we have proven that adding pyridine during alkaline treatment importantly modifies the classical desilication scheme. Pyridine allows to direct the desilication of mordenites, through its interaction with external hydroxides, which amount increases important by increasing the portion of pyridine during treatment. This hence allows to selectively direct desilication towards the achievement of small zeolite particles, which diffraction efficiency is insufficient to be detected by XRD. Pyridine remains present in the zeolite structure throughout the treatment and hence in the as-synthetized materials. During the calcination step the decomposition of the amine leads to dealumination and hence to the formation of internal EFAL. It has been found that both of these features importantly impact of the catalytic properties in *n*-hexane cracking, toluene dispropoartination and in the propene transformation. Whilst the reduction of the particle size allows for reducing diffusion path length the presence of EFAL leads to an exaltation of acidity yielding to superior activities in all the studied reactions.

Bibliographic references

[1] R. Chal, C. Gérardin, M. Bulut, S. van Donk, Overview and industrial assessment of synthesis strategies towards zeolites with mesopores, ChemCatChem 3 (2011) 67–81.

[2] J. C. Groen, T. Sano, J. A. Moulijn, J. Perez-Ramirez, Alkaline-mediated mesoporous mordenite zeolites for acid-catalyzed conversions, J. Catal. 251 (2007) 21–27.

[3] C. Bertrand-Drira, X. -W. Cheng, T. Cacciaguerra, P. Trens, G. Melinte, O. Ersen, D. Minoux, A. Finiels, F. Fajula, C. Gerardin, Mesoporous mordenites obtained by desilication: Mechanistic considerations and evaluation in catalytic oligomerization of pentene. Microporous Mesoporous Mater. 213 (2015) 142–149.

[4] N. Chaouati, A. Soualah, I. Hussein, J. -D. Comparot, L. Pinard, Effect of Brønsted acidity of HY zeolites in adsorption of methylene blue and comparative study with bentonite, Appl. Catal., A 256 (2016) 95–104.

[5] S. Stefanidis, K. Kalogiannis, E. F. Iliopoulou, A. A. Lappas, J. Martínez Triguero, M. T. Navarro, A. Chica, F. Rey, Mesopore-modified mordenites as catalysts for catalytic pyrolysis of biomass and cracking of vacuum gasoil processes Green Chem. 15 (2013) 1647–1658.

[6] D. Wang, L. Zhang, L. Chen, H. Wu, P. Wu, Postsynthesis of mesoporous ZSM-5 zeolite by piperidine-assisted desilication and its superior catalytic properties in hydrocarbon cracking, J. Mater. Chem. A 3 (2015) 3511–3521.

[7] A. Sachse, J. Garcia Martinez, Surfactant-templating of zeolites: From design to application, Chem. Mater. 29 (2017) 3827–3853.

[8] I. Batonneau-Gener, A. Sachse, Determination of the exact microporous volume and BET surface area in hierarchical ZSM-5, J. Phys. Chem. C 123 (2019) 4235–4242.

[9] B. D. Hall, D. Zanchet, D. Ugarte, Estimating nanoparticle size from diffraction measurements, J. Appl. Crystallogr. 33 (2000) 1335–1341.

[10] I. I. Ivanova, E. E. Knyazeva, Micro–mesoporous materials obtained by zeolite recrystallization: Synthesis, characterization and catalytic applications, Chem. Soc. Rev. 42 (2013) 3671–3688.

[11] I. I. Ivanova, I. A. Kasyanov, A. A. Maerle, V. I. Zaikovskii, Mechanistic study of zeolites recrystallization into micro-mesoporous materials, Microporous Mesoporous Mater. 189 (2014) 163–172.

[12] I. A. Kasyanov, A. A. Maerle, I. I. Ivanova, V. I. Zaikovskii, Towards understanding of the mechanism of stepwise zeolite recrystallization into micro/mesoporous materials, J. Mater. Chem. A 2 (2014) 16978–16988.

[13] K. Yamagishi, S. Namba, T. Yashima, Defect sites in highly siliceous HZSM-5 zeolites: a study performed by alumination and IR spectroscopy, J. Phys. Chem. 95-2 (1991) 872–877.

[14] R. M. Barrer, M. B. Maki, Molecular sieve sorbents from clinoptilolite, Can. J. Chem. 42 (1964) 1481–1487.

[15] H. Issa, J. Toufaily, T. Hamieh, J. -D. Comparot, A. Sachse, L. Pinard, Mordenite etching in pyridine: Textural and chemical properties rationalized by toluene disproportionation and *n*-hexane cracking, J. Catal. Accepted (2019).

[16] M. -C Silaghi, C. Chizallet, P. Raybaud, Challenges on molecular aspects of dealumination and desilication of zeolites, Microporous Mesoporous Mater. 191 (2014) 82–96.

[17] D. L. Bhering, A. Ramirez-Solis, C. J. A. Mota, A density functional theory based approach to extraframework aluminum species in zeolites, J. Phys. Chem. B 107 (2003) 4342–4347.

[18] Z. Qin, B. Shen, Z. Yu, F. Deng, L. Zhao, S. Zhou, D. Yuan, X. Gao, B. Wang, H. Zhao, H. Liu, A defect-based strategy for the preparation of mesoporous zeolite Y for high-performance catalytic cracking, J. Catal. 298 (2013) 102–111.

[19] M. S. Holm, S. Svelle, F. Joensen, P. Beato, C. H. Christensen, S. Bordiga, M. Bjørgen, Assessing the acid properties of desilicated ZSM-5 by FT-IR using CO and 2, 4, 6-trimethylpyridine (collidine) as molecular probes, Appl. Catal., A 356 (2009) 23–30.

[20] W. Lutz, C. H. Rüscher, D. Heidemann, Determination of the framework and non-framework [SiO_2] and [AlO_2] species of steamed and leached faujasite type zeolites: Calibration of IR, NMR, and XRD data by chemical methods, Microporous Mesoporous Mater. 55 (2002) 193–202.

[21] W. Lutz, R. Bertram, D. Heidemann, R. Kurzhals, C. Rüscher, G. Kryukosa, Z. Anorg, Reactivity of extra-framework species of USY zeolites in alkaline medium, Allg. Chem. 637 (2011) 75–82.

[22] M. Stockenhuber, J. A. Lercher, Characterization and removal of extra lattice species in faujasites, Microporous Mater. 3 (1995) 457–465.

[23] C. V. Mc Daniel, P. K. Maher, Molecular Sieves, in: Society of chemical Industry, R. M. Barrer (Ed.), London, 1968, 186–195.

[24] C. Miranda, J. Urresta, H. Cruchade, A. Tran, M. Bengahlem, A. Astafan, P. Gaudin, T. J. Daou, A. Ramírez, Y. Pouilloux, A. Sachse, L. Pinard, Exploring the impact of zeolite porous voids in liquid phase reactions: The case of glycerol etherification by tert-butyl alcohol, J. Catal. 365 (2018) 249–260.

[25] N. Chaouati, A. Soualah, M. Chater, L. Pinard, Beneficial changes in coke properties with alkaline treatment on aluminum-rich mordenite, J. Catal. 353 (2017) 28–36.

[26] N. Chaouati, A. Soualah, M. Chater, M. Tarighi, L. Pinard, Mechanisms of coke growth on mordenite zeolite, J. Catal. 344 (2016) 354–364.

[27] J. H. Lunsford, Surface interactions of NaY and decationated Y zeolites with nitric oxide as determined by electron paramagnetic resonance spectroscopy, J. Phys. Chem. 72 (1968) 4163–4168.

[28] J. Abbot, Cracking reactions of C6 paraffins on HZSM-5, Appl. Catal. 57 (1990) 105–125.

[29] V. L. Zholobenko, L. M. Kustov, L. E. Kazansky, U. Lohse, G. Oehlmann, On the nature of the sites responsible for the enhancement of the cracking activity of HZSM-5 zeolites dealuminated under mild steaming conditions: Part 2, Zeolites 11 (1991) 132–134.

[30] R. Gounder, A. J. Jones, R. T. Carr, E. Iglesia, Solvation and acid strength effects on catalysis by faujasite zeolites, J. Catal. 286 (2012) 214–223.

[31] M. Guisnet, L. Pinard, Characterization of acid-base catalysts through model reactions, Catal. Rev. 60 (2018) 337–436.

[32] F. Ngoye, L. Lakiss, Z. Qin, S. Laforge, C. Canaff, M. Tarighi, V. Valtchev, K. Thomas, A. Vicente, J. -P. Gilson, Y. Pouilloux, C. Fernandez, L. Pinard, Mitigating coking during methylcyclohexane transformation on HZSM-5 zeolites with additional porosity, J. Catal. 320 (2014) 118–126.

[33] M. Bjørgen, F. Joensen, M. S. Holm, U. Olsbye, K. P. Lillerud, S. Svelle, Methanol to gasoline over zeolite H-ZSM-5: Improved catalyst performance by treatment with NaOH, Appl. Catal., A 345 (2008) 43–50.

Chapter IV: Mordenite etching in pyridine: textural and chemical properties rationalized by toluene disproportionation and *n*-hexane cracking

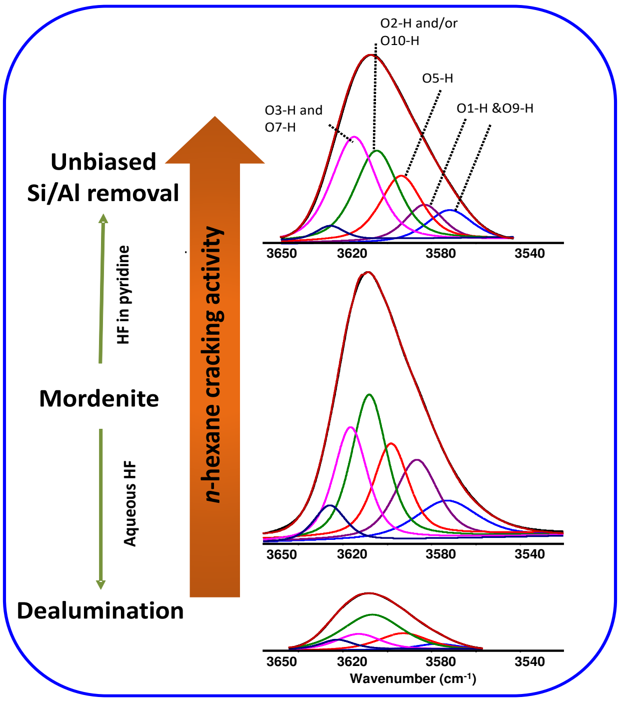

Based on publication accepted in the Journal of Catalysis

374, 409-421, 2019

Hussein Issa, Joumana Toufaily, Tayssir Hamieh, Jean Dominique Comparot,

Alexander Sachse, Ludovic Pinard

1. Introduction

As already stated in the previous chapter, the by far most simple and cost efficient hierarchization strategy is based on demetallation, which allows for the development of secondary, intracrystalline porosity.[1] These approaches rely on the removal of silicon and aluminium species from the zeolite framework, resulting in the formation of cavities. An extensive set of data has been published on the development and the fine tuning of such dealumination and desilication methods.[2]

The dealumination of mordenite through treatments with nitric acid solutions has revealed that the microporosity of materials increase, probably through an enlargement of the 8-MR side pockets.[3] Semagina and co-workers furthermore evidenced that despite of loss of crystallinity microporosity increases, due to selective removal of Al form T3 and T4 sites through acid treatment.[4] The development of microporosity upon dealumination has further been evidenced through computational simulations.[5]

Among the various dealumination strategies the etching of zeolites through aqueous HF solutions has firstly been described by Ghosh and Kydd.[6] Though not particularly devoted to the textural properties, the authors observed a substantial decrease in the BET surface area with increasing HF concentration, which can be related to the reduction of microporosity and crystallinity. Treatments of zeolites with aqueous HF solutions led to a preferential extraction of aluminium from the zeolite framework and hence to a substantial decrease in Brønsted acidity with important consequences on the catalytic performance.[7] Valtchev and co-workers pointed out that the HF etching process in aqueous solution can be tailored towards the biased removal of Si and Al from the zeolite framework, by altering the HF ionization equilibrium in water through the addition of NH_4F.[8]

Zeolite post-treatments result in both modifications of acid and textural properties. In this chapter we aimed at quantifying the actual gain provided through textural modification on the catalytic performances. Therefore, hierarchical catalysts were compared to a series of sodium exchanged catalyst, for which only the concentration of acidic sites varies. A new mordenite etching procedure has further been developed, which relies on the use of a pyridinic HF solution. The idea behind the use of pyridine as medium was motivated by the possibility to directing the post-synthetic treatment through impacting the HF dissociation equilibria. Additionally, HF in pyridine is a safer form to handle hydrogen fluoride as it is much less volatile. Materials obtained through this innovative strategy were compared to samples achieved by the classically strategy (*i.e.* etching with aqueous HF) in terms of textural and chemical properties.

2. Experimental section

Three different series of mordenite were compared in the present work using M10 as a parent protonic mordenite (Si/Al = 9) supplied by Süd Chemie;

1. Na$_x$: mordenite with a degree of Na exchange of 23%, 56%, 68%, and 83% (x represents the percentage of exchanged protons);
2. F$_x$: chemical etching of M10 by HF in aqueous solution (x indicates the molar concentration of HF).
3. PyF$_x$: chemical etching of M10 by HF in pyridine solution (x indicates the molar concentration of HF).

Table IV.1. Operating conditions for the three post-synthesis modifications.

Catalyst	**Medium**	**[Na]**	**[HF]**	**Time**	**T**	**Yield**
		µmol g^{-1}$_{zeolite}$	**M**		**°C**	**%**
Na$_{23\%}$	H_2O	504		16 h	80	93
Na$_{56\%}$	H_2O	7200		16 h	80	95
Na$_{68\%}$	H_2O	18000		16 h	80	91
Na$_{83\%}$	H_2O	36000		16 h	80	92
F$_{0.25}$	H_2O		0.25	6 min	25	83
F$_{0.50}$	H_2O		0.50	6 min	25	85
F$_{1.50}$	H_2O		1.50	6 min	25	45
PyF$_{0.25}$	Pyridine		0.25	6 min	25	80
PyF$_{0.50}$	Pyridine		0.50	6 min	25	78
PyF$_{1.50}$	Pyridine		1.50	6 min	25	51

[a] *Calculated from the weight difference before and after post-treatment.*

The synthesis conditions and the obtained yields of each treatment are summarized in supporting information (Table IV.1). The Na$_x$ series was obtained by cationic exchange of M10 in $NaNO_3$ aqueous solutions of different concentrations at 80 °C for 16 h under mechanical stirring (400 rpm), followed by static drying for 12 h at 110 °C. Mordenite etching was carried out through the use of an aqueous HF solution and a solution of HF in pyridine. In a 100 mL Teflon vessel were placed 1 g of the parent mordenite (M10). 20 mL of the HF solution of different concentrations (0.25, 0.50, and 1.50 M) was added at 25 °C for 6 min under mechanical stirring (500 rpm). Thereafter the zeolite suspensions were centrifuged at 6000 rpm for 10 min. The residue was washed with 40 mL demineralized water. Washing cycles were performed until neutral pH. Solids were dried at 100 °C for 12 h and calcined under air flow (100 ml min^{-1} per 1 g of zeolite) at 550 °C for 8 h.

3. Results and discussion

Tables IV.2 and IV.3 summarize the textural and acidic properties of the parent mordenite (M10) and of the three catalyst series resulting from the different post-treatments, *i.e.* Na exchange (Na), HF etching in aqueous (F), and pyridine (PyF) medium**.**

Table IV.2. Textural properties of the three catalyst series: Na_x, F_x, and PyF_x.

Catalyst	**Crystallinity (%)**	**CCS^b (nm)**	**Strain^c**	**V_{micro}^{d}**	**V_{meso}^{e}**	**V_{macro}^{f}**
				cm^3 g^{-1}		
M_{10}	100	62.8	8.8	0.19	0.09	0.35
$Na_{23\%}$				0.18	0.09	
$Na_{56\%}$				0.18	0.08	
$Na_{68\%}$				0.16	0.10	
$Na_{83\%}$				0.15	0.10	
$F_{0.25}$	70	39.0	14.7	0.17	0.08	
$F_{0.50}$	65	36.8	16.4	0.17	0.09	0.37
$F_{1.50}$	57	32.0	19.4	0.18	0.13	0.44
$PyF_{0.25}$	80	57.1	9.3	0.19	0.08	
$PyF_{0.50}$	84	57.3	9.3	0.16	0.12	0.41
$PyF_{1.50}$	79	55.0	9.7	0.18	0.15	0.47

^{a} Measured by XRD analysis; $^{b,\ c}$ Coherent crystal size and strain estimated by Williamson-Hall analysis; ^{d} Estimated by the t-plot method; ^{e} Mesopore volume = V_{total} - V_{micro} (V_{total}: determined from the adsorbed volume at P/P_0= 0.96); ^{g} Calculated from mercury porosimetry.

Table IV.3. Elemental analysis and acid properties of three catalyst series: exchanged with Na (Na$_x$) and etched with HF in aqueous (F) and pyridine (PyF) medium.

Catalyst	**Si/Al**[a]	**[Na]**[a]	**[F]**[b]	**[PyH$^+$]**[c]	**[PyL]**[c]	**[PyH$^+$] +2[PyL]**
	mol/mol	**µmol g^{-1}**				
M$_{10}$	9.0	0		1014 (1370)[d]	53	1120
Na$_{23\%}$	8.7	330		950	39	1028
Na$_{56\%}$	8.6	790		648	28	704
Na$_{68\%}$	8.8	950		425	15	455
Na$_{83\%}$	9.0	1130		201	14	229
F$_{0.25}$	10.9	0		570	130	830
F$_{0.50}$	12.1	0		560	143	846
F$_{1.50}$	17.5	0		410	106	622
PyF$_{0.25}$	8.6	0		740	96	932
PyF$_{0.50}$	8.5	0		700	119	938
PyF$_{1.50}$	9.0	0	0	820	127	1074

[a] Measured by ICP; [b] Measured by XRF; [c] Measured by pyridine adsorbed at 150°C, [d] theoretical acidity.

3.1 Textural and acidic properties of the parent zeolite (M10)

M10 is composed out of smaller crystals (approximately 100 nm in length inferred from TEM images) with an important degree of agglomeration (Figure IV.1a-c). By applying Williamson-Hall analysis to its XRD pattern (Figure IV.2) the CCS and the lattice strain were quantified (Table IV.2) and are 62.8 nm and 8.8, respectively. M10 can be considered as an aggregate of highly agglomerated nanocrystals. The intracrystalline space between nanocrystals yields to an inter-granular macroporous volume of 0.35 cm^3 g^{-1} (Table IV.2). The nitrogen adsorption isotherm at -196 °C is of type I as expected for a microporous material and a microporous volume of 0.19 cm^3 g^{-1} was calculated. (Figure IV.3)

The hydroxyl stretching vibration region of IR spectra before (dotted line) and after (green line) adsorption of pyridine at 150 °C is given in Figure IV.4. MOR exhibits an intense band, slightly asymmetric, at 3608 cm^{-1}, which can be assigned to the bridging hydroxyl groups (*i.e.* acidic hydroxyl groups) and less intensive bands at 3745, 3733, and 3655 cm^{-1} due to stretching vibrations of external and internal silanols Si-OH, and OH linked to EFAL, respectively.

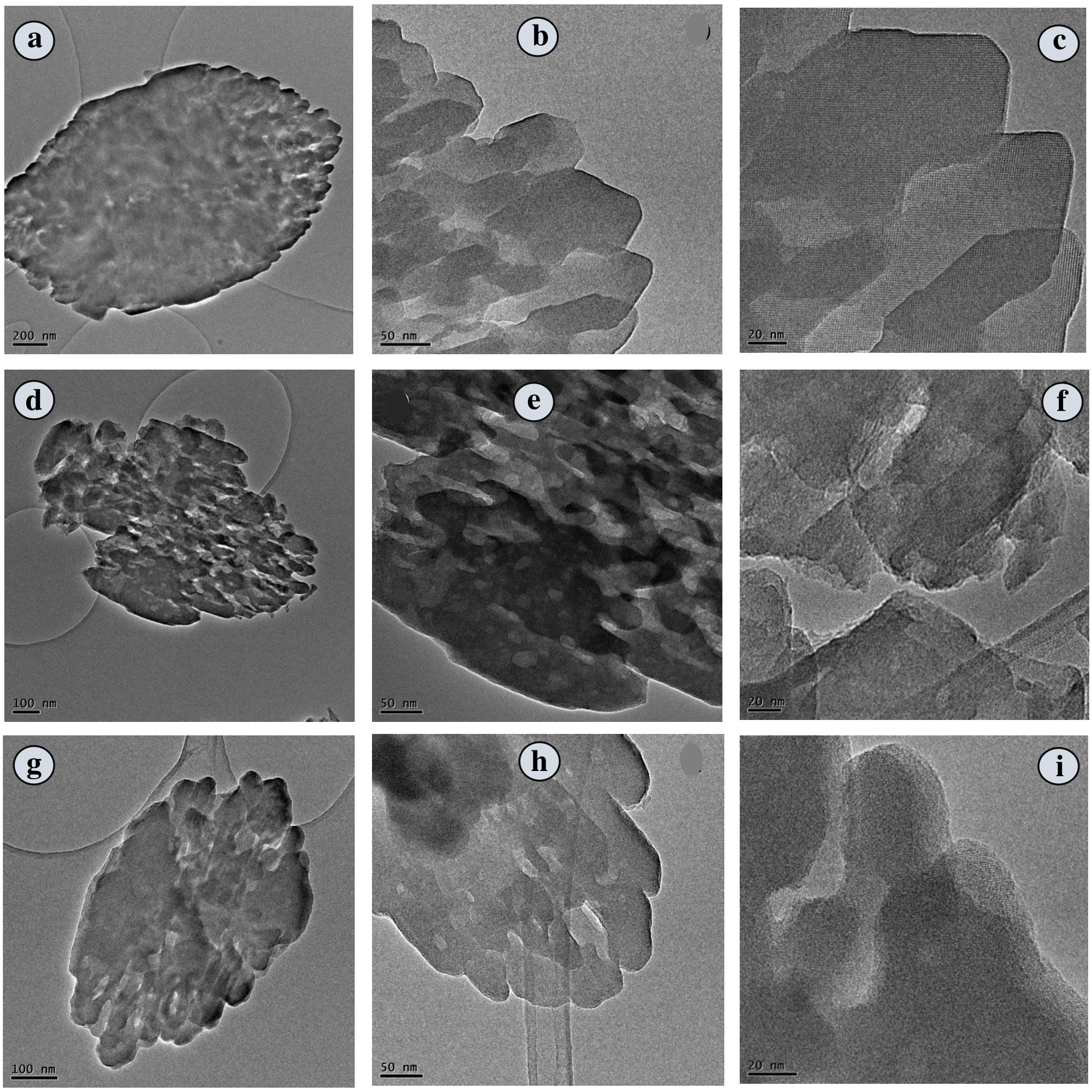

Figure IV.1. TEM images of M10 (a, b, and c), $F_{1.5}$ (d, e, and f), and $PyF_{1.5}$ (g, h, and i).

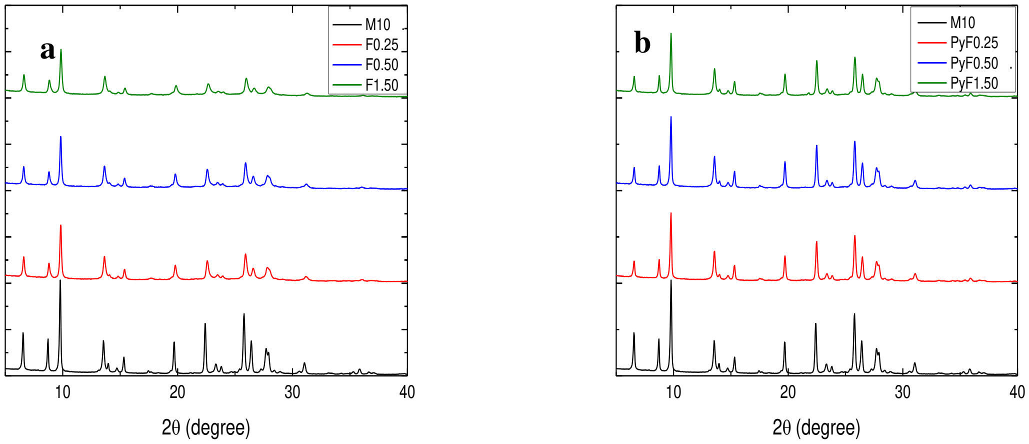

Figure IV.2. XRD patterns of F_x (a) and PyF_x (b) samples.

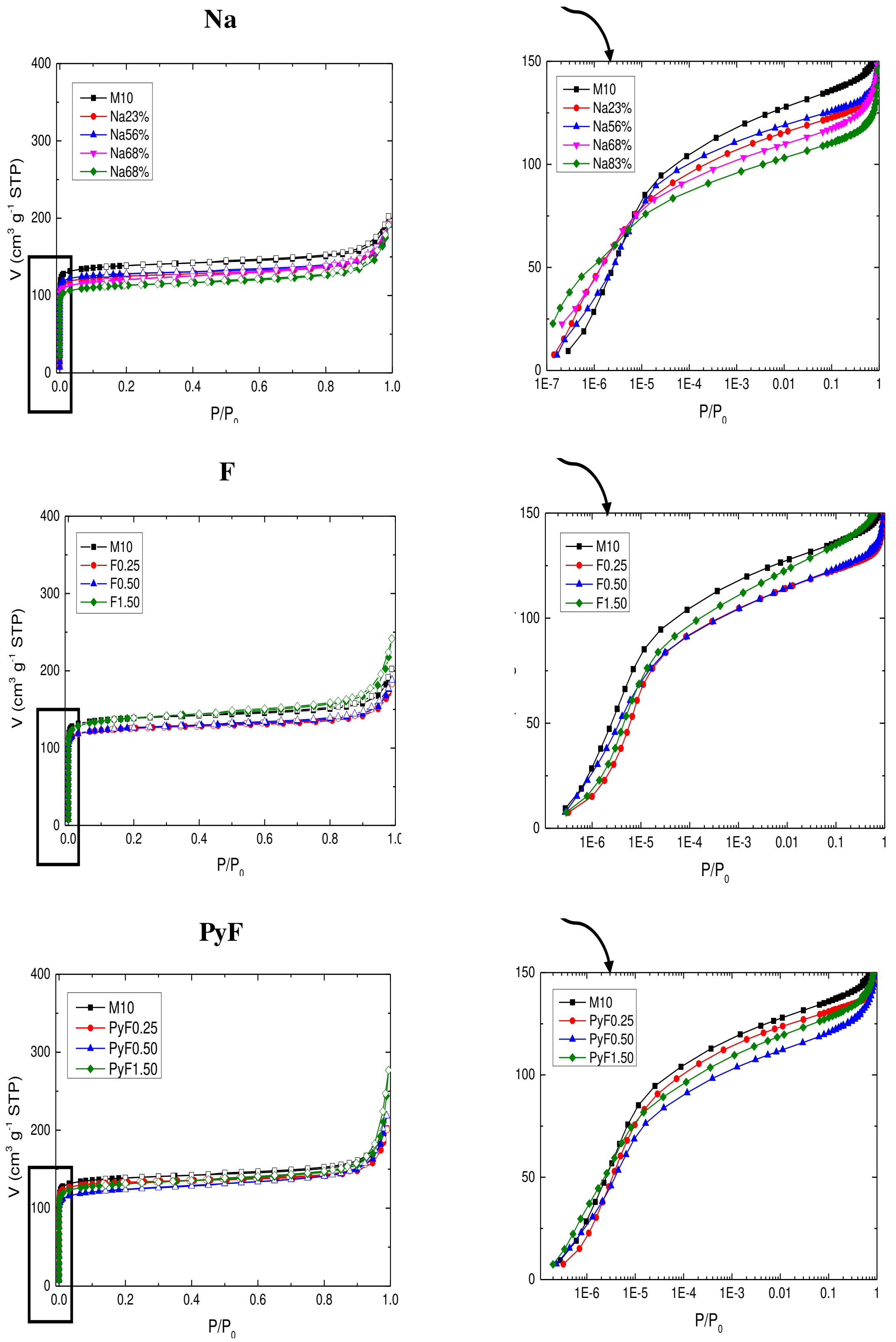

Figure IV.3. Nitrogen adsorption (full symbol) and desorption (open symbol) isotherms at -196 °C of Na, F_x, and PyF_x samples.

The adsorption of pyridine at 150 °C leads to a partial decrease of the intensity of the 3608 cm^{-1} band associated with a 20 cm^{-1} shift towards lower wavenumber. The thermodesorption of pyridine from 150 °C to 450 °C permits to observe the opposite effect, *i.e.* a shift of the position of the band maximum toward higher wavenumbers (3588 to 3605 cm^{-1}). The incomplete neutralization of bridged OH groups by pyridine is due to a set of inaccessible OH groups located within the 8-MR side pockets. Indeed, the number of BAS probed by pyridine is 1014 µmol g^{-1}, while the theoretical value calculated from the elemental analysis amounts to 1370 µmol g^{-1} (Table IV.3). Hence, 24% of the BAS are located in side pockets, this value is slightly higher than that drawn from the ratio between the areas of OH band before and after pyridine adsorption, *i.e.* 19%.

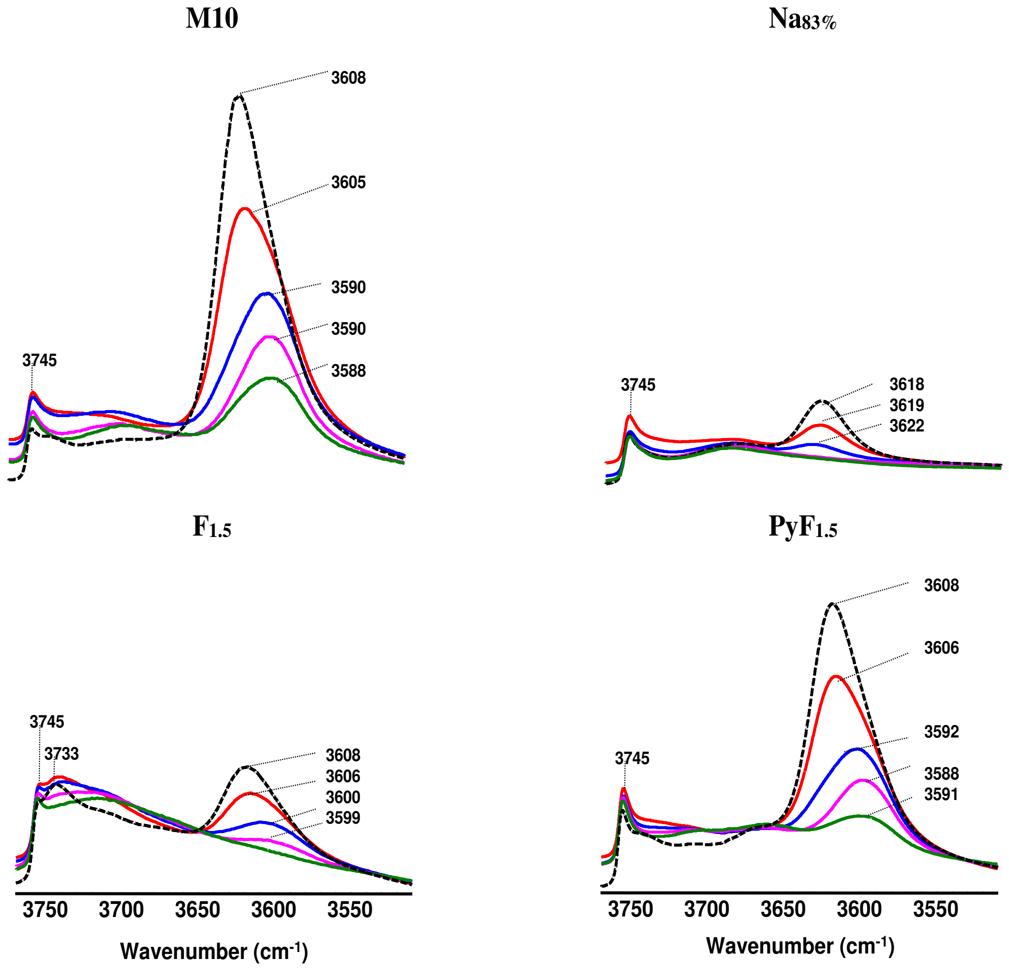

Figure IV.4. Infrared spectra in OH vibration region for selected F_x, Na_x, and PyF_x samples before (dotted line) and after pyridine adsorption followed by desorption at 150 °C (green line), 250 °C (purple) 350 °C (blue), and 450 °C (red). All spectra have the same scale.

3.2 Influence of the Na exchange on the physical properties of mordernite (Na_x series)

The shape of the isotherm is equal for the Na-exchanged samples as to the parent M10, yet the microporous volume decreases with increasing amount of Na-exchange and reaches 0.15 $cm^3\,g^{-1}$ for the $Na_{83\%}$ sample (Figure IV.3).

For sodium exchanged samples a decrease in the intensity of the stretching band of bridged OH groups as well as a shift to higher frequencies up to +10 cm^{-1} (for $Na_{83\%}$) was observed. As expected, the OH bands associated with internal and external silanol defects are not affected by sodium exchange. For $Na_{83\%}$ the adsorption of pyridine at 150 °C neutralizes all the acidic OH and its thermal desorption leads to the development of a peak, which maximum is centered at 3622 cm^{-1} (Figure IV.4). Indeed, the theoretical acidity drawn from the elemental analysis and the number of BAS probed by pyridine becomes identical starting from a degree of exchange of 23%. Hence, starting from this exchange degree the great majority of acid sites are located within the 12-MR channels (Figure IV.5). On the most exchanged mordenite zeolites: $Na_{68\%}$ and $Na_{83\%}$, the sum of Na content measured by ICP and that of H^+ by pyridine corresponds almost accurately to the Al content, which means that the amount of extraframework species is very low. Indeed, Lewis acidity amounts to less than 15 µmol g^{-1} (Table IV.2).

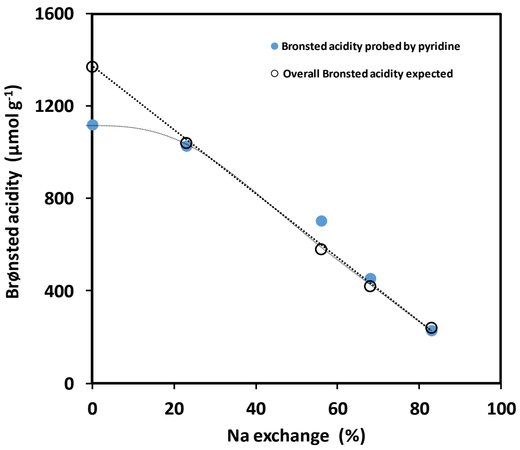

Figure IV.5. Amounts of Brønsted acid sites estimated from chemical analysis (overall acidity) and from pyridine adsorption (sites accessible) as function of degree of Na-exchange.

The shifting of the position of the maxima of the adsorption bands reveal the existence of at least three components (3588, 3608, and 3622 cm^{-1}), contributing to the asymmetry of the band of bridged OH groups. Differentiation between BAS in mordenites has been proposed in a number of spectroscopy studies with defined amounts of BAS varying from 2,[9-16] 3,[17] and 6.[18] According to Lukyanov *et al.*,[18] six distinct bands can be visualized by six single bands in Fourier self-deconvolution traces of the IR spectra. The assignment of the OH bands is linked to seven distinct crystallographic oxygen atoms (Scheme IV.1):

- 3581 and 3590 cm^{-1}: O1-H and O9-H hydroxyls in the small 8-MR channels;
- 3599 cm^{-1}: O5-H hydroxyl in the intersection between side pockets and 12-MR channels;
- 3609 cm^{-1}: O2-H and/or O10-H hydroxyls in the 12-MR channels;
- 3617 and 3625 cm^{-1}: O3-H and O7-H located in the 12-MR channels and linked to Na-exchange position VI.

Likewise, Schlenker *et al.*[19] described three crystallographic positions of Na^+ cations in MOR; *i.e.* I (8-MR channel), IV (intersection between side pockets and 12-MR channels), and VI in the 12-MR channels.

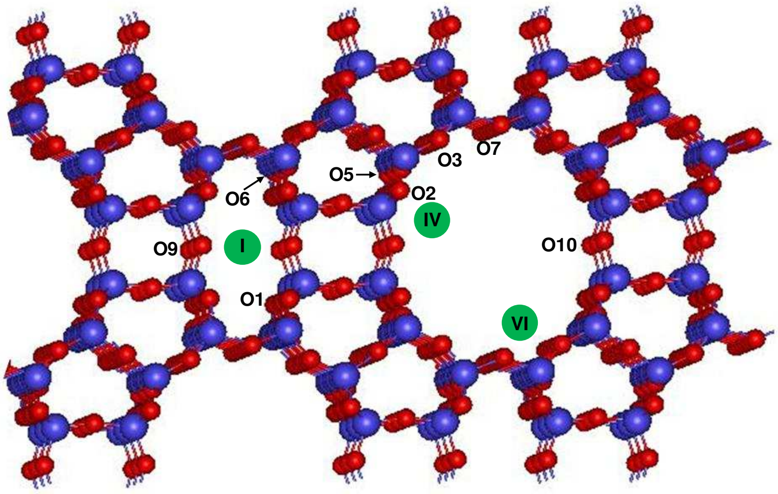

Scheme IV.1. Structure of MOR presented along the 12-MR and 8-MR channels. The positions of the framework O atoms and of the Na^+ are highlighted. (Red: oxygen atoms, blue: T atoms, green: Na^+ cations).

The deconvolution of the hydroxyl region of M10 allows to obtain six band centered at 3626, 3616, 3608, 3598, 3587, and 3573 cm^{-1} (Figure IV.6). From the height of each bands and using their relative extinction coefficient drawn from the reference [18] (Table IV.4), the distribution of BAS on the parent zeolite was calculate to be: ~18% in the 8-MR channels (a value that is slightly lower than that obtained from pyridine adsorption, 23%), ~18% at the intersection between side pockets and 12-MR channels, and ~64% are located within the 12-MR channels. Furthermore, the position of these bands allows to deduce the strength of individual BAS as indicated by Niwa *et al.*[20] As such, bands at higher wavenumbers correspond to “weak” BAS (*i.e.* unconstrained OH), whilst bands centered at lower wavenumbers to "stronger" BAS (*i.e.* constrained OH). Yet, the shift in the relative band position could further be related to a bathochromic effect, which originates from high electrostatic perturbation induced by the small size of the 8-MR channels.[21] Although the BAS on the small 8-MR channel are rapidly exchanged by sodium cations, their exchange is completed only after a 60% exchange degree (Table IV.4).

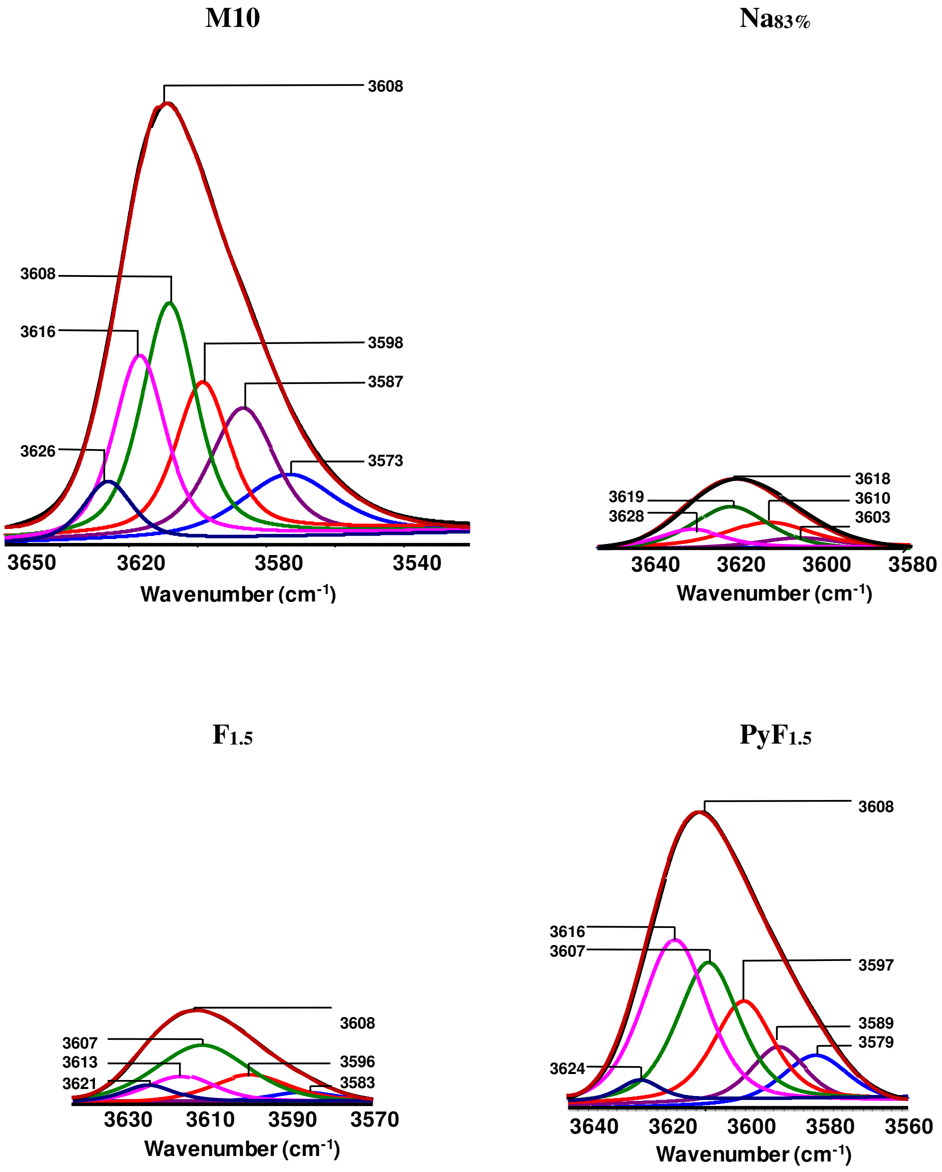

Figure IV.6. Deconvolution of the hydroxyl region of IR spectra of parent mordenite and selected Na_x, F_x, and PyF_x samples using six single bands.

Table IV.4. Height of the six deconvoluted bands of catalyst series: M10, Na_x, F_x, and PyF_x and their percentual distribution in brackets.

	Main channel			Intersection	Side pocket	
Band (cm^{-1})	**3625**	**3617**	**3609**	**3599**	**3590**	**3581**
ε	1	1.14	1.27	1.45	1.63	1.83
M_{10}	0.158	0.40	0.62	0.40	0.31	0.14
	(10.3)	(22.8)	(31.7)	(18.0)	(12.3)	(5.0)
$Na_{23\%}$	0.21	0.47	0.45	0.21	0.21	0.08
	(16.3)	(32.4)	(27.0)	(11.2)	(10.0)	(3.3)
$Na_{56\%}$	0.05	0.26	0.29	0.18	0.11	0.011
	(7.3)	(32.4)	(32.6)	(17.6)	(9.3)	(0.9)
$Na_{68\%}$	0.04	0.19	0.11	0.11	0.04	0
	(10.3)	(42.9)	(21.6)	(18.9)	(6.3)	(0)
$Na_{83\%}$	0.04	0.09	0.05	0.02	0	0
	(21.9)	(45.8)	(23.9)	(8.4)	(0)	(0)
$F_{0.25}$	0.07	0.14	0.15	0.12	0.10	0.04
	(15.2)	(25.6)	(24.6)	(17.1)	(13.1)	(4.5)
$F_{0.50}$	0.027	0.09	0.22	0.14	0.07	0.03
	(6.2)	(18.0)	(40.2)	(22.2)	(9.6)	(3.8)
$F_{1.50}$	0	0.10	0.14	0.13	0	0.08
	(0)	(26.4)	(33.8)	(26.5)	(0)	(13.2)
$PyF_{0.25}$	0.07	0.14	0.34	0.26	0.12	0.1
	(9.3)	(16.1)	(34.5)	(23.6)	(9.4)	(6.9)
$PyF_{0.50}$	0	0.25	0.34	0.18	0.14	0.04
	(0)	(30.4)	(36.9)	(17.0)	(12.5)	(3.3)
$PyF_{1.50}$	0.05	0.31	0.27	0.24	0.14	0.08
	(5.8)	(32.8)	(26.1)	(19.7)	(10.2)	(5.4)

**Relative extinction coefficient from the reference [18].*

According to Gounder and Iglesia,[22] the preferential exchange of H^+ site in the side pockets by Na^+ is due to their higher stabilization by the stronger dispersive forces in such confined environments. After full exchange in the 8-MR (*i.e.* sample Na_{56}), only four bands are observable (3603, 3610, 3619, and 3628 cm^{-1}), which can be attributed to BAS located at the intersections (8%) and in the 12-MR channels (remaining BAS). This means that during Na exchange, even at low exchange rates all the hydroxyl bands are more and less impacted. On the Na catalyst series, the concentration of OH bands located in the 12-MR channel and at the intersection is calculated using the extinction coefficient reported in reference [18], their concentration is close to that measured by pyridine chemisorption, which validates the values of the extinction coefficient (Figure IV.7).

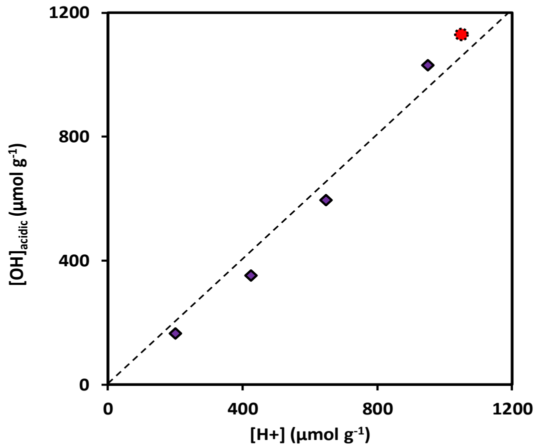

Figure IV.7. Amount of calculated hydroxyl groups from the six band deconvolution as function of the BAS determined by pyridine adsorption at 150 °C for the Na series.

3.3 Influence of the HF etching on the physicochemical properties of mordenite: F_x and PyF_x samples

Both, the HF etching of mordenite in aqueous (F) and pyridinic (PyF) solutions results in a slight decrease in the overall crystallinity of the samples (Figure IV.2, Table IV.2). The reduction of the diffraction efficiency indicates the disruption of crystalline planes during the treatment through the development of secondary porosity or defects.[23] For F samples the crystallinity decreases more importantly with increasing HF concentration compared to PyF samples. Moreover, the XRD patterns of the treated F samples allow to infer an increase of the FWHM. The lattice strain of the F samples is significantly higher compared to the parent mordenite and increases with increasing HF concentration (Table IV.2). This finding indicates that the fluorine etching induces an important strain on the lattice, most likely due to the enhanced formation of silanol defects. Interestingly, the lattice strain is comparable to that of the parent zeolite for PyF samples, indicating that in these samples the induced stress field is reduced (absence of silanol nests). A similar tendency can be deduced for the CCS which decreases up to almost the half for the F samples. The reduced CCS for F samples suggest that zeolite dissolution is favored on specific sites of the crystals; generating hence smaller crystalline domains. In previous studies it has indeed been reasoned that treatments of zeolites with aqueous HF solutions results in the preferential elimination of specific parts of the crystal which are rich in defects and are hence more prone to dissolution.[24,25] It is interesting to note that for PyF samples the CCS only slightly reduces compared to the parent mordenite, indicating that the action on HF in pyridine affects the zeolite in a different manner.

HF etching in aqueous solution acts within the crystal and allows to observe electron clear regions related to the presence of macropores in TEM images (Figure IV.1e). As for the HF etching in pyridine solution, the observed TEM images are very similar to the parent mordenite (Figure IV.1g-i). It is worth to mention that mordenites treated with HF in aqueous conditions, the development of a more important macroporous volume (0.44 $cm^3\ g^{-1}$) can be inferred (Table IV.2, Figure IV.8)

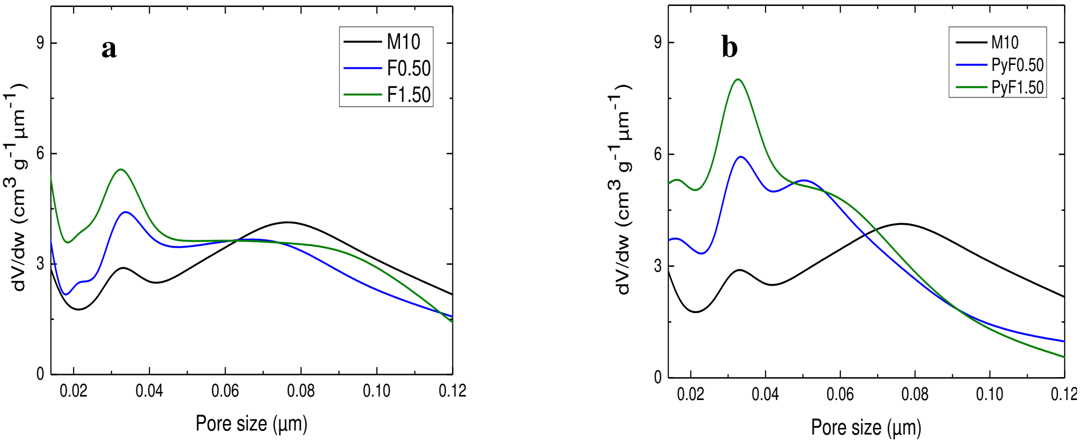

Figure IV.8. Pore size distribution derived from mercury intrusion of F_x and PyF_x samples (black: M10, blue: 0.5 M, green: 1.5 M).

In order to achieve further insights on the textural properties of the samples they were characterized through nitrogen and argon physisorption at -196 °C. The shape of the isotherms achieved for the etched F and PyF samples is very similar to those of the parent sample and is of type I (Figure IV.3). From the low relative pressure region of the argon adsorption isotherms a variation in the argon uptake for the modified samples can be inferred, which indicates a modification in the size of the micropores (Figure IV.9). Indeed, for F samples a smaller microporosity develops (argon uptake at 10^{-6} and 10^{-5} P/P_0), which might be related to the enlargement of some 8-MR side pockets. It is to note that the filling of the 8-MR is not observed in argon or nitrogen physisorption at -196 °C. Pastvova *et al.*[26] observed that the extraction of T4 atoms in mordenite as a result of the hydrolysis of Al-O and Si-O causes the merging of two 8-MRs leading to the development of a larger void space, which is hence accessible to bulkier molecules such as toluene. The authors further describe that the extraction of T2 sites might lead to the formation a larger deformed ring. Indeed, the modification of micropore size distribution of mordenite upon acid leaching has been observed by several groups.[3-4] It is to note that for PyF samples analog micropore filling is observed as for the parent M10, indicating that the pyridine treatment does not enlarge 8-MRs, due to a low demetallation of the zeolite framework.

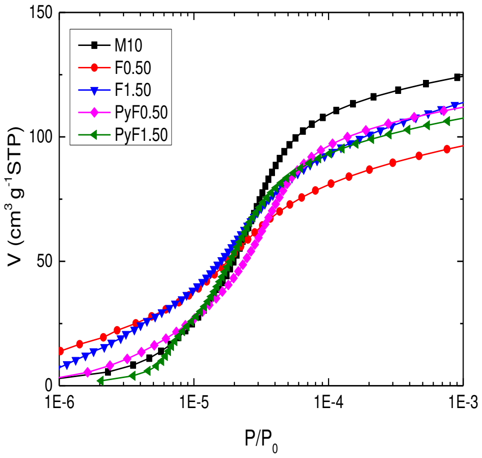

Figure IV.9. Low relative pressure ranges of the argon adsorption isotherms for: M10 (black), F (blue and red), and PyF (green and pink) samples.

The nature of the employed solvent in the HF etching has a major effect on the framework composition (Table IV.3). Preferential elimination of Al species has been observed for F samples. For the sample treated with the highest concentration of HF in aqueous conditions the Si/Al ratio almost doubled. Yet, contrariwise to what was observed by Ghosh *et al.*,[6] the use of concentrated HF solutions (1.5 mol L^{-1}) did not lead to the incorporation of fluorine in the zeolite framework. This difference can be ascribed to the preparation mode. Whilst in this study, after etching of the sample, the slurry is centrifuged and washed with water, in the protocol described by Ghosh *et al.* the liquid is evaporated to dryness, promoting hence the fluorine incorporation.[6] Thus, the short duration of etching treatment coupled with various washing cycles with demineralized water inhibits the incorporation of fluorine as confirmed through fluorescence spectroscopy (Table IV.3).

For samples treated with aqueous HF the intensity of the 3608 cm^{-1} band decreases through increasing the HF concentration during the treatment, whilst the 3734 cm^{-1} band slightly increases in intensity (Figure IV.4 and IV.10).

This finding indicates a decrease in the concentration of the BAS (Table IV.3) and further that the preferential elimination of Al species leads to a substantial increase in internal silanol defects (nests). This confirms to what has previously been inferred from the Williamson-Hall analysis of the X-ray diffractograms. The increase of the silanol band, in particularly external one, appears very limited in comparison with that observed during desilication with NaOH,[27] which confirms that HF etching leads to a biased extraction of Al and Si. In addition, the formation of internal defects suggests that the dealumination occurs on the core of the crystal.

Further the intensities of the deconvulated bands for the main band at 3622 cm^{-1} for all of the samples was realized. Here for the concentration of the six OH groups was plotted as function of the Brønsted acidity (Figure IV.11). For all samples the acidic OH groups are probed in the same manner, except for the two cases. Indeed, for the same number of acidic sites probed by pyridine, the number of constrained OH (in particular O1-H and O9-H) is slightly greater for the etched samples compared to the Na-exchanged mordenites. In other words, Na^+ preferentially exchanges H^+ sites in 8-MRs, while HF etching is non-selective.

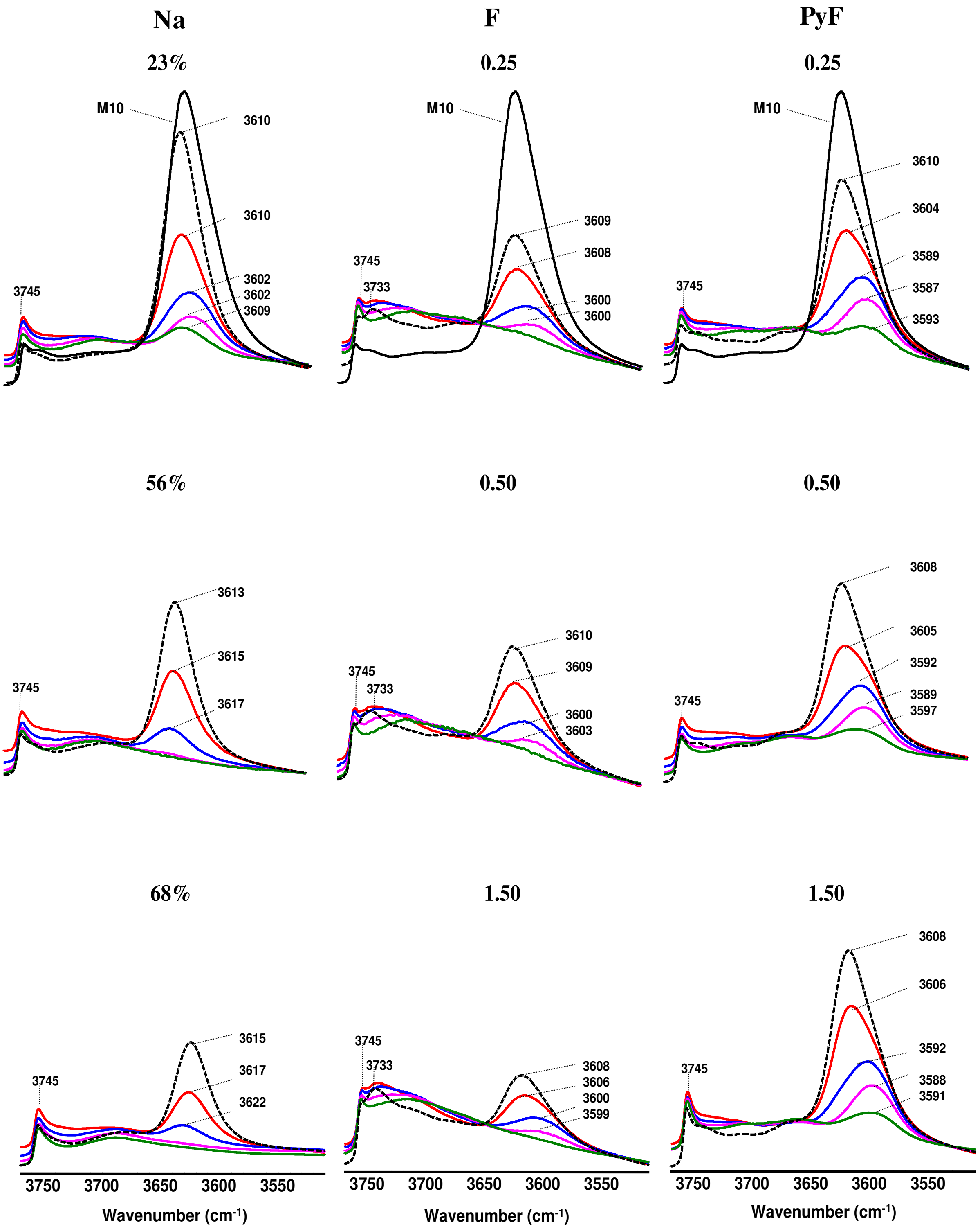

Figure IV.10. Infrared spectra of the OH vibration region for selected F_x, Na_x, and PyF_x samples before (dotted line) and after pyridine adsorption followed by desorption at 150 °C (green line), 250 °C (purple) 350°C (blue), and 450 °C (red). All spectra have the same scale.

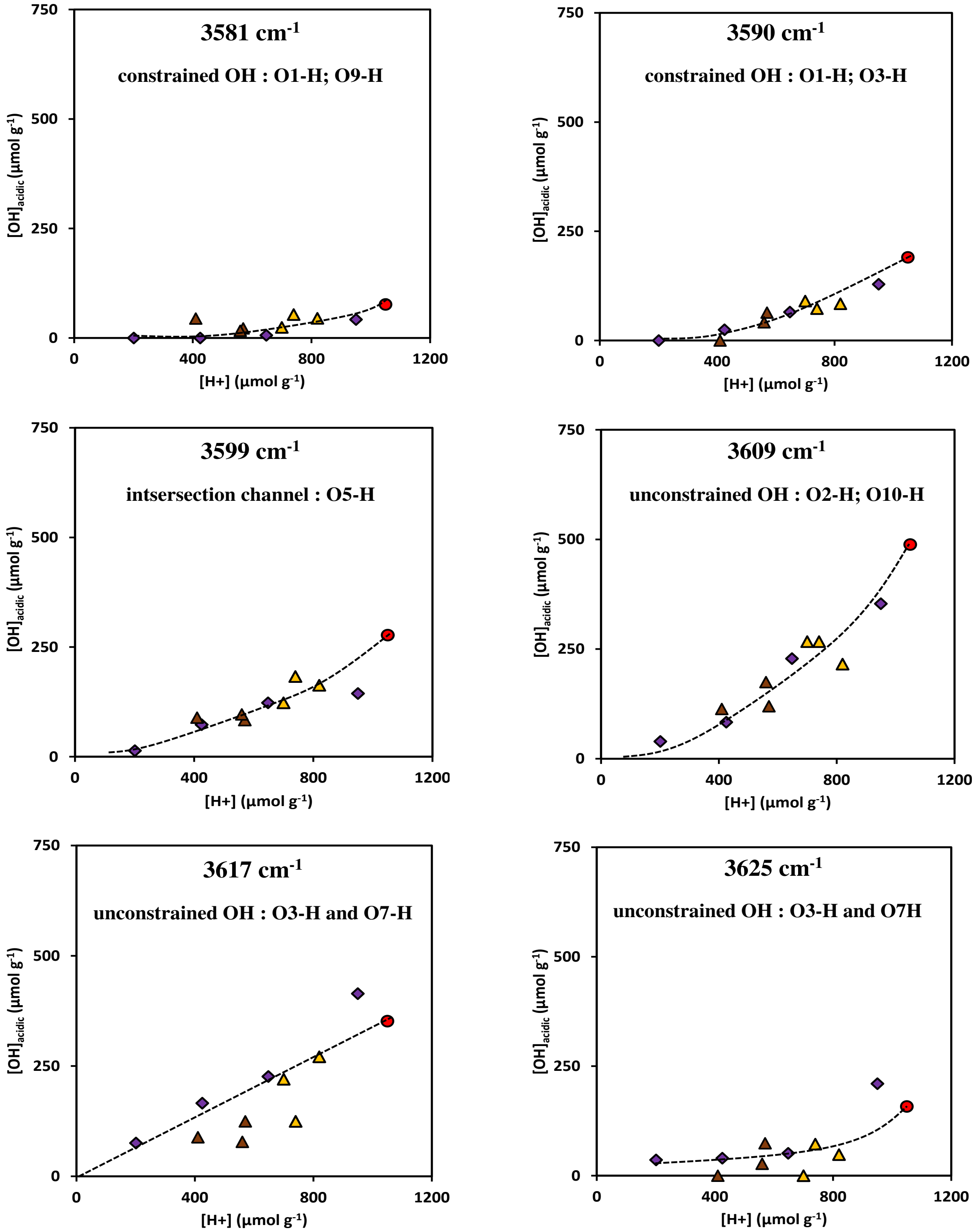

Figure IV.11. Concentration of acidic hydroxyl groups measured from six deconvoluted bands of catalyst series: M10 (red symbol), Na_x (violet), F_x (brown), and PyF_x (yellow) as a function of the Brønsted acidity probed by pyridine at 150 °C.

3.4 Role of pyridine in HF etching

It is worth to mention that the samples prepared through the treatment with HF in pyridine feature Si/Al ratios, which are comparable of those of the parent zeolite even for treatments that involve more concentrated solutions. The FT-IR spectra of samples treated with HF in pyridine feature a slight decrease of the intensity of the 3608 cm^{-1} band. The distribution of distinct BAS calculated using the six-bands deconvolution (Figure IV.6) is close to that of parent mordenite, which is ~16 % in the 8-MR channels, ~19% at the intersection between side pockets and 12-MR channels, and ~65% in the 12-MR channels (Table IV.4). During the HF etching in pyridine solution, the creation of Lewis acid sites indicates a slight dealumination of the zeolite framework. Assuming that the Lewis species are constituted of two aluminum atoms (*e.g.* Al_2O_3), the global acidity probed by pyridine ($[PyH^+] + 2[PyL]$) is close to the amount measured on the parent zeolite (*i.e.* 1014 μmol g^{-1}) (Table IV.3). As the global Si/Al composition, the acidity, and the accessibility of BAS remain constant, strongly indicates an unbiased extraction of Si and Al form the zeolite framework. Hence, some of the silicon and aluminium extra framework species are probably trapped within the zeolite micropores. This further explains the slight reduction of microporous volume upon HF treatment (Table IV.2). The total number of H^+ sites after etching increase with increasing concentrations of HF in pyridine (Table IV.3), which indicates that BAS are more preserved through increasing HF concentration in pyridine.

The treatment of zeolites by hydrofluoric acid yields to the formation of solubilised silicon and aluminium fluorinated complexes, such as $\mathrm{SiF_4}$, $\mathrm{SiF_6^{2-}}$and $\mathrm{AlF_4^-}$.

$$4\,\mathrm{HF} + (\mathrm{SiO_2})_z \longrightarrow \mathrm{SiF_4} + 2\,\mathrm{H_2O} \tag{1}$$

$$6\,\mathrm{HF} + (\mathrm{SiO_2})_z \longrightarrow \mathrm{SiF_6^{2-}} + 2\,\mathrm{H_3O^+} \tag{2}$$

$$4\,\mathrm{HF} + (\mathrm{AlO_2^-})_z \longrightarrow \mathrm{AlF_4^-} + 2\,\mathrm{H_2O} \tag{3}$$

We hence observe that the nature of the solvent in which the HF is solubilized has a major impact on the zeolite composition and thus on its acidity. As described by Kolasinski a variety of specie exist in diluted aqueous HF solutions, *i.e.* $[F-H-F]^-$, $\mathrm{H^+}$, $\mathrm{F^-}$, and undissociated HF molecules and following equilibria exist in solution:[28]

$$\mathrm{HF} + \mathrm{H_2O} \leftrightharpoons \mathrm{H_3O^+} + \mathrm{F^-} \tag{4}$$

$$\mathrm{HF} + \mathrm{F^-} \leftrightharpoons [F-H-F]^- \tag{5}$$

The consumption of fluorine ion through the formation of fluorinated complexes should shift the equilibrium toward both a higher dissociation of hydrofluoric acid and probably a reduction of the bifluoride ion concentration. It has experimentally been determined that in diluted aqueous HF solutions (0.1 – 2 M) the ionic activity is highest for $\mathrm{F^-}$, whilst the activity for $[F-H-F]^-$ and undissociated HF are smaller by factor of 5. The ionic activity of H^+ is even smaller (by a factor of 20 compared to $\mathrm{F^-}$). This explains why in aqueous HF solution the dealumination is favored. It has furthermore been described that the etching of silica is linearly dependent on the respective concentrations of undissociated HF and $[F-H-F]^{-}$ in aqueous solution.[29] Increasing the F^{-} concentration (through adding fluoride) allows to increase importantly the concentration of $[F-H-F]^{-}$ in solution (equilibrium 5). For a 1 M HF solution (containing 0.5 M NaF) the ionic activity of F^{-} and $[F-H-F]^{-}$are almost equal.[28] Vatchev and co-workers observed that the etching of ZSM-5 with an aqueous HF-NH_4F solution allows for an unselective removal of Si and Al species from the parent zeolites.[8] This finding has been rationalized by the increased concentration of $[F-H-F]^{-}$ species in solution, which hence leads to a higher rate of desilication.

The HF species present in pyridine have up to date only been rationalized for concentrated HF solutions.[29] In such systems pyridine-HF complexes are formed of the composition $PyH^{+} \cdot (HF)_{x}F^{-}$ which are in equilibrium with $(HF)_x$. Yet, in the present case diluted HF solutions are used in which pyridine largely exceeds the HF concentration. Taking into consideration that an increased concentration of HF_2^{-} has been identified for leading to a more pronounced desilication one could assume that the dissolution of HF in pyridine leads to a favored formation of this species. In a first step pyridine is protonated by HF leading to free F^{-} (equilibrium 6); these could then further shifts equilibrium 5 to the right and lead to an increased amount of HF_2^{-} .

$$HF + Py \leftrightharpoons PyH^{+} + F^{-} \tag{6}$$

Pyridine forms remarkably stable solution with anhydrous fluoride. Olah and co-workers[30] have shown by ^{1}H NMR and ^{19}F NMR that a solution containing 9 equivalents of HF to 1 equivalent of pyridine, the pyridinium ring is protoned and the development of polyhydrogen fluoride species, in which each fluorine atom is surrounded by four hydrogen atoms. The development of protonated pyridinic species has been investigated through recording liquid FT-IR spectra for on 0.25, 0.5, 1.5, and 5 M HF in pyridine solutions (Figure IV.12a). We observed the development of two new bands for the HF/pyridine spectra compared to that of pure pyridine. These are centered at 1450 and 1840 cm^{-1}. It is to note that the intensity of these bands increases with increasing amount of HF in the system (Figure IV.12b), and correlates with the increase in the total number of H^{+} after etching (Table IV.3). It is further to observe that the intensity of the 1581 cm^{-1} stretching band of pyridine decreases through increasing HF concentration, indicating that pyridine is protonated in the same manner despite the HF concentration. We further observed that the intensity of the band centered at 1602 cm^{-1}

increases with rising amount of HF and can hence be assigned to a vibration of the pyridinium ion.

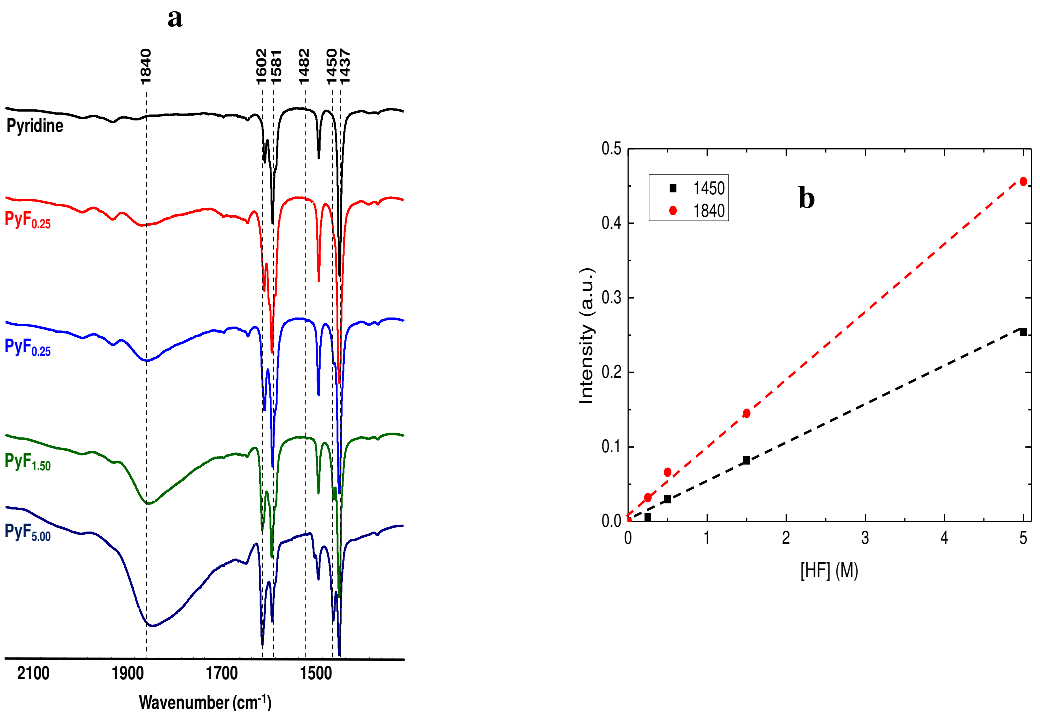

Figure IV.12. a) Transmittance spectra of pyridine HF solution of different concentration; b) Intensity of bands centered at the1450 (black), and 1840 cm^{-1} (red).

3.5 Active sites in toluene disproportionation and *n*-hexane cracking

3.5.1 Toluene disproportionation

The disproportionation of toluene, a bimolecular reaction, involves diphenylmethane intermediates as stated in the first chapter (Scheme I.6),[31] and yields a mixture of benzene and xylene (Figure IV.13), in proportion close to the thermodynamic equilibrium (20%, 60%, and 20% of *o*-, *m*-, and *p*-xylenes at 450 °C). The initial molar ratio of xylenes to benzene is significantly lower than unity (*i.e.* 0.2, Table IV.5). Benzene, which is smaller, diffuses faster and its desorption is favored, while a large part of the xylenes remains trapped in the micropores and then convert into coke (Table IV.5), which causes the deactivation of the catalyst.

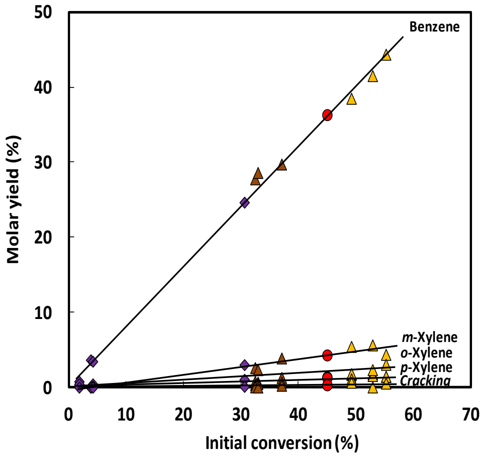

Figure IV.13. Molar yields as a function of the initial conversion for toluene disproportionation of catalyst series: M10 (red symbol), Na_x (violet), F_x (brown), and PyF_x (yellow).

The deactivation is much more important compared to *n*-hexane cracking (section 3.5.2, Figure IV.14), despite of chemical inhibiting effect of H_2 on coke formation.[31,32] The ratio of the residual (after 1 hour) to the initial activity (A_{60}/A_0) is lower than 0.2 on M10 and on etched zeolites. Indeed, for the aromatic disproportionation, reactant and products can already be considered as coke precursors. The HF etching in pyridine and water leads to an increase in the turnover frequencies per BAS, while the exchange of H^+ by Na^+ cation inhibits almost totally the disproportionation reaction. The effect of Na-exchange on aromatic disproportionation has previously been described Marie *et al.*,[33] through an *operando* infrared spectroscopy study at 350 °C. They proved by studying the evolution of the consumed hydroxyls in the xylene transformations that constrained BAS do not directly take part to the catalytic event; yet their impact is crucial on catalytic activity. Their discussion is based on the decomposition of the ν_{OH} band, which is corrected (by shifting and broadening of bands according to reference [33]) to take account of the influence of the reaction temperature. The authors suggested that the beneficial effect of the Na^+ exchange by H^+ in the 8-MR side pockets on the disproportionation reaction would be related to a modification in the void space within the micropores. Yet, the "strong" increasing in the micropore volume is rather limited and even negligible (+ 0.017 cm^{-3} g^{-1}).

Ratnasamy *et al.*[34] and Bankòs *et al.*[35] observed the same effect of the Na^+ exchange on the selectivity in the transformation of *o*-xylene. The appearance of the disproportionation products is concomitant with strong Brønsted acid sites, which appear at a high degree of Na^+ exchange. The authors postulated that the exaltation of the acidity resulted from the interaction between the BAS and the extraframework species which are created during the calcination of the ammonium form of the MOR zeolite. In both of these explanation attempts, the increase of the void volume or the exaltation of the force of the acidic sites, the common assumption is based on the progression of the disproportionation reaction exclusively catalyzed by H^+ in the 12-MR channels, rationalized on the basis of the bulkiness of the reaction intermediate (diphenylmethane), (Scheme I.6). This conclusion appears to be in disagreement with our observation, from which we infer that BAS located in the 8-MRs are active for toluene disproportionation. Indeed, Figure IV.15 presents the toluene disproportionation rate (per g) as a function of the number of OH (per g) located within the 8-MR side pockets, the 12-MR channels and at their intersection. Disproportionation rates increase with the number of H^+ within the 8MR channel or at their pore mouth (Figure IV.15a-b).

Table IV.5. Initial activity (A_0), turnover frequencies of BAS probed by pyridine at 150 °C (TOF), ratio of residual/initial activity after 1h reaction (A_{60}/A_0), and coke content measured by ATD-ATG for toluene disproportionation. X/B molar ratio correspond to xylenes/benzene.

Toluene disproportionation
(450 °C, 1 atm, P_{H2}/P_{Tol} =4, τ = 0.12s)

	A_0 mmol h^{-1} g^{-1}	**TOF** h^{-1}	**X/B** mol/mol	**A_{60}/A_0**	**Coke** %
M_{10}	100	99(374)	0.19	0.13	4.6
$Na_{23\%}$	68	72(398)	0.15	0.20	6.5
$Na_{56\%}$	8	6(112)	0.05	0.42	4.6
$Na_{68\%}$	9	22(360)	0.21	0.66	3.8
$Na_{83\%}$	4	20	/	0.35	3.5
$F_{0.25}$	8	146(965)	0.22	0.18	4.9
$F_{0.50}$	72	125(1241)	0.15	0.21	4.5
$F_{1.50}$	73	177(1659)	0.13	0.05	4.4
$PyF_{0.25}$	118	159(929)	0.18	0.13	7.0
$PyF_{0.50}$	110	156(965)	0.23	0.15	6.7
$PyF_{1.50}$	123	149(953)	0.16	0.15	7.4

[a] *Measured by ATD-ATG; In brackets TOF per H^+ in 8-MR side pockets.*

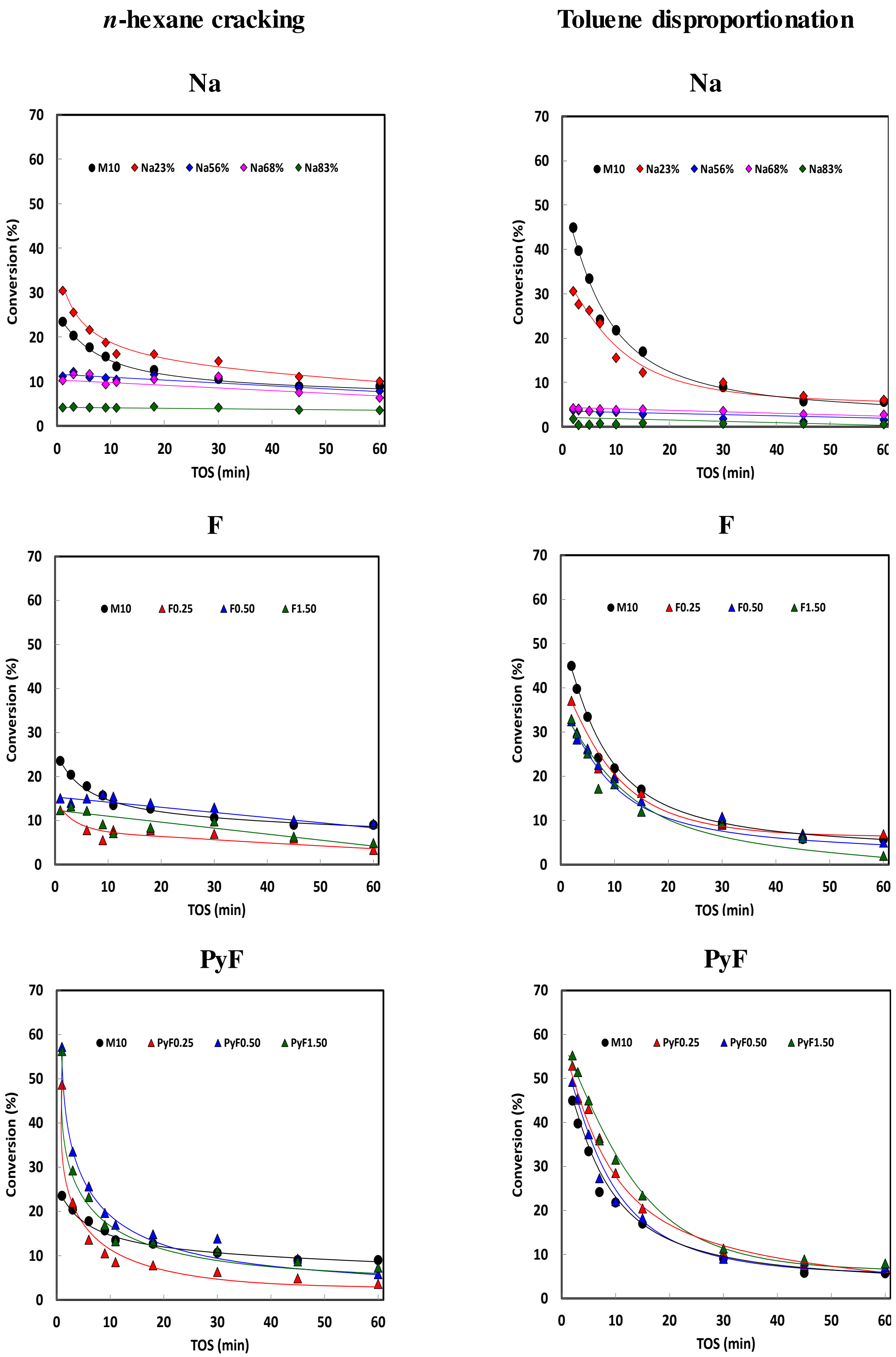

Figure IV.14. Conversion for *n*-C6 cracking and TDP as a function of the TOS obtained on the three catalysts series.

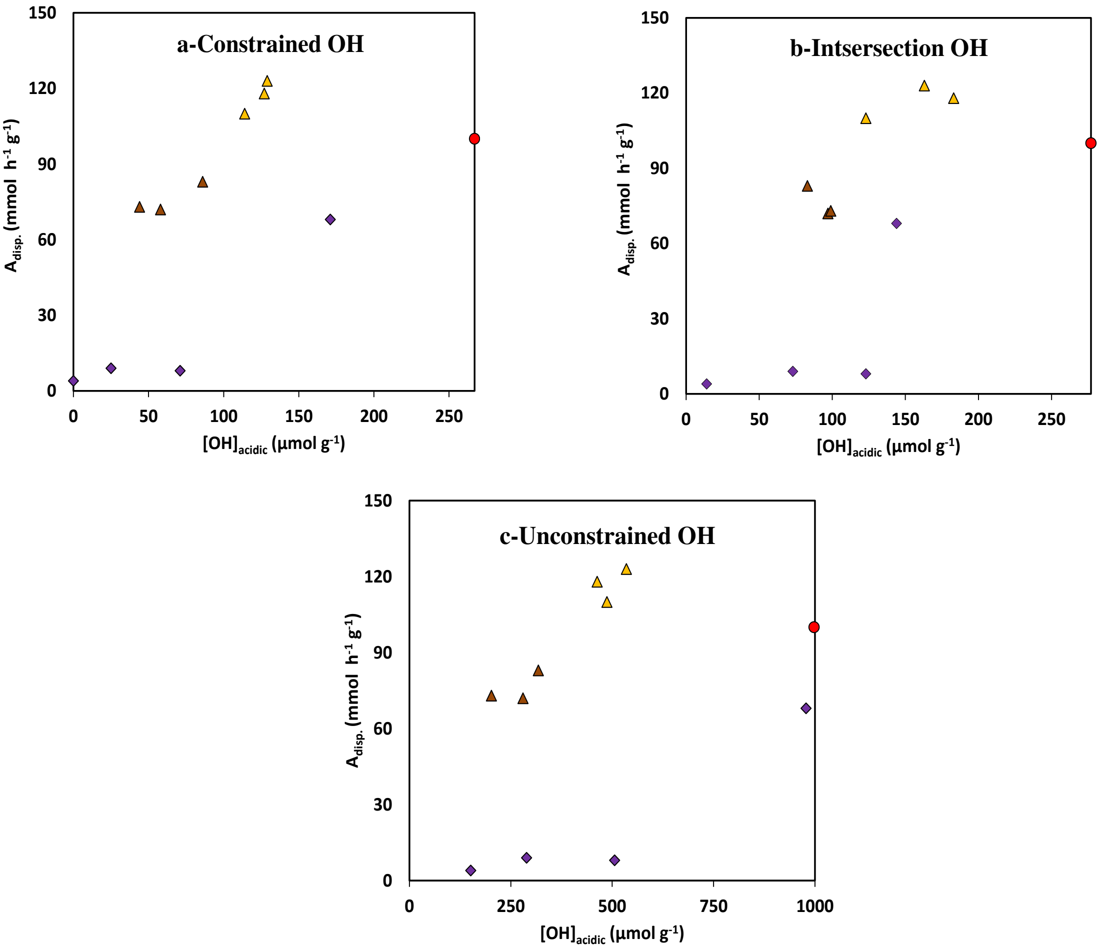

Figure IV.15. Toluene disproportionation rates (per gram) at 450 °C in H-MOR (red symbol), Na^+ exchanged (violet symbol), HF etched in aqueous (brown symbol), and pyridine (yellow symbol) media plotted against the density of Brønsted acid sites per gram in a) the 8-MR pockets of MOR, c) 12-MR channels of MOR and their intersection (b)

The involvement of constrained OH was previously observed. Bhan *et al.*[10] evidenced that the active sites for carbonylation of dimethyl ether to methyl acetate are only the protonic sites located within the 8-MRs. Further, Veefkind *et al.*[16] proposed that for the reaction of ethanol with NH_3 to produce ethylamine that the monoethyl amine intermediate was selectively stabilized within 8-MR channels. Finally, Gounder *et al.*[22] demonstrated that monomolecular alkane cracking and dehydrogenation turnovers occur quasi selectively in the 8-MR side pockets.

In the case of the toluene disproportionation, the catalytic involvement of constrained H^+ (in the 8-MR side pockets) is possibly provided if the reaction intermediate is partially confined. The kinetic diameter of toluene (5.85 Å) is just slightly larger than that of the 8-MRs (5.7 Å). At high temperatures the zeolite framework distorts[36] and fits the size requirements of toluene. Hence, the toluene adsorption in the 8-MR could mimic an enzymatic mechanism. Partially confined, the aromatic molecule would yield a stabilized benzylium ion (Scheme IV.2), which could react with a toluene molecule in the 12-MR channel and disproportionate into a desorbed benzene and methylbenzylium ion.

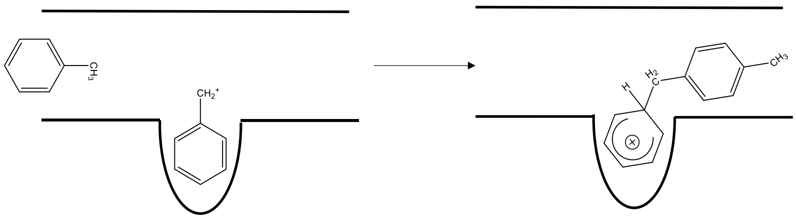

Scheme IV.2. Proposed involvement of 8-MR side pockets in the toluene disproportionation.

The TOF per constrained H^+ is the same independent of the degree of sodium exchange (excepted for $Na_{56\%}$), whilst the TOF calculated per total H^+ decrease with the Na content. We can hence conclude that the H^+ located in the 12-MR channels are inactive for the toluene disproportionation. After etching, regardless of the media used, TOF per H^+ in 8-MR side pockets is more than 2.5 times higher than of the Na series. The higher value of TOF for the F series could be related to the enlargement of 8-MR pocket as previously inferred from Ar physisorption (Figure IV.9).

3.5.2 *n*-Hexane cracking

The acidic properties of the achieved materials were further characterized by *n*-hexane cracking at 541 °C.[31] In a previous study[37] we observed on a series of MFI, *BEA, and FAU zeolites, under identical operating conditions, that the monomolecular cracking mechanism is favored and that the autocatalytic bimolecular route is limited despite a relative high partial pressure of *n*-hexane. The *n*-hexane cracking yields C_1, C_2, C_3, C_4, C_5 hydrocarbons. On M10, Na, and F catalyst series, reaction products are formed in strictly parallel reactions (Figure IV.16b) indicating a monomolecular cracking mechanism. It is worth to mention that a slight deviation is observed for the PyF series at high conversions, probably due the competition of the bimolecular mechanism (high conversions yield high olefin pressure).

The initial molar ratios for C_5/C_1 and C_4/C_2 (Figure IV.17) are mainly between 0.8 and 1, independent of the nature of the compounds (olefins or paraffins). This confers well to what has been reported by Babitz *et al.*[38] and Lercher *et al.*[39] On M_{10}, Na_x, and F samples, the C_5/C_1 ratios are lower than unity, (ca. 0.5), indicating the occurrence of secondary cracking, whilst on PyF samples, the ratios are higher (*i.e.* about 1.1) confirming a dimerization cracking mechanism.It is to note that reducing the contact time allows to minimize the occurrence of the bimolecular mechanism and the C_5/C_1 ratios agree to the ones of the other samples (Figure IV.17).

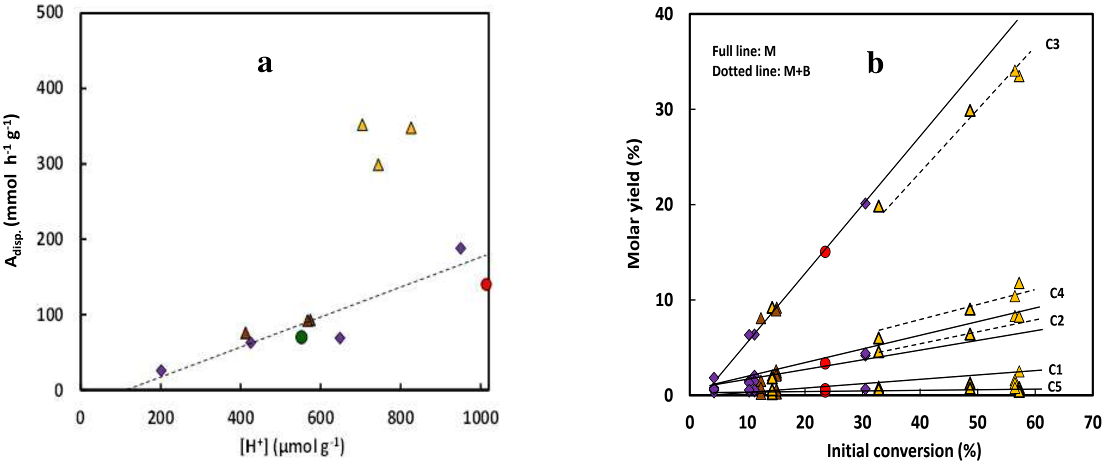

Figure IV.16. Activity of *n*-hexane cracking (a) as a function of the concentration of Brønsted acid sites. Molar yields as a function of the initial conversion for *n*-hexane cracking (b) of the parents M10 (red), M20 (green), and three catalyst series: Na_x (purpule), F_x (brown), and PyF_x (yellow).

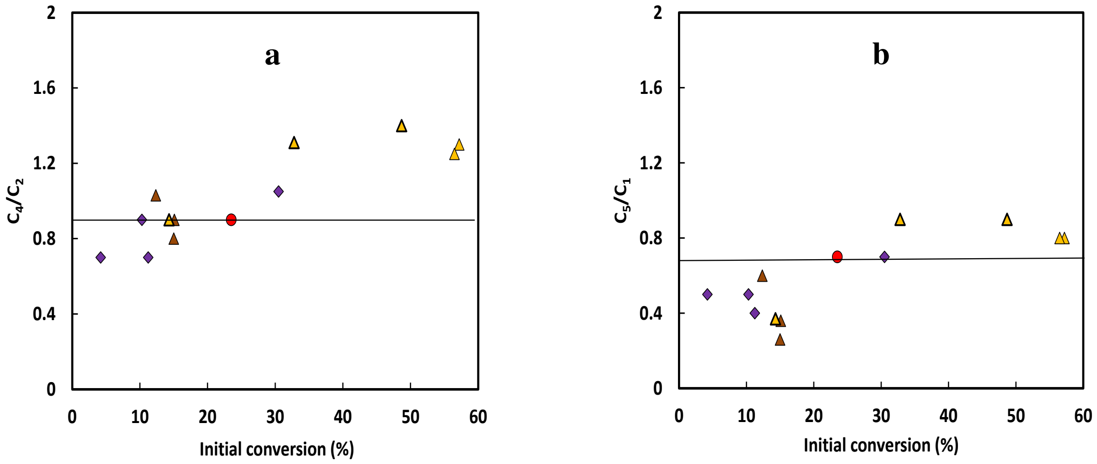

Figure IV.17. C_4/C_2 (a) and C_5/C_1 (b) ratio as a function of the initial conversion for all catalysts in *n*-hexane cracking.

On the parent zeolite and the etched samples with aqueous HF, the initial O/P ratios is close to unity (Table IV.6), which is in agreement with a monomolecular mechanism. On the PyF samples, the O/P ratio is lower than unity, indicating the consumption of olefins, which is consistent with the occurrence of a bimolecular mechanism. It is worth to mention that the presence of Na cations seems to promote the dehydrogenation of paraffin as O/P ratios higher than unity have been observed.

On M10 zeolite, Na_x and F_x samples, the deactivation due to coke formation (Table IV.6), is rather slow (Figure IV.14). The observation of such deactivation paths is consistent with a monomolecular mechanism. Contrariwise, on the PyF_x samples, the deactivation rate is fast and increases with the initial conversion due to a high partial pressure of olefins (P_O), which is hence consistent with a bimolecular mechanism. The relatively fast deactivation on mordenite is due to the "one-dimensional" nature of accessible diffusion channels and strong coke toxicity is thus observed for all samples. The coking mode occurs by pore blocking, which means that one coke molecule is enough to block the accessibility of reactants to all acid sites located within a given 12-MR channel.[40]

Table IV.6. Initial activity (A_0), ratio of residual/initial activity after 1 h reaction (A_{60}/A_0), and coke content measured by ATD-ATG for *n*-hexane cracking. O/P molar ratio correspond to olefins/paraffins.

***n*-hexane cracking (541 °C, 1 atm, $P_{N2}/P_{nC6} = 9$, $\tau = 0.04$ s)**				
	A_0 mmol h^{-1} g^{-1}	**O/P mol/mol**	**A_{60}/A_0**	**Coke[a] %**
M_{10}	145	1.0	0.38	7.7
$Na_{23\%}$	188	1.0	0.33	
$Na_{56\%}$	69	1.7	0.72	
$Na_{68\%}$	63	1.4	0.62	
$Na_{83\%}$	26	1.6	0.85	
$F_{0.25}$	93	1.1	0.22	5.2
$F_{0.50}$	92	1.2	0.62	5.8
$F_{1.50}$	76	1.1	0.36	3.4
$PyF_{0.25}$	299 (352)	0.5 (1.1)	0.07 (0.15)	10.0
$PyF_{0.50}$	352	0.9	0.12	11.4
$PyF_{1.50}$	348	0.6	0.13	9.3

[a]*Measured by ATD-ATG; In brackets data obtained for a* τ of 0.01s.

In contrast to the disproportionation reaction, sodium exchange does not cause a drastic loss of activity, but a continuous decrease (Figure IV.16a). This means that both BAS in 12-MR channels and in the 8-MR side pockets are active sites and catalyze *n*-hexane cracking. Yet, as the confining environment of these sites is different, an independent TOF for each site is observed. The participation of unconstrained H^+ is due to high temperature used for the reaction (541 °C). It is possible to calculate the TOF frequency of each site. On the $Na_{83\%}$ sample, the only BAS are within the 12-MR channels and consequently their TOF can be drawn directly from the initial activity. The TOF value of unconstrained OH is hence ca 130 h^{-1}. The activity can be expressed as: $A_0 = \left(TOF_{OH_{12-MR}} \times C_{OH_{12-MR}}\right) + \left(TOF_{OH_{8-MR}} \times C_{OH_{8-MR}}\right)$. From this equation, it is possible to calculate the TOF value of constrained OH. For example, using the activity of $Na_{23\%}$, the TOF of constrained OH it is ca. 4 times higher than of the TOF of unconstrained OH, *i.e.* 510 h^{-1}. It should be noted that the TOF of *n*-hexane cracking in the 12-MR channels is about 2.5 times less than that of the MFI and * BEA zeolites,[37] while that of the 8-MR side pockets is 1.5 times higher. By using TOF values of constraint and unconstraint OH, and knowing the concentration of each active site, a theoretical activity $(A_{theoritical})$ can be calculated, which corresponds to that measured one excepted for PyF_x samples (Table IV.6, Figure IV.18); the very good correlation validates the two calculated TOF values.

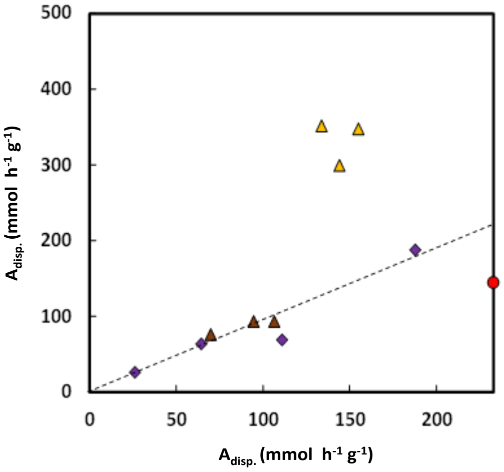

Figure IV.18. *n*-Hexane cracking activity as a function of the activity calculated with the follows formula : $A_0 = \left(TOF_{OH_{12-MR}} \times C_{OH_{12-MR}}\right) + \left(TOF_{OH_{8-MR}} \times C_{OH_{8-MR}}\right)$, where TOF of OH 12-MR and 8-MR is equal to 129 and 510 h^{-1}, respectively and C correspond to their concentration obtained from the deconvolution of the OH band.

The high activity observed for PyF_x samples could be due to improved mass transfer of *n*-hexane within the 12MR channels. Indeed, Tromp *et al.*[41] calculated an effectiveness factor of 0.3 for the *n*-hexane hydroisomerization at 250 °C over Pt/H-MOR catalyst. The authors observed that diffusion limitations significantly reduced after acid leaching with hydrochloric acid (1 M) on the parent zeolite. They hence attributed improved activities to the generation of a 3-D microporous structure as well as to the development of mesopores that reduce diffusion path length and allow to increase mass transfer. Yet, for *n*-hexane the kinetic diameter is 4.3 Å, which is significantly lower than the size of the 12-MRs (6.7 x 7.0 Å). Moreover, we have demonstrated that no mass transfer limitation occur during n-hexane cracking, even in medium pore zeolites (MFI: 5.4 x 5.6 Å) as well as on large MFI crystals (8 μm).[37] The textural modifications of the zeolite structure as a result of the HF etching are rather limited in aqueous solution (enlargement of site pocket aperture) and even less in pyridine solution. Hence, the improvement of the mass transfer should not account for the improved activity of the PyF_x samples. The higher performances observed for these samples could be ascribed to an auto-catalytic behavior. Despite the decrease in contact time in order to prevent the bimolecular mechanism, the catalytic activity of PyF_x is higher compared to the other samples, which makes it possible to exclude this explanation. Finally, the high activity of this series could be ascribed to a difference in the intrinsic BAS strength due to their exaltation by the EFAL species generated during the etching treatment. The exaltation of acidity can be quantified by the ratio $A_0/A_{theoretical}$, which is ca. 2. Finally, the EFAL double the strength of the Brønsted acid sites.

4. Conclusion

The etching of mordenite with HF in pyridine allowed to achieve catalysts with higher accessibility to BAS located within the 8-MRs. Yet, it is not the increased accessibility that was found to be responsible for the improved catalytic activities. It was found that in toluene disproportionation the active sites are exclusively located within the 8-MR. For n-hexane cracking the activities of BAS in 8-MR side pockets and 12-MRs could be quantified and it was found that BAS in side pockets have higher activity than those in the large channels. The results indicate that TOF is increased through stringer confinement of BAS. Furthermore, the acid strength can further be exalted through extra framework species.

Bibliographic references

[1] R. Chal, C. Gérardin, M. Bulut, S. van Donk, Overview and industrial assessment of synthesis strategies towards zeolites with mesopores, ChemCatChem 3 (2011) 67–81.

[2] M. -C. Silaghi, C. Chizallet, P. Raybaud, Challenges on molecular aspects of dealumination and desilication of zeolites, Microporous Mesoporous Mater.191 (2014) 82–96.

[3] N. Viswanadham, M. Kumar, Effect of dealumination severity on the pore size distribution of mordenite, Microporous Mesoporous Mater. 92 (2006) 31–37.

[4] A. A. C. Reule, J. A. Sawada, N. Semagina, Effect of selective 4-membered ring dealumination on mordenite-catalyzed dimethyl ether carbonylation, J. Catal. 349 (2017) 98–109.

[5] S. Ban, A. N. C. van Laak, J. Landers, A. V. Neimark, P. E. de Jongh, K. P. de Jong, T. J. H. Vlugt, Insight into the effect of dealumination on mordenite using experimentally validated simulations, J. Phys. Chem. C 114 (2010) 2056–2065.

[6] A. K. Ghosh, R. A. Kydd, Acidity and activity of fluorinated mordenites, J. Catal. 103 (1987) 399–406.

[7] A. G. Panov, V. Gruver, J. J. Fripiat, Fluorination of USY and modification of its catalytic properties, J. Catal. 168 (1997) 321–327.

[8] Z. Qin, L. Lakiss, J. -P. Gilson, K. Thomas, J. -M. Goupil, C. Fernandez, V. Valtchev, Chemical equilibrium controlled etching of MFI-Type zeolite and its influence on zeolite structure, acidity, and catalytic activity, Chem. Mater. 25 (2013) 2759–2766.

[9] D. B. Lukyanov, T. Vazhnova, J. L. Casci, J. J. Birtill, On the catalytic properties of Brønsted acid sites located in the small and large channels in zeolite mordenite. Book of Abstracts 1:13th International Congress on Catalysis, Paris, 2004, 219.

[10] A. Bhan, A. D. Allian, G. J. Sunley, D. Law, E. Iglesia, Specificity of sites within eight-membered ring zeolite channels for carbonylation of methyls to acetyls, J. Am. Chem. Soc. 129 (2007) 4919–4924.

[11] V. L. Zholobenko, M. A. Makarova, J. Dwyer, Inhomogeneity of Bronsted acid sites in H-mordenite, J. Phys. Chem. 97 (1993) 5962–5964.

[12] F. Wakabayashi, J. Kondo, A. Wada, K. Domen, C. Hirose, FT-IR studies of the interaction between zeolitic hydroxyl groups and small molecules. 1. Adsorption of nitrogen on H-mordenite at low temperature, J. Phys. Chem. 97 (1993) 10761–10768.

[13] J. Datka, B. Gil, A. Kubacka, Acidity of silica-alumina catalysts by amine titration using Hammett indicators and FT-IR study of pyridine adsorption, Zeolites 15 (1995) 501–506.

[14] M. Maache, A. Janin, J. -C Lavalley, E. Benazzi, FT infrared study of Brønsted acidity of H-mordenites: Heterogeneity and effect of dealumination, Zeolites 15 (1995) 507–516.

[15] M. A. Makarova, A. E. Wilson, B. J. Van Liemt, C. M. Mesters, A. W. de Winter, C. Williams, Quantification of Brønsted acidity in mordenites, J. Catal. 172 (1997) 170–177.

[16] V. A. Veefkind, M. L. Smidt, J. A. Lercher, On the role of strength and location of Brønsted acid sites for ethylamine synthesis on mordenite catalysts, Appl. Catal., A 194–195 (2000) 319–332.

[17] O. Marie, P. Massiani, F. Thibault-Starzyk, Infrared evidence of a third brønsted site in mordenites, J. Phys. Chem. B 108 (2004) 5073–5081.

[18] D. B. Lukyanov, T. Vazhnova, N. Cherkasov, J. L. Casci, J. Birtill, Insights into brønsted acid sites in the zeolite mordenite, J. Phys. Chem. C 118 (2014) 23918–23929.

[19] J. L. Schlenker, J. J. Pluth, J. V. Smith, Positions of cations and molecules in zeolites with the mordenite-type framework: VIII Dehydrated sodium-exchanged mordenite, Mater. Res. Bull. 14 (1979) 751–758.

[20] M. Niwa, K. Suzuki, N. Katada, T. Kanougi, T. Atoguchi, Ammonia IRMS-TPD study on the distribution of acid sites in mordenite, J. Phys. Chem. B 109 (2005) 18749–18757.

[21] P. A. Jacobs, W. J. Mortier, An attempt to rationalize stretching frequencies of lattice hydroxyl groups in hydrogen-zeolites, Zeolites 2 (1982) 226-230.

[22] R. Gounder, E. Iglesia, Catalytic consequences of spatial constraints and acid site location for monomolecular alkane activation on zeolites, J. Am. Chem. Soc. 131 (2009) 1958–1971.

[23] A. Sachse, A. Grau-Atienza, E. O. Jardim, N. Linares, M. Thommes, J. Garcia Martinez, Development of intracrystalline mesoporosity in zeolites through surfactant-templating, Crys. Growth. Des. 17 (2017) 4289–4305.

[24] D. Verboekend, G. Vilé, J. Pérez-Ramírez, Mesopore formation in USY and Beta zeolites by base leaching: Selection criteria and optimization of pore-directing gents, Cryst. Growth Des. 12 (2012) 3123–3132.

[25] Z. Qin, G. Melinte, J. -P. Gilson, M. Jaber, K. Bozhilov, P. Boullay, S. Mintova, O. Ersen, V. Valtchev, The mosaic structure of zeolite crystals, Angew. Chem., Int. Ed.128 (2016) 15273–15276.

[26] J. Pastvova, D. Kaucky, J. Moravkova, J. Rathousky, S. Sklenak, M. Vorokhta, L. Brabec, R. Pilar, I. Jakubec, E. Tabor, P. Klein, P. Sazama, Effect of enhanced accessibility of acid sites in micromesoporous mordenite zeolites on hydroisomerization of *n*-hexane, ACS Catal. 7 (2017) 5781–5795.

[27] N. Chaouati, A. Soualah, M. Chater, M. Tarighi, L. Pinard, Mechanisms of coke growth on mordenite zeolite, J. Catal. 344 (2016) 354–364.

[28] K. W. Kolasinski, The composition of fluoride solutions, J. Electrochem. Soc. 152 (2005) J99–J104.

[29] J. S. Judge, A study of the dissolution of SiO_2 in acidic fluoride solutions, J. Electrochem. Soc., 118 (1971) 1772–1775.

[30] G. A. Olah, J. T. Welch, Y. D. Vankar, M. Nojima, I. Kerekes, J. A. Olah, Synthetic methods and reactions. 63. Pyridinium poly(hydrogen fluoride) (30% pyridine-70% hydrogen fluoride): A convenient reagent for organic fluorination reactions, J. Org. Chem. 44 (1979) 3872–3881.

[31] M. Guisnet, L. Pinard, Characterization of acid-base catalysts through model reactions, Catal. Rev. 60 (2018) 337–436.

[32] T. -C. Tsai, Appl. Reactivation of acidic sites in mordenite used in toluene disproportionation, Appl. Catal., A 301 (2006) 292–298.

[33] O. Marie, F. Thibault-Starzyk, P. Massiani, Vibrational spectroscopic studies of catalytic processes on oxide surfaces, J. Catal. 230 (2005) 28–37.

[34] P. Ratnasamy, S. Sivankar, A. Vishnoi, Acidity and catalytic selectivity in the Na-H-Mordenite system, J. Catal. 69 (1981) 428–433

[35] I. Bankos, A. L. Klyachko, T. R. Brueva, G. I. Kapustin, Reat. Kinet. Catal. Lett., 30 (1986) 297-302.

[36] M. W. Dem, J. M. Newsam, J. A. Creighton, Fluctuations in zeolite aperture dimensions simulated by crystal dynamics, J. Am. Chem. Soc. 114 (1992) 7198–7207.

[37] C. Miranda, J. Urresta, H. Cruchade, A. Tran, M. Bengahlem, A. Astafan, P. Gaudin, T. J. Daou, A. Ramírez, Y. Pouilloux, A. Sachse, L. Pinard, Exploring the impact of zeolite porous voids in liquid phase reactions: The case of glycerol etherification by tert-butyl alcohol, J. Catal. 365 (2018) 249–260.

[38] S. M. Babitz, B. A. Williams, J. T. Miller, R. Q. Snurr, W. O. Haag, H. H. Kung, Monomolecular cracking of *n*-hexane on Y, MOR, and ZSM-5 zeolites, Appl. Catal., A 179 (1999) 71–86.

[39] T. F. Narbeshuber, H. Vinek, J. A. Lercher, Monomolecular conversion of light alkanes over H-ZSM-5, J. Catal. 157 (1995) 388–395.

[40] N. Chaouati, A. Soualah, M. Chater, L. Pinard, Beneficial changes in coke properties with alkaline treatment on aluminum-rich mordenite, J. Catal. 353 (2017) 28–36.

[41] M. Tromp, J. A. van Bokhoven, M. T. Garriga Oostenbrink, J. H. Bitter, K. P. de Jong, D. C. Koningsberger, Influence of the generation of mesopores on the hydroisomerization activity and selectivity of *n*-hexane over Pt/mordenite, J. Catal. 190 (2000) 209–214.

Chapter V: Toolbox of post-synthetic mordenite modification strategies: Impact on textural acidic and catalytic properties

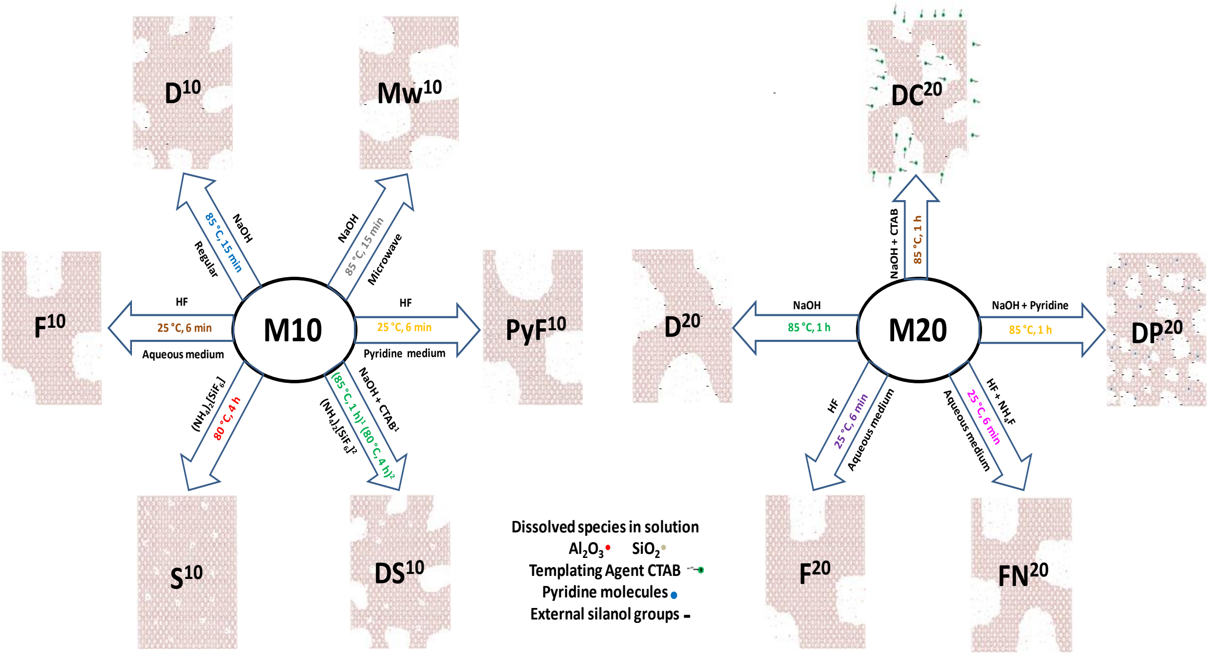

Based on publication accepted in ChemCatChem Journal

doi.org/10.1002/cctc.201900927, 2019

Hussein Issa, Nourrdine Chaouati, Joumana Toufaily, Tayssir Hamieh,

Alexander Sachse, Ludovic Pinard

1. Introduction

In order to realize the full potential of mordenite the development of secondary porosity within its structure has been put forward.[1] In this quest, a multitude of strategies have been proposed with the aim at achieving mordenite featuring hierarchical porosity.[2] Most of these strategies are related to post-synthetic modifications. Due to their simplicity and cost efficiency dealumination and desilication processes are the most prosperous strategies. The industrially applied steaming processes yield to dealuminated mordenites, which have proven to introduce secondary porosity to the systems.[3]

Treatments with certain chemical agents, such as silicon tetrachloride ($SiCl_4$) and ammonium hexafluorosilicate (AHFS) can further lead to dealumination. [4] The development of an aluminium gradient in the framework as a consequence of the AHFS treatment has been observed, indicating that the process is diffusion controlled.[5] This observation has further been correlated to a deposit of silica[6] accompanied by a slight reduction of the crystallinity and of the unit cell volume.[7]

A further post-synthetic strategy is etching using aqueous HF solutions, which allows to extract selectively aluminium from the zeolite framework and hence decrease the Brønsted acidity with important consequences on the catalytic performance.[8] The altering of the HF ionization equilibrium in water through the addition of NH_4F allows for the unbiased removal of Si and Al from the zeolite framework.[9] In our previous study stated in the previous chapter, we developed a new mordenite etching procedure, which relies on the use of a pyridinic HF solution.[10] It was observed that the HF etching in pyridine allows for the development of mordenite catalysts with superior catalytic properties.

The removal of silicon form the zeolite through alkaline treatment has proven very efficient for preserving acidic properties to a certain extend whilst allowing for the development of mesoporosity.[11] The use of microwave heating during the alkaline treatment has been found to accelerate the generation of defined intracrystalline mesopores due to the more efficient transfer of thermal heating to the zeolite solution.[12,13] The group of Ivanova substantially contributed to the understanding of the impact of surfactants during alkaline treatment of mordenite. Depending on the severity of the alkaline treatment various composite materials (mordenite/amorphous MCM-41 type phase featuring zeolite fragments in the pore walls) could be achieved.[14-16] The obtained materials have been found to be catalytically active in the dialkylation of naphthalene, for which the parent mordenite did not allow to observe any conversion due to accessibility issues.

When applying a post-synthetic treatment to a zeolite the balance of textural gain vs. chemical loss is of paramount importance. Yet, most of the existing studies take into consideration just a limited amount of parameters. The development of silanol defects, the accessibility to BAS, the impact of the presence of EFAL induced through the treatment, the coherent crystal size (CCS) and lattice strain, among others, are parameters that substantially impact catalytic outputs, which are often neglected when describing the impact of post-synthetic zeolite modifications in catalytic applications. The scope of this contribution is hence to resume the impact of the various post-synthetic modification techniques and compare them as texture and chemical property are concerned. In this chapter, a systematic study comparing key properties, such as synthesis yield, coherent crystal size, silanol defects, Brønsted and Lewis acidity, micro- and mesoporosity, Si/Al ratio, morphology, has been performed. These have further been correlated to the outputs observed in *n*-hexane cracking and toluene disproportionation, such as initial and final activity, selectivity and coke content.

2. Experimental section

Alkaline treatments, chemical dealumination and fluorine etching were carried out on protonic mordenite zeolites (Süd Chemie) with Si/Al ratio of 10 and 20 (noted M10 and M20). The operating conditions used and obtained yield are summarized in the Table V.1 and V.2.

Alkaline treatment: *Classical alkaline treatment* (D^{10} and D^{20} series) was performed by NaOH with 0.2 or 0.6 M at 85 °C for 60 min on M20 and for 15 min for M10 under stirring (400 rpm). The catalysts were recovered by centrifugation, washed with deionized water, dried and calcined at 550 °C for 4 h (heating rate 5 °C min^{-1}). The protonic form of the catalyst were obtained after three consecutive exchange cycles with a 1 M solution of NH_4NO_3 using 50 cm^3 g^{-1}. The exchange was carried out at 85 °C for 1 h. After careful washing to pH 7 the solids were dried at 80 °C during 12 h and then calcined 550 °C for 4 h. *CTAB assisted alkaline treatment* (DC^{20} series): Analogous to the classical alkaline treatment hexadecyltrimethylammonium bromide (CTAB, 0.27 M) was added to the alkaline solution prior to the addition of M20. *Pyridine assisted alkaline treatment (*DP^{20})*:* Analogous to the classical alkaline treatment, pyridine was added to the alkaline solution prior to the addition of the zeolite. The amount of pyridine added to the alkaline solution were 1650, 8250, and 16500 µmol g^{-1}, which correspond to ca 3, 15, and 30 times the number of Brønsted acid sites probed on M20 by pyridine at 150 °C. ***Alkaline treatment using microwaves* (Mw^{10}):** Classical dealumination on M10 was carried out in Teflon crucible that where heated in a microwave

(Microsynth, Milestone) using an input power of 250 W for 15 min. All the alkaline treatments were done at the ratio of 1g zeolite per 15 mL of basic solution.

Table V.1. Operating conditions for the post-synthesis modifications of M10.

Series	**Catalyst**	**Media**	**[SiF$_6^{2-}$]**	**[NaOH]**	**[CTAB]**	**[HF]**	**T**	**Time**	**Yield**[a]
			M				**°C**	**min**	**%**
D^{10}	**D$_{0.2}^{10}$**	H_2O		0.2			85	15	82
	D$_{0.4}^{10}$	H_2O		0.4			85	15	70
	D$_{0.6}^{10}$	H_2O		0.6			85	15	66
Mw^{10} **[13]**	**Mw$_{0.2}^{10}$**	H_2O		0.2			85	15	86
	Mw$_{0.4}^{10}$	H_2O		0.4			85	15	79
	Mw$_{0.6}^{10}$	H_2O		0.6			85	15	73
S^{10} **[5,7]**	**S$_{0.1}^{10}$**	H_2O	0.1				80	240	94
	S$_{0.2}^{10}$	H_2O	0.2				80	240	96
	S$_{0.4}^{10}$	H_2O	0.4				80	240	93
[17]	**DS$_{0.0}^{10*}$**	H_2O	0.0	0.6	0.27		85	60	50
DS^{10}	**DS$_{0.1}^{10}$**	H_2O	0.1				80	240	88
	DS$_{0.2}^{10}$	H_2O	0.2				80	240	84
	DS$_{0.4}^{10}$	H_2O	0.4				80	240	83
F^{10} **[10]**	**F$_{0.25}^{10}$**	H_2O				0.25	25	6	83
	F$_{0.50}^{10}$	H_2O				0.50	25	6	85
	F$_{1.50}^{10}$	H_2O				1.50	25	6	45
PyF^{10} **[10]**	**PyF$_{0.25}^{10}$**	Pyridine				0.25	25	6	80
	PyF$_{0.50}^{10}$	Pyridine				0.50	25	6	78
	PyF$_{1.50}^{10}$	Pyridine				1.50	25	6	51

HF etching was carried out through the use of an aqueous HF solution (F^{10}, F^{20}) or ammonium fluoride (4.5 M) on M20 (FN^{20}) and a solution of HF in pyridine on M10 (PyF^{10}). In a 100 mL Teflon vessel were placed 1 g of the parent mordenite. 20 mL of the HF solution of different concentrations ranging from 0.2 and 1.50 M was added at 25 °C for 6 min under mechanical stirring (500 rpm). Thereafter the zeolite suspensions were centrifuged at 6000 rpm for 10 min. The residue was washed with 40 mL demineralized water. Washing cycles were performed until neutral pH. Solids were dried at 100 °C for 12 h and calcined under air flow (100 ml min^{-1} per 1 g of zeolite) at 550 °C for 8 h.

Ammonium hexafluorosilicate (AHFS) treatment: 1 g of NH_4-MOR was preheated at 80 °C in a 50 mL of 3 M aqueous solution of NH_4OAc. Then 10 cm^3 of 0.1 M aqueous AHFS solution was added drop-wise during 1 h. The solution was then kept at 80 °C with constant stirring (400 rpm) for 3 h. The resulting solution was recovered by filtration and repeatedly washed with 1 L of hot water (80 °C). After that, the material was dried for 12 h at 100 °C followed by calcination at 650 °C for 4 h.

Table V.2. Operating conditions of the post-synthesis modifications of M20.

Series	Catalyst	[Py]	[OH]	[CTAB]	[HF]	[NH_4F]	Time	T	Yield[a]
		µmol $g_{zeolite}^{-1}$	(M)				(min)	°C	%
D^{20}	**$D_{0.2}^{20}$**		0.2				60	85	73
	$D_{0.6}^{20}$		0.6				60	85	66
DC^{20} [18]	**$D_{0.2}C^{20}$**		0.2	0.27			60	85	76
	$D_{0.6}C^{20}$		0.6	0.27			60	85	61
DP^{20} [18]	**$D_{0.6}\,P_{1650}^{20}$**	1650	0.6				60	85	77
	$D_{0.6}\,P_{8250}^{20}$	8250	0.6				60	85	76
	$D_{0.6}\,P_{16500}^{20}$	16500	0.6				60	85	72
F^{20} [9]	**$F_{0.2}^{20}$**				0.2		6	25	91
	$F_{0.5}^{20}$				0.5		6	25	94
	$F_{0.7}^{20}$				0.7		6	25	86
FN^{20} [9]	**$F_{0.2}N^{20}$**				0.2	4.5	6	25	86
	$F_{0.5}N^{20}$				0.5	4.5	6	25	83
	$F_{0.7}N^{20}$				0.7	4.5	6	25	82

[a] *Calculated from the weight difference before and after post-treatment*

3. Results

Eight chemical post-synthesis treatments were carried out on two commercial mordenite zeolites with Si/Al ratios of 10 and 20 (denoted M10 and M20, respectively). The alkaline treatments were carried out at 85 °C during 15 min on M10 and 60 min on M20 with different concentration of NaOH (D^{10} and D^{20}). The alkaline treatment was further carried out: *i*) assisted by microwaves (Mw^{10}), ii) in the presence of CTAB (DC^{20}), and iii) in the presence of pyridine (DP^{20}). The fluorine etching was carried out at 25 °C during 6 min in: iv) aqueous medium (F^{10} and F^{20}), v) adding ammonium fluoride (NF^{20}) or vi) in pyridine medium (PyF^{10}). The chemical dealumination was performed at 80-85 °C during 240 minutes on M10 by using vii) ammonium hexafluorosilicate ($(NH_4)_2SiF_6$) (S^{10}) or after viii) the desilication of the parent zeolite in presence of CTAB (DS^{10}).

3.1 Textural properties

Tables V.3 and V.4 summarize the textural properties (microporous and mesoporous volumes, coherent crystal size and strain) and Figures V.1 and V.2 compare the TEM image of the parent mordenites (M10 and M20) and of the eleven catalyst series resulting from the different post-synthetic treatments.

Table V.3. Crystallinity, coherent crystal size and strain, micropore and mesopore volumes of the modified M10.

Series	**Catalyst**	**Crystallinity**[a]	**CCS**[b]	**Strain**[c]	**V_{micro}**[d]	**V_{meso}**[e]
		(%)	**(nm)**		**(cm^3 g^{-1})**	
M^{10}	**M^{10}**	100	62.8	8.84	0.19	0.09
D^{10}	**$D_{0.2}^{10}$**	84	56.1	9.48	0.18	0.11
	$D_{0.4}^{10}$	83	55.4	9.54	0.17	0.16
	$D_{0.6}^{10}$	52	46.5	11.8	0.16	0.21
Mw^{10}	**$Mw_{0.2}^{10}$**	77	50.6	10.5	0.17	0.11
	$Mw_{0.4}^{10}$	76	48.1	10.9	0.16	0.12
	$Mw_{0.6}^{10}$	68	47.3	11.5	0.15	0.14
F^{10}	**$F_{0.25}^{10}$**	70	39.0	14.7	0.17	0.08
	$F_{0.50}^{10}$	65	36.8	16.4	0.17	0.09
	$F_{1.50}^{10}$	57	32.0	19.4	0.18	0.13
PyF^{10}	**$PyF_{0.25}^{10}$**	80	57.1	9.3	0.19	0.08
	$PyF_{0.50}^{10}$	84	57.3	9.3	0.16	0.12
	$PyF_{1.50}^{10}$	79	55.0	9.7	0.18	0.15
S^{10}	**$S_{0.1}^{10}$**	87	62.7	8.84	0.17	0.10
	$S_{0.2}^{10}$	86	60.8	8.71	0.17	0.10
	$S_{0.4}^{10}$	80	60.0	8.77	0.16	0.08
DS^{10}	**$DS_{0.0}^{10}$**	72	41.5	13.3	0.14	0.28
	$DS_{0.1}^{10}$	72	48.3	10.9	0.14	0.30
	$DS_{0.2}^{10}$	58	36.5	15.2	0.10	0.24
	$DS_{0.4}^{10}$	59	43.5	12.4	0.12	0.24

[a] *Measured by XRD analysis;* [b,c] *Coherent crystal size and strain estimated by Scherrer method;* [d] *Estimated by t-plot method;* [e] *Mesopore volume= V_{total} - V_{micro} (V_{total}: determined from the adsorbed volume at P/P_0= 0.96).*

Parent zeolites: Both parent zeolites M10 and M20 present very similar textural properties. They feature type I nitrogen adsorption and desorption isotherms as expected for microporous materials and feature a microporous volume of 0.19 and 0.18 cm^3 g^{-1}, respectively (Figures V.3 and V.4, Tables V.3 and V.4). The morphology of the parent zeolites can be described as aggregates of smaller zeolite particles with sizes comprised between 40 and 100 nm (Figures V.1 and V.2). Form Williamson-Hall analysis a coherent crystal size (CCS) of 63 and 66 nm for M10 and M20 were calculated with a lattice strain of 8.8 and 7.3, respectively (Tables V.3 and V.4).

For further considerations the crystallinity of the parent zeolites has been set as 100% and the impact of each of the modification strategies has been compared in terms of crystallinity of the obtained samples.

Table V.4. Crystallinity, coherent crystal size and strain, micropore and mesopore volumes of the modified M20.

Series	Catalyst	Crystallinity[a]	CCS[b]	Strain[c]	V_{micro}[d]	V_{meso}[e]
		%	nm		$cm^3\ g^{-1}$	
M^{20}	M^{20}	100	66.4	7.3	0.18	0.11
D^{20}	$D_{0.2}^{20}$	93	55.7	9.1	0.16	0.13
	$D_{0.6}^{20}$	60	56.3	8.9	0.09	0.54
DC^{20}	$D_{0.2}C^{20}$	98	57.8	8.2	0.18	0.15
	$D_{0.6}C^{20}$	68	48.7	10.5	0.09	0.36
DP^{20}	$D_{0.6}\ P_{1650}^{20}$	66	55.8	9.8	0.08	0.58
	$D_{0.6}\ P_{8250}^{20}$	59	58.1	9.9	0.10	0.72
	$D_{0.6}\ P_{16500}^{20}$	42	58.7	9.8	0.11	0.54
F^{20}	$F_{0.2}^{20}$	90	57.9	9.3	0.18	0.13
	$F_{0.5}^{20}$	86	57.0	9.9	0.17	0.13
	$F_{0.7}^{20}$	84	56.0	9.1	0.18	0.14
FN^{20}	$F_{0.2}N^{20}$	91	51.0	10.5	0.17	0.15
	$F_{0.5}N^{20}$	89	51.7	9.4	0.17	0.20
	$F_{0.7}N^{20}$	90	48.0	10.4	0.15	0.15

[a] Measured by XRD analysis; [b,c] Coherent crystal size and strain estimated by Scherrer method; [d] Estimated by t-plot method; [e] Mesopore volume= V_{total}-V_{micro} (V_{total}: determined from the adsorbed volume at P/P_0= 0.96).

Alkaline treatment: The treatment that most severely impacts microporosity is the alkaline treatment. As expected the basic treatment of the high silica mordenite (M20) affects microporosity more severely than the low silica M10 (Figure V.5a). The reduction of microporosity correlates well to the reduction of crystallinity (Series D^{10} and D^{20} in Tables V.3 and V.4). Indeed the samples for which microporosity is most impacted present the greatest increase in mesoporous volume (Figure V.5b). Mesoporous volume substantially develops with increasing concentration of the alkaline solution and amounts to 0.54 and 0.21 $cm^3\ g^{-1}$ for M20 and M10 treated with a 0.6 M NaOH solution, respectively. From the shape of the nitrogen adsorption and desorption isotherms it can be deduced that the mesoporosity that develops is of rather large size distribution and comprised between 5 and 30 nm (Figure V.3). This was confirmed from the TEM images, which present a rather homogeneous distribution of larger mesoporous (Figures V.1 and V.2). The use of an alternative heating source during alkaline treatment, *i.e.* microwave heating (Series Mw^{10}), does not allow for generating mesoporosity in the same manner as the thermal treatment (Table V.1). Indeed, even for the treatment with 0.6 M NaOH solution the shape of the isotherm is similar to the parent zeolite (Figure V.1), yet a more pronounced uptake in the relative pressure range close to saturation can be observed, indicating the creation of interparticular space. This observation is confirmed by the TEM images (Figure V.1), which reveal aggregates of particles smaller in size compared to the parent zeolite. Indeed an important reduction in CCS form 63 to 47 nm was calculated from the FWHM of the XRD peaks for the parent M10 and MW$_{0.6}$^{10} sample, respectively.(Table V.3)

The addition of pyridine to the desilication solution (Series DP^{20}) has substantial impact on the textural features. As such, the crystals are shaped into smaller zeolite particles, which can be inferred from the important nitrogen uptake in the adsorption isotherms at very high relative pressures, which is typical for intraparticular adsorption (Figure V.4; Series DP^{20}). Indeed, the higher the concentration of pyridine into the alkaline solution the stronger the difference to the classical desilication is observable (Figure V.4). The development of smaller zeolite particles can be readily inferred from the TEM images, which presents individual particles of sizes of a few nm (Figure V.2). The pyridine assisted desilication is the approach that allows for the strongest modification of textural properties. Indeed adding CTAB during the desilication (Series DC^{20}) importantly reduces the amount of developed mesopores, probably through reducing desilication kinetics (Figure V.5). For all of the desilication treatments merely little impact on the CCS and the lattice strain was observed (Tables V.3 and V4). Indeed, the development of large mesopores only slightly impacts the diffraction efficiency and hence CCS reduction is limited.

HF etching: With contrast to the alkaline treatments, HF etching (Series F^{10} and F^{20}) allows for preserving microporosity to a large extent (Tables V.3 and V4). All of the HF treatment procedures lead to the development of very lager intraparticular mesoporosity as indicated through the steep nitrogen uptake in the isotherms recorded at 77 K (Figures V.3 and V.4). As far as aqueous the HF etching is concerned, it is interesting to note that the Si/Al composition of the parent zeolite has a major impact on the CCS and lattice strain. Indeed the treatment with a 0.5 M aqueous HF solution only slightly reduces CCS for M20 whilst it almost halves for M10. This important decrease in CCS is related to the development of internal silanol defects through the treatment as supported by the development of characteristic IR bands (see below). Adding ammonium fluoride to HF solution (Series FN^{20}) only minor impacts textural properties of the mordenite, yet the amount of developed mesoporosity slightly increases.

Changing the solvent from water to pyridine importantly impacts the etching path. Indeed for M10, (Series PyF10 in Table V.3) CCS only reduces slightly, which indicates that the use of pyridine as solvent reduces the amount of internal silanol defects. For all of the samples achieved through HF etching only little textural and morphological changes can be observed through electronic microscopy (Figures V.1 and V.2).

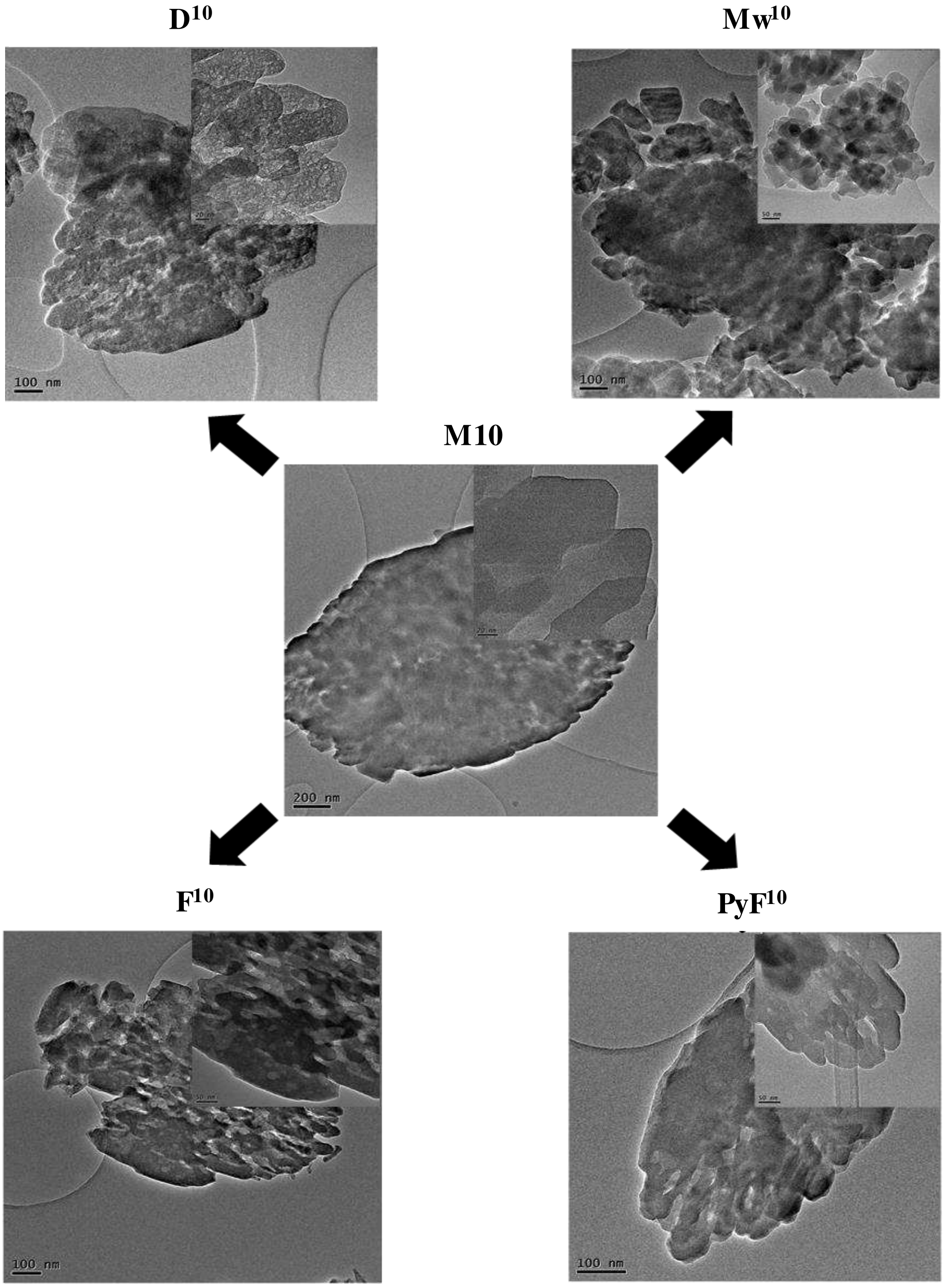

Figure V.1. TEM images of parent (M10) and modified mordenites.

AHFS treatment: Treating M10 with ammonim hexafluorosilicate hardly impacts textural properties (Series S^{10} in Table V.3). The treatment reduces negligibly microporosity and no mesoporosity is developed. Furthermore the CCS is comparable as that of the parent zeolite.

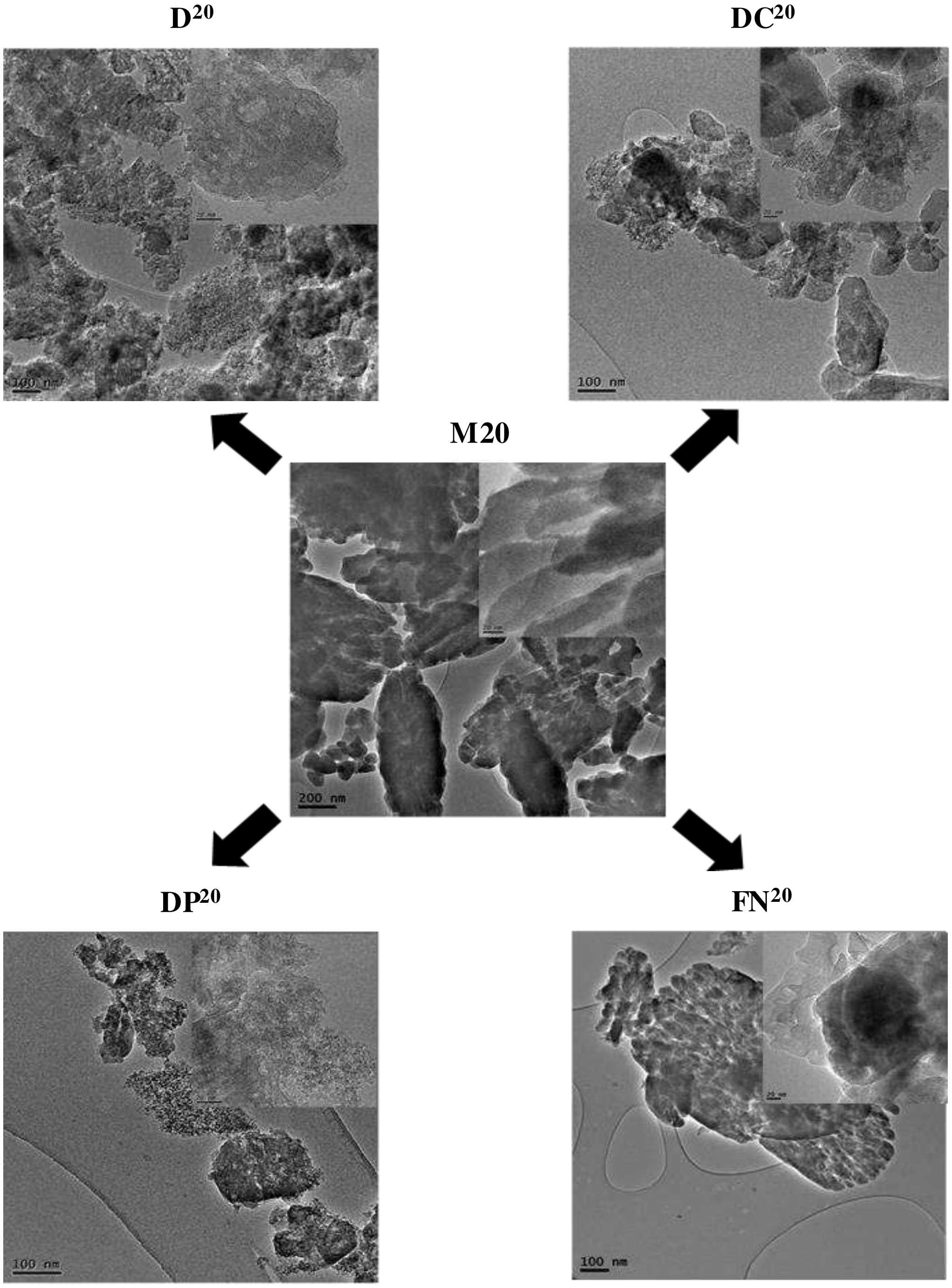

Figure V.2. TEM images of parent (M20) and modified mordenites.

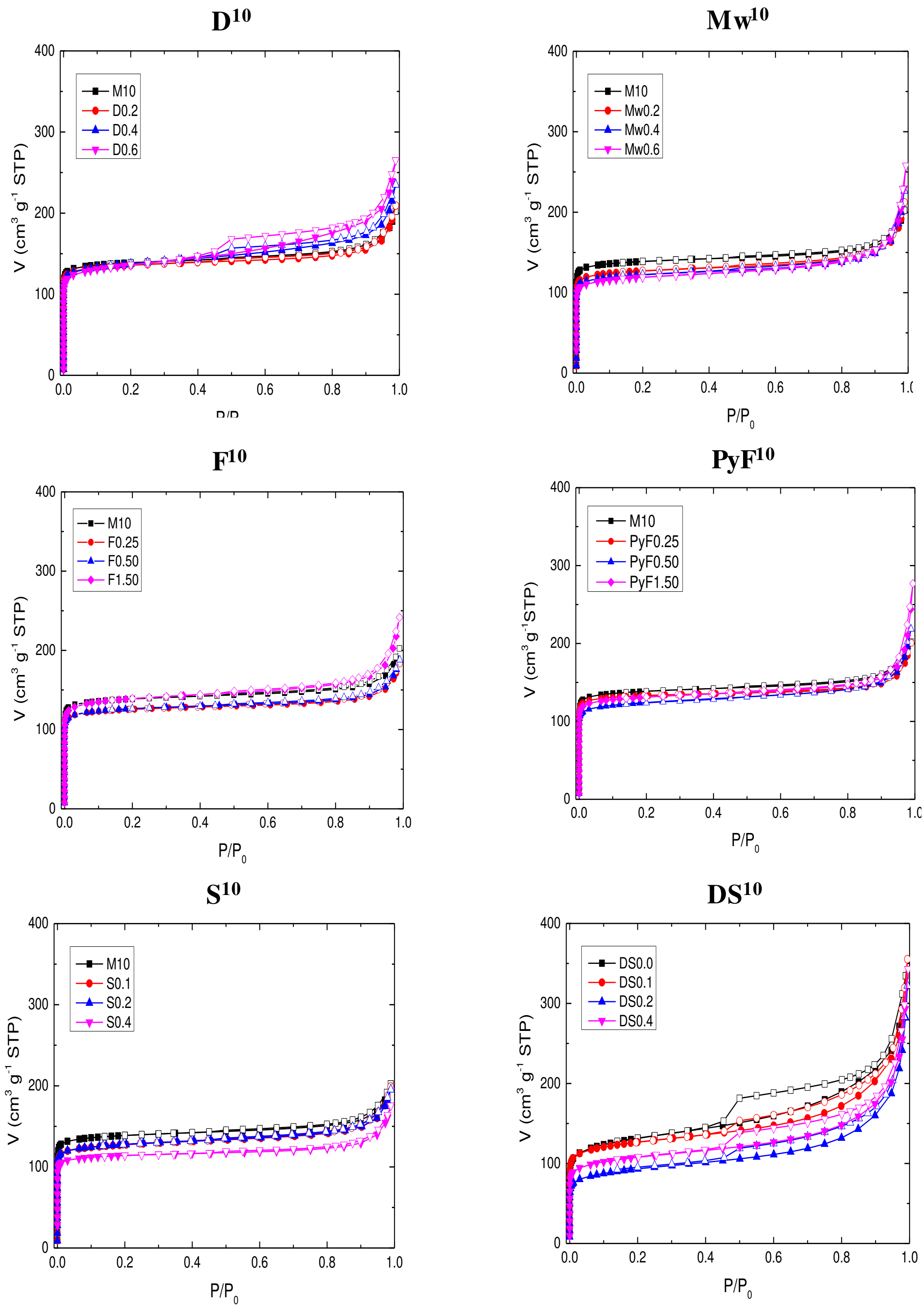

Figure V.3. Comparison of the nitrogen adsorption and desorption isotherms at 77 K of the parent mordenite (M10) and the six series: D^{10}, F^{10}, S^{10}, Mw^{10}, PyF^{10,} and DS^{10}.

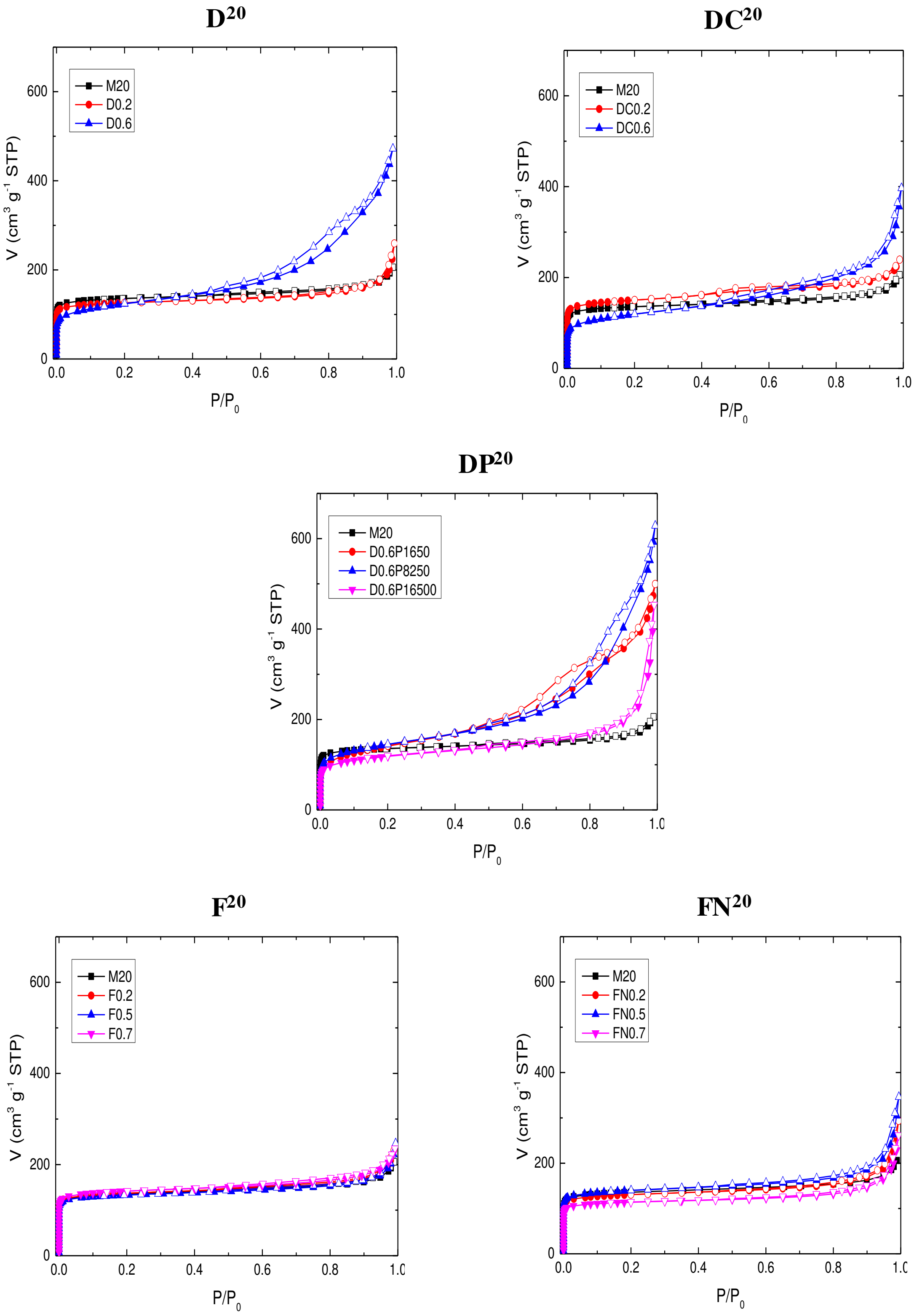

Figure V.4. Comparison of the nitrogen adsorption and desorption isotherms at 77 K of the parent mordenite (M20) and the five series: D^{20}, DC^{20}, DP^{20}, F^{20}, and FN^{20}.

Summary on textural properties: The choice of the agents used during the post-synthetic treatment of mordenite importantly impact both texture and morphology of the zeolite. Whilst alkaline treatments allow for significantly alter textural properties through the development of intracrystalline mesoporosity and through shaping the zeolite into smaller entities, etching and AHFS treatments have much less impact on texture (Figure V.5). The modification of textural properties of zeolite can importantly affect catalytic outputs through *e.g.* reducing diffusion path length. Yet as we will see below other factors (such as the presence of FEAL species) might even play a more crucial role as far as catalytic activity concerned.

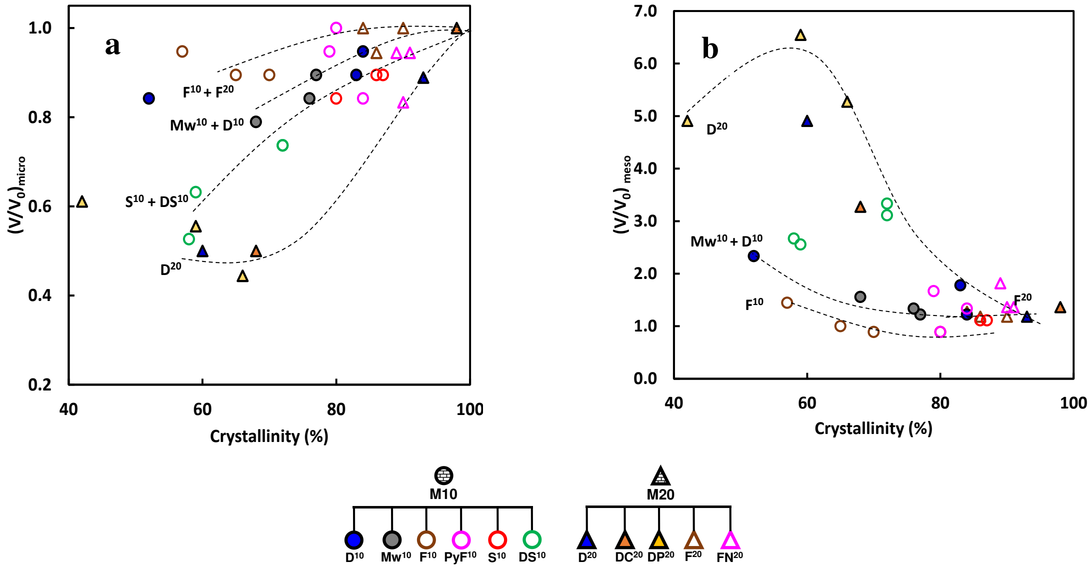

Figure V.5. Residual micropore volume **(a)** and mesopore volume **(b)** as a function of the crystallinity of the different catalyst series.

3.2 Acidic properties

The hydroxyl stretching vibration region of IR spectra before (full line) and after (dashed line) adsorption of pyridine at 150 °C on the eleven catalyst series are given in Figures V.6 and V.7. The Tables V.5 and V.6 report the global Si/Al ratio and the concentration of Brønsted and Lewis acid sites probed by pyridine at 150 °C for each sample.

Parent zeolites: M10 presents in Figure V.6 a high intense band centered at 3608 cm^{-1}, which is related to the bridged hydroxyl groups and three less intensed bands at 3745, 3733, and 3684 cm^{-1}, which can be attributed to the stretching vibrations of external and internal silanol groups and hydroxyl groups related to extraframework aluminium species (EFAL), respectively. M20 presents these four bands and an additional one at 3503 cm^{-1}, which is ascribable to the presence of hydroxyl nests and is due to its preparation process (dealumination), (Figure V.7). Contrary to M20, not all the bridged hydroxyl groups are neutralized after the adsorption of pyridine at 150 °C on M10, which means that part of the Brønsted acid sites (BAS) are inaccessible to the probe molecule. These inaccessible BAS are located in the side pockets and amount to 19%, as calculated by six bands deconvolution in our previuos study.[10]

Table V.5. Global Si/Al molar ratio, concentrations of Brønsted and Lewis acid sites probed by pyridine and accessibility of bridged hydroxyl groups of the modified M10.

Series	**Catalyst**	**Si/Al**^{a}	**[H**$^{+}$**]**^{b}	**[L]**^{c}	**Acc.**$^{\circ d}$
		mol/mol	**µmol g**$^{-1}$		
M^{10}	**M**^{10}	9.0	1014	53	0.81
D^{10}	**D**$_{0.2}^{10}$	7.5	514	68	0.663
	D$_{0.4}^{10}$	6.5	687	54	0.62
	D$_{0.6}^{10}$	6.3	247	58	0.37
Mw^{10}	**Mw**$_{0.2}^{10}$	6.8	375	80	0.70
	Mw$_{0.4}^{10}$	6.3	466	88	0.64
	Mw$_{0.6}^{10}$	6.3	409	73	0.63
F^{10}	**F**$_{0.25}^{10}$	10.9	574	131	1.00
	F$_{0.50}^{10}$	12.1	567	143	1.00
	F$_{1.50}^{10}$	17.5	412	106	1.00
PyF^{10}	**PyF**$_{0.25}^{10}$	8.6	744	96	0.90
	PyF$_{0.50}^{10}$	8.5	704	119	0.90
	PyF$_{1.50}^{10}$	9.0	826	127	0.90
S^{10}	**S**$_{0.1}^{10}$	9.3	280	34	0.51
	S$_{0.2}^{10}$	9.6	239	23	0.39
	S$_{0.4}^{10}$	10.2	180	16	0.18
DS^{10}	**DS**$_{0.0}^{10}$	9.6	592	88	0.80
	DS$_{0.1}^{10}$	9.9	353	86	0.55
	DS$_{0.2}^{10}$	11.0	98	30	0.32
	DS$_{0.4}^{10}$	12.1	107	33	0.19

[a] Measured by ICP; [b,c] Measured by pyridine adsorbed at 150 °C; [d] Drawn from the ration between the intensity of the hydroxyl group before and after the adsorption of pyridine at 150 °C.

Alkaline treatments: The alkaline treatment by both thermal or microwave heating leads to an important decrease of the Si/Al ratio (7.5-6.3), which is more important for samples treated with increasing NaOH concentration (Table V.5). The common alkaline treatment on M10 (D^{10} series) leads to a decrease of the intensity of the band at 3606 cm^{-1} (decreasing accessibility of pyridine to the bridged OH), yet without significant modification of the silanol bands (Figure

V.6). On M10 treated with a high concentration of NaOH (0.6 M, $D_{0.6}^{10}$), less than 40 % of bridged OH band are neutralized by the organic probe (Table V.5), which indicates an important accumulation of extra framework silicon and aluminium specie in the large channels of mordenite zeolite. The losses of the bridged OH and of their accessibility, yield to a significant decrease in the number of BAS, *i.e.* on the $D_{0.6}^{10}$ sample, the remaining concentration after alkaline treatment is only the quarter of the parent zeolite (Table V.5).

Table V.6. Global Si/Al molar ratio, concentrations of Brønsted and Lewis acid sites probed by pyridine and accessibility of bridged hydroxyl groups of the modified M20.

Series	**Catalyst**	**Si/Al[a]**	**[H+][b]**	**[L][c]**	**Acc.°[d]**
		mol/mol	**µmol g^{-1}**		
M^{20}	**M^{20}**	20.4	552	47	1.00
D^{20}	**$D_{0.2}^{20}$**	18.2	491	96	0.95
	$D_{0.6}^{20}$	17.1	324	40	0.67
DC^{20}	**$D_{0.2}C^{20}$**	18.6	531	77	1.00
	$D_{0.6}C^{20}$	18.4	329	59	0.84
DP^{20}	**$D_{0.6}\,P_{1650}^{20}$**	17.8	376	105	1.00
	$D_{0.6}\,P_{8250}^{20}$	18.6	300	87	1.00
	$D_{0.6}\,P_{16500}^{20}$	18.3	314	105	1.00
F^{20}	**$F_{0.2}^{20}$**	34.2	378	92	1.00
	$F_{0.5}^{20}$	34.1	324	72	1.00
	$F_{0.7}^{20}$	34.1	322	66	1.00
FN^{20}	**$F_{0.2}N^{20}$**	16.8	481	81	1.00
	$F_{0.5}N^{20}$	15.0	421	49	0.95
	$F_{0.7}N^{20}$	14.9	494	72	1.00

[a] Measured by ICP; [b,c] Measured by pyridine adsorbed at 150 °C; [d] Drawn from the ration between the intensity of the hydroxyl group before and after the adsorption of pyridine at 150 °C.

It is worth to mention that in this study no subsequent acid leaching was performed, which would allow to remove such EFAL specie. When the alkaline treatment is assisted by microwave heating (Mw^{10} series), many hydroxylated EFAL species (band at 3661 cm^{-1}) develop independently of the NaOH concentration. These species lead to an increased inaccessiblity of pyridine to BAS located within the zeolite micropores. Indeed, the alkaline treatment assisted by microwave heating promotes both the dislodgement of aluminium and silicon atoms of the zeolite framework and yields to a large amount of hydroxylaluminates (*e.g.* $Al(OH)^{2+}$, $Al(OH)^{+}_{2}$, AlOOH, $Al(OH)_3$).[19,20]

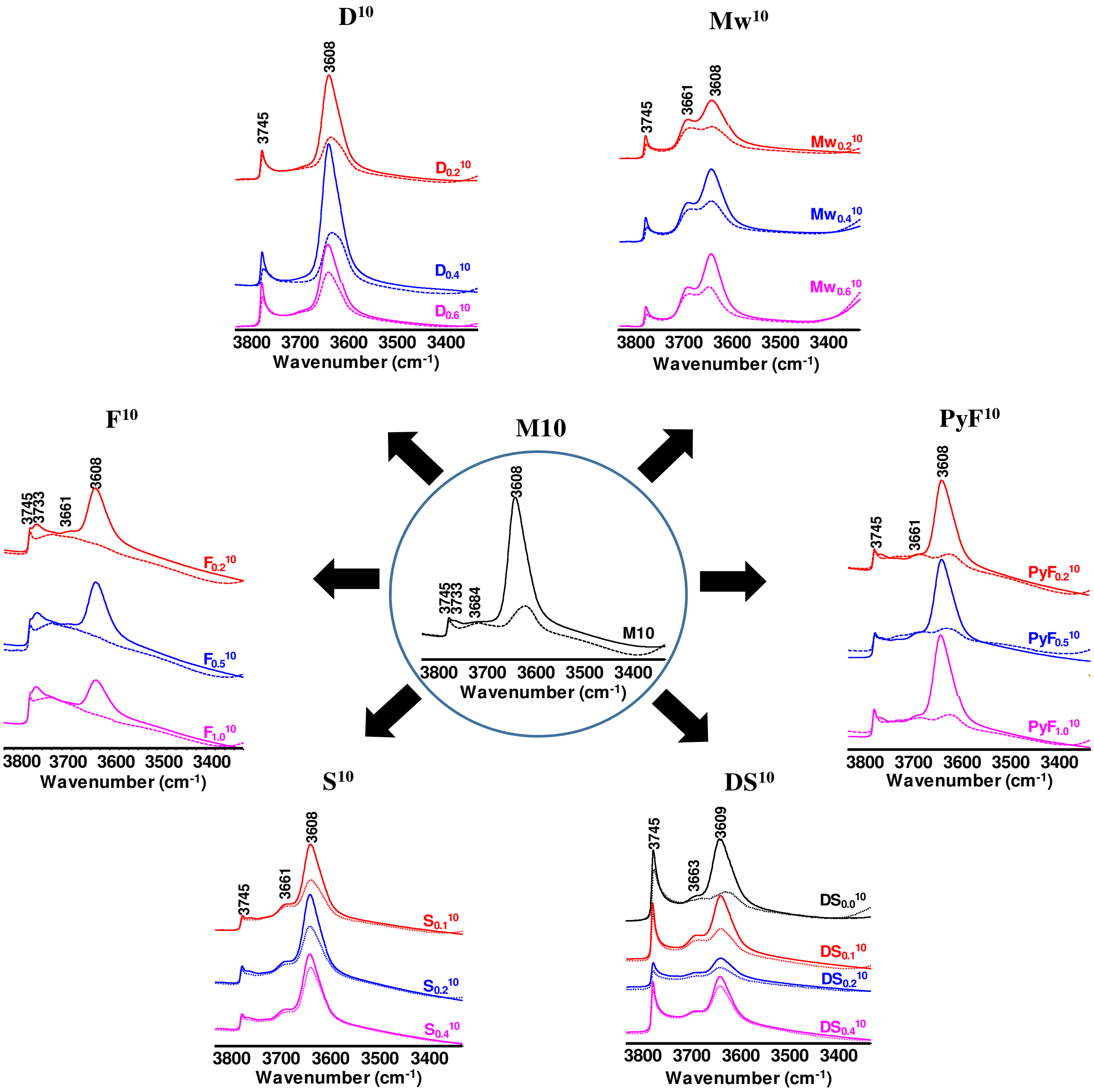

Figure V.6. Comparison of IR spectra before and after pyridine adsorption at 150 °C of M10 and the six catalyst series

On M20, the presence of pyridine and CTAB in solution during the basic treatment prevents even at high NaOH concentration (0.6 M) the desilication of the framework (Table V.6). The impact of alkaline treatment carried out with a low concentration of sodium hydroxide (0.2 M) is limited. While with 0.6 M, although the bridged OH are in large part preserved (unlike on M10), hydroxyl nests (band at 3503 cm^{-1}) are removed and the formation of external silanol (band at 3745 cm^{-1}), especially when desilication occurs in presence of pyridine, is favored (Figure V.7). Moreover the presence of pyridine allows preserving the accessibility to the BAS.

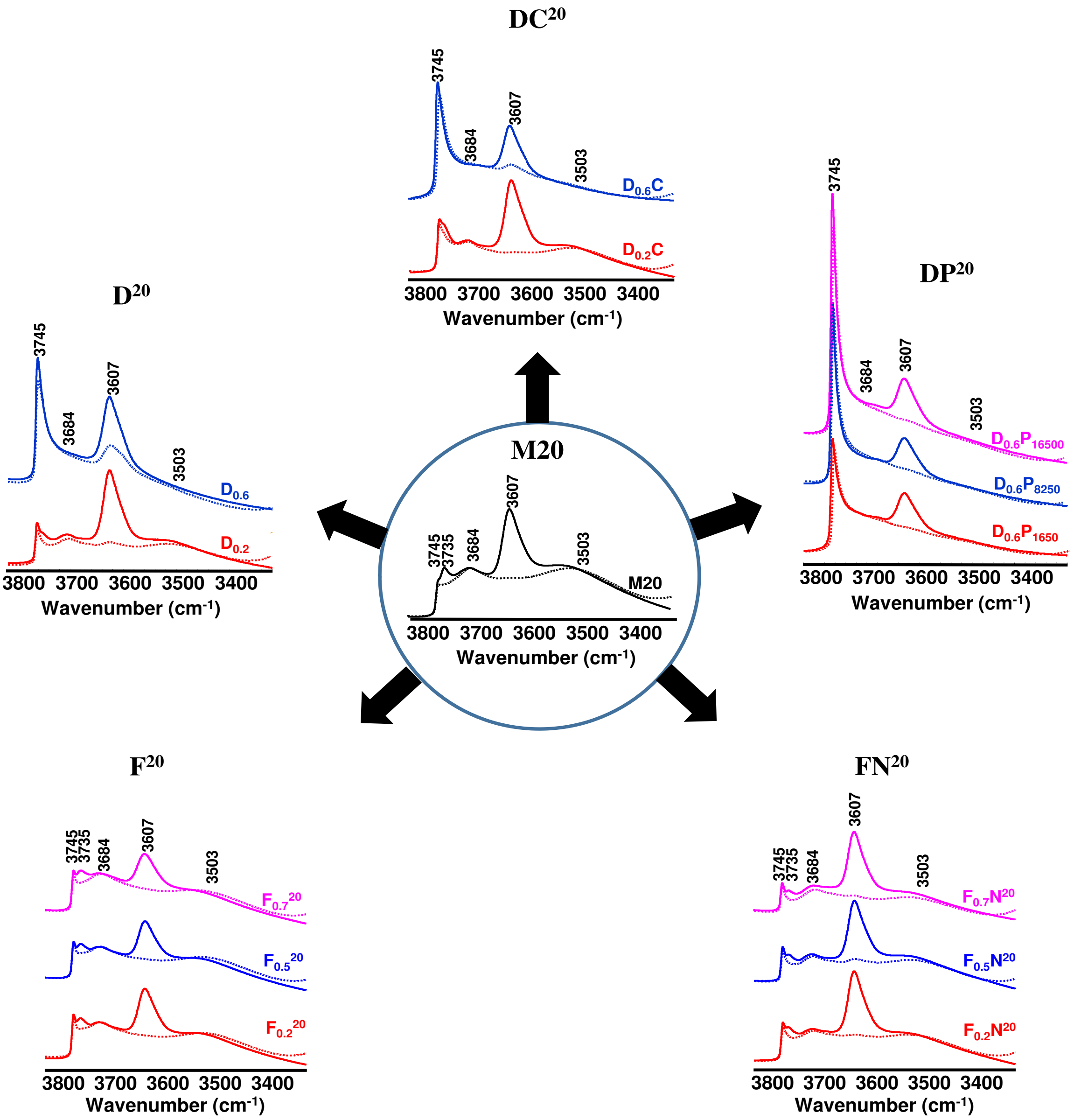

Figure V.7. Comparison of hydroxyl groups spectra before and after pyridine adsorption at 150 °C between M20 and the six catalyst series

HF etching: Fluorine etching on M10 and M20 (F^{10} and F^{20} series) only impacts the intensity of the band related to the framework aluminium species (band at 3608 cm^{-1}, Figures V.6 and V.7). The higher the employed HF concentration, the lower the intensity of the bridging OH band and the higher the obtained Si/Al ratio (Tables V.5 and V.6). The dealumination with HF leads, as expected, to the reduction of the concentration of Brønsted acid sites (Tables V.5 and V.6) and concomitantly with the appearance of the non-hydroxylated Lewis acid sites (such as Al$_2$O$_3$). Assuming that the Lewis species are constituted of two aluminum atoms, the global acidity probed by pyridine ([PyH$^+$] + 2[PyL]) is close to the amount measured on the parent zeolites. The addition of ammonium ions, *i.e.* NH_4^+ for FN^{20} and pyridinium ions for PyF^{10}, leads to an unbiased treatment,[9,10] thus preserving a large part of the acidic properties of the parent zeolites.

AHFS treatment: The chemical dealumination with ammonium hexafluorosilicate on M10 (S^{10} series) leads to a slight dealumination as indicated by the low increase of Si/Al ratio (Table V.5). The intensity of the bridged OH but especially their accessibility decreases with increasing concentration of hexafluorosilicate ion used during the treatment (Figure V.6). Only 20% of BAS are accessible to pyridine on $S_{0.4}^{10}$ against 80% on the parent zeolite (Table V.5). The presence of the band at 3661 cm^{-1} (which is related to the hydroxylated extraframework aluminium species) confirms the occurrence of dealumination. The loss of acid site accessibility is due to the deposition of EFAL specie and formation of silicon specie that block the micropore aperture. Washing of treated material with hot water is not sufficient to remove/dissolve these trapped species. Even the presence of intracrystalline mesopores (DS^{10} series) does not allow to preserve the accessibility of acidic sites. Hence, the most appropriate method would be to perform a subsequent mild acid leaching, which is known to remove such extraframework species.

Summary on acidic properties: The relative increase or decrease of the Si/Al molar ratio resulting from the various post-treatments is plotted as a function of crystallinity (Figure V.8a). After alkaline treatment, the final/initial Si/Al ratio is independent of the achieved crystallinity (even for the sample in which less than 50% crystallinity was preserved) and is 0.9 and 0.7 for M10 and M20, respectively. While after dealumination treatments, crystallinity decreases concomitantly with increasing Si/Al ratio, especially for samples in which M10 was used as parent zeolite. The dislodgement of several aluminum contrary to that of silicon atoms leads to a local collapse of the zeolite framework. Figure V.8b shows the relative intensity (I/I_0) of the bridged OH band as a function of crystallinity. The use of I/I_0 unlike that of the residual Brønsted acidity ($[BAS]/[BAS]_0$, Figure V.8c) makes it possible to avoid the accessibility issue. The relative intensity of the bridged OH band is proportional to the crystallinity of the zeolites modified by alkaline treatment, with the exception of those obtained by microwave heating (Mw^{10} series). Concerning the dealuminated zeolites, as expected the ratio of intensities (I/I_0) decreases more rapidly than the crystallinity, the loss of the acidity is mainly due to the dealumination and to a lesser extent to the decrease of the crystallinity. In addition, the alkaline treatment assisted by microwave heating leads to an unbiased dealumination and desilication of the zeolite.

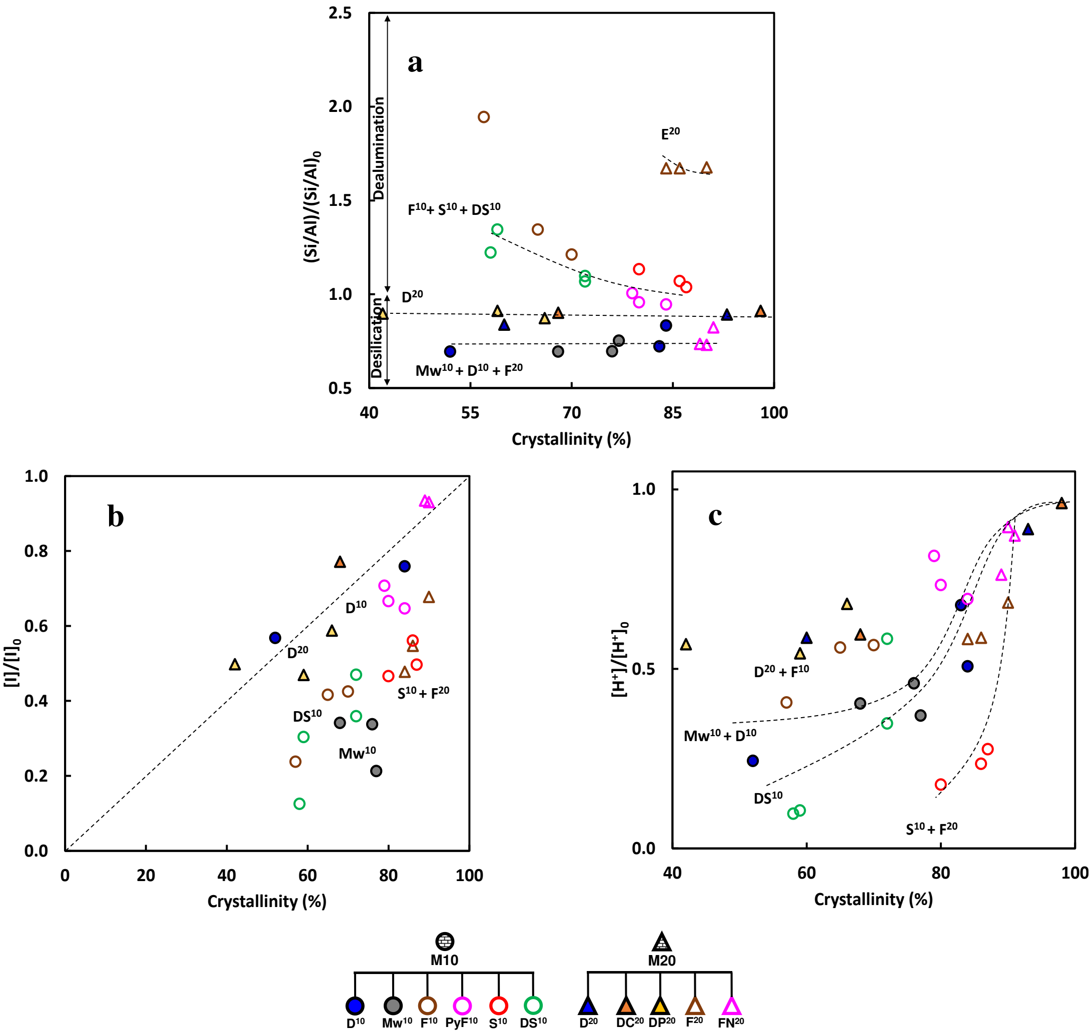

Figure V.8. Normalization of Si/Al molar ratio (a), intensity of the bridged hydroxyl IR band (3608 cm^{-1}) (b), and concentration of Brønsted acid sites (c) as a function of the crystallinity.

3.3 Catalytic properties

The acid properties of achieved catalysts are characterized by *n*-hexane cracking (α test) and toluene disproportionation.[21] No change of the mechanisms were observed, despite varying varying textural and acidic properties of catalysts. Cracking products are formed in strictly parallel reactions which indicates a monomolecular mechanism (Figure V.9a) and toluene disproportionation yields mixture of benzene and xylenes with the same selectivity at isoconversion (Figure V.9b).

Figure V.10 compares for all achieved catalysts the initial activity (A_0) and coke contents (%C) as a function of the concentration of Brønsted acid sites. Regarding to *n*-hexane cracking, no obvious correlation appear between acidity and initial activity or the coke deposition. This indicates that the formation of coke mainly depends on the origin of the parent zeolite and to a less important extent on the concentration of acid sites, which however is not consistent with the mechanism of coke formation.[22] As far as the toluene transformation is concerned, the initial activity and the coke content show to increase proportionally with BAS.

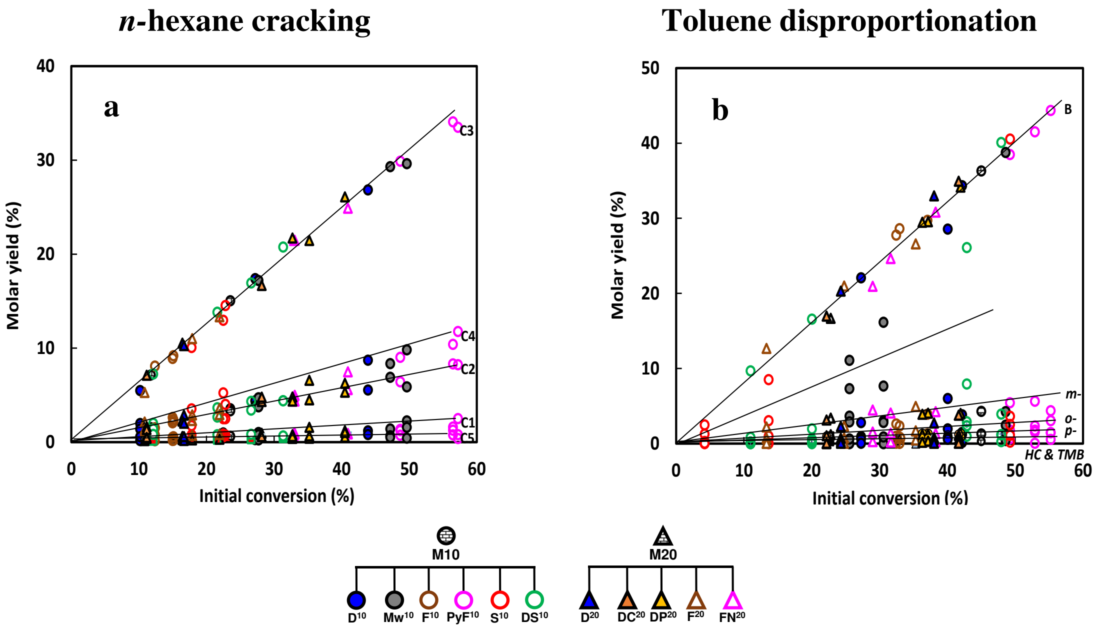

Figure V.9. Initial molar products yields of *n*-hexane cracking (a) and toluene disproportionation (b) as a function of the conversion.

The absence of the expected tendency in *n*-hexane cracking can be ascribed to the fact that only the number of BAS probed by pyridine were taken into consideration and not the actual number of active sites. While toluene and pyridine feature a similar kinetic diameter, *i.e.* 6.0 and 5.7 Å, respectively, the kinetic diameter *n*-hexane is lower (4.3 Å). The number of active sites encountered by *n*-hexane must therefore be higher. Accordingly, we assume that all bridged hydroxyl groups are accessible to *n*-hexane. The acidic sites concentration is thus corrected by the degree of accessibility derived from the IR study: $[H^+]_{corrected} = \frac{[H^+]_{probed\ by\ pyridine}}{accesibility\ degree}$. By applying this correction, we observe that the coke content increases with increasing concentration of acid sites and is higher on desilicated catalysts (*i.e* .D^{10}, D^{20}, DC^{20}, and Mw^{10}) and on the PyF^{10} series (Figure V.11b). This is consistent with what was previously reported, as desilicated catalyst promotes the coke retention.[19,21,23] The initial cracking activity is now proportional to concentration of the acid sites after having taken into account their accessibility (Figure V.11a), except for DP^{20}, FN^{20}, PyF^{10}, and Mw^{10}. The more important activity of these catalyst series could be ascribed to an exaltation of BAS by EFAL species generated during the calcination of the zeolite containing ammonium or pyridinium ions or during microwave heating.[10,24,25]

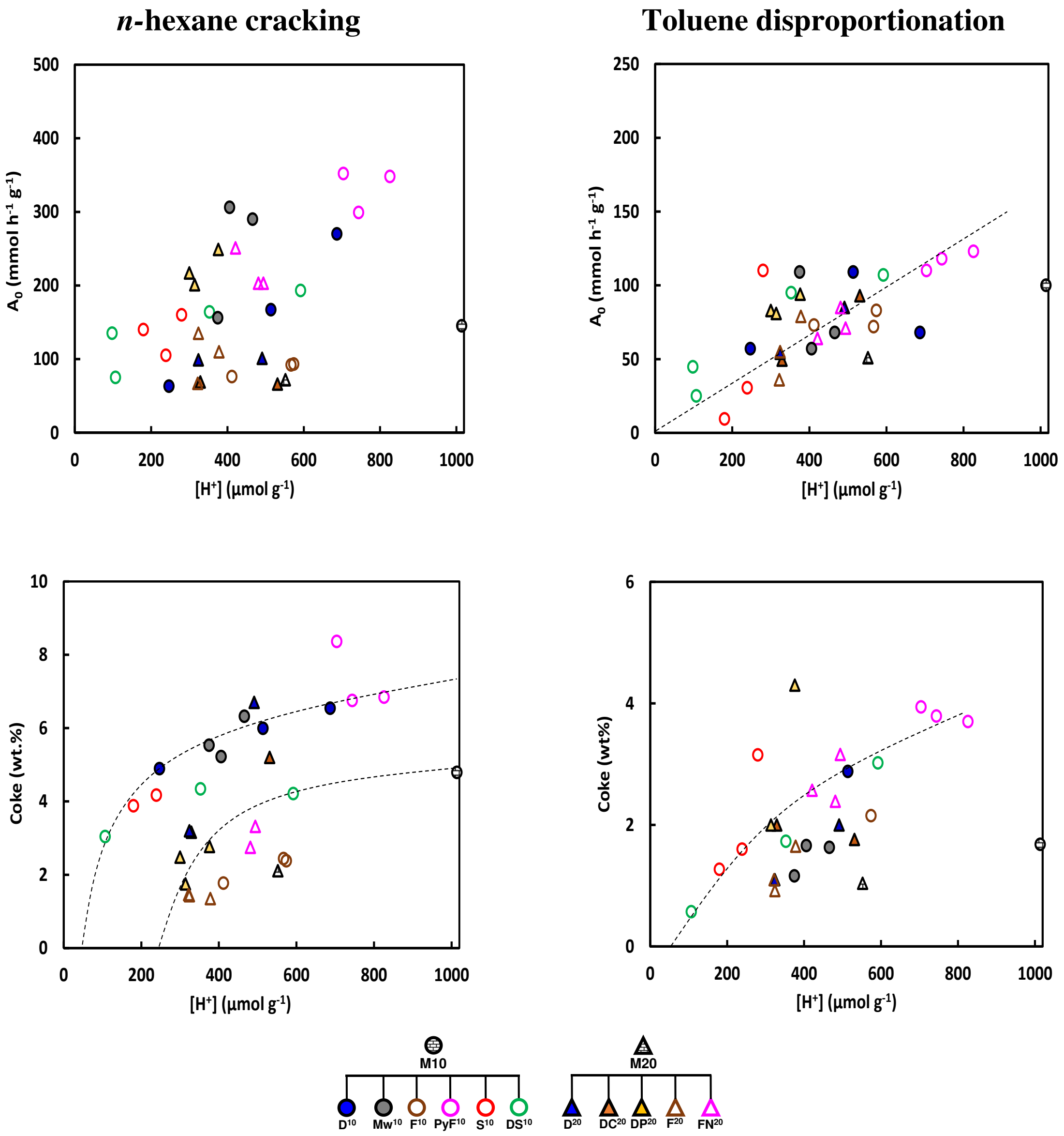

Figure V.10. *n*-Hexane cracking at 541 °C and toluene disproportionation at 450 °C on achieved catalysts: initial activity (top) and coke content after 1 h of reaction (bottom) as a function of the concentration of the Brønsted acid sites probed by pyridine.

Figure V.12 reports the residual activity (A/A_0) after 1 hour of *n*-hexane cracking and toluene disproportionation as a function of the coke content. For both reactions, A/A_0 decreases rapidly with increasing coke content. On the mordenite zeolite, a low coke content is already sufficient to block the access to all the acidic sites located within a given 12-MR channel.[22] In the toluene disproportionation, the coke toxicity is independent of the applied treatment, whereas for the *n*-hexane cracking different catalyst series can be lumped together according to their tolerance to coking. As such we observe that the most coke resistant catalysts are those achieved through desilication (D^{10}, D^{20}, and DC^{20} series), followed by FN^{20} and PyF^{10} catalysts. Finally the most sensitive catalysts to coking are those prepared through etching **F^{10}**, **F^{20}**, and **DP^{20}**.

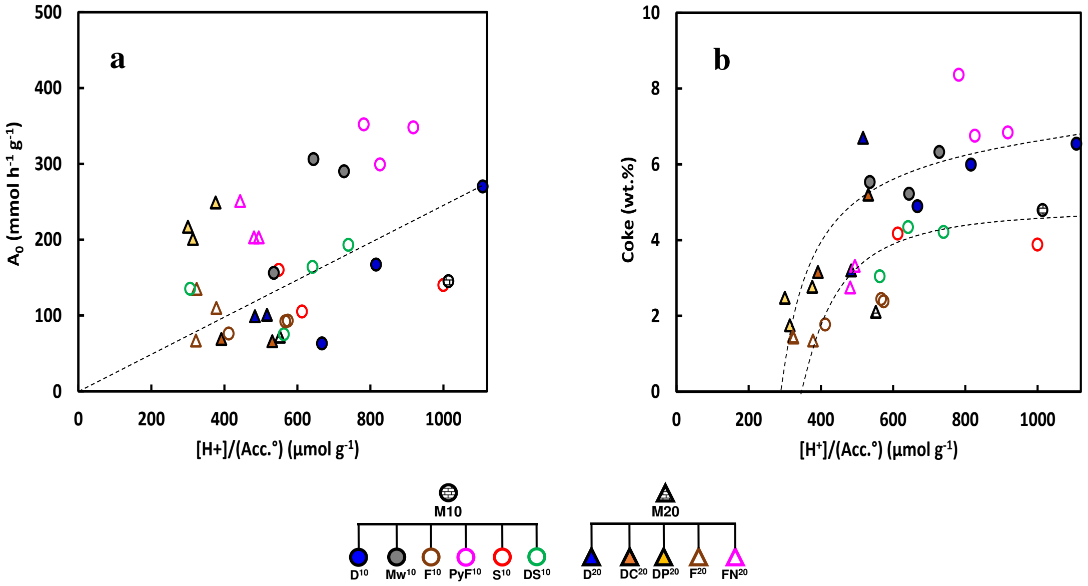

Figure V.11. Initial cracking activity (a) and coke content (b) as a function of the concentration of the actual accessible Brønsted acid sites.

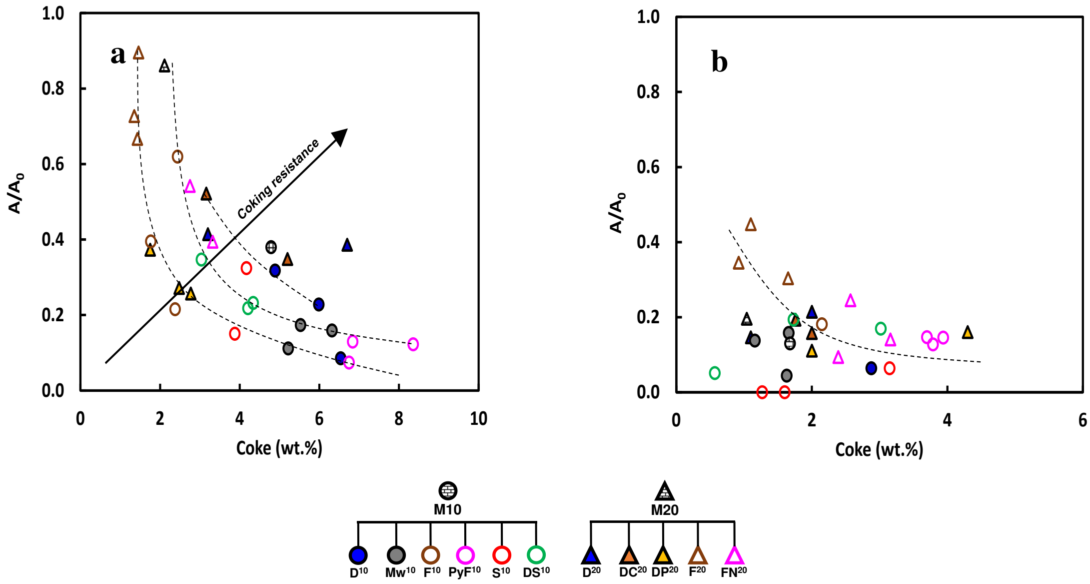

Figure V.12. Residual activity after 1 hour reaction of *n*-hexane cracking (a) and toluene disproportionation (b) a as a function coke content.

3.4 Summary and outlook

The quest to impact textural properties of mordenites has allowed for developing a large plethora of post synthetic techniques. Table V.7 gives an overview of the impact of the different post-synthetic mordenite modification strategies that have been investigated on textural, acidic and catalytic properties.

Neither of the described treatments allows to completely preserve Brønsted acidity of the parent zeolites, as the reduction of BAS is due to the reduction of crystallinity. The strongest reduction of BAS is observed for alkaline treatments, which generate an important amount of external silanol defects. Yet, desilication is the method of choice for the development of intracrystalline mesoporosity. It is the generation of mesoporosity that allows for observing improved resistance to coking, by promoting the desorption of coke precursors, through a reduction of the diffusion path length. Yet, this does not allow to achieve higher catalytic activities. Indeed, the catalysts that allow for increasing catalytic outputs are those in which extraframework species are present and which exalt the strength of the Brønsted acid sites and increase confinement. The best strategy in terms of catalyst activity (which *de facto* includes the preservation of acidity) is the fluorine etching in presence of pyridine.

As outlook of this work we highlight the necessity for developing diligent post-synthetic modification strategies that would allow for concomitantely design secondary intracrystalline porosity and tailors extraframework species within microporosity in order to achieve mordenite based catalyst with high resistance to deactivation and high catalytic activities.

Table V.7. Overview on post-synthetic mordenite modification strategies: Impact on textural, acidic and catalytic properties.

Treatment	**Alkaline treatment**					**Acid etching**				**Chemical dealumination**	
series	**D**		**Mw**	**DC**	**DP**	**F**		**FN**	**PyF**	**S**	**DS**
Si/Al	10	20	10	20	20	10	20	20	10	10	10
Yield	--	-	-	--	--	--	--	-	--		-
Crystallinity	--	--	-	-	---	--	-		-	-	--
CSS	-		--	--	-	---	--	-			-
Strain	+	+	++	++	+	+++	+++	+			++
V_{micro}	-	--	-	--	-						-
V_{meso}	+	++		+	++						+
Si/Al	--	-	--	-	-	++	++	--			+
$\nu_{3745\ cm^{-1}}$		++		++	+++						+
$\nu_{3735\ cm^{-1}}$						+	+	+			
$\nu_{3661\ cm^{-1}}$			++							+	+
$\nu_{3608\ cm^{-1}}$	--	-	--	-					-	---	---
Accessibility	--	-	--	-					-	---	---
[H^+]	--	-	--	-		--	-	-	-	---	---
[L]			+		++	++	+		++	+	
$A^{n\text{-}C6}$			++		++			++	++		-
$Coke^{Resistance}$	++	++			-	-	-			-	

-/+ Weak; --/++moderate; ---/+++ strong loss or gain

Bibliographic references

[1] M. S. Holm, E. Taarning, K. Egeblad, C. H. Christensen, Catalysis with hierarchical zeolites, Catal. Today 168 (2011) 3–16.

[2] Xianfeng Li, Roel Prinsa, Jeroen Anton van Bokhoven, J. of Catal. 262 (2009) 257–265. X. Li, R. Prinsa, J. A. van Bokhoven, Synthesis and characterization of mesoporous mordenite, J. Catal. 262 (2009) 257–265.

[3] G. S. J. Lee, J. M. Garces, G. R. Meima, M. J. M. van der Aalst, Alkylation of aromatic compounds, WO Patent 000317 (1993).

[4] H. –M. Kao, Y. -C. Chen, C. -C. Ting, P. T. Chen, J. -C. Jiang, Characterization of extraframework aluminium in H-mordenite dealuminated with ammonium hexaflourosilicate, Catal. Today 97 (2004) 13–23.

[5] Q. L. Wang, M. Torrealba, G. Giannetto, M. Guisnet, G. Perot, M. Cahoreau, J. Caisso, Dealumination of Y-zeolite with ammonium hexaflourosilicate: A SIMS-XPS study of the aluminium distribution, Zeolites 10 (1990) 703–706.

[6] G. Garralon, V. Fornes, A. Corma, Faujasites Dealuminated with ammonium hexafluorosilicate: Variables affecting the method of preparation, Zeolites, 8 (1988) 268–272.

[7] J. M. Silva, M. F. Riberio, F. R. Ribeiro, E. Benazzi, N. S. Gnep, M. Guisnet, Influence of the treatment of mordenite by ammonium hexaflourosilicate on physiochemical and catalytic properties, Zeolites 16 (1996) 275–280.

[8] A. K. Ghosh, R. A. Kydd, Acidity and Activity of Fluorinated Mordenites, J. Catal. 103 (1987) 399–406.

[9] Z. Qin, L. Lakiss, J. –P. Gilson, K. Thomas, J. –M. Goupil, C. Fernandez, V. Valtchev, Chemical Equilibirium Controlled Etching of MFI-Type Zeolite and its Influence on Zeolite Structure, Acidity, and Catalytic Activity, Chem. Mater. 25 (2013) 2759-2766.

[10] H. Issa, J. Toufaily, T. Hamieh, J. -D. Comparot, A. Sachse, L. Pinard, Mordenite etching in pyridine: Textural and chemical properties rationalized by toluene disproportionation and *n*-hexane cracking, J. Catal. Accepted (2019).

[11] J. C. Groen , T. Sano , J. A. Moulijn, J. Pérez-Ramírez, Alkaline-mediated mesoporous mordenite zeolites for acid-catalyzed conversions, J. Catal. 251 (2007) 21–27.

[12] S. Abello, J. Perez-Ramirez, Accelerated Generation of Intracrystalline Mesoporosity in Zeolites by Microwave-Mediated Desilication, Phys. Chem. Chem. Phys. 11 (2009) 2959–2963.

[13] V. Piaxao, R. Monteiro, M. Andrade, A. Fernandes, J. Rocha, A. P. Carvalho, A. Martins, Desilication of MOR Zeolite: Conventional Versus Microwave Assisted Heating, Appl. Catal., A 402 (2011) 59–68.172

[14] I. I. Ivanova, E. E. Knyazeva, Micro-mesoporous materials obtained by zeolite recrystallization: synthesis, characterization and catalytic applications, Chem. Soc. Rev. 42 (2013) 3671–3688.

[15] I. I. Ivanova, I. A. Kasyanov, A. A. Maerle, V. I. Zaikovskii, Mechanistic study of zeolites recrystallization into micro-mesoporous materials, Microporous Mesoporous Mater. 189 (2013) 163–172.

[16] I. A. Kasyanov, A. Maerle, I. I. Ivanova, V. I. Zaikovskii, Towards understanding of the mechanism of stepwise zeolite recrystallization into micro/mesoporous materials, J. Mater. Chem. A 2 (2014) 16978–16988.

[17] H. Wei, S. Xie, N. Gao, K. Liu, X. Liu, W. Xin, X. Li, S. Liu, L. Xu, Alkali treatment upon MCM-49 zeolite with various contents of HMI in the presence of CTAB and application in anisole acylation with acetic anhydride, App. Catal., A 495 (2015) 152–161.

[18] H. Issa, J. Toufaily, T. Hamieh, A. Sachse, L. Pinard, Pyridine assisted desilication of mordenite, Appl. Catal., A Submitted.

[19] M. -C Silaghi, C. Chizallet, P. Raybaud, Challenges on molecular aspects of dealumination and desilication of zeolites, Microporous Mesoporous Mater. 191 (2014) 82–96.

[20] D. L. Bhering, A. Ramirez-Solis, C. J. A. Mota, A Density Functional Theory Based Approach to Extraframework Aluminum Species in Zeolites, J. Phys. Chem. B 107 (2003) 4342-4347.

[21] M. Guisnet, L. Pinard, Characterization of acid-base catalysts through model reactions, Catal. Rev. 60 (2018) 337–436.

[22] N. Chaouati, A. Soualah, M. Chater, L. Pinard, Beneficial changes in coke properties with alkaline treatment on aluminum-rich mordenite, J. Catal. 353 (2017) 28–36.

[23] F. Ngoye, L. Lakiss, Z. Qin, S. Laforge, C. Canaff, M. Tarighi, V. Valtchev, K. Thomas, A. Vicente, J. -P. Gilson, Y. Pouilloux, C. Fernandez, L. Pinard, Mitigating coking during methylcyclohexane transformation on HZSM-5 zeolites with additional porosity, J. Catal. 320 (2014) 118–126.

[24] P. Ratnasamy, S. Sivankar, A. Vishnoi, Acidity and catalytic selectivity in the Na-H-Mordenite system, J. Catal. 69 (1981) 428–433

[25] I. Bankos, A. L. Klyachko, T. R. Brueva, G. I. Kapustin, Reat. Kinet. Catal. Lett. 30 (1986) 297–302.

General Conclusion

The present PhD thesis was devoted to the comparison and development of new mordenite post-synthetic modifications strategies and to understand their impact on textural, chemical and catalytic properties. We have substantially contributed on the actual state-of-the-art on mordenite post-synthesis treatments (Chapter I). As such we developed two innovative post-synthetic approaches based on the pyridine assisted desilication (chapter III) and on the HF etching of mordenite using pyridine as solvent (chapter IV). The extensive set of data achieved during this thesis has allowed for the understanding of the key factors that are essential for diligently design mordenite post-synthetic treatments (Chapter V).

We designed a novel mordenite post-synthetic treatment through the use of pyridine during mordenite desilication using aqueous sodium hydroxide (Chapter III). We observed that the addition of pyridine importantly modifies the classical desilication path. We observed that the pyridine assisted alkaline treatment allows to direct the desilication of mordenites, through its interaction with external hydroxides, which amount increases important by increasing the portion of pyridine during treatment. We further observed that this strategy allows to selectively direct desilication towards the achievement of small zeolite particles, which diffraction efficiency is insufficient to be detected by XRD. Pyridine remains present in the zeolite structure throughout the treatment and hence in the as-synthetized materials. During the calcination step the decomposition of the amine leads to dealumination and hence to the formation of internal EFAL. It has been found that both of these features importantly impact of the catalytic properties in *n*-hexane cracking and toluene disproportionation. Whilst the reduction of the particle size allows to diffusion path length the presence of EFAL leads to an exaltation of acidity yielding to superior activities in all of the studied reactions.

Moreover, we developed a new mordenite HF etching protocol through switching from water to pyridine as solvent (Chapter IV). We observed that contrary to the HF etching in aqueous medium, the etching in pyridine allows to preserves the global composition and acidity of parent mordenites. Zeolites etched in pyridine have a similar distribution of Brønsted acid sites (BAS) as the parent, *i.e.* 16% in 8MR channels, 19% at the intersection between side pockets and 12MR channels, and 65% in the 12MR channels. Etching in aqueous HF failed to preserve BAS distribution due to strong dealumination, which further leads to enlargement of side pockets. Mordenites etched with HF in pyridine allow for superior catalytic performance in both *n*-hexane cracking and toluene disproportionation. It was found that in toluene disproportionation the active sites are exclusively located within the 8-MR. For *n*-hexane cracking the activities of BAS in 8-MR side pockets and 12-MRs could be quantified and it was found that BAS in side pockets have higher activity than those in the large channels. The results indicate that TOF is increased through stronger confinement of BAS. Furthermore, the acid strength can further be exalted through extra framework species.

In the last chapter of this PhD thesis we present a thorough overview on various post-synthetic strategies on silica poor and rich mordenites (Chapter V). For this propose numerous approaches based on alkaline treatment (in the presence of organic cataions or organic bases) assisted through thermal and microwave heating, HF etching (in various solvents/or using additives) and ammonium hexafluorsilicate treatments were compared. None of the described treatments allows to completely preserve Brønsted acidity of the parent zeolites, which is due to the reduction of crystallinity. The strongest reduction of BAS is observed for alkaline treatments, which generate an important amount of external silanol defects. Yet, desilication is the method of choice for the development of intracrystalline mesoporosity. It is the generation of mesoporosity that allows for observing improved resistance to coking, by promoting the desorption of coke precursors, through a reduction of the diffusion path length. Yet, this does not allow to achieve higher catalytic activities. Indeed, the catalysts that allow for increasing catalytic outputs are those in which extraframework species are present and which exalt the strength of the Brønsted acid sites and reduce the void volume. The best strategy in terms of catalyst activity (which includes the preservation of acidity) is the fluorine etching in presence of pyridine.